

Shaping Effects on Aerodynamics of Long-Span Cable-Supported Bridge Deck by Unsteady RANS

Md. Naimul Haque

2015

Shaping Effects on Aerodynamics of Long-Span Cable-Supported Bridge Deck by Unsteady RANS

(非定常RANSによる長大吊形式橋梁橋桁の空力安定性への形状効果検討)

A DISSERTATION

SUBMITTED TO THE GRADUATE SCHOOL OF
URBAN INNOVATION IN PARTIAL FULFILLMENT OF THE
REQUIREMENTS

for the degree

DOCTOR OF PHILOSOPHY (IN ENGINEERING)

By

Md. Naimul Haque



Department of Civil Engineering
YOKOHAMA NATIONAL UNIVERSITY
September, 2015

Abstract

Cable-supported bridge is one of the most popular structural forms adopted for long-span bridges. The applications of cable-supported bridge are increasing with the growing number of long-span bridges due to their aesthetic view and wide navigation facility. The decks of the cable-supported bridges are hanged only by the cables to span over long distance without any intermediate support. As a result, flexibility becomes an inherent property of the cable-supported bridge decks increasing the importance of aerodynamic behavior. The shape of the bridge deck plays an important role and aerodynamic performance can be improved by shaping the bridge deck appropriately without requiring any post-construction structural or aerodynamic counter-measures. There are a number of important shaping parameters for conventional bridge decks. Their influences on aerodynamics as well as response should be well understood for shaping the bridge deck efficiently and facilitating the bridge deck design procedure.

In this context, the present study examined the influence of various important shaping parameters on aerodynamic responses of single box bridge deck by employing unsteady RANS simulation. Detailed verification and validation studies were carried out for various bluff bodies and bridge sections to check the performance of two-dimensional unsteady RANS. The main parametric study was devoted for single-box bridge deck with and without fairing due to their frequent application for long-span bridges.

A large number of practical bridge decks were surveyed for obtaining general idea about the shaping parameters and their range in practical bridges. Important shaping parameters such as top plate slope (θ_T), bottom plate slope (θ_B), side ratio (R) and width ratio (W) were considered as a main parameters of interest. Further, practical issues like, Reynolds number (Re_B) effects, influence of handrail type, effects of curb and inspection rail on aerodynamic response and flow fields were also researched.

Both for bridge deck with and without fairing, the influence of various shaping parameters on static force coefficients were investigated. It was found that the response altered significantly due to variation of shaping parameters and showed minimal value for particular combination of shaping parameters. By exploiting pressure, velocity and vorticity distribution, obtained steady-state

responses were explained. Some important and common flow features were also identified and their roles on steady-state responses were discussed.

Based on steady-state responses and flow field analysis, some specific bridge decks were chosen as a representative case for dynamic analysis. For those specific shapes, flutter derivatives were calculated and unsteady pressure characteristics were explored to evaluate their aeroelastic characteristics and reveal the roles of previously identified important flow features on flutter instability, respectively. Finally, conclusions were drawn regarding flow mechanism due to variation of shaping parameters and recommendations were provided for shaping the single-box bridge deck with and without fairing.

To my parents and sister

Acknowledgments

Alhamdulillah (all praise belongs to Allah).

Pursuing Ph.D. in a foreign country without family, relatives and friends is not an easy task. However, it became a lot easier for me as I was blessed with some nice persons around me. Now it is time to acknowledge all of their support, dedication, advice, help, inspiration and prayer for me.

First of all I would like to express my heartfelt and sincere gratitude to my supervisor, Professor Dr. Hiroshi Katsuchi for his deliberate guidance, time and continuous encouragement during the study period at the Yokohama National University. It was my pleasure and privilege to work with him during my Ph.D. course.

I would also like to thank my other advisors, Professor Dr. Hitoshi Yamada and Associate professor Dr. Mayuko Nishio for their constructive advices and suggestions they gave me during the research period. I am also grateful to my other two committee members, Professor Dr. Tatsuya Tsubaki and Associate Professor Dr. Dionysius M. Siringoringo for their important comments and recommendations.

I am highly obliged and grateful to Japanese Government (MONBUKAGAKUSHO:MEXT) for their incessant financial assistance and Japanese people for their friendly attitude during my study period in Japan.

I would like to thank all of my laboratory members for their kind cooperation, support and assistance. Specially, I would like to thank Mr. Keita Ishizeki and Mr. Jun Hitomi for helping me in

various issues those occasionally appeared. Very special thanks go to Dr. Haeyoung Kim and Zhang Kai for allowing me to access their personal computing system for research purpose.

I would like to thank Dr. Mohammad Fatehy Solaiman, Mr. Koji Inoue, Dr. Humayun Kabir, Dr. Russeldul Islam, Dr. Bijon Mitra and Aftabur Rahman for their love and affection. I would also like to extend my thanks to Dr. Palash Kumar Sarkar, Dr. Nur Mostafa, Mr. Imtiaz Hasan, Mr. Mahbub Alam, Mr. Ehsan Khaled, Mr. Mohammad Asaduzzaman and Mohammad Raknuzzaman for being such a nice friend and well-wisher.

At last but certainly not the least, I am very much thankful to my parents, sister and uncle for their love, care, support, inspiration and prayer those helped me to achieve this degree.

Contents

Abstract	ii
Dedication	iv
Acknowledgements	v
Contents	vii
List of Figures	xii
List of Tables	xx
Nomenclatures	xxi
1 Introduction	1
1.1 Problem Statement	4
1.2 Aim, Scope and Objectives	7
1.3 Methodology	8

1.4	Organization of the Thesis	10
2	General Background	12
2.1	Type of Long-Span bridge Deck	13
2.2	Shaping Parameters of Bridge Deck	14
2.3	Aerodynamic Analysis	16
2.3.1	Steady State Force Coefficients	16
2.3.2	Flutter Derivatives	18
2.3.2.1	Mathematical Background	18
2.3.2.2	Extraction of Flutter Derivatives	20
2.3.2.3	Role of Flutter Derivatives	22
2.3.3	Calculation of Unsteady Pressure Characteristics	23
2.4	Concluding Remarks	24
3	Governing Equation, Numerical Method, Grid and Validation	25
3.1	Equation of Fluid Flow	26
3.2	Reynolds-Averaged Navier-Stokes Equation	27
3.3	Turbulence Model	29
3.4	Finite Volume Method of Discretization	32
3.4.1	Discretization of the Solution Domain	32
3.4.2	Equation Discretization	33
3.4.2.1	Spatial Discretization of Convective Term	34
3.4.2.2	Spatial Discretization of Diffusive Term	36
3.4.2.3	Spatial Discretization of Source Term	38
3.4.2.4	Temporal Discretization	38
3.5	Boundary Conditions	40

3.6	Solution Procedure	40
3.6.1	Discretized Pressure and Navier-Stokes Equation	42
3.6.2	Solution of the Algebraic Equation	43
3.6.3	Pressure-Velocity Coupling	44
3.7	Handling Moving Boundaries	46
3.7.1	Arbitrary Lagrangian Eulerian Approach	46
3.7.2	Grid Deformation Solver	47
3.7.3	Assigning Boundary Movement	48
3.8	Computational Domain	49
3.9	Grid System	51
3.9.1	Proposed Strategy to Generate Grid System	53
3.9.1.1	Equation for Initialization of First Grid Height (y)	54
3.9.1.2	Performance of the Obtained Equations	55
3.9.1.3	Influence of Growth Factor (GF)	57
3.9.2	Application of the Proposed Strategy	60
3.10	Validation	62
3.10.1	Static Responses	64
3.10.1.1	Influence of Side Ratio (R)	64
3.10.1.2	Square Cylinder (R of 1)	64
3.10.1.3	Elongated Rectangular Cylinder (R of 5)	67
3.10.1.4	Streamlined Bridge Deck	67
3.10.1.5	Pentagonal Bridge Deck	68
3.10.2	Dynamic Responses	71
3.10.2.1	Great Belt Bridge Deck	72
3.10.2.2	Elongated Rectangular Cylinder (R of 5)	72

3.10.2.3	Pentagonal Bridge Deck without Curb	75
3.11	Concluding Remarks	76
4	Bridge Deck Shaping effects on Aerodynamics: With Fairing	77
4.1	Behavior of Deck with Edge Fairing	78
4.1.1	Influence of Top (θ_T) and Bottom (θ_B) Plate Slope	78
4.1.1.1	Steady State Force Coefficients	78
4.1.1.2	Pressure Distribution	81
4.1.1.3	Velocity Distribution	83
4.1.2	Influence of Handrail Types	85
4.1.3	Influence of Nose Location	87
4.2	Behavior of Streamlined Bridge Deck	89
4.2.1	Influence of Width Ratio (W)	90
4.2.1.1	Steady State Force Coefficients	91
4.2.1.2	Pressure Distribution	93
4.2.1.3	Velocity Distribution	94
4.2.2	Influence of Side Ratio (R)	97
4.2.3	Influence of Reynolds Number (R_{eB})	99
4.3	Concluding Remarks	102
5	Bridge Deck Shaping Effects on Aerodynamics: Without Fairing	104
5.1	Behavior of Pentagonal Bridge Deck	105
5.1.1	Influence of Bottom plate Slope (θ_B)	106
5.1.1.1	Steady State Force Coefficients	106
5.1.1.2	Pressure Distribution	108
5.1.1.3	Velocity Distribution	110

5.1.2	Influence of Curb Height (h/D)	111
5.1.3	Influence of Curb Angle (β)	114
5.1.4	Influence of Reynolds Number (R_{eB})	115
5.2	Behavior of Hexagonal Bridge Deck	118
5.2.1	Influence of Width Ratio (W)	118
5.2.2	Influence of Inspection Rail	122
5.2.3	Influence of Side Ratio (R) and Median Curb	124
5.3	Concluding Remarks	126
6	Bridge Deck Shaping Effects on Dynamic Response	128
6.1	Behavior of Bridge Deck with Fairing	129
6.1.1	Bridge Deck With Edge Fairing ($W=1$)	129
6.1.2	Streamlined Bridge Deck ($W=0.5$)	133
6.2	Behavior of Bridge Deck without Fairing	136
6.2.1	Influence of Separation Interference Method (SIM)	137
6.2.2	Influence of Bottom Plate Slope (θ_B)	139
6.3	Concluding Remarks	141
7	Conclusions	143
7.1	Main Findings of the Study	143
7.2	Areas of Future Research	146
	Bibliography	148

List of Figures

1.1	A comparison of old style and modern bridges	2
1.2	Oscillation and collapse of old Tacoma Narrows Bridge, November 1940	3
1.3	General aerodynamic response of long-span cable-supported bridge	3
1.4	Vortex induced vibration observed in Great Belt Bridge, May 1998	5
1.5	An example of streamlined bridge deck utilized in Sutong Bridge	5
1.6	Important parameters of a streamlined single box bridge deck	6
1.7	Considered various long-span cable supported bridge deck: (a) Edge fairing ($W=1$), (b) Streamlined deck ($W=0.6$) and Hexagonal Deck without fairing	6
2.1	Various deck shapes used for long-span cable-supported bridge	13
2.2	Survey results on type of long-span cable-supported bridge deck	14
2.3	Shaping parameters of practically constructed streamlined bridge deck	15
2.4	Definition of positive forces and characteristics length	17
3.1	Concept of control volume and various notations adopted during discretization process	33
3.2	Variation of diffusion coefficient among neighboring CV s	37
3.3	Vector notation for orthogonal and non-orthogonal grids	37

3.4	General procedure of GAMG method	45
3.5	Solution steps of dynamic simulation in OpenFOAM	50
3.6	Important notations, domain size and the boundary conditions adopted in the present study for bluff body simulation	51
3.7	Domain size employed for simulating flow around bridge deck	51
3.8	Concept of near-wall treatment and various important notations in grid system	52
3.9	Considered non-uniform grid arrangement to discretize the flow around square cylinder	56
3.10	Mean value of surface pressure distribution around square cylinder at Re_B of 1.22×10^4 . Experimental results are: Otsuki (1978) at $Re_B = 7 \times 10^4$, Bearman & Obasaju (1982) at $Re_B = 2 \times 10^4$; Lee (1975) at $Re_B = 1.76 \times 10^4$	58
3.11	Grid convergence indexes calculated based on mean surface pressure of square cylinder	59
3.12	Considered non-uniform mesh arrangement to discretize the flow domain around the elongated rectangular cylinder ($R=5$)	60
3.13	Mean value of surface pressure distribution around rectangular cylinder of side ratio (R) of 5 at $Re_B = 6.1 \times 10^4$. Experimental results are: Matsumoto (2005) at $Re = 1 \times 10^5$ (as cited in Mannini <i>et al.</i> 2010b); Galli (2005) at $Re = 2.1 \times 10^5$; Ricciardelli & Marra (2008) at $Re = 2.7 \times 10^5$ for R of 5	61
3.14	Grid convergence indexes calculated based on mean surface pressure of rectangular cylinder ($R=5$)	62
3.15	Influence of side ratio (R) on steady state force coefficients and Strouhal number (St_B). Experimental results are: Nakaguchi <i>et al.</i> (1968) at $Re = 10^5$, Sakamoto <i>et al.</i> (1989) at $Re = 5.5 \times 10^4$, Okajima (1983) at $Re = 0.42 \times 10^5$, Otsuki <i>et al.</i> (1974) at $Re = 2.2 \times 10^4 - 5.5 \times 10^5$	65
3.16	rms value of surface pressure distribution at Re_B of 1.22×10^4 . Experimental results are: Bearman & Obasaju (1982) at $Re_B = 2 \times 10^4$; Lee (1975) at $Re_B = 1.76 \times 10^4$ and Pocha (1971) at $Re_B = 9.2 \times 10^4$	66
3.17	Normalized longitudinal velocity distribution along the flow domain at Re_B of 1.22×10^4 . Experimental and numerical result: Lyn <i>et al.</i> 1988 at $Re = 2.14 \times 10^4$, Izuka <i>et al.</i> (1999) at $Re = 2.2 \times 10^4$ and Haque <i>et al.</i> (2014) at $Re = 2.2 \times 10^4$	66
3.18	Mean value of surface pressure distribution around rectangular cylinder of side ratio (R) of 5 at $Re_B = 6.0 \times 10^4$. Experimental results are: Matsumoto (2005) at $Re = 1 \times 10^5$ (as cited in Mannini <i>et al.</i> 2010b); Galli (2005) at $Re = 2.1 \times 10^5$; Ricciardelli & Marra (2008) at $Re = 2.7 \times 10^5$ for R of 5	68

3.19	Time-averaged flow pattern around rectangular cylinder having side ratio (R) of 5	68
3.20	Cross-sectional details and the computational grid system adopted for the streamlined bridge deck	69
3.21	Mean surface pressure distribution around the streamlined bridge deck compared with past experimental work of Sarkic <i>et al.</i> (2012)	69
3.22	Computation grid system adopted for the pentagonal shaped bridge deck	70
3.23	Surface pressure distribution around the pentagonal shaped bridge deck at a Reynold number (Re_B) of 6.0×10^4	70
3.24	Comparision of the wind speed ratio around the pentagonal shaped bridge deck. In experimental work same colour bar level was used like the numerical work (0-1.6)	71
3.25	Comparison among flutter derivatives of Great Belt bridge deck evaluated numerically (current study) and experimentally (by Reinhold <i>et al.</i> (1992) as cited in Stærdahl <i>et al.</i> (2007)): (a), (b) and (c) Evaluated directly by torsional and heaving mode vibration and (d) Calculated from the interdependency relationship among the flutter derivatives	73
3.26	Flutter derivatives of the rectangular cylinder having side ratio (R) of 5 extracted from forced torsional oscillation	74
3.27	Unsteady pressure characteristics of the rectangular cylinder having side ratio (R) 5	75
3.28	Computational grid system for the pentagonal shaped bridge deck without curb	75
3.29	Torsional (A_2^* and H_3^*) flutter derivatives of the pentagonal bridge deck at Re_B of 6.0×10^4	76
4.1	Edge fairing applied to the Bronx-Whitestone Bridge deck	79
4.2	Schematic view of the considered bridge deck and various important notations	79
4.3	Mean value of steady state force coefficients	80
4.4	rms value of steady state force coefficients and Strouhal number	80
4.5	After-body velocity fluctuations for selected shapes of fairing. Velocity fluctuations were measured at the point, 1D downstream and 1D down from the trailing edge bottom corner of the bridge deck	81
4.6	Mean surface pressure distribution around the bridge deck	82

4.7	Boundary layer velocity profile at the trailing edge	82
4.8	rms value of surface pressure around the bridge deck	83
4.9	Instantaneous velocity field for $\theta_T40-\theta_B40$ along one lift cycle at 0° (a), 90° (b) and 270° (c)	84
4.10	Instantaneous velocity field for $\theta_T40-\theta_B20$ for maximum (a) and minimum (b) value of lift	84
4.11	Instantaneous velocity field for $\theta_T40-\theta_B10$ along one lift cycle at 0° (a), 90° (b) and 270° (c)	85
4.12	Instantaneous velocity field for $\theta_T30-\theta_B10$ along one lift cycle at 0° (a), 90° (b) and 270° (c)	85
4.13	Various types of handrails utilized for investigation	86
4.14	Influence of handrail types on steady state force coefficients	86
4.15	Comparison of time averaged flow field distribution around the bridge deck ($\theta_T40-\theta_B20$) for different handrail type	87
4.16	The concept of nose location in edge fairing and the range of top and bottom plate slope used for investigation	88
4.17	Influence of nose location on steady state force coefficients	88
4.18	Influence of nose location on mean wind speed ratio around the bridge deck	89
4.19	Influence of nose location on boundary layer at the mid deck width	89
4.20	Application of streamlined bridge deck for practically constructed bridges	90
4.21	Difference of streamlined deck from edge faring and various important notations	90
4.22	Cross-sectional details of the streamlined decks employed for investigation	91
4.23	Influence of bottom plate slope (θ_B) and width ratio (W) on mean value of steady state force coefficients	92
4.24	Influence of bottom plate slope (θ_B) and width ratio (W) on rms value of steady state force coefficients and the Strouhal number	93
4.25	Mean surface pressure distribution for bottom plate slope (θ_B) of 25°	94
4.26	Mean surface pressure distribution for bottom plate slope (θ_B) of 12°	94
4.27	rms surface pressure distribution for bottom plate slope (θ_B) of 25°	95

4.28	rms surface pressure distribution for bottom plate slope (θ_B) of 12°	95
4.29	Comparison of time averaged velocity distributions around the bridge decks for bottom plate slopes (θ_B) of 25° and 12°	95
4.30	Comparison of Vorticity plot around bridge deck for bottom plate slopes (θ_B) of 14° and 12°	96
4.31	Relationship between the width ratio (W) and the inclined plate slopes (θ_B and θ_T) of practically constructed streamlined bridge decks	98
4.32	Influence of side ratio (R) on steady state force coefficients	98
4.33	Comparison of time averaged velocity distributions around the bridge deck for side ratio (R) of 5 and 8 with a bottom plate slope (θ_B) of 14°	99
4.34	Reynolds number effects (R_{eB}) on mean and rms value of steady state force coefficients	100
4.35	Reynolds number effects on time averaged velocity field for a bottom plate slope (θ_B) of 14°	100
4.36	Reynolds number (R_{eB}) effects on various important flow features for streamlined bridge deck	101
4.37	Reynolds number effects on flow field of a bridge section obtained by Schewe (2001). The Reynolds number (R_{eB}) in the figure increases from left to right and reaches up to a value of 15×10^5	101
5.1	Cross-section of the pentagonal bridge deck and important notations	106
5.2	Influence of bottom plate slope (θ_B) on mean and rms value of steady state force coefficients	107
5.3	Influence of bottom plate slope (θ_B) on flutter wind speed (U/fB) for curb angle (β) of 30° based on the experimental work by Kubo <i>et al.</i> (2007)	108
5.4	Mean surface pressure distribution around the bridge deck section with a curb angle (β) of 27° for various bottom plate slopes (θ_B)	109
5.5	rms surface pressure distribution around the bridge deck section with a curb angle (β) of 27° for various bottom plate slopes (θ_B)	109
5.6	Instantaneous velocity field for deck shape having bottom plate slope (θ_B) of 14° along one lift cycle at 0° (a), 90° (b), 180° (c) and 270° (d)	109
5.7	Influence of bottom plate slope on time averaged flow field around the bridge decks	110

5.8	Influence of bottom plate slope (θ_B) on trailing edge separation	111
5.9	Influence of bottom plate slope (θ_B) on the wake size of the bridge deck	111
5.10	Procedure of changing curb height (h/D) for a fixed curb angle ($\beta=30^\circ$)	112
5.11	Influence of curb height (h/D) on mean and rms value of steady state force coefficients	112
5.12	Influence of curb height (h/D) on wind speed ratio around the bridge decks	113
5.13	Influence of curb height (h/D) on trailing edge slow separation	113
5.14	Influence of curb angle (β) on steady state force coefficients	114
5.15	Influence of curb angle (β) on wind speed ratio around the bridge decks	115
5.16	Influence of Reynolds number (Re_B) on steady state force coefficients	116
5.17	Influence of Reynolds number (Re_B) on flow field for the pentagonal bridge deck	116
5.18	Influence of Reynolds number (Re_B) on various flow features	117
5.19	Cross-sectional view of the hexagonal bridge deck and importation notations	119
5.20	Procedure changing the width ratio (W) and bottom plate slope (θ_B) for deck without fairing	119
5.21	Influence of width ratio (W) on steady state force coefficients	120
5.22	Influence of bottom plate slope (θ_B) on flow field for the pentagonal and hexagonal bridge deck	121
5.23	Influence of bottom plate slope (θ_B) on leading and trailing edge flow separation	121
5.24	Inspection rail and its location	122
5.25	Influence of inspection rails on the flow field around the bridge deck	123
5.26	Influence of inspection rail on the bridge deck wake size	124
5.27	Influence of side ratio (R) and median curb on the steady state force coefficients	125
5.28	Influence of side ratio (R) and median curb on flow field around the bridge deck	125
5.29	Influence of side ratio (R) and median curb on the trailing edge boundary layer flow separation	126

6.1	Comparison of the considered bridge deck for the edge fairing ($W=1$)	130
6.2	Influence of bottom plate slope (θ_B) on torsional mode flutter derivatives for the width ratio (W) of 1	130
6.3	Influence of bottom plate slope (θ_B) on heaving mode flutter derivatives for the width ratio (W) of 1 determined from the interrelationship among the flutter derivatives	131
6.4	Comparison of time averaged velocity field for large and small bottom plate slopes (θ_B) of the bridge deck with the width ratio (W) of 1	131
6.5	Influence of bottom plate slope (θ_B) on work done by the unsteady pressure in torsional mode for the width ratio (W) of 1	132
6.6	Influence of bottom plate slope (θ_B) on work done by the unsteady pressure in heaving mode for the width ratio (W) of 1	133
6.7	Considered bridge deck with distinct aerodynamic responses for the streamlined bridge deck	133
6.8	Influence of bottom plate slope (θ_B) on torsional mode flutter derivatives for the width ratio (W) of 0.5	134
6.9	Influence of bottom plate slope (θ_B) on heaving mode flutter derivatives for the width ratio (W) of 0.5 determined based on the interrelationship among the flutter derivatives	135
6.10	Comparison of time averaged velocity field for large and small bottom plate slopes (θ_B) of the bridge deck with a width ratio (W) of 0.5	135
6.11	Influence of bottom plate slope (θ_B) on work done by the unsteady pressure in torsional mode for width ratio (W) of 0.5	136
6.12	Influence of bottom plate slope (θ_B) on work done by the unsteady pressure in heaving mode for width ratio (W) of 0.5	137
6.13	Considered bride deck to show the influence of SIM on flutter derivatives	137
6.14	Influence of SIM on torsional flutter derivatives	138
6.15	Influence of SIM on the flow field ($\theta_B=12^\circ$ and $R=5$)	138
6.16	Influence of SIM on unsteady pressure characteristics of the deck top surface . .	139
6.17	Considered bridge deck to show the influence of bottom plate slope on torsion flutter	139
6.18	Influence of bottom plate slope (θ_B) on torsional flutter derivatives	140

6.19	Influence of bottom plate slope (θ_B) on time averaged velocity field	140
6.20	Influence of bottom plate slope (θ_B) on unsteady pressure characteristics	141

List of Tables

2.1	Streamlined bridge deck surveyed to obtained detailed information about shaping parameters	15
2.2	Survey results of various shaping parameters of hexagonal bridge deck without fairing	16
2.3	Role of flutter derivatives on flutter instability (Trein <i>et al.</i> 2010)	22
3.1	Properties of the considered grids having various y^+ values for square cylinder (R) of 1 at $Re_B=1.22 \times 10^4$	56
3.2	Comparison in between the required first grid height (y/d) and calculated first grid height (y/d) from the obtained equations	56
3.3	Influence of growth factor (GF) on aerodynamic characteristics of square cylinder ($R=1$) for G2 (Table 3.1) at $Re_B=1.22 \times 10^4$. Previous works: Shimada and Ishihara (2002) at $Re=10^4$, Sakamoto <i>et al.</i> (1989) at $Re=5.5 \times 10^4$ and Okajima (1982) at $Re=70-2 \times 10^4$	58
3.4	Aerodynamic characteristics of bluff body for side ratio (R) of 5 at $Re_B=6.1 \times 10^4$. Previous works: Mannini <i>et al.</i> , (2010b) at $Re=10^5$, Tamura and Ito (1996) at $Re=104$, Shimada and Ishihara (2002) at $Re=104$, Okajima (1982) at $Re=70-2 \times 10^4$	61
5.1	Influence of inspection rail and its location on aerodynamic response	123

Nomenclatures

Roman Symbols

A_i^*	Flutter derivatives for pitching moment
a	Side depth of the bridge deck without fairing
a_p	Diagonal coefficients
a_N	Off-diagonal coefficients
B	Top horizontal plate width of the bridge deck
B_l	Full-width of the bridge deck
b	Bottom horizontal plate width of the bridge deck
C_o	Courant number
C_D	Drag force coefficients
C_f	Coefficient of skin-friction
C_L	Lift force coefficients
C_M	Moment coefficients
C_P	Pressure coefficients
C_{PI}	Imaginary part of the unsteady pressure

$C_{L\alpha o}$	Amplitude of lift force coefficient in torsional mode
$C_{L\eta o}$	Amplitude of lift force coefficient in heaving mode
$C_{M\alpha o}$	Amplitude of moment coefficient in torsional mode
$C_{M\eta o}$	Amplitude of moment coefficient in heaving mode
$C_L(t)$	Time-varying lift force coefficient
$C_M(t)$	Time-varying moment coefficient
$C_P(x, t)$	Total pressure coefficient at location x in time t
$\bar{C}_p(x)$	Mean pressure coefficient
$ C_P(x, t) $	Unsteady pressure coefficient at location x at time t
$ C_P(x) $	Amplitude of the unsteady pressure
D	Bridge deck depth
d	Vector between center of control volume (P) and neighbor (E)
E	Point in the center of the neighboring control volume
e	Percentage relative error
F	Mass flux through face
F_D	Drag Force per unit span
F_L	Lift force per unit span
F_M	Moment per unit span
$F(k)$	Real part of the Theodorsen function
f	Oscillation frequency
f_v	Vortex shedding frequency
f_η	Heaving frequency
f_α	Torsional frequency
GF	Growth factor
$G(k)$	Imaginary part of the Theodorsen function

H_i^*	Flutter derivatives for lift force
H	Height of the computational domain
h	Height of the curb
I	Mass moment of inertia per unit span
k	Reduced frequency and turbulent kinetic energy
$L(t)$	Time varying lift force per unit span length
$M(t)$	Time varying moment per unit span length
m	Mass per unit span
n_f	Outward-pointing face area vector
P	Pressure and point in the center of control volume
R	Side ratio
Re_B	Reynolds number
r	Gradient ratio and normalized distance and refinement factor
rms	Root mean square
S_C	Constant part of the source term
S_f	Face area vector
S_P	Dependent part of the source term
St	Strouhal number
S_ϕ	Source term
T	Time
U	Velocity vector
U	Inlet velocity
u^*	Friction velocity
V	Volume
V_P	Volume of the cell

V_E/V_W	Volume of the neighboring cell
VM	Validation metric
W	Width ratio and point in the center of the neighboring control volume
\mathbf{x}	Position vector
X_d	Upstream distance of the computational domain
X_u	Downstream distance of the computational domain
y	Nose location of the bridge deck and the first grid height
y^+	Non-dimensional wall distance

Greek Symbols

α	Torsional displacement
α_o	Amplitude of torsional oscillation
β	Curb angle and constant in turbulence model
Δt	Time step
Δx	Smallest cell size
Γ_ϕ	Diffusivity
η	Heaving displacement
η_o	Amplitude of heaving oscillation
μ	Dynamic viscosity
μ_T	Turbulent eddy viscosity
ν	Kinematic viscosity
ν_t	Kinematic eddy viscosity
ω	Circular frequency and turbulent specific dissipation rate
ω_α	Circular frequency of the torsional oscillation
ω_η	Circular oscillation of the heaving oscillation
ρ	Density

θ_B	Bottom plate slope of the bridge deck
θ_T	Top plate slope of the bridge deck
$\varphi_{L\eta}$	Phase lag from maximum angle of attack to the lift force in heaving mode
$\varphi_{L\alpha}$	Phase lag from maximum angle of attack to the lift force in torsional mode
$\varphi_{M\eta}$	Phase lag from maximum angle of attack to the moment in heaving mode
$\varphi_{M\alpha}$	Phase lag from maximum angle of attack to the moment in torsional mode
ζ_α	Structural damping ratio to critical for torsional mode
ζ_η	Structural damping ratio to critical for heaving mode

Chapter 1

Introduction

Bridge is one of the greatest inventions of human being that connected people across the world separated by streams, lakes, rivers, seas and valleys. With the passage of time this invention has gone through various modifications and developments to fulfill the ever growing needs of human. Fig.1.1 makes a comparison between one of the old style and modern bridges. Fabricus Bridge is an arch bridge made of tuff and built in 62 BC with a span length of 24.5 m (O'connor 1993 and Tylor 2002), on the other hand, Akashi-Kaikyo Bridge is a suspension bridge made of steel and built in 1998 with a span length of 1991 m (Cooper 1998). Conspicuously changes can be noticed both in terms of length, structural form and material.

Human being had always fascination towards bridging over wide to wider lands apart increasing the span length of the bridge. To achieve this goal, they required new and improved structural forms of bridge system and material having enough strength and less production cost. With the improvement of cable-supported bridge concept at the beginning of 19th century (Dennie and Hall 1809 and Myerscough 2013) and improvement of steel production technology in the mid of 19th century (Swank 1892), the concept of long-span cable-supported bridge emerges at the end of 19th century.

Cable-supported bridges require less number of deep piers or supports inside the bride saving cost and providing wide navigation for the water transportations. Soon it became a popular structural form of bridge system for the long-span bridges. In the beginning of 20th century based on the conventional deflection theory a number of cable-supported bridges were built both in the form of cable-stayed and suspension bridges (Matsumoto *et al.* 2007 and Myerscough 2013).



Tylor 2002

a) Fabricius Bridge (Buil in 62 BC)

<http://www.yokogawa-bridge.co.jp/>

(b) Akashi-Kaikyo Bridge (Built in 1998)

Figure 1.1: A comparison of old style and modern bridges

That approach had a significant flaw that appears through the collapse of famous Tacoma Narrows Bridge in 1940 (Ammann *et al.* 1941). That bridge was one of the major suspension bridges of that time spanning 853 m and made of steel. In the design process no dynamic behavior of structures and acting natural forces were taken into consideration due to lack of knowledge. The bridge collapsed due to dynamic action of wind, only at a wind speed of 19 m/s, known as torsional flutter (Farquharson 1949, Billah and Scanlan 1991 and Matsumoto *et al.* 2003). Fig.1.2 shows the vibration mode and the collapse of the bridge. Since then, the importance of wind-resistant design of long-span cable-supported bridges has been realized and dedicated countless number of researches on wind actions on bridges, introducing a new branch of scientific research named as a bridge aerodynamics.

Long-span cable-supported bridges are low damped flexible structures possess low natural frequencies varies from 0.05 to 0.5 Hz (Holmes 2004 and Fujino and Siringoringo 2013) depending on the span length, stiffness and the mass of the bridge system. This makes it more susceptible to wind forces rather than earthquake as the dominant frequency of wind and earthquake forces lies between 0.005 to 1 Hz and 0.1 to 10 Hz, respectively (Holmes 2004). When the wind blows around the bridge deck, it interacts with the bridge deck and excites it. As a result, the deck exhibits various aeroelastic phenomena. In Fig.1.3 the general aerodynamic response of a long-span cable-supported bridge is shown. At various levels of wind speed the response changes from static to dynamic and limited to divergent type vibration.

At low wind speed range, the deck exhibits limited amplitude vortex shedding vibration. When the blowing wind leaves the deck at the trailing edge, it creates alternating shedding vortices with a certain frequency (f_v). The shedding frequency, f_v , depends on the shape of the bridge deck and wind velocity (U). Under certain circumstances, the frequency of the vortices (f_v) matches with the natural frequency (f_n) of certain mode of vibration and the deck vibrates either in torsional or bending mode. As almost all the constructed bridges experience vortex shedding wind speed ranges during their design life time, to ensure serviceability criteria special attention is paid for vortex shedding excitation in the design stage.

The static aerodynamic forces such as drag (C_D), Lift (C_L) and moment (C_M) govern the aerodynamic response at medium to high wind speed range. The deck should stand without much translation, deformation and rotation under smooth and turbulent flows. At high wind speed range the long-span cable-supported bridges are susceptible to flutter instability. This is a divergent type



Figure 1.2: Oscillation and collapse of old Tacoma Narrows Bridge, November 1940

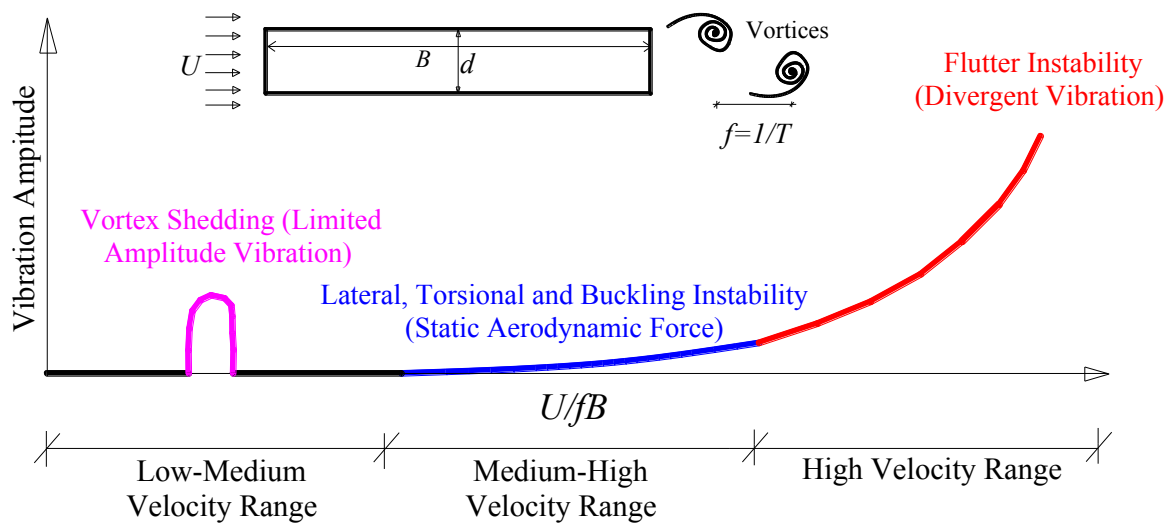


Figure 1.3: General aerodynamic response of long-span cable-supported bridge

vibration appears both in the form of classical flutter and stall flutter. At high wind speed, when the vertical and torsional modes frequencies come closer causing coupling among them occurs classical flutter, while stall flutter occurs in single mode of vibration associated with flow separation. In both of the forms of flutter negative aerodynamic damping also plays an important role (Chen *et al.* 2000).

With this advancement of knowledge, improvement of wind tunnel facilities and aerodynamic analysis methodology, engineers now can dream to construct a bridge spanning over more than couple of kilometers remaining the deck hang in the air such as 3.3 km span Messina Straits (Brancaleoni and Diana 1993), 3.5 km span Sunda Strait (Wangsadinata 1997) and 5 km span Gibraltar Strait (Lin and Chow 1991), yet there are lots to reveal and clarify about aerodynamics of long-span bridge decks to ensure safe and sustainable bridge system.

Still engineers face difficulties to make the bridge deck stable against wind and a number of long-span bridge decks suffered from aeroelastic problem after construction. For example, Deer Isle Bridge (Kumarasena 1989), Kessock Bridge (Owen 1996), Rio-Niterio Bridge (Battista 2000), Great Belt Bridge (Frandsen 2001), Osteroy Bridge (Strommen and Hjorth-Hansen. 2001), Severn Bridge

(Macdonald *et al.* 2002), Tokyo bay Bridge (Fujino and Yoshida 2002), Wye Bridge (Holmes 2004), and Shin-minato Bridge (Tran *et al.* 2014) bridges exhibited vortex induced vibration. Fig.1.4 illustrates the vortex induced vibration observed in Great Belt Bridge. Further, engineers struggle in the design process to reduce the steady state forces (Diana *et al.* 1999) and to increase the flutter wind speeds of the deck (Tanaka 1999, Xian and Ge 2007, Wang 2009) to satisfy the maximum wind speed at the construction site.

A number of countermeasures have already been developed to improve the steady state response and to control the aeroelastic vibration. Structural countermeasure and aerodynamic countermeasure are two common approaches. In case of structural countermeasure, the vibration is suppressed rather than eliminating the cause of vibration by means of increasing the damping. Basically, tuned mass damper is used as a structural measure in long-span bridges (Wardlaw 1992, Honda *et al.* 1993, Gu *et al.* 1994 and Strommen and Hjørth-Hansen. 2001). However, they demand extra construction and maintenance cost.

In aerodynamic countermeasure, the cause of vibration is eliminated by changing the flow field around the bridge deck. Normally, the shape of the bridge deck is modified or additional member such as flaps, spoiler, deflector, wind nose, guide vanes and spoiler are attached to the deck (Wardlaw 1992, Simiu and Miyata 2006 and Fujino *et al.* 2012). Nevertheless, each of these additional devices has effectiveness for specific type of aeroelastic problem (Fujino and Siringoringo 2013). Furthermore, like structural countermeasures these devices also incur extra construction and maintenance cost. From engineering point of view it is always given the highest priority to the solutions having less cost and simplicity in construction. Therefore, if it is possible to improve aerodynamic response and eliminate aeroelastic problem only by shaping the bridge deck properly, it would be the most desired solution for many future long-span bridges.

The gravity and the importance of the context motivated us to explore the insights of the aerodynamics of long-span bridge decks. The focus was to reveal and understand how the variation of bridge deck shapes affects the aerodynamic response and the flow field to maximize the improvement of the aerodynamics that can be achieved by shaping the long-span bridge deck appropriately.

1.1 Problem Statement

Until now, various bridge deck shapes have been utilized for long-span cable-supported bridges. To narrow down the option, we surveyed 81 cable-supported long-span bridge decks span length varies from 200 to 1991 m to find the most common and widely used deck shape. Detailed survey results are provided in chapter 2. We found that single box streamlined deck is the most common form of deck for long-span bridges. Fig.1.5 depicts an example of single box streamlined deck shape used in Sutong Bridge. The streamlined shape is achieved by means of the inclined bottom plate of the girder and addition of a small fairing at the side of the deck to reduce the along wind load and strength of the vortices at the trailing edge (Teres-Nicoli *et al.* 2007 and Teres-Nicoli and Kopp 2009).

Much research has already been dedicated regarding this kind of shape. Yamaguchi *et al.* (1986) compared among venting and fairing to check their performance against vortex-induced

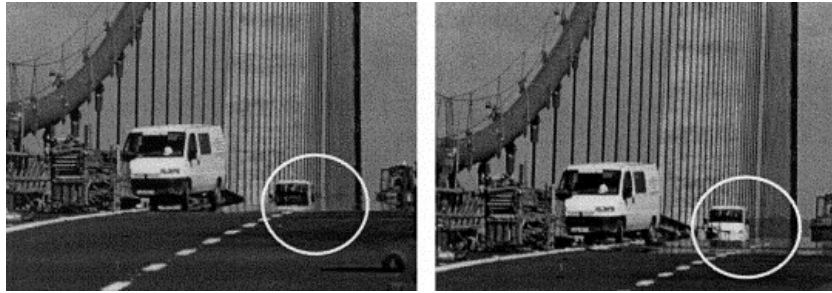


Figure 1.4: Vortex induced vibration observed in Great Belt Bridge, May 1998 (Larsen *et al.* 2000). Both the camera and the marked vehicle was in stationary

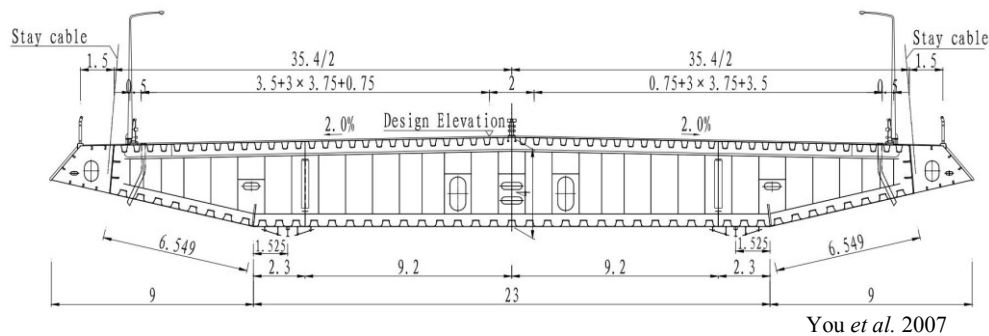


Figure 1.5: An example of streamlined bridge deck utilized in Sutong Bridge

vibration and flutter instability. They found that shape of the fairing influences the aerodynamic response and recommended further investigation. Then, Nagao *et al.* (1993), Kawatani *et al.* (1993), Sakai *et al.* (1993), Larsen (1993), De Marinda and Bartoli (2001) and Sukamta *et al.* (2008) investigated the influence of fairing on aerodynamic response. They also found that fairing has effectiveness to improve mean force coefficients, vortex shedding behavior and flutter wind speed. However, discussion was limited to its effectiveness only as no specific shape was found to be effective for general consideration.

Then, Larsen and wall (2012) conducted wind tunnel investigation on a streamlined deck having girder bottom plate slope of 25° , 20° and 14.8° . They recommended a bottom plate slope of 14.8° to eliminate vortex-induced vibration. He found that at bottom plate slope of 14.8° , the flow separation at the trailing edge stops and the vortex forms away from the body. As a result the deck doesn't exhibit vortex-induced vibration. Before that, Wang *et al.* (2009) also conducted detailed wind tunnel investigation to select the deck shape for Nanjing 4th Bridge having various bottom plate slopes to improve the flutter wind speed. They found that the flutter wind speed increases dramatically for a bottom plate slope of less than 16° .

However, for this kind of shape the bottom plate slope is not the only influential parameter. There are some other parameters, they may also influence the aerodynamic behavior and affect the effectiveness of bottom plate slope. Fig.1.6 shows the detailed of streamlined shape. As can be seen that not only the bottom plate slope (θ_B), the shape of the deck also depends on the top plate slope (θ_T), the top deck width (B), the depth of the deck (D) and the bottom deck width (b). And, it is already known from past researches that aerodynamic response of a bridge deck is highly sensitive

to the variation of the deck shape (Nagao *et al.* 1993, Kawatani *et al.* 1993, Sakai *et al.* 1993, Larsen 1993, De Marinda and Bartoli 2001 and Sukamta *et al.* 2008).

As a result, the variation of the top plate slope (θ_T), side ratio (R) and deck width ratio ($W=b/B$) will also affect the aerodynamic response and depending on that the mechanism of bottom plate slope (θ_B) may also alter. For example, if the width of bottom horizontal plate (b) changes the shape of the deck alters significantly as shown in Fig. 1.7 (a) and (b). We surveyed some of the famous streamlined deck of long-span cable-supported bridges in details. In chapter 2 detailed survey results are provided. We found that the width ratio (W) varies a lot from 1 to 0.5. Hence, their influence on aerodynamic behavior is obvious. Not only width ratio (W), other parameters such as bottom plate slope (θ_B), top plate slope (θ_T) and side ratio (R) also varies pretty well. Interestingly, all those bridge deck shapes were selected based on rigorous wind tunnel test and all those shapes are supposed to possess improved aerodynamic behavior. This implies that bottom plate slope (θ_B) is not only influential parameter and the optimum value of bottom plate slope (θ_B) may depend on other parameters too.

Further, the influence of Reynolds Number (Re_B) is another important and widely discussed topic that should be taken into consideration, as practical bridges experience Reynolds number (Re_B) of more than millions. Even though, it is quite impossible to reveal the complete influence of Reynolds number, yet at least the trend in results should be known that how the bridge deck response as well as the flow field alter at increasing Reynolds number (Re_B). This effectiveness of shaping parameters and the flow mechanism may also depend on Reynolds number (Re_B).

Even so, in past works very few of these parameters were considered systematically in a single research. Investigations were carried out individually with different conditions. There was difference in terms of side ratio, Reynolds number, types of handrail and the way parameter was altered. For example, for bottom plate slope (θ_B), Wang *et al.* (2009) changed that by changing the nose location, where Larsen and Wall (2012) changed by changing the bottom deck leading edge toe without shifting the nose location. Moreover, in past works only the vibration amplitudes at various wind speeds were focused rather than exploring the flow field systematically in detailed to understand the

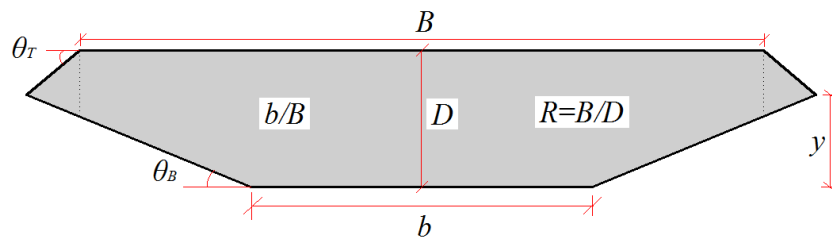


Figure 1.6: Important parameters of a streamlined single box bridge deck

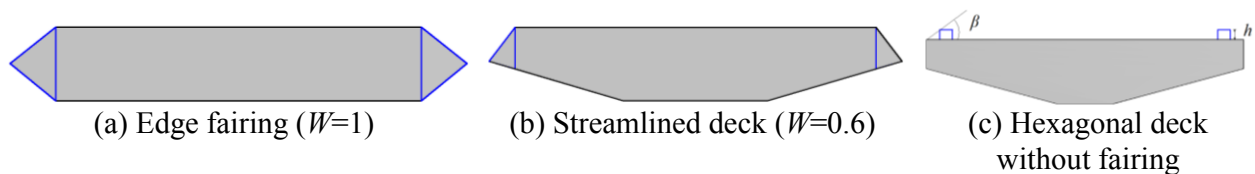


Figure 1.7: Considered various long-span cable supported bridge deck

influence of those shaping parameters on flow field to reveal the flow mechanism. In addition, issue like steady state response such as drag force, lift force and moment coefficients is also important and should be treated equally similar to the dynamic responses as they are the basic wind forces act on the bridge. Influence of shaping parameters on steady state force coefficients should be also clarified. Hence, there are a number of obscure points and only a handful amount of meaningful information can be extracted from past wind tunnel investigations.

Still engineers need to go through very lengthy process to finalize their wind resistant design of long-span bridge, where the first step starts with the modification of the deck cross-section and continues updating the deck shape until the safety criteria are satisfied (Miyata *et al.* 1992 and Fujino *et al.* 2012). Basically, the updating regarding the shape of the deck is carried out by trial and error approach and based on engineer's experience. The situation becomes even more complicated as the preliminary shape of the deck is basically determined based on the structural, maintenance or architectural point of view. This incurs constrain for some of the shaping parameters (B , b and d) and their magnitude differ from one bridge to another. Therefore, the updating process of the shape varies from bridge to bridge and this consumes a lot of time, budget and efforts to find the optimum shape of the bridge deck. This process can be made way far faster and design friendly if the flow mechanism of the deck shape is well understood making the engineers capable of selecting appropriate shape promptly.

Another aspect is, a number of cable-supported bridges decks in Japan have been without adding the fairing at the side of the deck. Fig.1.7(c) shows the hexagonal bridge deck without fairing. This type of deck has superiority over streamlined deck as they don't even require fairing at the side of the deck saving construction cost. Like streamline deck, they also have similar shaping parameters except the top plate slope (θ_T). Instead of top plate slope (θ_T), they have two new shaping parameters such as curb angle (β) and curb height (h/D). Therefore, for this type of bridge also has a number of important shaping parameters: i) Bottom plate slope (θ_B), ii) Width ratio (W), iii) Side ratio (R), iv) Curb angle (β) and v) Curb height (h/D). The influence of these parameters on aerodynamic response and flow field hexagonal bridge deck is not completely clear as no detailed research has been dedicated yet.

Basically, the hexagonal deck shape is the extended version of the pentagonal shaped deck that was proposed by Kubo and his associates (Yoshida *et al.* 2006, Kubo *et al.* 2007 and Noda *et al.* 2009) based on Separation Interference Method (SIM) (Kubo *et al.* 1993 and 2008) and exists some recommendations regarding the bottom plate slope (θ_B). However, the behavior of a hexagonal shaped bridge deck will be different from that of a pentagonal shaped deck, as in case of hexagonal deck a new shaping parameter bottom deck width (b) appears. It is also important to compare the aerodynamic response of deck with (streamlined) and without (hexagonal) fairing for better understanding the influence of fairing and the insights of aerodynamics to alleviate the shaping procedure of bridge deck.

1.2 Aim, Scope and Objectives

The aim of the present study was to clarify the influences of various shaping parameters on the aerodynamic response and the flow field of a single box bridge deck to reveal the flow mechanism behind that to facilitate the wind-resistant design procedure of long-span bridge deck.

The scope of the present study covers various shaping parameter of a single box deck such as top inclined plate slope (θ_T) and bottom inclined plate slope (θ_B), width ratio (W) and side ratio (R). Regarding the flow type, we considered only smooth flow, yet the Reynolds number influence was tried to explore up to an affordable range. At the present study we basically focused on the influence of aforesaid parameters on steady state response and the flow field. By exploring and understanding the flow field well, we tried to explain the possible effects of shaping parameters on dynamic responses such as vortex shedding and flutter instabilities.

To accomplish the aim of the study within this scope, the specific objectives of the research are to:

- Collect the detailed dimension of existing long-span cable-supported bridge decks to extract information regarding the value of various shaping parameters practiced practically and their range of values.

- Investigate the influence of shaping parameters for range of values determined previously on steady state response of single box deck with and without fairing to find trend in the result.

- Analyze the flow field in details to determine the most influential aerodynamic flow features that controls the steady state response and their behavior due to variation of shaping parameters to grasp the mechanism behind the trend in results.

- Investigate the influence of Reynolds number (Re_B) on steady state response and the flow features identified previously.

- Demonstrate the influence of important shaping parameters on dynamic behavior of the bridge deck and to comprehend the role of various flow features on dynamic responses such as vortex shedding and flutter instabilities.

1.3 Methodology

In the present study it was intended to investigate the influence of various shaping parameter on aerodynamics of the bridge deck to evaluate their relative performance and understand the flow mechanism. In bridge aerodynamics field usually wind tunnel investigation is carried out, where the wind speed is gradually increased and vibration amplitude is recorded for vortex shedding vibration and flutter instability to evaluate aerodynamic performance. However, from this kind of investigation method only quantitative response can be obtained without understanding mechanism behind the response. Further, in this kind of method it is difficult to compare aerodynamic performance for deck having various shapes as the response depends on velocity and structural properties of the model.

To understand the flow mechanism that means the cause behind the response it is more rational to go for detailed response such as pressure distribution and visualization of flow those controls the aerodynamic response. Past researchers (Nakamura and Nakashima 1986, Hourigan *et al.* 2001, Mills *et al.* 2002, Mills *et al.* 2003, Tan *et al.* 2004) also utilized surface pressure distribution, observation of flow field, shedding frequency as a parameter of interest to reveal the

flow mechanism of vortex induced vibration of sharp edge bluff bodies. In bridge aerodynamic field also researchers often focus on pressure distribution (Kubo *et al.* 1992, Noda *et al.* 2009, Noda 2010, Šarkić *et al.* 2012, and Haque *et al.* 2015), visualization flow field (Kubo *et al.* 1992, Nagao *et al.* 1997, Kubo *et al.* 2007, Noda 2010, Larsen and Wall 2012, and Haque *et al.* 2015) and detailed analysis of the velocity field (Terres-Nicoli and Kopp 2009, Taylor *et al.* 2009, Taylor *et al.* 2012 and Haque *et al.* 2015) around the deck to unveil the cause behind and for better comprehension of the quantitative aerodynamic response obtained by wind tunnel investigation.

Therefore, in the present study we also adopted similar but different strategy. We considered mean and root mean square (rms) value of steady state force coefficients (Simiu and Scanlan 1996) as a static parameter of interest and investigated influence of various shaping parameters on them. We scrutinized the data and tried to find the trend in the result due to variation of shaping parameters. Basically, these aerodynamic force coefficients are the resultant of various flow features those take place around the bridge deck and meaningful information regarding the static and dynamic response of the deck. For example a deck having less mean value of aerodynamic coefficients implies that the deck will experience less aerodynamic loading and displacement at high wind speed. Further, sign or direction of the force also plays an important role. A negative lift value entails that the deck will experience downward force increasing the cable tension and overall stiffness on the bridge deck. On the other hand, the rms value of steady state force coefficients provides a general idea of the dynamic response of the bridge deck.

Then, the pressure, velocity, streamlines and vorticity fields around the deck were plotted in detailed to explore the flow field. The data were scrutinized to determine the most influential flow features those controls the steady state responses, their roles on steady state response, their behavior due to change in shape and Reynolds number (Re_B). After understanding their role on steady state response and behavior due to variation of shaping parameter, then we focused on dynamic behavior of the deck such as vortex induced vibration and flutter instability.

Based on flow field and steady state response, we selected a number of deck shapes as a representative case to evaluate their dynamic behavior. To evaluate their dynamic response, we calculated flutter derivatives (Scanlan and Tomko 1971) as they can be used as a metric for dynamic characteristics of bluff bodies as shown by Matsumoto (Matsumoto 1996, Matsumoto *et al.* 1996, 1997, 1999, 2007, 2008a and 2008b). Further, we also concentrated on unsteady pressure characteristics and calculated the aerodynamic damping on the deck surface to elucidate the influence of those flow features on dynamic behavior of the bridge decks as it already had been adopted by number of past researchers (Miyata *et al.* 1983, Matsumoto *et al.* 1993, Nagao *et al.* 1997 and Sukamta *et al.* 2008) to analyze dynamic behavior of the bridge deck.

Aforesaid responses can be obtained either by wind tunnel experiment or by Computational Fluid Dynamics (CFD) techniques. In wind tunnel, small-scale bridge model is made maintaining similarities in terms of structural and aerodynamic properties with the prototype structure to reproduce the actual aerodynamic response in a wind tunnel. The accuracy of the results depends on the quality of the model and accuracy of the model set-up. Nevertheless, making accurate model is cumbersome and quite expensive in terms of time and money. Specially, for flow field analysis by Particle Image Velocimetry (PIV) or Laser-Induced Fluorescence (LIF) is considerably costly, the model setup procedure is completed and the quality deteriorates at higher velocity and for complicated geometry as the laser light obstructed by the parts of the model (Blocken 2014). Those made an obstacle for the present study to go for wind tunnel approach, as a number of shaping parameters were altered requiring a large number of models of the bridge deck.

We went for the Computational Fluid Dynamics (CFD) techniques by employing OpenFOAM (V2.2), an open source code of as a solver to obtain the target aerodynamic response as discussed earlier. Over the last few decades researchers has dedicated enormous efforts to establish CFD as a research and practice tools in wind engineering (Blocken 2014). A number of CFD applications can be found in bridge aerodynamics in the literature (Shirai and Ueda 2001, Bruno and Mancini 2002; Watanabe and Fumoto 2008; Sarwar *et al.* 2008; Sarwar and Ishihara 2010, Nieto *et al.* 2010; Mannini *et al.* 2010a, Šarkić *et al.* 2012 and Brusiani *et al.* 2013, Miranda *et al.* 2014, Nieto *et al.* 2015 and Patruno 2015) and becoming an increasingly attractive tool in bridge and bluff body aerodynamics field. CFD has some particular advantages over wind tunnel experiment. It provides the complete information of all the flow variables in the flow domain under controlled environment and number of simulation is out of economic constrains. This makes CFD a suitable and better approach for the present study.

Specially, CFD is capable of generating distribution of various flow variables that makes it even better choice for the present study to adopt it as a research tool. Further, no detailed numerical investigation has been devoted until now on bridge deck shaping effects on aerodynamic response. However, the accuracy and reliability of CFD simulation results and the computational cost in terms of time are matter of concern. We choose two-dimensional unsteady Reynolds-Averaged Navier-Stokes (RANS) simulation to cope with the computational cost as large number simulations were carried out. Basically, two-dimensional simulation provides conservative results as it assumes uniform flow behavior in the span-wise direction. Further, in the present study only cross-sectional shaping parameters were altered lessening the demand of three-dimensional analysis. On the other hand, unsteady RANS simulation is computationally less expensive and possesses moderate accuracy having efficiency to grasp the flow field and trend in results (Mannini *et al.* 2010a, Nieto *et al.* 2015 and Haque *et al.* 2015). A number application of two-dimensional unsteady RANS can be found in bridge aerodynamics field (Shirai and Ueda 2001; Nieto *et al.* 2010; Mannini *et al.* 2010a, Sarkic *et al.* 2012, Brusani *et al.* 2013 and Nieto *et al.* 2015).

To deal with the issue regarding the accuracy and reliability, we carried out detailed verification and validation studies to increase the accuracy and reliability of the simulation result, respectively. We devoted elaborate grid dependency tests by following standard procedure (Roache 1998) and proposed a methodology to obtain grid independent result for bluff bodies promptly and with less effort. We validated both the static and dynamic results for rectangular cylinder of side ratio (R) of 5, for streamlined deck and for hexagonal shaped bridge deck by comparing with past experimental works (Okajima 1982, Reinhold *et al.* 1992, Matsumoto *et al.* 1996, Ricciardelli & Marra 2008, Šarkić *et al.* 2012 and Noda 2010) and quantified the quality of validation with proper validation metric (Oberkampf and Trucano 2002).

1.4 Organization of the Thesis

The thesis is consists of seven chapters. The first two chapters are introductory chapter. In third chapter the details of the adopted CFD techniques are discussed. Chapter 4, 5 and 6 presents the results of the study. Last chapter draws conclusions and provides some recommendations for future works. Tables and figures are embedded in the text and all the references cited in the text are listed at the end of thesis. The nomenclatures are consistent throughout the thesis. The detailed organization of the thesis is summarized as follows:

Chapter 1 introduces the evolution, advancement, current status and challenges in aerodynamic of long-span cable-supported bridges. It reviewed past works to solve the existing challenges and discussed the problem in detail. Then, the aim, objectives and methodology is mentioned. At the end, the outline of the thesis is presented.

In Chapter 2, survey results of practically constructed bridges are presented. The detailed sing convention and methodology for aerodynamic analysis are also introduced. Chapter 3 presents the background of the CFD techniques utilized in the present research. The governing equations, turbulence model, numerical methods adopted for equation discretization and solution technique are described. The grid independency and validation study results are provided at the last part of the chapter.

Chapter 4 discusses the effects of top plate slope (θ_T), bottom plate slope (θ_B), nose location (h) and handrail types on steady state force coefficients of a single box deck with edge fairing ($W=1$). The obtained trends in the results are explored by means of pressure and velocity distribution. Then, the influence of width ratio (W) is discussed for various bottom plate slopes (θ_B) on steady state force coefficients and mechanism is tried to elucidate by means of pressure, velocity and vorticity fields.

In Chapter 5 the aerodynamic behavior of the bridge deck without fairing is presented. First, the aerodynamic response of pentagonal shaped deck ($W=0$) is analyzed. Then, the influence of width ratio (W) is discussed for various bottom plate slopes (θ_B) on steady state force coefficients and flow field is explored by means of pressure, vorticity and velocity field.

Chapter 6 demonstrates the flutter derivatives of some selected deck sections with and without fairing. Unsteady pressure characteristic is explored and the role of influential flow features on aerodynamic damping is analyzed to apprehend the shaping effects on dynamic behavior of the bridge decks.

The general conclusions and recommendations are summarized in Chapter 7.

Chapter 2

General Background

Over the last few decades a large number of long-span cable-supported bridges have been constructed and going to be constructed in future. As the span length of the bridge increases, the deck becomes susceptible to aerodynamic problem due to their inherent flexibility and low damping. Aerodynamic responses are sensitive to the shape of the bridge deck (Nagao *et al.* 1993, Kawatani *et al.* 1993, Sakai *et al.* 1993, Larsen *et al.* 1993, De Marinda and Bartoli 2001 and Sukamta *et al.* 2008) and can be improved by shaping it properly (Wang *et al.* 2009 and Larsen and Wall 2013).

There are a number of shaping parameters that may affect the aerodynamic response as discussed in the last chapter. However, their detailed influence and mechanism behind the response is not well known yet. As a result, engineers need to go through lengthy design procedure to select the appropriate and optimum deck cross-section. In this study the influence of various shaping parameter of a streamlined deck with and without fairing was carried out on aerodynamic response and tried to clarify the mechanism behind that to facilitate the bridge deck design procedure.

This chapter provides general background information required to read this dissertation. First, detailed survey result regarding the type of the deck shapes employed for long-span cable-supported bridge and the range of the shaping parameters are presented. Then, the theory, expressions and aerodynamic analysis procedure adopted for the evaluation of steady state force coefficients, flutter derivatives and aerodynamic damping are discussed.

2.1 Type of Long-Span Bridge Deck

The aim of the present study was to investigate the influence of various shaping parameters of long-span cable-supported bridge deck on aerodynamic response. However, for long-span cable-supported bridges various types of deck shapes are adopted based on structural and aerodynamic point of view. It is quite impossible and irrational to investigate all those deck shapes. Therefore, to make it affordable it was important to narrow down the type of deck shape. From preliminary observation, we found that truss deck, single box streamlined deck, twin box deck are the most common forms of deck shape used for long-span bridges. Some others forms of deck shapes are also available. Fig.2.1 shows the various types of bridge deck used for long-span cable-supported bridge deck.

We surveyed a total number of 81 long-span cable-supported bridge decks spanning from 200 m to 1991 m all over the world. The data were collected from Tatsumi (2010), Svensson (2012) and webpages of various consultant and construction companies. We found that out of 81 bridge decks, 38 bridge decks were single box streamlined deck. In Fig.2.2 we plot the survey results. As can be seen 47% of the bridge decks are single box streamlined deck. 15% of them are truss deck, 10% of them are twin box deck and remaining 28% are other type including hexagonal deck without fairing. Therefore, we focused on single box streamlined bridge deck as they are the most widely used bridge deck for long-span cable-supported bridge. Further, taking this opportunity we also focused on hexagonal deck without fairing (Fig.2.1(e)) as the background was already discussed in Chapter 1 (Section 1.1) that recently a number of medium span cable-supported bridges in Japan have adopted this type of deck shape. Furthermore, we also intended to make a relative comparison between the aerodynamic response and flow field of deck with and without fairing to elucidate the effect of fairing in a better way. This would also ease the shaping procedure of many future bridge decks and explicate the wind tunnel results.

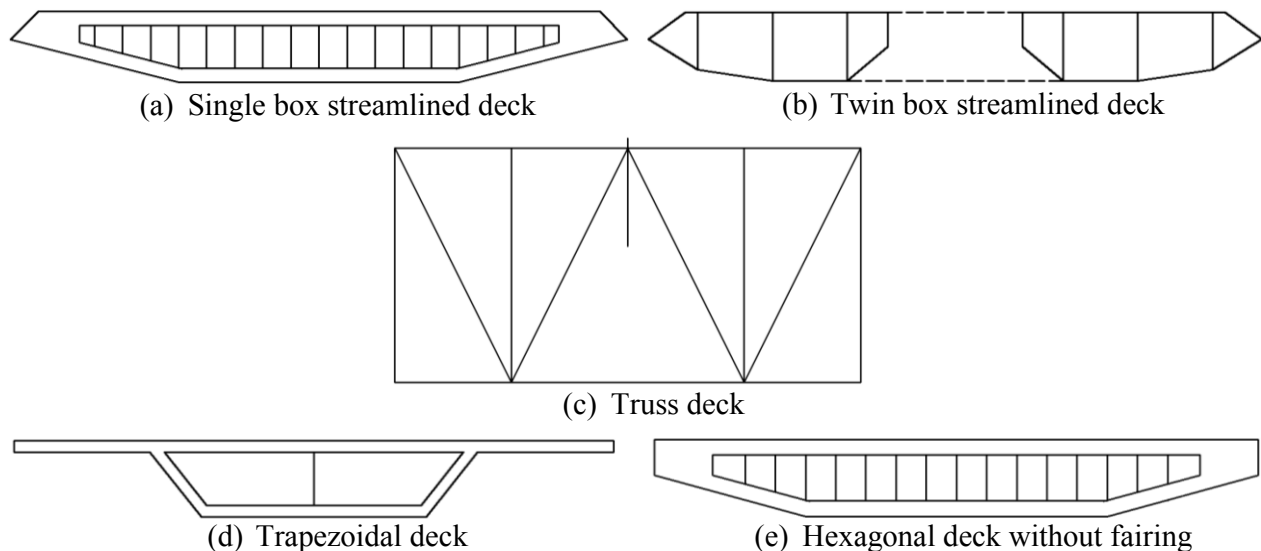


Figure 2.1: Various deck shapes used for long-span cable-supported bridge

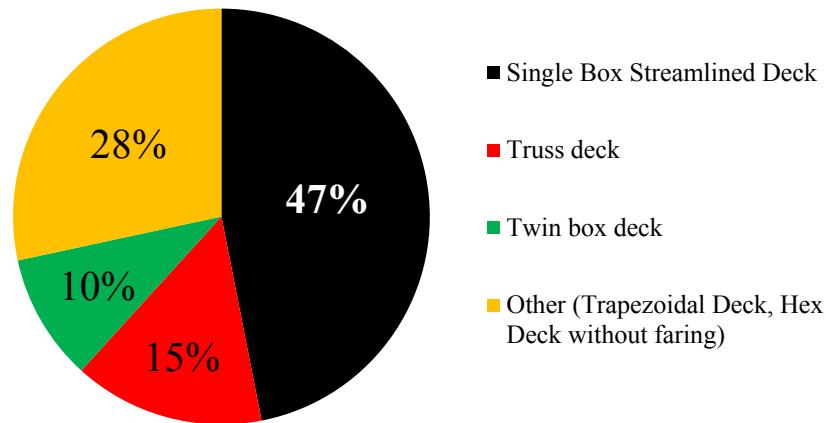


Figure 2.2: Survey results on type of long-span cable-supported bridge deck

2.2 Shaping parameters of Bridge Deck

It was important to have the detailed information of shaping parameters of practically constructed streamlined deck before commencing the investigation. We could manage detailed information of 22 streamlined bridge decks, those were taken from Strommen and Hjorth-Hansen (2001), Yu Ng (2007), Wang *et al.* (2009), Teres-Nicoli and Kopp (2009), Tatsumi (2010), Jurado *et al.* (2012), Jensen (2013), Virola (2013). Table 2.1 provides the general information and the detailed shaping parameters of the streamlined bridge deck those were surveyed. Some of the displayed shaping parameters may slightly differ from the actual one as they were retrieved from the pictures. Fig.2.3 plots the survey results for various shaping parameters. In Fig.2.3(a) the top (θ_T) and bottom plate slopes (θ_B) are plotted. These two parameters are the two most important shaping parameters. The bottom plate slope (θ_B) varies from 10° to 30° , yet the top plate slope (θ_T) varies a lot from 15° to 60° . All of those bridge deck shapes were selected based on wind tunnel study to fulfill the wind-resistant design criteria, yet varies a lot.

In Fig.2.3(b) diagrams the side ratio (R) and width ratio (W) of long-span bridge deck. The term, Side ratio (R) is an established parameter in bridge aerodynamics field defined as the ratio of the width (B) to the height (D) of the deck. On the other hand the width ratio (W) was defined newly in this work as the ratio of the bottom (b) to the top (B) horizontal deck width. These two parameters basically depend on structural design and the traffic volume. The side ratio (R) varies larger than the width ratio (W). The side ratio (R) varies from 5 to 12.5, while the width ratio (W) varies from 0.5 to 0.8. However, the width ratio (W) may be as high as 1, when the fairings are attached at the side of the deck such as Deer Isle (USA), Bronx-whitestone (USA), Hakucho (Japan) and Tempoan (Japan) bridges. These data are absent in Fig.2.3(b), as we couldn't manage shaping information of those bridge decks.

For hexagonal deck without fairing, we could collect shaping information of only four bridge decks constructed in Japan from Tatsumi (2010), Matsuyama (2013), Takada (2011), Nippon Engineering Consultant. Table 2.2 incorporates the shaping information including the general information of the decks. The side ratio (R) varies from 5 to 8. For smaller side ratio (R) of around 5, the width ratio (W) is maintained around 0.2, yet for higher side ratio (R) the width ratio (W) may

Table 2.1: Streamlined bridge deck surveyed to obtained detailed information about the shaping parameters

Name of the Bridge	Country	Span Length (m)	Side Ratio (R)	Width Ratio (W)	Top Plate Slope (θ_T)	Bottom Plate Slope (θ_B)
Great Belt Bridge	Denmark	1642	6.75	0.70	33.70	26.60
Nanjin-4 Bridge	China	1418	10.20	0.62	57.40	15.50
Tasing Ma Bridge	China	1377	4.60	0.80	36.00	31.20
Huga Kuston Bridge	Sweden	1210	4.45	0.55	35.50	22.60
Halogaland Bridge	Denmark	1145	5.00	0.53	41.40	15.80
Sutong Bridge	China	1088	9.5	0.60	49.10	15.50
Taizhou Bridge	China	1080	10.50	0.58	30.72	17.35
Edong Bridge	China	926	10.30	0.69	33.69	19.44
Jingyue Bridge	China	816	9.55	0.73	45.00	24.22
Incheon Bridge	Korea	800	11.00	0.50	55.30	11.25
Shanghai Bridge	China	730	12.50	0.67	59.00	17.08
Nanjin-3 Bridge	China	648	10.70	0.63	33.70	15.80
Nanjin-2 Bridge	China	628	8.60	0.73	45.00	28.50
Osteroy Bridge	Norway	595	5.30	0.63	62.85	29.50
Meikou Chuoo Bridge	Japan	590	10.00	0.72	26.70	21.00
Tsurumi Tsubasa Bridge	Japan	510	8.75	0.50	33.70	16.30
Miekou Higashi Bridge	Japan	410	9.9	0.72	25.30	22.00
Meikou Nishi Bridge	Japan	405	6.35	0.55	35.80	23.45
Japan-Egypt Bridge	Egypt	404	8.00	0.53	42.00	16.07
Oshima bridge	Japan	350	3.80	0.67	15.70	22.62
Shinonomichi Bridge	Japan	215	9.90	0.65	43.53	15.43
Cantho Bridge	Vietnam	210	9.30	0.50	60.25	16.39

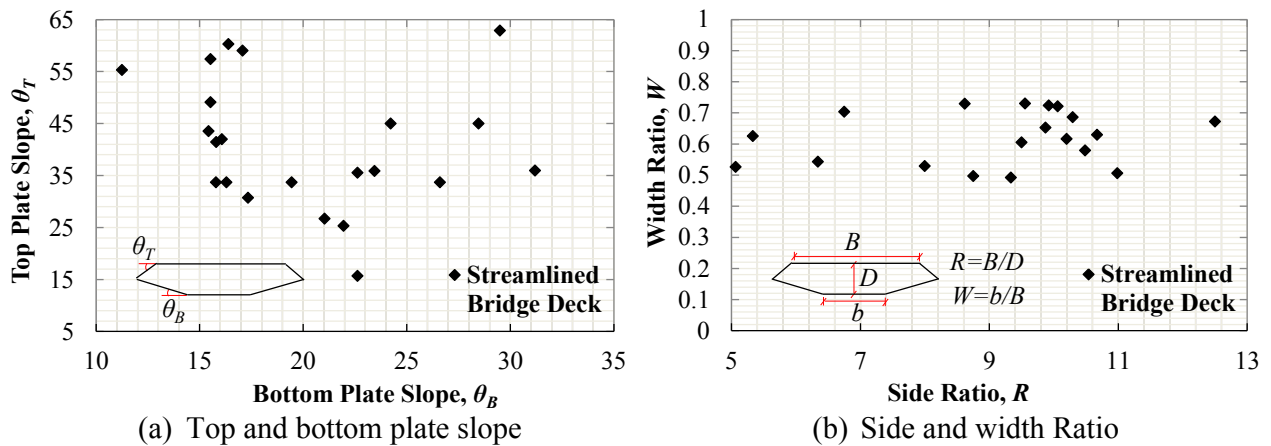
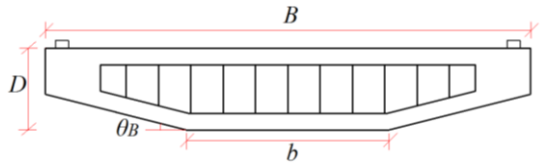


Figure 2.3: Shaping parameters of practically constructed streamlined bridge deck

Table 2.2: Survey results of various shaping parameters of hexagonal bridge deck without fairing

Name of the Bridge	Span Length (m)	Bottom plate Slope (θ_B)	Side Ratio (R)	Width Ratio (W)	Notations
Takeshima Ohashi	400	15.8°	5.85	0.45	
Shintenmom Bridge	264	14.96°	5.20	0.21	
Oshima Bridge	226	11.95°	5.50	0.23	
Kesennuma Bridge	360	12.18°	7.81	0.47	

reach up to 0.5. The bottom plate slope (θ_B) varies from 12° to 16°. Basically, the bottom plate slope (θ_B) is maintained around 12° based on the recommendation of Kubo *et al.* (2007). Where investigation was carried out for a pentagonal shaped bridge deck and showed that at a bottom plate slope (θ_B) of 12° the deck experiences minimum aerodynamic loading and the flutter wind speed increases. However, practically constructed bridges are hexagonal in shape and their aerodynamics would be different from that of a pentagonal shaped bridge deck. Therefore, the optimum bottom plate slope (θ_B) for a pentagonal shaped deck may not be optimum for hexagonal shaped bridge as a new shaping parameter the bottom horizontal plate (b) appears.

2.3 Aerodynamics Analysis

We conducted both static and dynamic aerodynamic analysis of bridge decks. We calculated steady state force coefficients of bridge decks and focused on their mean and root-means-squared (rms) value. We also conducted forced vibration simulation to estimate the flutter derivatives and aerodynamic damping of the bridge decks. In this section the detailed procedure of aerodynamic analysis and formulations are described.

2.3.1 Steady State Force Coefficients

For design of flexible structure like long-span bridge deck, aerodynamic forces and moments are important design parameter and considered at the very first stage of design to estimate the wind load (Miyata *et al.* 1992 and Fujino *et al.* 2012). The deck is always tried to design to have less wind load exhibiting nominal translation, deformation and rotation at the maximum design wind speed. For two-dimensional analysis, two aerodynamic forces and moment are considered: i) Drag force (F_D), ii) Lift force (F_L) and iii) Moment (F_M).

The aerodynamic forces and moments depend on number of geometric and flow parameters. Normally, the aerodynamic forces or moment are normalized with the velocity head ($\rho U^2/2$) and the characteristics length (D or B) to make them dimensionless (Simiu and Scanlan 1996). This conversion has significant advantages in the aerodynamic calculations and makes calculation simple. For example, the forces and moments acting on practical bridges are quite large quantity; the same forces and moments acting on a scale model obtained by wind tunnel experiment or by numerical simulation are quite small, yet in both of the case the aerodynamic coefficients will be the same. In the present study during analyzing the static responses, these coefficients were named as steady state force coefficients as the model was in static condition when the forces and moments were measured.

Fig.2.4 shows the direction of the positive forces, moments and characteristics length of the bridge deck. The aerodynamic forces and moment can be expressed in terms of steady state force coefficients as shown in Eq.2.1 to Eq.2.3: Where: F_D , F_L and F_M are the drag force, lift force and moment acting on the bridge deck respectively. ρ is the air density, B and D are the characteristic length, U is the flow velocity. In Eq.2.1 to Eq.2.3, the forces and moment can be calculated by integrating the pressure on the body surface in the along-flow and across-flow directions. In numerical simulation, the pressure can be obtained directly by solving the governing equations at any point in the flow domain. Other variables in Eq.2.1, Eq.2.2 and Eq.2.3 are problem dependent and known by the user.

In case of bridge deck without handrail the force and moment were normalized by the deck depth (D) only. For bridge deck with handrail cases, Eqs.2.1 to 2.3 were normalized by the total depth of the deck ($D'=D + d$, where, d , is the depth of the handrail). In case of static response, the steady state force coefficients were normalized by the top width (B) of the bridge deck, yet for

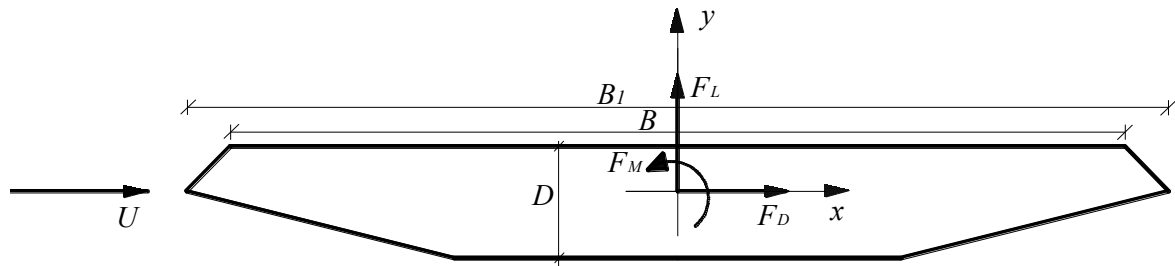


Figure 2.4: Definition of positive forces and characteristics length

dynamic response (flutter derivatives) those coefficients were normalized by the total width (B_I) of the bridge deck. Other parameters, such as Strouhal number ($S_{tB}=f_v B/U$, where, f_v , is the shedding frequency) and Reynolds number ($Re_B=UB/\nu_t$, where, ν_t is the kinematic viscosity of the fluid) were mostly normalized by the width of the bridge deck (B). In some cases the depth (D) of the bridge deck was also utilized and was indicated by the subscript.

The steady state force coefficients are obtained as a function of time from numerical simulations. We focused on the mean and root mean square (rms) value of the fluctuating force coefficients. The mean value was the static component and the rms value was the dynamic component of the fluctuating force coefficients, provides a measure of the energy associated with the specific data set. The mean and rms value of time-varying steady state force coefficients were calculated as described by Eq.2.4 and 2.5, respectively.

$$\mu_f = \frac{1}{N} \sum_{i=1}^N f_i(t) \quad (2.4)$$

$$\psi_f = \sqrt{\frac{1}{N} \sum_{i=1}^N [f_i(t) - \mu_f]^2} \quad (2.5)$$

2.3.2 Flutter Derivatives

Flutter derivatives are empirical coefficients by means of them the aeroelastic forces acting on a bridge decks can be expressed (Scanlan and Tomko 1971 and Scanlan, *et al.* 1974) and widely used in bridge and bluff body aerodynamic fields to assess the dynamic behavior of the bridge deck under wind action such as flutter (Matsumoto *et al.* 1996, 1999, 2007, Chen 2007, Matsumoto *et al.* 2008a, 2008b). It was first derived by Scanlan and Tomko (1971) and proposed only 6 flutter derivatives- A_1^* , A_2^* , A_3^* , H_1^* , H_2^* and H_3^* . However, 2 more flutter derivatives i.e. A_4^* and H_4^* were included later for two-dimensional analysis (Simiu and Scanlan 1996) and in case of three-dimensional total 18 flutter derivatives (Chen *et al.* 2000 and Chen *et al.* 2002) are required to apprehend the complete aerodynamic phenomena concerning the fluid-structure interactions. In this work two-dimensional simulation were conducted, hence only 8 flutter derivatives are needed.

2.3.2.1 Mathematical Background

In this section we will briefly introduce the governing equation of motion and self-excited force of a bridge deck in a smooth flow. Interested readers are referred to Simiu and Scanlan (1996) for detailed formulation of equation of motion and its solution. In two-dimensional flow the motion of a bridge deck can be described by two degrees of freedom: bending (η) and torsional (α) displacement. The bridge deck system was considered as a rigid body hang in balance around its mid-chord. For this system according to Theodorsen (1935) and Scanlan and Rosenbaum (1951) the equation of motion can be written as follows,

$$m \cdot [\ddot{\eta} + 2 \cdot \zeta_{\eta} \cdot \omega_{\eta} \cdot \dot{\eta} + \omega_{\eta}^2 \cdot \eta] = L(t), \quad (2.6)$$

$$I \cdot [\ddot{\alpha} + 2 \cdot \zeta_{\alpha} \cdot \omega_{\alpha} \cdot \dot{\alpha} + \omega_{\alpha}^2 \cdot \alpha] = M(t), \quad (2.7)$$

where $L(t)$ and $M(t)$ are, respectively, the self-excited aerodynamic lift and moment acting on the bridge deck per unit span; ω_{η} and ω_{α} are the circular frequencies $2\pi f_{\eta}$ and $2\pi f_{\alpha}$ of the heaving (η) and torsional (α) oscillations; η is the heaving displacement; α is the torsional displacement; the dots ($\dot{}$) and ($\ddot{}$) mean the derivatives with respect to time t ; m is the mass of the bridge deck per unit span; I is the mass moment of inertia per unit span length of the bridge deck; ζ_{η} and ζ_{α} are the heaving and torsional motions damping ratios-to-critical.

It was first Theodorsen (1935) who gave the expressions of $L(t)$ and $M(t)$ for a thin airfoils in incompressible flow based on the potential flow theory. The self-excited force and moment were expressed in terms of some coefficients referred as aeroelastic coefficients. Two theoretical functions $F(k)$ and $G(k)$ were required to define those aeroelastic coefficients. However, those expressions of self-excited force were not applicable for bluff bodies like bridge deck section. Then, Scanlan and Tomko (1971) derived the expressions of self-excited lift and moment for bluff bodies. It was showed that like airfoil, in case of bluff body also the self-excited $L(t)$ and $M(t)$ could be expressed in terms of some aeroelastic coefficients, yet those coefficients were functions of reduced velocity (U/B_l). Eq.2.8 and Eq.2.9 shows the expressions of self-excited $L(t)$ and $M(t)$ having two-degrees of freedom.

$$L(t) = \frac{1}{2} \cdot \rho \cdot U^2 \cdot B_l \cdot \left[k \cdot H_1^* \cdot \frac{\dot{\eta}}{U} + k \cdot H_2^* \cdot B_l \cdot \frac{\dot{\alpha}}{U} + k^2 \cdot H_3^* \cdot \alpha + k^2 \cdot H_4^* \cdot \frac{\eta}{B_l} \right], \quad (2.8)$$

$$M(t) = \frac{1}{2} \cdot \rho \cdot U^2 \cdot B_l^2 \cdot \left[k \cdot A_1^* \cdot \frac{\dot{\eta}}{U} + k \cdot A_2^* \cdot B_l \cdot \frac{\dot{\alpha}}{U} + k^2 \cdot A_3^* \cdot \alpha + k^2 \cdot A_4^* \cdot \frac{\eta}{B_l} \right], \quad (2.9)$$

where $L(t)$ and $M(t)$ are the time-varying self-excited lift force and moment per unit span of the bridge deck, respectively; ρ is the air density; U is the mean wind speed; k is reduced frequency, $k=B_l \cdot \omega/U$; ω is circular frequency, $2\pi f$; B_l is the full-width of the bridge deck; η is the heaving displacement; α is the torsional displacement; the dot ($\dot{}$) represents first time derivatives; H_i^* and A_i^* are the aeroelastic coefficients known as flutter derivatives. Eq.2.8 and Eq.2.9 can also be written in terms of time-varying self-excited lift ($C_L(t)$) and moment ($C_M(t)$) coefficients as follows:

$$C_L(t) = \left[k \cdot H_1^* \cdot \frac{\dot{\eta}}{U} + k \cdot H_2^* \cdot B_l \cdot \frac{\dot{\alpha}}{U} + k^2 \cdot H_3^* \cdot \alpha + k^2 \cdot H_4^* \cdot \frac{\eta}{B_l} \right]. \quad (2.10)$$

$$C_M(t) = \left[k \cdot A_1^* \cdot \frac{\dot{\eta}}{U} + k \cdot A_2^* \cdot B_l \cdot \frac{\dot{\alpha}}{U} + k^2 \cdot A_3^* \cdot \alpha + k^2 \cdot A_4^* \cdot \frac{\eta}{B_l} \right]. \quad (2.11)$$

2.3.2.2 Extraction of Flutter Derivatives

A number of system identification methods have been formulated over the times either in time or frequency domain to extract the flutter derivatives from wind tunnel tests (Scanlan and Tomko 1971, Sarkar *et al.* 1992, Yamada *et al.* 1992, Bogunovic-Jakobsen and Hijorth-Hansen 1995, Singh *et al.* 1996, Matsumoto *et al.* 1996, Chen *et al.* 2002, Chowdhury and Sarker 2003, and Bartoli and Righi 2006). The methods are different in terms of algorithm, yet can be divided into two wide categories (Sarker *etl al.* 2009): i) Free vibration method and ii) Forced vibration method. In wind tunnel study generally free vibration technique is adopted as experimental setup is simpler, yet requires completed system identification methods. On the other hand, forced vibration technique requires complicated model setup, yet calculation of flutter derivatives is easier and simple. In the present numerical work we adopted a forced vibration technique to extract the flutter derivatives.

To extract the flutter derivatives from Eq.2.10 and 2.11, it is required to be assumed that the bridge deck is in a harmonic motion in time as expressed by Eq.2.12 and Eq.2.13.

$$\eta = \eta_o \cdot e^{i\omega t}, \quad (2.12)$$

$$\alpha = \alpha_o \cdot e^{i\omega t}, \quad (2.13)$$

where, η_o is the amplitude of the given heaving motion, α_o is the amplitude of the given torsional motion and ω is the circular frequency of motion, same both in heaving and torsional mode. Now assuming the aerodynamic process is linear, it can also be assumed that the motion induced forced are also harmonic in time with the same frequency ω of excitation, yet shifts by a phase of amount φ relative to the motion. Based on all these assumptions by exploiting Eq.2.10, Eq.2.11, Eq.2.12 and Eq.2.13 the following expressions of flutter derivatives can be obtained (Larsen and Walther 1998, and Nieto *et al.* 2015):

$$H_2^* = -\frac{C_{L\alpha o} \cdot \sin(\varphi_{L\alpha})}{\alpha_o \cdot k^2}, \quad (2.14)$$

$$H_3^* = \frac{C_{L\alpha o} \cdot \cos(\varphi_{L\alpha})}{\alpha_o \cdot k^2}, \quad (2.15)$$

$$A_2^* = -\frac{C_{M\alpha o} \cdot \sin(\varphi_{M\alpha})}{\alpha_o \cdot k^2}, \quad (2.16)$$

$$A_3^* = \frac{C_{M\alpha o} \cdot \cos(\varphi_{M\alpha})}{\alpha_o \cdot k^2}, \quad (2.17)$$

$$H_1^* = -\frac{C_{L\eta o} \cdot B \cdot \sin(\varphi_{L\eta})}{\eta_o \cdot k^2}, \quad (2.18)$$

$$H_4^* = \frac{C_{L\eta_0} \cdot B \cdot \cos(\varphi_{L\eta})}{\eta_o \cdot k^2}, \quad (2.19)$$

$$A_1^* = -\frac{C_{M\eta_0} \cdot B \cdot \sin(\varphi_{M\eta})}{\eta_o \cdot k^2}, \quad (2.20)$$

$$A_4^* = \frac{C_{M\eta_0} \cdot B \cdot \cos(\varphi_{M\eta})}{\eta_o \cdot k^2}, \quad (2.21)$$

where in general, C_{L_o} is the amplitude of the time varying lift force coefficient ($C_L(t)$), C_{M_o} is the amplitude of the time varying moment coefficient ($C_M(t)$), φ_M is the phase lag between the moment and the imposed motion (η or α) and φ_L is the phase lag between the lift force and the imposed motion (η or α). It should be noted that instead of lift force ($L(t)$) and moment ($M(t)$) history, we can directly work with the lift force ($C_L(t)$) and moment ($C_M(t)$) coefficients.

Now, to calculate these flutter derivatives, in CFD a single degree of freedom torsional (α) or heaving (η) oscillations were assigned by Arbitrary Lagrangian-Eulerian (ALE) technique (Donea *et al.* 2004) to collect the lift force ($C_{L\alpha}(t)$ or ($C_{L\eta}(t)$) and moment ($C_{M\alpha}(t)$ or $C_{M\eta}(t)$) coefficients history. Thereafter, to calculate the amplitude of the lift force ($C_{L\alpha o}$ or $C_{L\eta o}$) and moment ($C_{M\alpha o}$ or $C_{M\eta o}$) coefficients of the time history data obtained as a numerical output, the high frequency components were filtered out from the obtained time history data by employing curve fitting techniques as like Stærdahl *et al.* (2007), Brusiani *et al.* (2013) and Patruno (2015). Then, the phase lag ($\varphi_{L\alpha}$ and $\varphi_{M\alpha}$ or $\varphi_{L\eta}$ and $\varphi_{M\eta}$) between the fitted curve ($C_{L\alpha}(t)$ and $C_{M\alpha}(t)$ or ($C_{L\eta}(t)$ and $C_{M\eta}(t)$) and the incurred motions (α or η) were estimated.

By exciting the bridge deck in torsional mode the torsional flutter derivatives (Eq.2.14 to Eq.2.17) can be evaluated. In this study we fundamentally focused on torsional flutter derivatives both for streamlined decks and hexagonal decks without fairing. Computing total 8 flutter derivatives directly from the force-vibration simulation is quite time consuming as the simulation is required to be conducted both in heaving and torsional mode for a number of reduced velocity (U/fB_I) separately. The heaving mode flutter derivatives were calculated by exploiting the interdependency relationships among the flutter derivatives. Only for few sections at a particular reduced velocity, heaving mode simulations were carried out to explore the unsteady pressure characteristics,

The heaving mode flutter derivatives (A_1^* , A_4^* , H_1^* and H_4^*) can be calculated from interdependency relationships among the flutter derivatives. A number of past researches have already mentioned about the interdependency among eight flutter derivatives for two-dimensional characterization of the bridge decks (Matsumoto 1996, Matsumoto *et al.* 1996, Scanlan *et al.* 1997, and Tubin 2005). Matsumoto (1996) showed the interdependency relationships among the flutter derivatives for rectangular bluff bodies and recommended a lower bound of rectangular cylinder of side ratio (R) of 5 to use his proposed relationships. Later, Tubin (2005) checked again the interdependency relationships among the flutter derivatives and found that the interdependency relationships among the flutter derivatives hold even better for streamlined deck rather than the bluff decks. Further, this kind of procedure has already been adopted in CFD approach to estimate flutter derivatives to reduce the computation load (Nieto *et al.* 2015).

Therefore, using the opportunity of the present study we also used the interdependency relationships among flutter derivatives for some cases to calculate the heaving mode flutter derivatives to lessen the number of simulation. The following expressions were considered to evaluate the heaving mode flutter derivatives (A_1^* , A_4^* , H_1^* and H_4^*) given by Matsumoto (1996):

$$H_1^* = k \cdot H_3^* \quad (2.22)$$

$$H_4^* = -k \cdot H_2^* \quad (2.23)$$

$$A_1^* = k \cdot A_3^* \quad (2.24)$$

$$A_4^* = -k \cdot A_2^* \quad (2.25)$$

2.3.2.3 Role of Flutter Derivatives

The flutter derivatives are capable of explaining distinct aerodynamic properties of bridge and bluff bodies. The derivatives are classified into two categories: i) Coupled and ii) non-coupled. A_2^* , A_3^* , H_1^* and H_4^* are the non-coupled flutter derivatives and affects the corresponding degree of freedom they are associated with. On the other hand, A_1^* , A_4^* , H_2^* and H_3^* are the coupled flutter derivatives affects the other degree of freedom (Trein 2009).

A_1^* and A_2^* provide information regarding the heaving and torsional aerodynamic damping, respectively, A_3^* related to the aerodynamic stiffness and A_4^* to the torsional displacement. Similarly, like A_i^* , H_i^* has also alike interpretations: H_1^* and H_2^* associated with the heaving and torsional aerodynamic damping, respectively, H_3^* concerns the aerodynamic stiffness and H_4^* related to heaving displacements.

Matsumoto *et al.* (1996, 1999, 2007, 2008a and 2008b) dedicated detailed investigations to explain the aeroelastic instability by means of the flutter derivatives and their roles on aeroelastic instability. By means of Step-By-Step analysis (Matsumoto *et al.* 1996), the role of each of the flutter derivative was tried to clarify in the generation of flutter instability. The results were well summarized by Trein and Shirato (2010) and presented here in Table 2.3. Furthermore, for elongated bluff body having a $H_1^* < 0$ and $A_2^* < 0$ indicates the possibility of coupled flutter instability and

Table 2.3: Role of flutter derivatives on flutter instability (Trein and Shirato 2010)

Derivatives	Stabilization	Destabilization
A_1^*	low absolute values	high absolute values
A_2^*	negative values	positive values
A_3^*	low absolute values	high absolute values
H_1^*	negative values	positive values, low absolute values
H_3^*	low absolute values	high absolute values

increases the importance of other six flutter derivatives (Chen 2007). Single-heaving-mode flutter (Galloping) can be occurred only when $H_1^* > 0$ and single-torsional-mode flutter (Torsional flutter) for $A_2^* > 0$ (Chen 2007).

2.3.3 Calculation of Unsteady Pressure Characteristics

Based on flutter derivatives the general information about the genesis of flutter instability can be obtained. However, for detailed understanding the inside mechanism of aerodynamic instability, unsteady pressure distribution should be considered and bears meaningful information regarding the complex fluid-structure interaction.

In the present work, both in heaving and torsional mode the bridge decks were oscillated in a harmonic motion to extract the unsteady pressure characteristics of bridge deck in some particular reduced velocity (U/fB_1). The pressure was probed at both at the top and bottom deck surface at various locations (x) from the center. The pressure had mean and unsteady component due to harmonic oscillation and depends on the wind velocity (U) and the density (ρ) of the fluid. In order to make it comparable among different cases the pressures were normalized with dynamic pressure, $\frac{1}{2}\rho.U^2$ and resulted mean ($\bar{C}_p(x)$) and unsteady pressure coefficients ($|C_p(x,t)|$).

The heaving and torsional oscillation was defined by cosine function (Eq.2.26 and Eq.2.27) and the total pressure coefficient ($C_p(x,t)$) was defined as like Eq.2.28.

$$\alpha(t) = \alpha_o \cdot \cos(2 \cdot \pi \cdot f_\alpha \cdot t), \quad (2.26)$$

$$\eta(t) = \eta_o \cdot \cos(2 \cdot \pi \cdot f_\eta \cdot t), \quad (2.27)$$

where: $\alpha(t)$ and $\eta(t)$ are the torsional and heaving displacement at a given time t , respectively, α_o and η_o are the amplitude of torsional and heaving oscillation, respectively, f_α and f_η are the torsional and heaving oscillation frequency of the model.

$$C_p(x,t) = \bar{C}_p(x) + |C_p(x,t)|. \quad (2.28)$$

The mean pressure coefficient ($\bar{C}_p(x)$) can be obtained by averaging over time and doesn't alter significantly whether the body is in static or moving. On the other hand, the unsteady pressure coefficient ($|C_p(x,t)|$) is dependent on the amplitude of vibration. The unsteady pressure coefficient ($|C_p(x,t)|$) was defined by the magnitude of unsteady pressure ($|C_p(x)|$) and the phase lag ($\varphi(x)$) between the motion of the body and the pressure. The magnitude of unsteady pressure ($|C_p(x)|$) was taken as the amplitude of the periodic pressure coefficient history caused by the forced vibration only ignoring the high frequency component due to vortex shedding. The phase lag ($\varphi(x)$) was

defined as a difference in phase between the maximum relative angle of attack of the bridge deck and the maximum negative pressure at a distance x . Eq.2.29 shows the expression of unsteady pressure coefficient utilized.

$$|C_p(x, t)| = -|C_p(x)| \cdot \cos(2 \cdot \pi \cdot f \cdot t + \varphi). \quad (2.29)$$

The imaginary part of the unsteady pressure ($|C_p(x, t)|$) is proportional to the velocity of the motion and defines as $C_{PI} = |C_p(x)| \cdot \sin\varphi(x)$, is related to the aerodynamic damping of the bridge deck (Miyata *et al.* 1993, Nagao *et al.* 1997, Matsumoto *et al.* 1997 and Sukamta *et al.* 2008). In the present work for heaving motion, the positive value of $|C_p(x)| \cdot \sin\varphi(x)$ on the top deck surface was considered as a excitation force and negative value as an damping force to the system. On the bottom deck surface this was is in contrast with the top deck surface. In the case of torsional motion, the positive value was considered as an excitation force and negative value was a damping force on the top deck leading edge side and was altered at the trailing edge top bridge deck surface. Opposite sign convention was adopted on the bottom deck surface in relation to the top deck surface at the leading and trailing edge side.

The work done by the unsteady pressure can be calculated as follows,

$$C_{PI} \cdot r = \left(\frac{x}{B}\right) \cdot |C_p(x)| \cdot \sin\varphi(x) \quad (2.30)$$

where r is the normalized distance from the center of the bridge deck to the both sides.

2.4 Concluding Remarks

At the beginning of the chapter various types of deck shapes utilize for long-span cable-supported bridges were introduced. The range of various shaping parameters for selected deck shapes were presented based on the survey results of practically constructed bridges. Then, an overview of the static and dynamic aerodynamic analysis and formulation were demonstrated those should be considered as a reference for the remaining parts of this dissertation.

Chapter 3

Governing Equation, Numerical method, Grid and Validation

In the present research Computational Fluid Dynamics (CFD) techniques was employed to predict the bridge deck response as mentioned earlier. OpenFOAM¹ (Open Source Field Operation And Manipulation), an open source CFD software package was used as an solver. The development of the code started in the late of 1980s at Imperial College using Fortran programming language. Later, it was changed to C++ due to its large modularity and object oriented features. Recently, it is drawing attention of researchers from various fields dealing with fluid related problem including bluff body and bridge aerodynamicists due to its wide range of numerical methods, pre/post-processing utilities and flexibility of customization.

We choose OpenFOAM, since it is a free code under GNU general public license. This allowed us as to conduct large numbers of simulations with parallel computing system without any restriction of license. Besides that, OpenFOAM allows customizing and accessing inside the code that gives user opportunity for extension and understanding the programming techniques those were adopted.

In this chapter the details of the theoretical background of turbulence model, numerical methods for discretization and the solution techniques those were selected during the case setup process in OpenFOAM is presented. The chapter is divided broadly into two parts. The first part deal with the theoretical background and the second part validates the numerical results.

¹www.openfoam.com/

First the governing equations of fluid and the basics of unsteady Reynolds-Averaged-Navier-Stokes (RANS) simulation is introduced. Then, the theory of turbulence model is presented. Various discretization techniques utilized for discretizing the equation are discussed and the solution strategy of discretized equation is also demonstrated. A strategy to obtain promptly and easily the grid independent solution are proposed too. At the end of the chapter both the static and dynamic solution results are validated for bluff bodies of rectangular cylinders and bridges decks having different shapes.

3.1 Equation of Fluid Flow

The wind flow around a bluff body can be represented by the Navier-Stokes equation. The Navier-Stokes equation is a set of partial differential equations can be derived from the conservation law of physics, i.e. mass, momentum and energy. The detailed derivation of the equation can be found in Anderson (1995) and Drikakis and Rider (2005). The whole system of equations includes conservation of mass, momentum and energy. However, in wind flow around a bluff body thermal effect is neglected (Simiu and Scanlan 1996), hence the energy equation was not considered in the present study assuming the flow is incompressible in nature as the Mach number (M) lay well below than 0.3 (Anderson 2010, Fletcher 1996). For incompressible flow the Navier-Stokes equation can be written in differential form as follows,

$$\frac{\partial u}{\partial x} + \frac{\partial v}{\partial y} + \frac{\partial w}{\partial z} = 0, \quad (3.1)$$

$$\frac{\partial u}{\partial t} + \frac{\partial u^2}{\partial x} + \frac{\partial uv}{\partial y} + \frac{\partial uw}{\partial z} = -\frac{1}{\rho} \frac{\partial p}{\partial x} + \nu \left(\frac{\partial^2 u}{\partial x^2} + \frac{\partial^2 u}{\partial y^2} + \frac{\partial^2 u}{\partial z^2} \right), \quad (3.2)$$

$$\frac{\partial v}{\partial t} + \frac{\partial uv}{\partial x} + \frac{\partial v^2}{\partial y} + \frac{\partial vw}{\partial z} = -\frac{1}{\rho} \frac{\partial p}{\partial y} + \nu \left(\frac{\partial^2 v}{\partial x^2} + \frac{\partial^2 v}{\partial y^2} + \frac{\partial^2 v}{\partial z^2} \right), \quad (3.3)$$

$$\frac{\partial w}{\partial t} + \frac{\partial uw}{\partial x} + \frac{\partial vw}{\partial y} + \frac{\partial w^2}{\partial z} = -\frac{1}{\rho} \frac{\partial p}{\partial z} + \nu \left(\frac{\partial^2 w}{\partial x^2} + \frac{\partial^2 w}{\partial y^2} + \frac{\partial^2 w}{\partial z^2} \right), \quad (3.4)$$

where u , v and w are the velocity components in x , y and z directions, ρ is the density and ν is the kinematic viscosity. The above mentioned continuity and momentum equations can be written in much compact differential form as shown in Eq.3.5 to 3.6 and will be written other equations throughout this chapter in this form.

$$\nabla \cdot \mathbf{U} = 0. \quad (3.5)$$

$$\frac{\partial \mathbf{U}}{\partial t} + \nabla \cdot (\mathbf{U}\mathbf{U}) = -\frac{1}{\rho} \nabla p + \nu \nabla^2 \mathbf{U}. \quad (3.6)$$

The analytical solutions of Navier-Stokes equations are exceedingly difficult due to nonlinear and coupled natures of the equations. Moreover, most of the engineering processes deal with high Reynolds number (Re_B) flow that is turbulent in nature. The turbulent flow is chaotic and random in nature, where the pressure and velocity alters on a wide range of time and length scale. The solution becomes even more complicated when it is dealt with turbulent flows.

However, with the development of efficient numerical techniques and advancement of high speed computing technology, a number of possible approaches for numerical simulation of turbulent flow exist now. The most widely uttered methods are the Direct Numerical Simulation (DNS), Large Eddy Simulation (LES) and unsteady Reynolds-Averaged Navier-Stokes (RANS) simulation. DNS is the most intuitive one doesn't require any modeling, where the governing equations are resolved for all the length and time scales of the turbulence spectrum numerically. For LES appropriate modeling is required for high frequency parts of the turbulence spectrum and the governing equations are solved numerically all through the inertial sub-range of the spectrum. We will not deepen the discussion on these two approaches, interested readers are referred to Hoffmann and Chiang (2000), Pope (2000), Sagaut (2005), Jiang and Lai (2009) and Dewan (2011).

Both of this approach is computationally expensive as they require very fine meshes and small time steps to resolve the wide range of turbulent scales. Currently, DNS is used for benchmark studies and academic applications, while the application of LES for industrial problems is becoming practical due to availability of high performance computing system and development of parallel computing algorithm. Still it is not appropriate and affordable for simulation around objects having long boundary layer and for large number of simulations at high Reynolds number (Re_B). Consequently, in the present study unsteady RANS simulation was opted due to its computational lightness and reasonable accuracy. The applicability of unsteady RANS simulation in bridge aerodynamics field was discussed already in section 1.3 of Chapter 1. In the next section the concept and governing equations of unsteady RANS simulation are introduced.

3.2 Reynolds-Averaged Navier-Stokes Equation

In unsteady RANS simulation all the unsteadiness due to turbulence is averaged out. The fluctuating flow variables are decomposed into averaged and fluctuating component is known as Reynolds decomposition (Pope 2000, Wilcox 2006 and Versteeg and Malalasekera 2007). The RANS equations are obtained by time averaging the Navier-Stokes equation.

Let us decompose the flow variables i.e., velocity (U) and pressure (p) of the incompressible Navier-Stokes equation,

$$U(x,t) = \bar{U}(x) + U'(x,t), \quad (3.7)$$

$$p(x,t) = \bar{p}(x) + p'(x,t), \quad (3.8)$$

where $\bar{U}(x)$ is the mean value part and $U'(x,t)$ is the fluctuating part in Eq.3.7. Similar notation can be followed for Eq.3.8. The mean value component $\bar{U}(x)$ can be obtained either by time averaging as shown in Eq.3.9 for statistically steady turbulence or by ensemble averaging as shown in Eq.3.10 for unsteady turbulence. For unsteady RANS simulation the ensemble averaging is required to eliminate the effects of fluctuations.

$$\bar{U}(x) = \lim_{T \rightarrow \infty} \frac{1}{T} \int_t^{t+T} U(x,t) dt, \quad (3.9)$$

$$\bar{U}(x,t) = \lim_{N \rightarrow \infty} \frac{1}{N} \sum_{i=1}^N U(x,t), \quad (3.10)$$

here t is the time, T is the averaging interval and N is the ensemble number must be large enough to eliminate the effects of fluctuations. Now, substituting Eq.3.7 and Eq.3.8 into Eq.3.5 and Eq.3.6 the desired unsteady RANS equation can be obtained as follows

$$\nabla \cdot \bar{U} = 0. \quad (3.11)$$

$$\frac{\partial \bar{U}}{\partial t} + \nabla \cdot (\bar{U}\bar{U}) = -\frac{1}{\rho} \nabla \bar{p} + \nu \nabla^2 \bar{U} - \frac{1}{\rho} \nabla \cdot \tau^R. \quad (3.12)$$

The unsteady RANS equation is similar to Navier-Stokes equation, except a new term τ^R appears known as Reynolds-stress tensor. Sometimes Reynolds-stress tensor is mentioned also as τ_{ij} in Cartesian tensor format. In three-dimension, the Reynolds-stress tensor (τ^R) is a symmetrical second order tensor consists of six components and representing the transfer of momentum due to turbulent fluctuations.

$$\tau^R = -\rho(\overline{U'U'}) = -\begin{pmatrix} \overline{\rho u'u'} & \overline{\rho u'v'} & \overline{\rho u'w'} \\ \overline{\rho v'u'} & \overline{\rho v'v'} & \overline{\rho v'w'} \\ \overline{\rho w'u'} & \overline{\rho w'v'} & \overline{\rho w'w'} \end{pmatrix}. \quad (3.13)$$

Now, if we count the number of unknowns by scrutinizing Eq.3.11, Eq.3.12 and Eq.3.13, total ten unknowns can be found, i.e., the three velocity components (u, v, w), the pressure and six components of the Reynolds-stress tensor ($-\rho(\overline{U'U'})$). Nevertheless, we have one continuity and three momentum equations to solve. Therefore, the system is not close. We require six more equations to close the system and this is what known as Turbulence modeling.

This number of unknowns can be reduced from six to one by the Boussinesq Hypothesis. In 1877 Boussinesq proposed that the Reynolds stress might be proportional to the mean rates of deformation. It was presumed that a relationship or analogy exists among the molecular and turbulent viscosity. Since then enormous applications of this hypothesis can be found in various

fields of CFD and yields reasonable results for large number of flows. Therefore, based on Boussinesq's eddy viscosity approach the Reynolds-stress tensor can be related to the mean velocity gradient as follows,

$$\tau^R = -\rho(\overline{U'U'}) = \mu_T \left[\nabla \bar{U} + (\nabla \bar{U})^T \right] - \frac{2}{3} \rho k \mathbf{I}, \quad (3.14)$$

$$k = \frac{1}{2} \overline{U' \cdot U'}, \quad (3.15)$$

here $\frac{1}{2}(\nabla \bar{U} + (\nabla \bar{U})^T)$ is Reynolds-averaged strain-rate tensor and denotes as S_{ij} in tensor format, \mathbf{I} is the identity matrix, k is the turbulent energy per unit mass and μ_T is the turbulent eddy viscosity. Now, we require the only one equation for the turbulent eddy viscosity (μ_T) to make the unsteady RANS equations solvable. In the next section we will introduce how the turbulence eddy viscosity (μ_T) was modeled in this study, also known as turbulence modeling. In OpenFOAM, the momentum equation was implemented as follows:

```
...
(
    fvm::ddt(U)
    + fvm::div(phi, U)
    + turbulence->divDevReff(U)
);
UEqn.relax();
...
```

The third term is related to the modeling of the turbulence viscosity that will be discussed in the following section. It is worthy to mention that, the connection to the previous time step was maintained through the last line of the code as shown here.

3.3 Turbulence Model

A number of two-equation turbulence models have been developed over the years to model the eddy viscosity (μ_T). The most widely used models are the $k-\varepsilon$ model, $k-\omega$ model and the (Shear Stress Transport) SST $k-\omega$ model (Versteeg and Malalasekera 2007). Each of these models has their own advantages and disadvantages. The $k-\varepsilon$ model is weak at the boundary layer with adverse pressure gradient and overestimates the turbulence shear stress, yet at the free stream turbulent location away from the body or wall the results are less sensitive to the arbitrary assumed values of variables at the inlet. On the other hand, the $k-\omega$ model has better performance near wall without requiring wall-damping function but free stream results is sensitive to the arbitrary assumed values at the inlet boundaries.

Then, Menter (1992a, 1992b, 1994 and 1997) suggested a hybrid model named as SST $k-\omega$ model, where he took the advantages of these two models. Near the wall he applied the $k-\omega$ model and away from the wall at the free stream fully turbulent region, the $k-\varepsilon$ model was implemented. In the present study we also adopted the SST $k-\omega$ model for modeling turbulence. The model was implemented by selecting $k\Omega$ SST in *RASProperties* dictionary of OpenFOAM. In bridge aerodynamic field a number of recent applications (Šarkić *et al.* 2012, Brusani *et al.* 2013, Nieto *et al.* 2015 and Patruno 2015) can be found using this turbulence model. The model is described below.

To improve the results at the location of adverse pressure gradient, wake of the body and to reduce the production of turbulence kinetic energy, the eddy viscosity was modeled as follows

$$\frac{\mu_T}{\rho} = \nu_t = \frac{a_1 k}{\max(a_1 \omega, SF_2)}, \quad (3.16)$$

$$S = \sqrt{2S_{ij}S_{ij}} \quad \text{and} \quad F_2 = \tanh \left[\left[\max \left(\frac{2\sqrt{k}}{\beta^* \omega y}, \frac{500\omega}{y^2 \omega} \right) \right]^2 \right], \quad (3.17)$$

where ν_t is the kinematic eddy viscosity, S is the modulus of Reynolds-averaged strain-rate tensor, y is the wall distance, F_2 is a blending function. To model the eddy viscosity two more addition transport equations for turbulent kinetic energy (k) and turbulent specific dissipation rate (ω) were required. The equation for turbulent kinetic energy (k) was as follows,

$$\frac{\partial k}{\partial t} + \nabla \cdot (\bar{U}k) = P_k - \beta^* k \omega + \nabla \cdot [(\nu + \sigma_k \nu_T) \nabla k], \quad (3.18)$$

$$P_k = \min \left(\tau_{ij} \frac{\partial U_i}{\partial x_j}, 10\beta^* k \omega \right). \quad (3.19)$$

In openFOAM, SST $k-\omega$ model was implemented in $k\Omega$ SST.C file. The function $\text{divDevReff}()$, related to the eddy viscosity mentioned earlier was defined in $k\Omega$ SST.C as,

```
...
tmp<fvVectorMatrix> kOmegaSST::divDevReff(volVectorField& U) const
{
    return
    (
        - fvm::laplacian(nuEff(), U)
        - fvc::div(nuEff()*dev(T(fvc::grad(U))))
    );
}
```

```
}
...
```

The k -equation was implemented as follows,

```
...
(
    fvm::ddt(k_)
  + fvm::div(phi_, k_)
  - fvm::laplacian(DkEff(F1), k_)
  ==
    min(G, c1_*betaStar_*k_*omega_)
  - fvm::Sp(betaStar_*omega_, k_)
);
...
```

The equation for the turbulent specific dissipation rate (ω) was as follows,

$$\frac{\partial \omega}{\partial t} + \nabla \cdot (\bar{U} \omega) = \alpha S^2 - \beta \omega^2 + \nabla \cdot [(\nu + \sigma_\omega \nu_T) \nabla \omega] + 2(1 - F_1) \sigma_{\omega 2} \frac{1}{\omega} \frac{\partial k}{\partial x_i} \frac{\partial \omega}{\partial x_i}. \quad (3.20)$$

$$F_1 = \tanh \left[\min \left[\max \left(\frac{\sqrt{k}}{\beta^* \omega y}, \frac{500 \nu}{y^2 \omega} \right), \frac{4 \sigma_{\omega 2} k}{CD_{k\omega} y^2} \right] \right]^4 \text{ and } CD_{k\omega} = \max \left(2 \rho \sigma_{\omega 2} \frac{1}{\omega} \frac{\partial k}{\partial x_i} \frac{\partial \omega}{\partial x_i}, 10^{-10} \right). \quad (3.21)$$

This transport equation was coded in OpenFOAM in the following way,

```
...
(
    fvm::ddt(omega_)
  + fvm::div(phi_, omega_)
  - fvm::laplacian(DomegaEff(F1), omega_)
  ==
    gamma(F1)
    *min(S2, (c1_/a1_)*betaStar_*omega_*max(a1_*omega_,
b1_*F23()*sqrt(S2)))
  - fvm::Sp(beta(F1)*omega_, omega_)
  - fvm::SuSp
    (
        (F1 - scalar(1))*CDkOmega/omega_,
        omega_
    )
);
```

);
...

all the terms a_l , α , β^* , β , σ_k and σ_ω mentioned in the Eq.3.16 to Eq.3.21 are coefficients. Further details on the model can be found in Menter (1992a, 1992b, 1994 and 1997) and Menter *et al.* (2003).

3.4 Finite Volume Method of Discretization

In the last section we described the governing equations of unsteady RANS simulation. These equations are continuous partial differential equation and can't be solved analytically. Any standard discretization technique such as Finite Element Method (FEM), Finite Difference Method (FDM) or Finite Volume Method (FVM) is required to transfer those partial differential equations into discrete algebraic form to make them solvable.

In OpenFOAM Finite Volume Method (FVM) was implemented to discretize the governing equation of unsteady RANS as shown in the last two sections. In FVM the continuous partial differential equations are transformed into a set of discrete algebraic equations to solve them either adopting certain direct or iterative method. The process consists of two main steps: the discretization of the solution domain and the discretization of the governing equations. In the following section we briefly summarize the Finite Volume Method (FVM). The materials were extracted from Jassak (1996), Versteeg and Malalasekera (2007) and OpenFOAM (2015a). For further detail about the method and implementation technique interested readers are referred to Patankar (1980), Jassak (1996), LeVeque (2002), Ferziger and Perić (2002), Versteeg and Malalasekera (2007), Toro (2009), OpenFOAM (2015a) and OpenFOAM (2015b).

3.4.1 Discretization of the Solution Domain

The solution discretization involves both the time and the domain discretization known as temporal and spatial discretization, respectively. The spatial discretization is also known as grid generation or mesh generation. This determines the location of the nodes where the unknown solution variables of the governing equations will be evaluated in space and time.

In temporal discretization the time is divided into finite number of discrete intervals usually known as time steps. Depending on the solution strategy both the uniform or variable time steps can be used. The size of the time step is determined based on how frequent the solutions are required to grasp the natural phenomenon or based on courant number (C_o) from stability point of view.

In spatial discretization the computational domain is decomposed into a finite number of discrete subdomains or regions called control volumes (CV s) along with the nodes where the solution of the governing equations are evaluated. Fig. 3.1(a) shows the planar view of the spatially

discretized system. The summation of all the control volume yields the computational domain. The control volumes don't overlap and numbered sequentially with specific procedure.

Fig. 3.1(b) shows a typical hexahedral control volume and its notation. The control volume is denoted as V_p and surrounded by a number of flat faces f . Each of these faces are attached to the neighboring control volumes. The face area vector S_f is located at the center of the corresponding face, pointing outward (n_f) and possess a magnitude equal to the area of the face. The point P is the centroid of the control volume V_p and E , W are the centroid of the neighboring control volumes. The vector d represents the distance between the centroids of the two neighboring control volumes E and W . All the variables are calculated at these centroids i.e., collocated arrangement.

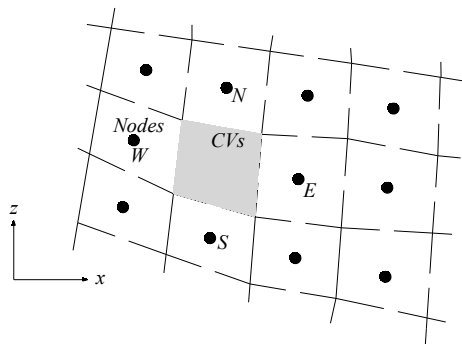
3.4.2 Equation Discretization

In FVM method, the integral form of the equation is used based on generalized form of Gauss Theorem to discretize the equation. The governing equation presented in section 3.2 and 3.3 can be written in a generic form of transport equation for a scalar property ϕ as follows,

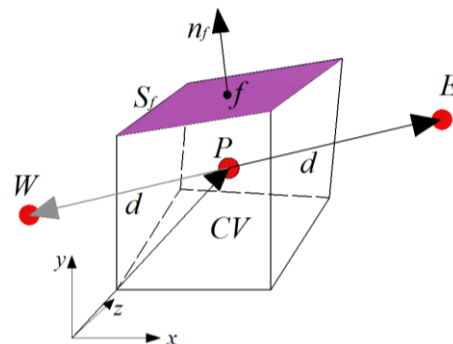
$$\frac{\partial \rho \phi}{\partial t} + \nabla \cdot (\rho U \phi) - \nabla \cdot (\rho \Gamma_\phi \nabla \phi) = S_\phi(\phi), \quad (3.22)$$

here ϕ represents the transported quantity such as U , k or ω and Γ_ϕ is the diffusion coefficient of the transported quantities. In FVM the transported equation are written in integral form to discretize the equation and apply the Gauss or divergence theorem. Hence, the generic equation can be rewritten in integral form in the following way,

$$\underbrace{\int_{V_p} \frac{\partial \rho \phi}{\partial t} dV}_{\text{Unsteady Term}} + \underbrace{\int_{V_p} \nabla \cdot (\rho U \phi) dV}_{\text{Convective Term}} - \underbrace{\int_{V_p} \nabla \cdot (\rho \Gamma_\phi \nabla \phi) dV}_{\text{Diffusive Term}} = \underbrace{\int_{V_p} S_\phi(\phi) dV}_{\text{Source Term}}. \quad (3.23)$$



(a) Planar view



(b) Hexahedral control volume

Figure 3.1: Concept of control volume and various notations adopted during discretization process

Now, based on Gauss theorem this volume integral can be converted into surface integrals. According to Gauss theorem the volume integrals of the divergence of a vector in a region inside the control volume can be expressed in terms of the integral of the outwards flux normal to the surface surrounds the control volume. Therefore, Eq. 3.23 can be rewritten as below

$$\frac{\partial}{\partial t} \int_{V_P} (\rho \phi) dV + \underbrace{\oint_{\partial V_P} dS \cdot (\rho U \phi)}_{\text{Convective Flux}} - \underbrace{\oint_{\partial V_P} dS \cdot (\rho \Gamma_\phi \nabla \phi)}_{\text{Diffusive Flux}} = \int_{V_P} S_\phi(\phi) dV. \quad (3.24)$$

This equation physically implies that the rate of change of transported quantity ϕ within the control volume V_P is equal to the summation of rate of change of the convective and diffusive fluxes at the surface confines the control volume and the net rate of evolution of ϕ within the control volume. Now, we will go in detailed one by one each of these terms starting with the convective term.

3.4.2.1 Spatial Discretization of Convective Term

As can be seen from Eq.3.24 the convective term is a product of a surface integral. If we want to evaluate this term we need the value of transport property ϕ at the face of the control volume which is unknown. To obtain the surface value we need to approximate the distribution of transport properties on a face of the control volume and the nature of contribution of neighboring control volumes sharing that particular face.

We assumed that the transport property ϕ varies linearly over each face f of the control volume V_P and may be presented by its mean value at the centroid of each face f . Based on this approximation we can now express the surface integral as a product of the transport quantity at the centroid of the face f and the face area. This approximation has second-order accuracy. Based on this approximation the convective term in Eq.3.24 can be presented as follows,

$$\underbrace{\oint_{\partial V_P} dS \cdot (\rho U \phi)}_{\text{Convective Flux}} = \sum_f \int_f dS \cdot (\rho U \phi) \approx \sum_f S_f \cdot (\overline{\rho U \phi})_f = \sum_f S_f \cdot (\rho U \phi)_f = \sum_f S_f \cdot (\rho U)_f (\phi)_f = \sum_f F(\phi)_f, \quad (3.25)$$

where F is the mass flux. Now we need a relation through which we can calculate the face center value of the transport property from the centroid value (P , E or P , W) of the control volume is known as interpolation scheme. There are a number of interpolation schemes available in the literature such as Upwind (UD) scheme, Central Differencing (CD) scheme, QUICK Scheme. Each of these schemes has their weak and strong points. Detailed can be found in Patankar (1980), Jasak 1996, LeVeque (2002), Ferziger and Perić (2002), Versteeg and Malalasekera (2007) and Toro (2009). UD scheme is very stable and doesn't yield any wiggles but lower accuracy, whereas CD and QUICK have higher order accuracy having low stability. In the present study we utilized Total Variation Diminishing (TVD) scheme that has adopted the best of these two worlds.

The interpolated value of the transport property at the face centroid can be expressed as below,

$$\phi_f = f_x \phi_p + (1 - f_x) \phi_E, \quad (3.26)$$

where f_x is the interpolation factor and can be defined as the ratio of distance fE and PE . Now, if we assume the distance between the centroids of two neighboring control volumes are uniform, i.e., d , then any kind of scheme and the nature of the scheme can be expressed by the appropriate function $\psi(r)$ (Versteeg and Malalasekera 2007). Later, this function will be called as limiter function and can be expressed as follows,

$$\phi_f = \phi_p + \frac{1}{2} \psi(r) (\phi_E - \phi_p), \quad (3.27)$$

where,

$$r = \left(\frac{\phi_p - \phi_w}{\phi_E - \phi_p} \right). \quad (3.28)$$

Here, r represents the gradient ratio and for one dimensional flow from P to E it can be written as above. For UD scheme the $\psi(r)$ is 0, which means the face centroid value is equal to its upwind sides control volumes centroid value (P). Similarly for CD scheme the value is 1. Now, a scheme to be stable, non-oscillatory and higher-order accurate it should possess monotonicity-preserving properties (Versteeg and Malalasekera 2007). The schemes having this monotonicity-preserving properties is so called Total Variation Diminishing (TVD) scheme.

The mathematical criteria of a scheme to be TVD scheme was given by Sweby (1984). According to sweby (1984) a scheme to be TVD:

- 1) $\psi(r) \leq 2r$ for $0 < r < 1$ and,
- 2) $\psi(r) \leq 2r$ for $r \geq 1$.

According to these criteria UD, CD and QUICK all of them are TVD for a particular range of gradient ratio (r). For example, CD is not TVD for a value less than 0.5 but becomes TVD for higher than that value. Therefore, we need an appropriate expression of $\psi(r)$ i.e., limiter function that will convert these schemes to the TVD scheme for any value of gradient ratio (r).

Over the years a number of limiter functions have been developed by following Sweby's criteria. In OpenFOAM a variant of the Sweby Limiter (Sweby 1984) was implemented and that can be state as below,

$$\psi(r) = \max \left[\min \left(\frac{2}{\beta} r, 1 \right), 0 \right] \quad 0 < \beta \leq 1 \quad (3.29)$$

In the present work we employed Central Differencing (CD) scheme with Sweby limiter function to ensure the monotonicity criteria is named as *Gauss limitedLinear* scheme in OpenFOAM. The sweby limiter function in OpenFOAM was implemented as follows,

```

...
{
    scalar r = LimiterFunc::r
    (
        faceFlux, phiP, phiN, gradcP, gradcN, d
    );
    return max(min(twoByk_*r, 1), 0);
}
...

```

3.4.2.2 Spatial Discretization of Diffusive Term

As like convective terms, the diffusive term in Eq.3.24 can be also be written as in Eq.3.25. The diffusive term can be discretized as shown like Eq.3.30.

$$\int_{\partial V_P} \underbrace{dS \cdot (\rho \Gamma_\phi \nabla \phi)}_{\text{Diffusive Flux}} = \sum_f \int_f dS \cdot (\rho \Gamma_\phi \nabla \phi)_f \approx \sum_f S_f \cdot (\overline{\rho \Gamma_\phi \nabla \phi}) = \sum_f S_f \cdot (\rho \Gamma_\phi \nabla \phi)_f = \sum_f (\rho \Gamma_\phi)_f S_f \cdot (\nabla \phi)_f. \quad (3.30)$$

The diffusion coefficient Γ_ϕ at the face can be interpolated by Central Differencing (CD) scheme, i.e., with linear interpolation between the control volume V_P and V_E . as sketched in Fig.3.2. The basic concept of CD scheme in terms of face conductivity can be expressed as Eq.3.31.

$$(\Gamma_\phi)_f = f_x (\Gamma_\phi)_P + (1 - f_x) (\Gamma_\phi)_E \quad (3.31)$$

where

$$f_x = \frac{fE}{PE} \quad (3.32)$$

f_x is the interpolation scheme and becomes 0.5 when the CV s have a uniform size. In Eq.3.30 the face gradient term $(\nabla \phi)_f$ arises from the spatial discretization of diffusive term requires approximation. When the grid system is orthogonal, i.e., the vector d and S are parallel as shown in Fig.3.3(a), the gradient term can be computed as follows,

$$S \cdot (\nabla \phi)_f = |S| \frac{\phi_E - \phi_P}{|d|}. \quad (3.33)$$

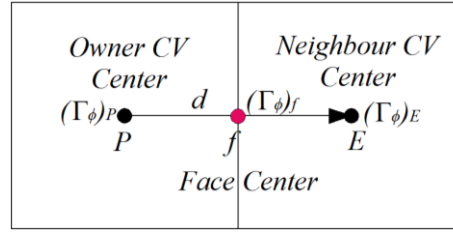
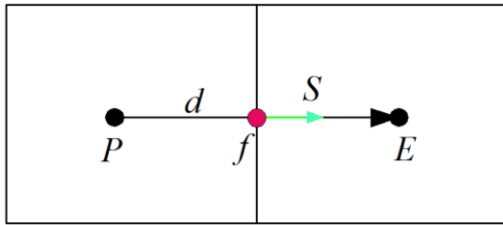
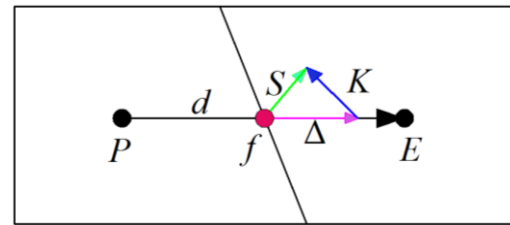


Figure 3.2: Variation of diffusion coefficient among neighboring CVs



(a) Vector d and S on an Orthogonal grid



(b) vector d and S on non-orthogonal grid

Figure 3.3: Vector notation for orthogonal and non-orthogonal grids

However, this method can be applied for orthogonal grid only. For non-orthogonal grid like as Fig.3.3(b) special treatment is required. Various treatments can be found in the literature (Jasak 1996 and Blazek 2003). Basically, the gradient term is decomposed into two parts,

$$\mathbf{S} \cdot (\nabla \phi)_f = \underbrace{\Delta_o \cdot (\nabla \phi)_f}_{\text{Orthogonal Contribution}} + \underbrace{\mathbf{K} \cdot (\nabla \phi)_f}_{\text{Non-orthogonal Contribution}} \quad (3.34)$$

The orthogonal contribution $\Delta_o \cdot (\nabla \phi)_f$ can be modeled in a number of ways (Jasak 1996); one of the robust ways is over-relaxed approach. In this approach the orthogonal contribution $\Delta_o \cdot (\nabla \phi)_f$ is modeled such that the contribution from ϕ_P and ϕ_E increases with the increase of non-orthogonality and can be expressed like below,

$$\Delta_o = \frac{d}{d \cdot \mathbf{S}} |\mathbf{S}|^2 \quad (3.35)$$

For the non-orthogonal contribution, the face interpolated value of $\nabla \phi$ can be obtained by linear interpolation as like Eq.3.31. In this study the diffusive terms were discretized by second-order accurate Central Differencing schemes with non-orthogonal correction and implemented by selecting *Gauss linear corrected* scheme in *fvSchemes* dictionary of OpenFOAM. The detailed programming algorithm regarding this scheme can be found in *gaussLaplacianScheme.C*, *correctedSnGrad.C* and *surfaceInterpolation.C* files.

3.4.2.3 Spatial Discretization of Source Term

In the governing equation not all the terms can be expressed in the form of convection, diffusion and temporal terms. The terms can't be expressed on those terms are expressed as source term, $S_\phi(\phi)$, which is a general function of ϕ . But it is important to linearize the source term before the actual discretization and can be conducted as follows,

$$S_\phi(\phi) = S_C + S_P\phi, \quad (3.36)$$

here S_C is the constant part of the source term and S_P is the depended part depends on ϕ . Now, assuming similar approximation as for the surface integrals, i.e., ϕ varies linearly over the control volumes, the source term can be expressed as follows:

$$\int_{V_P} S_\phi(\phi) dV = S_C V_P + S_P V_P \phi_P. \quad (3.37)$$

This approximation is exact either ϕ is constant or varies linearly over the cell, otherwise, it is a second-order accurate (Jassak 1996 and Ferziger and Perić 2002).

3.4.2.4 Temporal Discretization

Before starting the temporal discretization of the governing equation, we need to rewrite Eq.3.23 considering the time derivatives. The Eq.3.23 can be rewritten as follow,

$$\int_t^{t+\Delta t} \left[\frac{\partial}{\partial t} \int_{V_P} \rho \phi dV + \int_{V_P} \nabla \cdot (\rho \mathbf{U} \phi) dV - \int_{V_P} \nabla \cdot (\rho \Gamma_\phi \nabla \phi) dV \right] dt = \int_t^{t+\Delta t} \left(\int_{V_P} S_\phi(\phi) dV \right) dt. \quad (3.38)$$

Now, taking into consideration the assumption we made in the last sections and the output in Eq.3.25, Eq.3.30 and Eq.3.37, the Eq.3.38 can be expressed as like below,

$$\int_t^{t+\Delta t} \left[\left(\frac{\partial \rho \phi}{\partial t} \right)_P V_P + \sum_f S_f \cdot (\rho \mathbf{U} \phi)_f - \sum_f S_f \cdot (\rho \Gamma_\phi \nabla \phi)_f \right] dt = \int_t^{t+\Delta t} (S_C V_P + S_P V_P \phi_P) dt. \quad (3.39)$$

This expression is known as the semi-discretized form of the transport equation (Hirsch 1991). This equation is discrete in space but continuous in time. In the preset study we discretized the unsteady term with a second-order accurate implicit method, namely, Backward Differencing (BD) method to discretize the complete transport equation with second-order accuracy. The method was implemented by choosing *backward* for *ddtSchemes* in *fvSchemes* dictionary of OpenFOAM. The method is described below. As the method is implicit, hence it uses both the obtained and the desired

value of the variable ϕ . This method utilize total three time levels to calculate the temporal derivative as mentioned below,

$$\begin{aligned}\phi^{n-2} &= \phi^{t-\Delta t} \\ \phi^{n-1} &= \phi^t \\ \phi^n &= \phi^{t+\Delta t}.\end{aligned}\tag{3.40}$$

Now the time level n-2 and n-1 can be expanded by using Taylor expansion around n and we get

$$\phi^{n-2} = \phi^n - 2\left(\frac{\partial\phi}{\partial t}\right)^n \Delta t + 2\left(\frac{\partial^2\phi}{\partial t^2}\right)^n \Delta t^2 + O(\Delta t^3),\tag{3.41}$$

and

$$\phi^{n-1} = \phi^n - \left(\frac{\partial\phi}{\partial t}\right)^n \Delta t + \frac{1}{2}\left(\frac{\partial^2\phi}{\partial t^2}\right)^n \Delta t^2 + O(\Delta t^3).\tag{3.42}$$

Adding these two equations and we can obtain the second-order approximation for the temporal derivative after some simple manipulations as follows,

$$\left(\frac{\partial\phi}{\partial t}\right)^n = \frac{\frac{3}{2}\phi^n - 2\phi^{n-1} + \frac{1}{2}\phi^{n-2}}{\Delta t}.\tag{3.43}$$

It is to be noted that the volume integral of the unsteady term in Eq.3.39 can be written to $\left(\frac{\partial\phi}{\partial t}\right)^n$ based on the assumption we made before that the variable varies linearly around the point P in space and time. This implicit time scheme can tolerate larger time step than the explicit time scheme, where Courant number ($C_o = (U \cdot \Delta t) / \Delta x$) must be less than 1. In the present study the time step (Δt) was determined based on the Courant number value (C_o). In most of the cases the Courant number was near about 0.5, yet in some cases it reached a value of around 0.7. The detailed programming algorithm of the Backward Differencing (BD) method can be found in *backwardDdtScheme.C* file in OpenFOAM.

Finally, neglecting the temporal variation in the face fluxes and derivatives we can write the complete discretized transport equation having second-order accuracy as similar to Eq.3.44.

$$\frac{\frac{3}{2}\rho\phi^n - 2\rho\phi^{n-1} + \frac{1}{2}\rho\phi^{n-2}}{\Delta t}V_p + \sum_f S \cdot (\rho U)_f (\phi)_f^n - \sum_f (\rho \Gamma_\phi)_f S \cdot (\nabla \phi)_f^n = S_c V_p + S_p V_p \phi_p^n. \quad (3.44)$$

It is worthy to mention that this time derivative expression is valid only for constant time step (Δt) and in this research all the simulations were carried out with constant time step (Δt) strategy.

3.5 Boundary Conditions

Boundary conditions are required to be defined for the boundaries of the computational domains and they appear as source terms. Various type of boundary conditions are implemented in bluff body aerodynamics field those are well summarized in Haque *et al.* (2013). The following boundary conditions are used in the present work:

Zero-gradient Boundary Condition: This boundary condition can be implemented in OpenFOAM by typing *zeroGradient* in the input files. The solution gradient is set to zero at the boundary. This is a Neumann-type boundary condition, i.e. $\partial\phi/\partial n=0$.

Fixed-value Boundary Condition: This boundary condition can be implemented by writing *fixedValue* in the input files of OpenFOAM. A specific value of the solution is set at the boundary. An initial value is required when this kind of boundary conditions are enforced. This is a Dirichlet-type boundary condition, i.e., $\phi=b$.

Slip Boundary Condition: This boundary condition can be carried out simply by typing *Slip* in the input files. The flow is assumed to pass along the boundary and can't pass through it, i.e., $u=U$, $v=0$ and $\partial u/\partial y=0$.

A non-slip type boundary condition, i.e., fixed-value ($u=0$ and $v=0$) for velocity and zero-gradient for pressure were imposed on the bluff body or bridge deck surface (bridge deck). A fixed-value boundary condition for velocity ($u=U$ and $v=0$) and zero-gradient boundary condition for pressure were implemented at the inlet of the domain, while zero-gradient for velocity and fixed-value for pressure ($P=0$) were applied at the outlet of the domain. A slip boundary condition was imposed at the top and bottom of the domain wall.

3.6 Procedure of Solution

In this section we discuss the solution strategy adopted for the solution of the discretized governing equation. The general form of the governing equation that was discretized in the last section requires additional processing to obtain discretized Navier-Stokes equation for solution. There are a number of issues need to be considered.

If we substitute U as a transport property in the discretized convective term in the Eq.3.25, we obtain,

$$\begin{aligned}
 \oint_{\partial V_P} dS \cdot (\rho U U) &= \sum_f \int_f dS \cdot (\rho U U) = \sum_f S_f \cdot (\rho U U)_f = \sum_f S_f \cdot (\rho U)_f (U)_f, \\
 &= \sum_f F(U)_f, \\
 &= a_P U_P + \sum_N a_N U_N.
 \end{aligned} \tag{3.45}$$

Here, F , a_P and a_N are function of U . By observing this equation, we can understand that the velocity is being transported by itself. Therefore, the discretized convective term would be a quadratic function of velocity and as a result the system of algebraic equation would be non-linear in nature. Further, as the mass flux F is required to satisfy the continuity equation (Eq.3.5), hence the continuity and momentum equation will simultaneously increase the non-linearity even more.

This issue can be coped with either by using a non-linear solver or linearizing the convective term. However, implementation of non-linear solver is complicated and computationally quite expensive; therefore the convective term is linearized. The linearization means that mass fluxes will be calculated from an existing velocity field satisfying the continuity equation. As the fluxes are calculated from the existing velocity field that means information is lagged. To grasp the non-linearity and to reduce the error, small time steps should be used, so that variation between the consecutive solutions remains small and becomes possible to lag the non-linearity (Jassak 1996).

Another aspect is that pressure and velocity is coupled in the Navier-Stokes equations. We need some iterative procedures to solve this coupled system. In this work, we employed PISO algorithm (Issa 1986) for static simulation named as a PISOFOAM in OpenFOAM and PIMPLE algorithm for dynamic simulation named as a PimpleDyMFOAM in OpenFOAM. Further, as a part of the iterative procedure, we need one additional pressure equation. Since, due to pressure velocity coupling the momentum equation demands an existing pressure field. If the pressure from the initial guess or the pressure solution of previous time step is used, then the velocity solution of the momentum equation doesn't satisfy the continuity equation demanding addition pressure equation. Furthermore, we need to adopt a solution strategy for solving the matrix of linear algebraic equation obtained by discretization.

In the following sections these aspects are discussed briefly, elaborate derivation and background can be found in Patankar (1980), Jassak (1996) and Versteeg and Malalasekera (2007). First, the discretized pressure and Navier-Stokes equations are presented. Then, the solution strategy adopted for solving the matrix of linear algebraic equations is discussed. Finally, the solution steps of the iterative method, namely, PISO algorithm for solving the coupled Navier-Stokes equation system is presented.

3.6.1 Discretized Pressure and Navier-Stokes Equation

The momentum equation can be written in the semi-discretized form in order to derive the pressure equation,

$$a_p U_p = H(U) - \nabla P, \quad (3.46)$$

and

$$H(U) = -\sum_N a_N U_N + \frac{U^O}{\Delta t} \quad (3.47)$$

where a_p and a_N are the diagonal and off-diagonal coefficients respectively. ΔP is the pressure gradient and $H(U)$ consists of transport part, source part of the transient term and the source terms excluding the pressure gradient. Hence, this is a function of present velocity (U) and the velocity of the previous time level U^O (for backward differencing both of U^O and U^{OO}).

Now, Eq.3.46 can be solved to obtain the cell center (P, E, W) velocity by dividing with a_p , i.e.,

$$U_p = \frac{H(U)}{a_p} - \frac{1}{a_p} \nabla P. \quad (3.48)$$

The velocity at the cell face can be found from the cell centers through interpolation as below,

$$U_f = \left(\frac{H(U)}{a_p} \right)_f - \left(\frac{1}{a_p} \right)_f (\nabla P)_f. \quad (3.49)$$

During solution time, this equation will also be utilized to calculate the face fluxes. The discretized continuity equation can be written as follows,

$$\nabla \cdot U = \sum_f S \cdot U_f = 0. \quad (3.50)$$

Now, if we substitute Eq.3.49 into Eq.3.50 and after simple manipulation we can find the discretized pressure equation,

$$\nabla \cdot \left(\frac{1}{a_p} \nabla P \right) = \sum_f S \cdot \left[\left(\frac{1}{a_p} \right)_f (\nabla P)_f \right] = \sum_f S \cdot \left(\frac{H(U)}{a_p} \right)_f. \quad (3.51)$$

Finally, discretized Navier-Stokes equation system can be written as follows,

momentum equation,

$$a_p U_p = H(U) - \nabla P, \quad (3.52)$$

pressure equation,

$$\sum_f S \cdot \left[\left(\frac{1}{a_p} \right)_f (\nabla P)_f \right] = \sum_f S \cdot \left(\frac{H(U)}{a_p} \right)_f, \quad (3.53)$$

and the face fluxes F , we mentioned in the previous section were calculated from Eq.3.54,

$$F = S \cdot U_f = S \cdot \left[\left(\frac{H(U)}{a_p} \right)_f - \left(\frac{1}{a_p} \right)_f (\nabla P)_f \right]. \quad (3.54)$$

3.6.2 Solution of the Algebraic Equation

In the last section discretized pressure and Navier-Stokes equation was derived. As can be seen the pressure and momentum equations are coupled. We will introduce a segregated method to decouple the equation and to obtain a converged solution of the system of equations. However, before that we need a matrix solver that will solve each of those discretized algebraic equation over the complete flow domain. In the present study we adopted iterative methods rather than direct methods, i.e., Gauss elimination, LU decomposition etc. as they are efficient to solve the matrices of equations. The pressure equation was solved by employing Geometric-algebraic multi-grid (*GAMG*) solver with Gauss-Seidel smoother and all other equations of transport properties such as, U , k or ω were solved by means of Preconditioned bi-conjugate gradient (*PBiCG*) solver. In the following section we introduce the basics of both of these methods. For detailed of the methods reader are referred to Hackbusch and Trottenberg (1982) Wesseling (1992), and Briggs *et al.* (2000) for *GAMG* method and Fletcher (1976), Shewchuk (1994) and Press *et al.* (2007) for *PBiCG* method.

Multi-grid method like, *GAMG* is an efficient technique to solve linear or non-linear systems of discretized equation. The method is consists of a basic iterative scheme called smoother (Gauss-

Seidel) and a coarse grid corrector. The smoother (Gauss-Seidel) on its first few iterations can remove the high frequency error, yet the low frequency errors are more persistent and convergence requires $O(N^2)$ iteration in a fine grid (So called multi-grid level), that is unbearable. Hence, the solutions are mapped into coarse grid, as a result low-frequency error of fine grid becomes high-frequency-error in a coarse grid and can be removed easily.

In this way only a few iterations are required before changing from fine to coarse and coarse to fine and with a fixed number of iterations the method can diminish the residual very fast increasing the accuracy of the solution. A general schematic view of the method is drawn in Fig.3.4. The method was implemented by typing *GAMG* in *fvSolution* dictionary of OpenFOAM. The detailed programming algorithm can be found in *GAMGSolver.C*, *GAMGSolverAgglomerateMatrix.C*, *GAMGSolverInterpolate.C* and *GAMGSolverSolve.C* files in OpenFOAM. .

Preconditioned bi-conjugate gradient (*PBiCG*) is a popular iterative method for solving a system of linear algebraic equations forms asymmetric matrix. Basically, the method searches the solution of a system of equations through an iterative process and reaches the final solution by the conjugate directions. These conjugate directions (search directions) are the conjugate of the residuals that is preconditioned with a proper preconditioner. By preconditioning, the original system of equations is transformed into a new system (preconditioned system) to increase the convergence and the new system (preconditioned system) is much easier to solve than the original system of equations. The method reaches the solution utmost at n iterations if the system contains n linear equations with n unknowns.

If we consider a system of linear equations as $A\phi=b$ and starts with an initial guess of solution x_o having an initial residual r_o , then the initial search direction is p_o that is determined based on the initial residual with a proper preconditioner. At each iteration, residual is calculated and at k -th iteration, the residual r^k ($r^k=b-A\phi^k$) is orthogonal to the Krylov subspace generated by b . The solution at k -th iteration, ϕ^k , is the product of the last iteration plus a constant multiplication of the last search direction and continues until the residual reaches the set criteria. The detailed procedure and the expressions can be found in Fletcher (1976), Shewchuk (1994) and Press *et al.* (2007). We employed the *PBiCG* method as a solver by typing *PBiCG* in *fvSchemes* dictionary of OpenFOAM. The programming algorithm of *PBiCG* can be found in *PBiCG.C* file within OpenFOAM.

3.6.3 Pressure-Velocity Coupling

In last two sections we derived the discretized pressure equation, Navier-Stokes equation, described the matrix solver for solving the set of algebraic equation and before that we discretized the other transport equations. Now, it is possible to solve this coupled system of equations by an appropriate solution technique. In the present study we adopted PISO algorithm for static simulation and Pimple algorithm for dynamic simulation. PISO algorithm is a segregated approach, where equations are solved in a sequence and was proposed by Issa (1986). Detailed can be found in Issa (1986) and Versteeg and Malalasekera (2007). The main procedure of the transient PISO solver adopted in OpenFOAM for incompressible turbulent flow is briefly presented below:

- 1) Initialize the flow field for all variables and setup the boundary conditions.

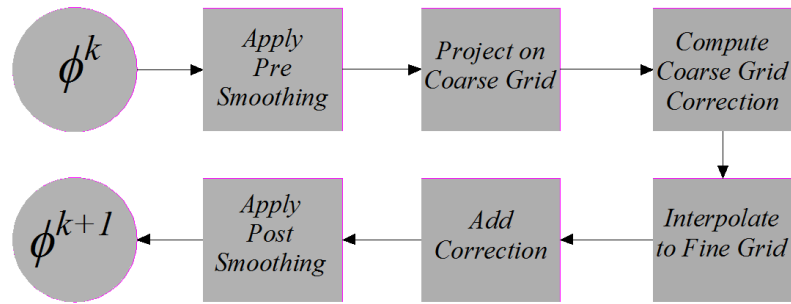


Figure 3.4: General procedure of GAMG method

- 2) Start the calculation for a new time step.
- 3) Solve the discretized momentum equation (Eq.3.52) for approximation of the new velocity field by using pressure field data of previous time step or by initial value. This step is known as momentum predictor.
- 4) Calculate a new set of conservative face fluxes satisfying the continuity equation (Eq.3.54).
- 5) Solve the pressure correction equation (Eq.3.53) and repeat for the assigned number of non-orthogonal corrector steps (*nNonOrthogonalCorrectors*).
- 6) Correct the velocity field and repeat the PISO loop from step 4 until the prescribed number of PISO loop.
- 7) Use this pressure and velocity solution for the current time step and also consider the new set of fluxes.
- 8) Solve the other transport equations (k and ω) discretized similar to Eq.3.44 and update all the turbulent quantity and the eddy viscosity.
- 9) Update the time and start the calculation for a new time step from step 2 until the final time is reached.

In OpenFOAM, the number of times the PISO loop will be run is directly assigned by a parameter called *nCorrectors*. We set a *nCorrectors* number of 3. The PISO algorithm was activated by selecting PISO in *fvSolution* dictionary of OpenFOAM. Detailed programming algorithm of PISO algorithm can be found in *pisoFOAM.C* file.

For dynamic simulation to attain the pressure velocity coupling, we employed PIMPLE algorithm, which is a variant of PISO algorithm. In case of PIMPLE algorithm there is an additional outer loop (Step 3 to Step 8 of PISO steps) on PISO algorithm. In this loop the final value of the last iterations is considered as an initial guess and repeats the calculation from Step 3 to Step 8 of PISO algorithm. This outer loop is called *nOuterCorrectors*. By means of that much larger time steps can be implemented when PIMPLE algorithm is adopted to attain pressure-velocity coupling. We assigned a *nOuterCorrectors* number of 2 for PIMPLE algorithm.

3.7 Handling Moving Boundaries

In the presented study along with the static simulation, forced vibration dynamic simulation was also conducted to extract the dynamic properties such as aerodynamic derivatives and damping of the bridge deck. In forced vibration simulation the bridge deck was assigned to oscillate either in heaving or torsional mode at a constant frequency and amplitude. Hence, the boundary of the bridge deck was required to move during the time of simulation. Various methods are available to move the boundaries of a moving body (Tezduyar *et al.* 2008). We adopted Arbitrary Lagrangian-Eulerian (ALE) (Ferziger and Perić 2002 and Donea *et al.* 2004) method to accommodate the movement of the bridge deck boundary.

In previous sections we introduced the Eulerian approach, where the grid was fixed in space and the fluid flows through the grids. However, to simulate the movement of a particular boundary, Lagrangian formulation is required where the grid moves along with the fluid properties. ALE formulation combines both the Eulerian and Lagrangian method, the Lagrangian part allows the grid to move and deform according to the movement of the moving boundary, where the Eulerian part focuses on the fluid flow through the deformed grids. In the following section we briefly introduce the modified transport equation for the moving boundaries and the discretized form of the equations those were summarized from Tuković (2005), Tuković and Jasak (2007), Jasak and Tuković (2010) and Tuković and Jasak (2012) for details.

3.7.1 Arbitrary Lagrangian Eulerian Approach

Recall Fig.3.1(b) and Eq.3.23. For a general transport property ϕ , the conservation equation for a moving control volume V_P surrounded by a surface S_f can be rewritten as follows,

$$\frac{\partial}{\partial t} \int_{V_P} \rho \phi dV + \oint_S \rho n \cdot (U - U_s) \phi dS - \oint_S \rho \Gamma_\phi n \cdot \nabla \phi dS = \int_{V_P} S_\phi(\phi) dV \quad (3.55)$$

where n is the outward pointing unit normal vector on the boundary surface, U_s is the velocity of the moving boundary surface. A relationship is required between the rate of change of the volume V_P and the velocity of the boundary surface. It was defined by so-called Space Conservation law (SCL) or Geometric Conservation Law (GCL) (Thomas and Lombard 1979, Lesoinne and Farhat 1996 and Demirdžić and Perić 1988):

$$\frac{\partial}{\partial t} \int_{V_P} dV - \oint_S n \cdot U_s dS = 0. \quad (3.56)$$

This equation implies that the volume swept by the cell boundary at a time step is equal to the change in volume of each control volume. For stable simulation it is always required to be satisfied Eq.3.56, violation of Eq.3.56 may endanger the equation due to generation of artificial mass sources that accumulates with time.

Now, Eq.3.55 can be discretized by second-order Finite Volume Method (FVM) as already discussed earlier, where surface integrals are transform into the sums of the face integrals with proper approximation and volume integrals to second order accurate using the mid-point rule. By using second-order accurate Backward time scheme for temporal discretization, the Eq.3.55 in the discretized form for control volume V_P can be written as below (Tuković 2005 and Jasak and Tuković 2010),

$$\begin{aligned} \frac{3\rho_P^n \phi_P^n V_P^n - 4\rho_P^{n-1} \phi_P^{n-1} V_P^{n-1} + \rho_P^{n-2} \phi_P^{n-2} V_P^{n-2}}{2\Delta t} + \sum_f (\dot{m}_f^n - \rho_f^n \dot{V}_f^n) \phi_f^n \\ = \sum_f (\rho \Gamma_\phi)_f^n S_f^n n_f^n \cdot (\nabla \phi)_f^n + S_\phi^n V_P^n, \end{aligned} \quad (3.57)$$

where the subscript P denotes the cell values, f is the face centered values and the superscripts n , $n-1$ and $n-2$ are, respectively, the new, present (old) and past (older) values. The mass flux through the face is given by $\dot{m}_f = n_f \cdot U_f S_f$ and the cell face volume change by $\dot{V}_f = n_f \cdot U_{sf} S_f$, here U_{sf} is the cell face velocity. The mass flux can be found as a part of the solution (\dot{m}) by satisfying the conservation of mass. The cell volume (V_P^n , V_P^{n-1} and V_P^{n-2}) and the volumetric face flux (\dot{V}) can be determined from geometric consideration and by satisfying the Space Conservation Law (SCL) (Demirdžić and Perić 1988).

3.7.2 Grid Deformation Solver

In ALE grid moving approach, the computational grid moves and deforms to follow the movement of the moving boundary in every time steps of transient simulation. To ensure the quality and validity of the grid, it is important to move the internal points (fluid) along with the movement of the moving boundary points.

There are various methods available and adopted in OpenFOAM to calculate the motion of internal points. In previous versions of OpenFOAM both the Laplace equation with variable diffusivity (Lohner and Yang 1996) and Solid Body Rotation Stress equation (SBR Stress) (Dwight 2004) were implemented. However, both of these methods can maintain high quality of the grid for limited boundary rotation only. Currently, OpenFOAM has implemented Radial Basis Function (RBF) (Bos 2009) to calculate the internal motion of the points by maintaining high quality of the grid.

RBF interpolation method uses an interpolation function ($S(X)$) to calculate the displacement of the internal points for a given movement of the boundary points. Rather than using partial differential equation, a purely algebraic formulation was used to make the grid motion technique

faster and more robust. The interpolation function describes the displacements of all the computational grid points. The RBF interpolation formula can be mentioned as below,

$$S(X) = \sum_{j=1}^{N_b} \gamma_j \phi(\|X - X_{bj}\|) + q(X), \quad (3.58)$$

where X is the interpolate location, X_{bj} (x_{bj} , y_{bj} and z_{bj}) is the known displacements of the boundary points, N_b is the number of boundary points, q is a polynomial, ϕ is a given basis function as a function of the Euclidean distance $\|X\|$, γ_j is a coefficient that is used to define the polynomial q . Based on small number of control points on the moving boundary, the RBF interpolation is derived. This control points are used as “known point data”. Then by exploiting the RBF interpolation in Eq.3.58, the displacements of all the other grid points are calculated. Further details of the RBF interpolation and the choice of radial basis function can be found in Bos (2009). The algorithm can be found in `sixDoFRigidBodyMotionSolver.C` within OpenFOAM.

3.7.3 Assigning Boundary Movement

In last two sections, the concept of moving grid was introduced, where if the displacement of the control points on the moving boundary is known then the computational domain can absorb that displacement by moving the grid points and changing the volume of the grid. Now, we need to give the desired displacement on the target moving boundary.

In this study, we aimed to conduct single degree-of-freedom forced vibration. We used an advanced solver that is capable of mesh morphing for six degree-of-freedom motion, when three dimensional simulation is conducted. The algorithm can simulate free vibration of target body if the geometry, mass, center of mass, moments of inertia, stiffness and damping properties are properly tuned. The algorithm demands one additional file in the *Constant* folder, namely, *dynamicMeshDict* file where the desired properties can be input. The algorithm imagines that the model is supported by springs. Usually, two types of springs are used, namely, linear spring and linear angular spring those controls the translational and angular movement of the body.

In this research, we considered two dimensional flow domain having a infinitesimally small dimension in the span-wise direction and intention was to conduct one degree-of-freedom forced vibration simulation. Hence, by assigning appropriate value in the *Constrain* option in the *dynamicMeshDict* file, we released only vertical heaving and torsional movement (recall Fig.2.4). During the time of simulation, the spring-supported model was allowed for two degrees-of-freedom vibration. If we denote the stiffness of the vertical linear spring as k_η and angular spring as k_α , the equation of motion (recall Eq.2.6 and 2.7) for per unit span length can be rewritten as:

$$m \cdot \ddot{\eta} + 2 \cdot m \cdot \zeta_\eta \cdot \omega_\eta \cdot \dot{\eta} + k_\eta \cdot \eta = L_\eta(t), \quad (3.59)$$

$$I \cdot \ddot{\alpha} + 2 \cdot I \cdot \zeta_\alpha \cdot \omega_\alpha \cdot \dot{\alpha} + k_\alpha \cdot \alpha = M_\alpha(t). \quad (3.60)$$

As the simulation progress, the $L_\eta(t)$ and $M_\alpha(t)$ are calculated by integrating the pressure over the bridge deck or bluff body surface. As the simulation time elapsed, $L_\eta(t)$ and $M_\alpha(t)$ accumulates and tries to excite the body. However, the goal of the current study was to simulate the single degree-of-freedom forced vibration. To generate forced heaving and torsional mode vibration, target frequency (f_η and f_α) can be simulated by inputting appropriate stiffness value (k_η and k_α), the desired amplitude of vibration can be obtained by assigning initial displacement (modeled by adjusting *restLength* and *angularMomentum*) and the given amplitude can be maintained by making the damping zero in the corresponding direction in *dynamicMeshDict* file. To ignore the influence of $L_\eta(t)$ and $M_\alpha(t)$ on vibration frequency and amplitude, a very large mass can be assigned to the modeled bridge deck section.

For example, when heaving mode single degree-of-freedom forced vibration was simulated, a quite large mass equivalent to the real bridge section was assigned to this scaled two dimensional model to ignore the influence of aeroelastic force, the *linearSpring* stiffness and *restLength* were tuned to simulate desired vibration frequency and amplitude, respectively and the vertical direction damping was set to zero. At the same time, the very large stiffness and damping values were set in the torsional direction. By following the same procedure the torsional mode single degree-of-freedom forced vibration can also be generated. In, OpenFOAM the linear and angular spring was implemented in *linearSpring.C* and *linearAxialAngularSpring.C* files, respectively.

The dynamic simulation was activated by choosing *PimpleDyMFOAM* algorithm and typing *pimpleDyMFoam* in *fvSolution* dictionary of OpenFOAM. The main difference between the PISO and PIMPLE algorithm were discussed at the end of section 3.6.3 and demands one additional dictionary file, namely, *dynamicMeshDict* as discussed in the last section. Fig.3.5 shows a brief flowchart of *PimpleDyMFoam* algorithm.

3.8 Computational Domain

The above mentioned all the computations should be carried out within a finite computational domain. Special attention should be paid for selecting the size of the computational domain. From practical point of view, the domain should be as large as possible so that boundary of the domain doesn't affect the response around the target object. In past work this issue was investigated vigorously to reduce the uncertainty in the solution due to domain size. Detailed and clear guidelines can be found in the literature to set up the domain size. In a two-dimensional domain, there are three important parameters: i) the upstream distance (distance between the inlet and object, X_u), ii) the downstream distance (distance between the object and the outlet, X_d) and iii) the height of the domain (H).

An upstream distance (X_u) of 10 times of the height of the object (D) was recommended by Kelkar and Patankar (1992) in order to get an independent result. Later, Sohankar *et al.*, (1995)

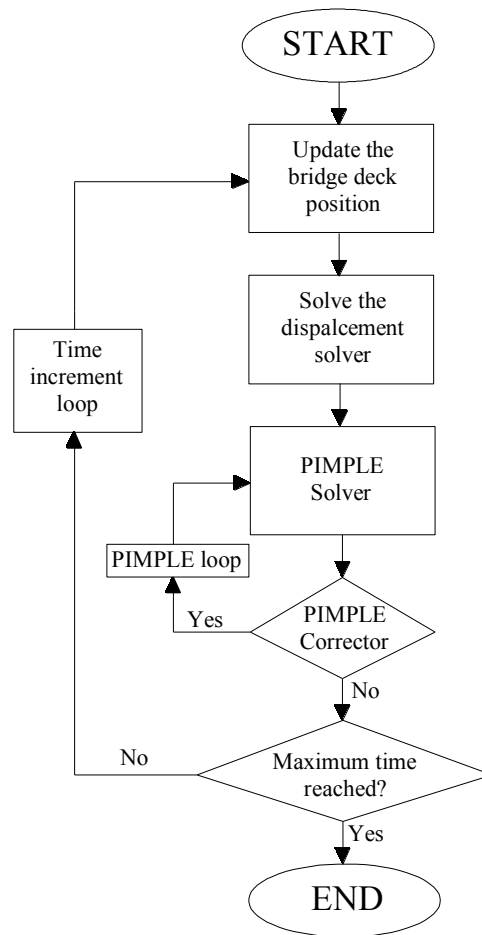


Figure 3.5: Solution steps of dynamic simulation in OpenFOAM

found noticeable but not significant effect of the inlet distance on RMS lift force when it was varied from $7.5D$ to $11D$. Similar recommendation can also be found in building aerodynamics field, where an upstream distance of $10D$ was recommended (Franke *et al.*, 2004 and Tominaga *et al.*, 2008). In this study we placed the inlet at $15D$ upstream of the bluff body by following the recommendation made by past research works.

The downstream distance also plays a vital role and influences the simulation result. A downstream distance (X_d) of $15D$ was recommended by Behr *et al.*, (1995) based on simulation on a circular cylinder. Similarly, Cowan *et al.*, (1997), Scaperdas and Gilham (2004) and Bartiz *et al.*, (2004) suggested a downstream distance of $15D$. However, downstream distance (X_d) is influenced by the type of the outlet boundary condition. It was shown by Sohankar *et al.*, (1998) that a downstream distance of $15D$ is required for convective boundary condition (CBC), whilst a downstream distance of $25D$ is required for Neumann Boundary Condition (NBC). In the present study we placed the outlet at $25D$ downstream of the object as Neumann-type boundary condition was incurred at the outlet of the domain.

The height of the domain should be selected based on the blockage ratio (D/H) and tried to be maintained it as low as possible. In building aerodynamics field the height of the domain was advised to maintain $6D$ or higher. Sohankar *et al.*, (1998) investigated the influence of blockage ratio

on a square cylinder by changing from 5% to 2.5% and found a slight decrease (less than 1.5%) in mean drag, rms lift and strouhal number. It should be mentioned that based on the guidance of wind tunnel modeling the maximum blockage was suggested to be below 10% (Franke *et al.*, 2007). We selected the domain height of $25D$ to lessen the influence of blockage ratio. Fig.3.6 shows the detailed size of the computational domain and incurred boundary conditions. It is important to mention that during the time of simulating bridge deck, an upstream distance (X_u) of $18D$ was maintained as shown in Fig.3.7.

3.9 Grid System

The open-source toolbox OpenFOAM has already been verified extensively in various past researches (Jasak 1996, Juretic 2004, Tuković 2005, Jasak *et al.* 2004, Tuković and Jasak 2007, Bos *et al.* 2009 and Jasak and Tuković 2010). What is left for uses is the accurate generation of grid system for the spatial discretization of the flow, as it is completely problem oriented. An accurate

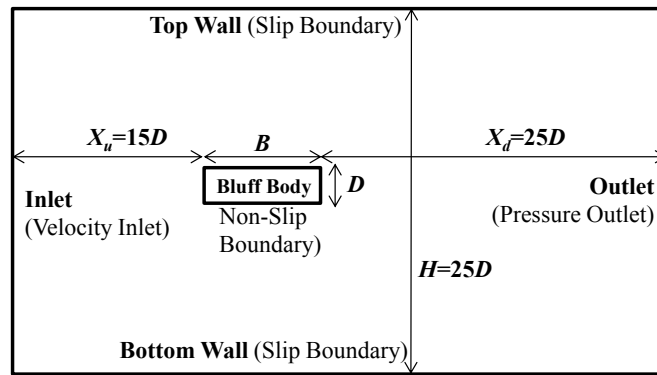


Figure 3.6: Important notations, domain size and the boundary conditions adopted in the present study for bluff body simulation

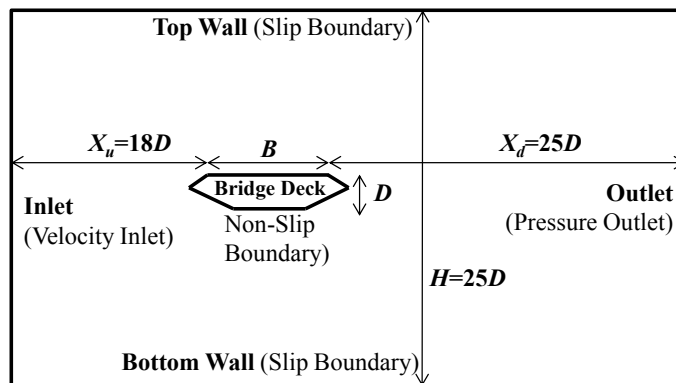


Figure 3.7: Domain size employed for simulating flow around bridge deck

generation of grid system is also very important as it is one of the major sources of error in numerical analysis.

In CFD, a grid system needs to fulfill two important criterions to be an accurate and optimum grid system. Firstly, the first grid or cell height (y) away from the body should be at the viscous sublayer (for non-slip boundary condition) for an accurate modeling of the boundary layer flow, is known as near-wall treatment (Menter *et al.*, 2002 and Franke *et al.*, 2007). In bridge and bluff body aerodynamics fields also grids are generated by following this criterion (Bruno *et al.*, 2010 and 2012; Šarkić *et al.*, 2012, Brusiani *et al.* 2013 and Nieto *et al.* 2015). In viscous sublayer, the viscous stress dominants over the Reynolds stress and situate where the non-dimensional wall distance (y^+) is less than a value of 5 (Pope 2000) as shown in Fig.3.8. The y^+ value can be defined as,

$$y^+ = \frac{u^* y}{\nu}, \quad (3.61)$$

where u^* is the friction velocity, y is the first grid height and ν is the kinematic viscosity.

Secondly, there should be sufficient number of grids all through the domain to discretize the flow such that the solutions converges and reaches the asymptotic range of convergence. To find the first grid height (y) that will be within the viscous sublayer ($y^+ < 5$) and to find the number of grids all through the domain to have a converged solution, requires number of trials. Basically, the grid convergence test is carried out to generate accurate and optimum grid system where grids with various sizes and numbers are tested to find the best one.

Nevertheless, the conventional grid convergence test is a lengthy and time consuming procedure that requires huge computational efforts. Jinyuan *et al.*, (2006) also mentioned that in a

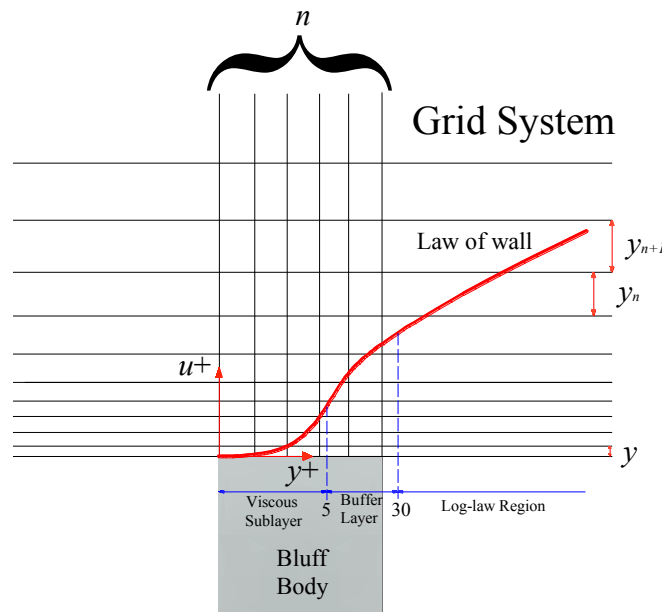


Figure 3.8: Concept of near-wall treatment and various important notations in grid system

CFD project majority of the time is dedicated for the generation of a successful grid system. Specially, for the beginner or user having less experience it takes prolonged time to obtain an accurate and converged grid system. Therefore, CFD needs to pass through the bottleneck like generation of accurate and optimum grid system for spatial discretization of the flow without much effort.

Considering aforesaid issues, in this work a strategy was proposed to generate an efficient and optimum grid system for yielding accurate result without much effort for two-dimensional bluff bodies. First, in the following section the strategy is proposed to generate the efficient grid system easily and promptly. Then, the strategy is demonstrated and checked by generating grid system for a square cylinder of side ratio ($R=B/D$) of 1. Solutions were also compared with past experimental works to check the accuracy of the results obtained from the grid system generated based on the proposed strategy. After that, the strength and efficiency of the proposed strategy is reconfirmed by generating grid for an elongated rectangular cylinder of side ratio (R) of 5 by comparing the solution with past experimental work.

3.9.1 Proposed Strategy to Generate Grid System

To generate an efficient and optimum grid system for two-dimensional bluff bodies, one needs to assure appropriate near-wall treatment ($y^+ < 5$) and sufficient number of grids all through the domain to resolve the flow. To fulfill these criteria, we selected widely used and numerically efficient structured non-uniform grid system (Casey & Wintergerste, 2000; Menter *et al.*, 2002; Ferziger & Perić, 2002). This type of grid can be generated by selecting a first grid height (y) near the object and a growth factor ($GF=y_{n+1}/y_n$) that is used to increase the grid size gradually in all direction away from the object as shown in Fig.3.8.

Our proposed strategy was, the first grid height (y) can be determined based on near-wall treatment such that it lies in the viscous sublayer ($y^+ < 5$) and the growth factor (GF) can be selected such that the solution reaches the asymptotic range of convergence. One needs to know these two parameters to generate an accurate and converged grid system: i) the first grid height (y) and ii) the growth factor (GF).

Now, to make this strategy applicable, quick and smart, we needed further consideration that how to determine the first grid height (y) that would yield a desired y^+ value (< 5) without much trials and how to determine the value of growth factor (GF) that will yield a converged solution. In the following section we discuss these issues one by one in details.

First, we derived an equation to initialize the first grid height (y) in terms of dimension of the object (B), fluid properties (U , ρ and ν) and y^+ value to reduce the number of trials. Then, we tried to find the appropriate value of growth factor (GF) that will yield a converged solution when the first grid (y) lies in the viscous sublayer. All the simulations were conducted for a bluff body of square cylinder ($R=1$).

3.9.1.1 Equation for Initialization of First Grid Height (y)

As we already know, to fulfill the near-wall treatment the first grid height (y) should be in the viscous sublayer and we can confirm this if the grid possess a y^+ value smaller than 5. But to get this target wall y^+ value we need trials on grid by changing the first grid height (y) away from the body to get the target y^+ value. An equation can be derived very easily for initializing the first grid height (y) to make easier and faster the procedure of finding the desired first grid height (y). Through this equation the first cell height (y) can be related with the characteristics length of the body or object in the flow direction (B), Reynolds number ($R_{eB}=UB/\nu$) and y^+ value of the grid. The equation can be derived as follows,

$$y = \frac{y^+ \mu}{\rho u^*}, \quad (3.62)$$

where, y is the first cell height, μ is the dynamics viscosity of fluid, u^* is the friction velocity, and can be given by,

$$u^* = \sqrt{\frac{\tau_w}{\rho}}, \quad (3.63)$$

where, τ_w is the wall shear stress and can be expressed as,

$$\tau_w = C_f \cdot \frac{1}{2} \cdot \rho \cdot U^2, \quad (3.64)$$

where, U is the free stream velocity and C_f is the coefficient of skin-friction.

Now, we require a general expression of C_f that will work well for most of the time. Various expressions of C_f are available depending on the circumstances. We thought the expression of skin friction coefficients (C_f) for a flat plate under turbulent boundary layer would be the most suitable and versatile. In the literature, various equations of skin friction coefficients (C_f) for a flat plate can be found. We considered three established equation of skin friction for a flat plate under the turbulent flow to make comparison among them and choose the most appropriate one. The expressions were as follows,

$$C_f = 0.0592 \cdot R_{eB}^{-1/5}, \quad (3.65)$$

$$C_f = 0.074 \cdot R_{eB}^{-1/5}, \quad (3.66)$$

$$C_f = 0.0307 \cdot R_{eB}^{-1/7}, \quad (3.67)$$

where, R_{eB} is the Reynolds number. Eq.3.65, 3.66 and 3.67 were given by Schlichting (Schlichting 1979), Prandtl (Prandtl 1927) and Falkner (as cited in Loitsyanskiy 1995). Now, putting the expression of friction velocity (u^*), wall shear stress (τ_w) and skin friction coefficients (C_f) in Eq.3.62 and after some simple manipulations the following three equations can be found,

$$y = 5.81 \cdot y^+ \cdot B \cdot R_{eB}^{-0.9}, \quad (3.68)$$

$$y = 5.19 \cdot y^+ \cdot B \cdot R_{eB}^{-0.9}, \quad (3.69)$$

$$y = 8.07 \cdot y^+ \cdot B \cdot R_{eB}^{-0.929}. \quad (3.70)$$

Finally, an equation for initializing the first grid height (y) is derived, relating the characteristic length (B), y^+ value and Reynolds number (R_{eB}). Using any of these equations, one can easily predict the required first grid height (y), as all the right hand side quantities are known. Similar type of equation can also be found in various online based CFD discussion forums such as the CFD-Online (2015). However, in the present study different expressions of skin friction coefficient (C_f) were used resulting new equations and their performance of predicting the first grid height (y) in bridge and bluff body aerodynamic field was also explored which was not done previously. In the following section the relative performance of the derived equations were checked that how accurately they can predict the first grid height (y) and to choose the most appropriate one.

3.9.1.2 Performance of the Obtained Equations

If the obtained equations work for bluff section, then the equations should also work for elongated or streamlined section, as the expression of flat plate skin friction (C_f) was utilized to derive them. Hence, to check the performance of the equations, we considered the square cylinder ($R=1$) and generated three grids having different y^+ values for the square cylinder ($R=1$) by changing the first grid height (y) at a Reynolds number (R_{eB}) of 1.22×10^4 . An arbitrary but small growth factor (GF) of 1.05 was selected for all these grids to increase the grid size gradually away from the body. The grid number ($n_1=B/2y$; $n_2=D/2y$) along the perimeter of the body was determined by dividing the corresponding length of the body by twice the size of the first cell height ($2y$), this implies all the first grid elements near the cylinder were rectangular in shape. Fig.3.9 shows the considered grid system for the square cylinder ($R=1$).

Table 3.1 shows the first grid height (y) and the obtained y^+ values for the three considered grid systems. The average y^+ value of grid 1 lay well within the viscous sublayer, for grid 2 also it lay within the viscous sublayer and for grid 3 the value lay just outside the range. Then, this obtained y^+ value was used as an input to the obtained equation to calculate the first grid height (y) and compared with the required first grid height (y) to check the performance of the obtained equation. Nevertheless, we decided to utilize the maximum y^+ value as an input to the equation instead of average y^+ value to obtain a conservative result.

Table 3.2 shows the required first grid height (y) and the first grid height (y) calculated by using the obtained three equations. As can be seen for the third grid system (G3), when the first grid (y) is laid just outside the viscous sublayer ($y^+ < 5$), then all the three equations provided conservative results. On the other hand, when the first grid (y) is laid in the viscous sublayer, they underestimated

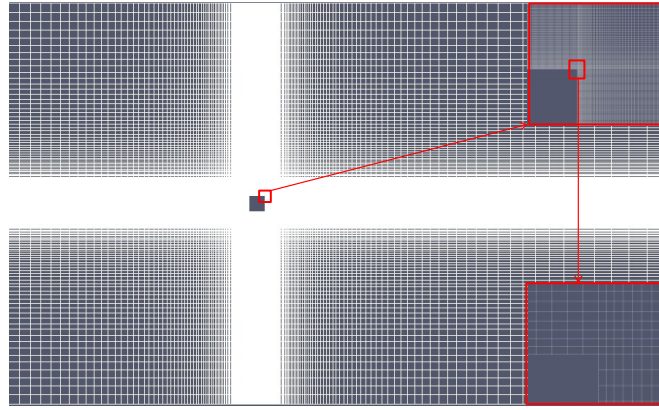


Figure 3.9: Considered non-uniform grid arrangement to discretize the flow around square cylinder

Table 3.1: Properties of the considered grids having various y^+ values for square cylinder (R) of 1 at $Re_B=1.22 \times 10^4$

Grid Name	Required First grid Height (y/d)	Obtained y^+ value		
		Minimum	Average	Maximum
G1	0.004	0.412	1.876	5.139
G2	0.0065	0.831	2.926	6.692
G3	0.015	1.831	5.700	10.64

Table 3.2: Comparison in between the required first grid height (y/d) and calculated first grid height (y/d) from the obtained equations

Required (y/D)	Input Parameters of the Equations			Calculated (y/D) from the Equation		
	Target max. y^+	Reynolds number, Re_B	Charac. Length (B/D)	$y/D = 5.81y^+(B/D)Re_B^{-0.9}$	$y/D = 5.19y^+(B/D)Re_B^{-0.9}$	$y/D = 8.07y^+(B/D)Re_B^{-0.929}$
0.004	5.139	1.22×10^4	1	0.0063	0.0056	0.0066
0.0065	6.692			0.0082	0.00729	0.00863
0.015	10.64			0.0129	0.01160	0.01373

a bit the first grid height (y). The variation is usual, as the considered shape is too bluff in shape. However, the second equation (Eq.3.69) provides the closest prediction. This implies that the equation derived by using the skin friction coefficients given by Prandtl (1927) would be the suitable one to initialize the first grid height (y) for bluff bodies.

Therefore, one can now initialize the first grid height (y) directly by using the obtained equation (Eq.3.69) to place the first grid in the viscous sublayer ($y^+ < 5$) by choosing a y^+ value near about 5 as an input to the equation (Eq.3.69) and this will reduce the number of trials significantly.

In case, users want to keep the maximum y^+ value well within the viscous sublayer, one can even use much smaller value than 5 as an input to the equation to initialize the first grid height (y). From this section we obtained an equation to predict the first grid height (y), now we need to know the value of growth factor (GF) to expand the grid gradually away from the body to produce a converged solution. In the next section the influence of growth factor was discussed in detail.

3.9.1.3 Influence of Growth Factor (GF)

In finite volume method, the grid system is very crucial to get accurate results. The grid should be expanded gently in regions of high gradients, to keep the truncation error small. Franke *et al.*, (2007) and Tominaga *et al.*, (2008) recommended a growth factor (GF) of 1.3 to avoid numerical error in regions of high gradient. Scaperdas and Gilham (2004) and Bartiz *et al.*, (2004) even recommend a smaller growth factor (GF) of 1.2 to expand the grid. However, these recommendations were based on the criteria to avoid truncation error in high gradient regions. Along with this, there also should be sufficient number of grids all through the domain so that, the solution reaches the asymptotic range of convergence and important physical phenomena can be captured.

One can fulfill these criteria by choosing an appropriate growth factor (GF). Nevertheless, the value of growth factor (GF) requires producing a converged solution depends on the first grid height (y). For smaller first grid height relatively larger growth factor (GF) will be sufficient to produce a converged solution, yet for larger first grid height (y) smaller growth factor (GF) will be required to converge the solution.

We already discussed that to fulfill the near-wall treatment, the first grid should be in the viscous sublayer (Menter *et al.*, 2002 and Franke *et al.*, 2007) and this can be achieved if the grid possess a y^+ value of less than 5 (Pope 2000). Further, it was also known that we require smaller first grid height (y) to achieve smaller y^+ value. Therefore, if we can determine the growth factor (GF) requires to have converged solution based on larger first grid height (y) that would be conservative and also applicable for the smaller first grid height (y).

As a result, the influence of growth factor (GF) was investigated on the square cylinder ($R=1$) for the second grid (G2) considered in the previous section, as the maximum y^+ value is near about 5. The same Reynolds number (Re_B) was utilized and three growth factors (GF- 1.1, 1.07 and 1.05) were considered much smaller than the existing recommended value (Franke *et al.*, 2007; Tominaga *et al.*, 2008; Scaperdas and Gilham 2004 and Bartiz *et al.*, 2004) from numerical error point of view. The grid with a growth factor (GF) of 1.05 possessed a total 67,974 number of elements.

Table 3.3 shows the influence of growth factor (GF) on global parameters along with previous experimental and numerical result. As the growth factor (GF) decreased from 1.1 to 1.07 the variation of response decreases. For example, the rms of lift coefficient (C_L') varies only 2.9% $((1.479-1.436)/1.479)$ when the growth factor altered from 1.07 to 1.05, yet for 1.1 to 1.07 it varied around 9.5% $((1.635-1.479)/1.635)$. Similarly, the Strouhal number (S_t) remained unchanged when the growth factor altered from 1.07 to 1.05. Further, the present simulation could reproduce the aerodynamic responses closer to the experimental work as compared to past numerical work.

The surface pressure coefficients (C_p) are plotted in Fig.3.10. This is an important aerodynamic parameter that is used to estimate the wind loading and explains the aerodynamic behavior of structures. As can be seen from Fig.3.10 that the growth factor (GF) doesn't have noticeable influence on the front (0-1) surface pressure coefficients (C_p), it basically influences the

Table 3.3: Influence of growth factor (GF) on aerodynamic characteristics of square cylinder ($R=1$) for G2 (Table 3.1) at $R_{eB}=1.22 \times 10^4$. Previous works: Shimada and Ishihara (2002) at $R_e=10^4$, Sakamoto *et al.* (1989) at $R_e=5.5 \times 10^4$ and Okajima (1982) at $R_e=70-2 \times 10^4$

	Number of Element	C_D	C_L	C_L'	S_t
Current (GF -1.1)	30,331	2.182	0.0163	1.635	0.102
Current (GF-1.07)	45,317	2.144	-0.0197	1.479	0.099
Current (GF-1.05)	67,974	2.110	-0.0020	1.436	0.099
Numerical (Shimada & Ishihara 2002)		2.043		1.423	0.139
Experimental (Sakamoto <i>et al.</i> 1989)		2.236		1.469	
Experimental (Okajima 1982)					0.121

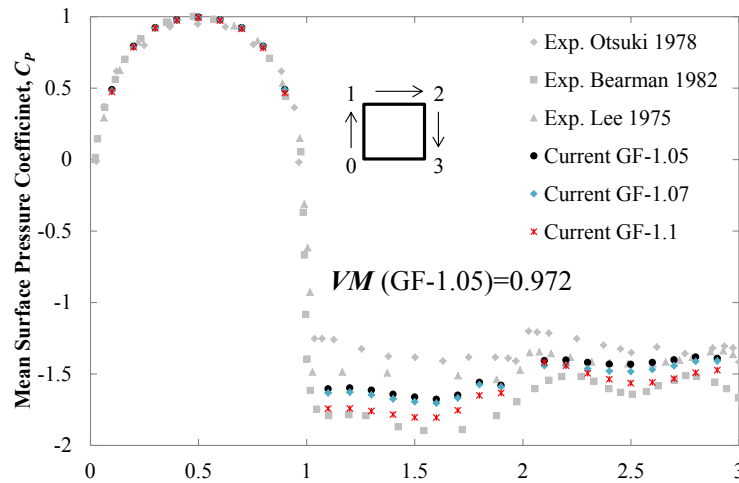


Figure 3.10: Mean value of surface pressure distribution around square cylinder at R_{eB} of 1.22×10^4 . Experimental results are: Otsuki (1978) at $R_{eB}=7 \times 10^4$, Bearman & Obasaju (1982) at $R_{eB}=2 \times 10^4$; Lee (1975) at $R_{eB}=1.76 \times 10^4$

top (1-2) and the back (2-3) surface pressure coefficients (C_p). Here also like global parameter, with the decrease of growth factor (GF) the difference among the responses also decreased. Specially, at the top (1-2) and back surface (2-3), the C_p increased noticeably when the growth factor (GF) was decreased from 1.1 to 1.07, yet very small variation can be noticed when the growth factor (GF) was reduced from 1.07 to 1.05.

This implies that when the first grid height (y) lies within the viscous sublayer ($y^+ \leq 5$), by using a growth factor (GF) of 1.05 one can achieve the asymptotic range of convergence in solution. Even though, it is important to check by establish methodology that whether the grid has really reached the asymptotic range of convergence or not. Therefore, we adopted a standard and widely used methodology proposed by Roache (1998) to check the convergence of grid system.

To apply the mentioned grid convergence method one should consider three grids and we already have three grids with total number of elements are 67,974 (1), 45,317 (2) and 30,331 (3) having different growth factor (GF). Then following the prescribed method, we considered two important indexes to check the convergence of solution. The first one was the finest grid relative error (e_{12}) as follows,

$$e_{12} = \left| \frac{\phi_1 - \phi_2}{\phi_1} \right|, \quad (3.71)$$

where, ϕ is the solution of important variable. In our calculation we considered the mean surface pressure value as a ϕ .

Another considered index was the check for asymptotic range of convergence of the computed solution. It was calculated as follows,

$$\text{Asymptotic range of convergence} = \frac{e_{23}}{e_{12} \times r^p}, \quad (3.72)$$

Where, r is the refinement factor and p is the observed order of convergence calculated from the prescribed equation (Roache 1998). The grid solution will be at the asymptotic range of convergence if Eq.3.72 yields a value of 1. Fig.3.11 shows the two considered indexes for the square cylinder ($R=1$). As can be seen the maximum relative error (e_{12}) for the finest grid (GF of 1.05) lay below 3.55% and the solutions were in the asymptotic range of convergence.

We also compared the computed surface pressure with previous experimental work to confirm that the computed solutions are not only converged but also accurate. In Fig.3.10, at the first sight it can be judged that that present solution could reproduce the solution very close to past experimental

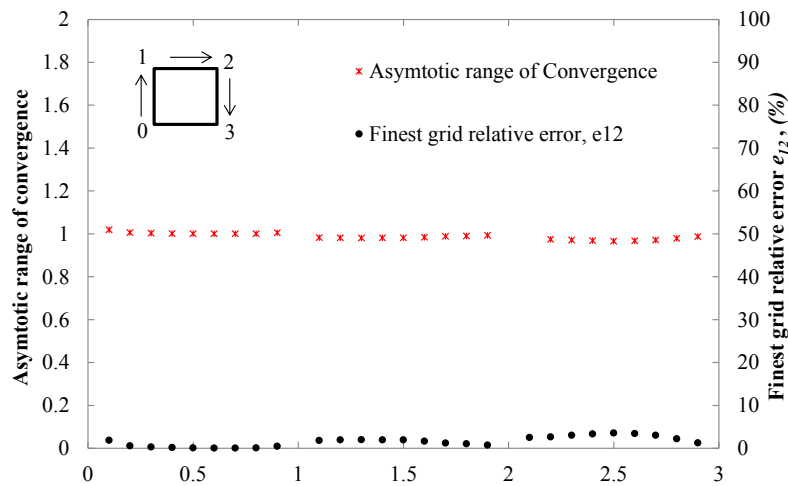


Figure 3.11: Grid convergence indexes calculated based on mean surface pressure of square cylinder

work. Both the magnitude and the trend of the surface pressure coefficients (C_p) were in well accordance with past experimental work.

3.9.2 Application of the Proposed Strategy

In previous section we developed, demonstrated and checked the performance of the proposed strategy for a square cylinder ($R=1$). In this section we applied the proposed strategy to generate the grid system for an elongated rectangular cylinder of side ratio ($R=5$). We checked the performance of the proposed strategy by comparing computed results with past experimental results.

According to the strategy, the first grid height was initialized by Eq.3.69, assuming a maximum y^+ value of 5.5 to obtain a grid having the average y^+ value well below than 5 (lies in the viscous sublayer). Then, the grids were gradually expanded away from the cylinder with a growth factor of 1.05. The grid number ($n_1=B/2y$; $n_2=D/2y$) along the perimeter of the cylinder was determined by dividing the corresponding length of the cylinder by twice the size of the first cell height ($2y$). Simulation was conducted at Reynolds number (Re_B) of 6.1×10^4 . Fig.3.12 shows the grid system having a total 1, 09,026 number of elements.

Table 3.3 shows the computed global parameter and obtained y^+ for the rectangular cylinder of side ratio (R) of 5. As can be seen that the maximum y^+ value is bit higher than the inputted one like in case of square cylinder, yet the average y^+ value is well below than 5 as expected earlier. However, depending on the turbulence model, importance of the work and availability of high performance computing system, one can even initialize the first grid height (y) by using Eq.3.69 with much smaller y^+ value to obtain a grid having maximum y^+ less than 5 or 1. The computed global parameters also compared with past numerical and experimental works. At the very first trial, current computation reproduces the global parameter with reasonable accuracy.

The mean surface pressure coefficients are plotted in Fig.3.13 along with past experimental work. The current simulation could grasp the pressure distribution pretty accurately. In validation section results were validated with proper validation metric, will be discussed in the next section. Then, we tried to check whether the grid reaches the asymptotic range of convergence or not when a

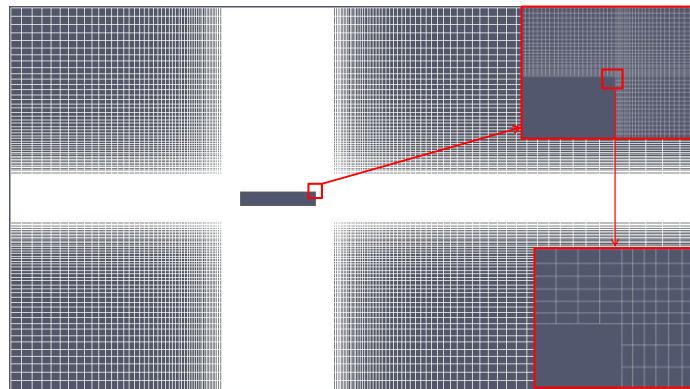


Figure 3.12: Considered non-uniform mesh arrangement to discretize the flow domain around the elongated rectangular cylinder ($R=5$)

Table 3.4: Aerodynamic characteristics of bluff body for side ratio (R) of 5 at $Re_B=6.1 \times 10^4$. Previous works: Mannini *et al.*, (2010b) at $Re=10^5$, Tamura and Ito (1996) at $Re=104$, Shimada and Ishihara (2002) at $Re=104$, Okajima (1982) at $Re=70-2 \times 10^4$

	Obtained y^+			C_D	C_L	C_L'	S_t
	Avg.	Min.	Max.				
Current	2.961	0.845	6.834	1.15	-0.0116	0.178	0.104
2D RANS (Mannini <i>et al.</i> , 2010)				1.15			0.103
3D RANS (Tamura & Ito 1996)				0.98		0.15	0.101
2D RANS (Shimada & Ishihara 2002)				0.98		0.05	0.117
Exp. (Okajima 1982)							0.109

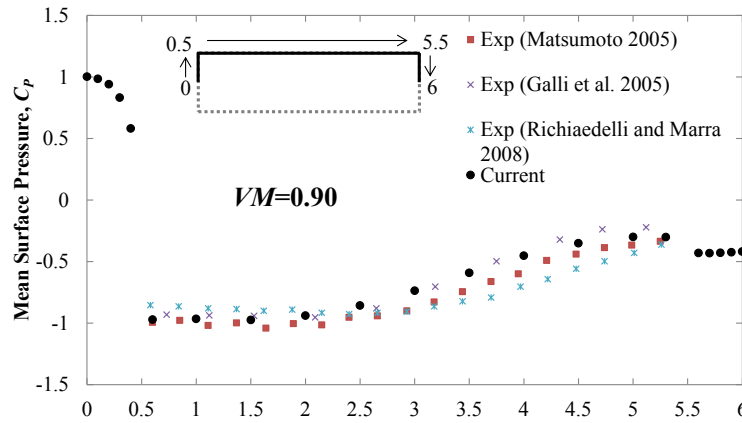


Figure 3.13: Mean value of surface pressure distribution around rectangular cylinder of side ratio (R) of 5 at $Re_B=6.1 \times 10^4$. Experimental results are: Matsumoto (2005) at $Re=1 \times 10^5$ (as cited in Mannini *et al.* 2010b); Galli (2005) at $Re=2.1 \times 10^5$; Ricciardelli & Marra (2008) at $Re=2.7 \times 10^5$ for R of 5

growth factor (GF) of 1.05 is utilized for this elongated cylinder.

Therefore, we generated two more grid systems having growth factor (GF) of 1.07 and 1.1. The three considered grids possessed a total 1,09,026 (GF-1.05), 72,616 (GF-1.07) and 48,124 (GF-1.1) number of elements. After that, we followed the same procedure as described in section 3.3 to check grid convergence. Fig. 3.14 shows the convergence indices. It depicts that the solution was in the asymptotic range of convergence and had a maximum relative error of the finest grid less than 7%. For this elongated rectangular cylinder also we found that a growth factor (GF) of 1.05 can yields a converged solution when the first grid (y) lies in the viscous sublayer ($y^+ < 5$).

This implies that the proposed strategy can be applied for generating grid system to obtain converged grid system in bridge and bluff body aerodynamic field. In the present study all the grid

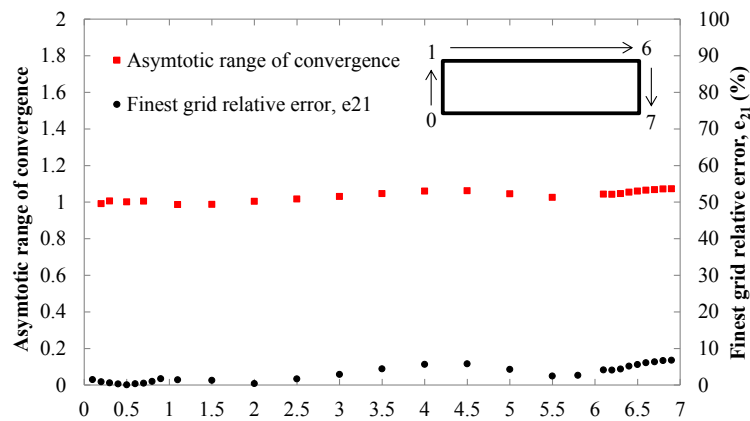


Figure 3.14: Grid convergence indexes calculated based on mean surface pressure of rectangular cylinder ($R=5$)

systems for various bridge deck sections and bluff bodies were generated by following this strategy. This saved the computational time and effort significantly.

3.10 Validation

A validation is a process through which it is assessed how closely or accurately the numerical model and setup can target predict the target or real responses. According to AIAA the definition of the term “Validation” is as follows:

“The process of determining the degree to which a model is an accurate representation of the real world from the perspective of the intended uses of the model.” (AIAA 1998)

It is important to validate the numerical results before applying it for the target problem to attain some level of confidence and to ensure the reliability of the numerical model, setup, boundary condition and grid system those were adopted. In the present study our target was to investigate the shaping effects on aerodynamic response of bridge decks. Basically, steady state force coefficients, surface pressure, velocity distribution and flutter derivatives were evaluated. Therefore, we conducted both static and dynamic simulations for bluff bodies having various shapes and tried to validate the results by comparing with past experimental works. Normally, numerical results are compared with experimental or full scale data. However, in bridge and bluff body aerodynamics field the full scale data is quite rare, hence the current numerical results were validated by comparing with past experimental works.

When a validation study is carried out, it is always appreciable to check the level of validation or measure the quality of validation. Basically two main streams of validation procedures are adopted in the CFD field those were given by Stern *et al.* (2001a and 2001b) and Oberkampf and Trucano (2002). Both of these approaches are well established and widely used. According to the validation procedure by Stern *et al.* (2001a and 2001b) a number of experimental data sets are

required to estimate the uncertainty. Similarly, the validation procedure by Oberkampf and Trucano (2002) also requires a number of experimental data sets, yet the procedure can also be simplified where only single set of data is available and widen the area of applicability. Hence, in the present study we adopted the standard Validation Metric (VM) proposed and recommended by Oberkampf and Trucano (2002) to measure the level of validation of the numerical results where it is applicable. Essentially, we estimated the VM to measure the level of validation for mean and rms of surface pressure distribution.

The metric was simple and straightforward; it takes the average of the number of experimental results at the discrete probing points and constructs a continuous cubic spline function. Then, the difference of the numerical and experimental function is integrated all through the length to calculate the metric. The metric could have a maximum value of 1. A higher value near about 1 is expectable. However, the metric is conservative as it takes the average of experimental results. The considered validation metric was as follows,

$$VM = 1 - \frac{1}{L} \int_0^L \tanh \left| \frac{\phi(x) - \bar{\phi}(x)}{\bar{\phi}(x)} \right| dx, \quad (3.73)$$

and

$$\bar{\phi}(x) = \frac{1}{N} \sum_{n=1}^N \phi_n(x_i), \quad (3.74)$$

where, N is the number of experimental data set, x_i is the discrete probing locations along the body surface, L is the length of the body, ϕ stands for numerical results and ϕ stands for the experimental results. The number of experimental data should be as high as possible to incorporate the influence of uncertainty. In the case of only one set of available experimental data, the uncertainty associated with the experiment can be ignored. According to Oberkampf and Trucano (2002) when there is no uncertainty or error in the experimental data the above mentioned equation can be simplified to the following one,

$$VM = 1 - \frac{1}{I} \sum_{i=1}^I \tanh \left| \frac{\phi(x_i) - \phi(x_i)}{\phi(x_i)} \right|, \quad (3.75)$$

where, I is the number of discrete probing locations. If the VM is calculated based on Eq.3.75 for a set of experimental and numerical data, the metric will estimate how closely the numerical result matches with the experimental one. A VM having a value of 1 means the numerical results matches completely with the experimental one.

3.10.1 Static Responses

Fundamentally, the mean and rms value of steady state force coefficients, Strouhal number (S_{td}), surface pressure distribution, velocity field was utilized in the present study as a static response of the bridge deck. However, in the literature not much experimental data are available for the bridge deck section. Hence, along with bridge deck section, we also considered the bluff body section such as square cylinder and elongated cylinder to validate the numerical setup. If we can validate the code and numerical setup for bluff section, from analytical point of view that should also work for streamlined section like bridge deck with fairing.

Total five validations for various shapes and sections was conducted and included herewith. Grid was generated by following the strategy discussed in Section 3.9. The first grid height (y) was initialized by Eq.3.69 to place it in the viscous sublayer ($y^+ < 5$) and the grid was stretched away from the target body or bridge deck with a geometric progression of 1.05 in all direction. In static response we focused both the global and local flow parameters such as the mean and rms value of steady state force coefficients along with the surface pressure and the velocity distribution.

3.10.1.1 Influence of Side Ratio (R)

When the side ratio (R) of the sharp edged rectangular cylinders are altered the steady state force coefficients and Strouhal number (S_{td}) exhibits an unique distribution. In bluff body aerodynamics it is often tried to simulate the side ratio effects on steady state force coefficients to evaluate the performance of the numerical setup (Tamura and Ito 1996, Shimada and Ishihara 2002 and Sohankar 2008). We altered the side ratio (R) from 1 to 8 and calculated the mean and rms value of the steady state force coefficients. Simulations were carried out at a Reynolds number (Re_B) varying from 1.2×10^4 to 9.76×10^4 .

Fig.3.15 illustrates the influence of side ratio (R) on mean drag (C_D), rms of lift (C_L) and Strouhal number (S_{td}) and compares the current results with past experimental and numerical results. The current simulation could reproduce the trend and magnitude quite well. In this test the side ratio (R) was altered and that was also a kind of change in shape and current simulation results had very good coherence with past results. One point should be noticed that the experimental results are well scattered and the current results lie within the upper or lower bound of past results. In this section global response are checked for varying side ratio (R). Starting from the next section we concentrate for a particular section and explore its detailed responses.

3.10.1.2 Square Cylinder (R of 1)

Simulation was conducted for a square cylinder (R of 1) at a Reynolds number of 1.2×10^4 . In section 3.9.1.3 we already have presented the steady state force coefficients (Table 3.3) and the mean surface pressures were compared with past experimental works (Fig.3.10). The magnitude of the validation metric (VM) calculated by using Eq.3.73 was shown in Fig.3.10. As be seen the validation metric (VM) possess a value of 0.972, that is very close to unity.

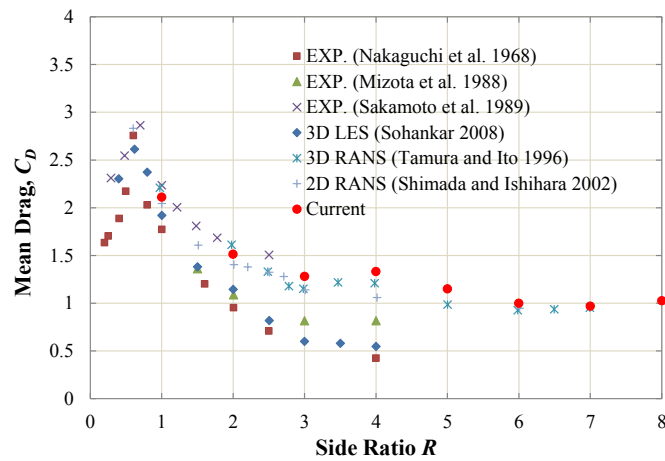
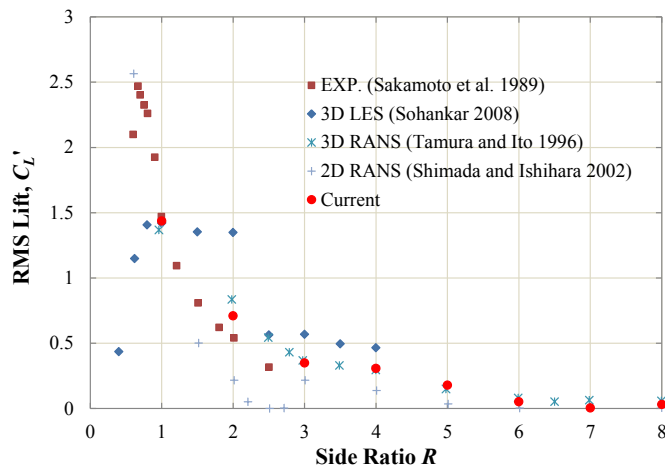
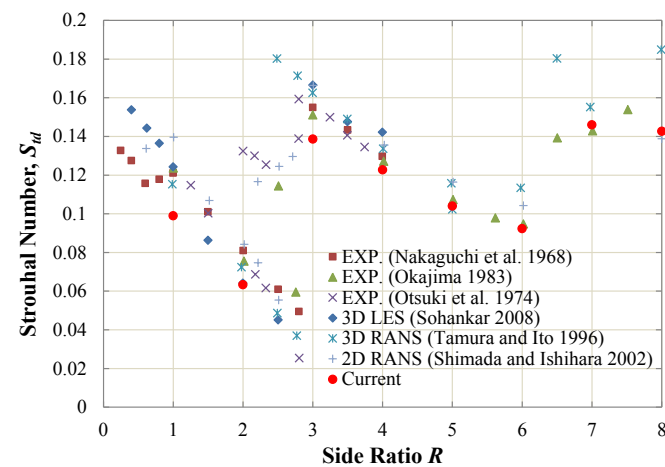
(a) Mean drag force coefficient (C_D)(b) rms of lift force coefficients (C_L')(c) Strouhal number (S_{tB})

Figure 3.15: Influence of side ratio (R) on steady state force coefficients and Strouhal number (S_{tB}). Experimental results are: Nakaguchi *et al.* (1968) at $Re=10^5$, Sakamoto *et al.* (1989) at $Re=5.5 \times 10^4$, Okajima (1983) at $Re=0.42 \times 10^5$, Otsuki *et al.* (1974) at $Re=2.2 \times 10^4$ - 5.5×10^5

Then, the rms value of surface pressure distribution is plotted in Fig.3.16 and compared with past experimental work. The rms value has also good agreement with past work like mean value, even though the fluctuating component in unsteady RANS was modeled completely by *SST k- ω* model. The present model and setup worked well in case of short bluff body like square cylinder (R of 1) where the complete separation of flow occurs at the side surface. A validation metric (VM) value of 0.782 was obtained as indicated in Fig.3.16.

The longitudinal velocity distribution is shown in Fig.3.17. Results are compared with past experimental and numerical works. Good accordance with past work can be noticed in the velocity distribution too. However, at the wake of body the current simulation recovers the velocity a bit faster than the experimental work.

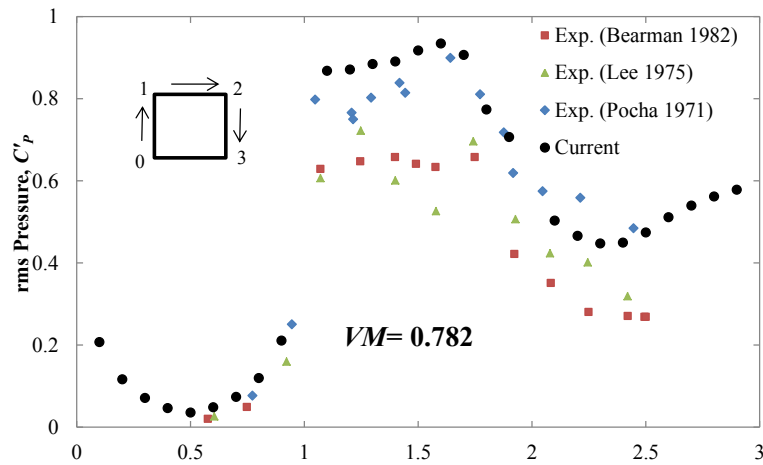


Figure 3.16: rms value of surface pressure distribution at Re_B of 1.22×10^4 . Experimental results are: Bearman & Obasaju (1982) at $Re_B = 2 \times 10^4$; Lee (1975) at $Re_B = 1.76 \times 10^4$ and Pocha (1971) at $Re_B = 9.2 \times 10^4$

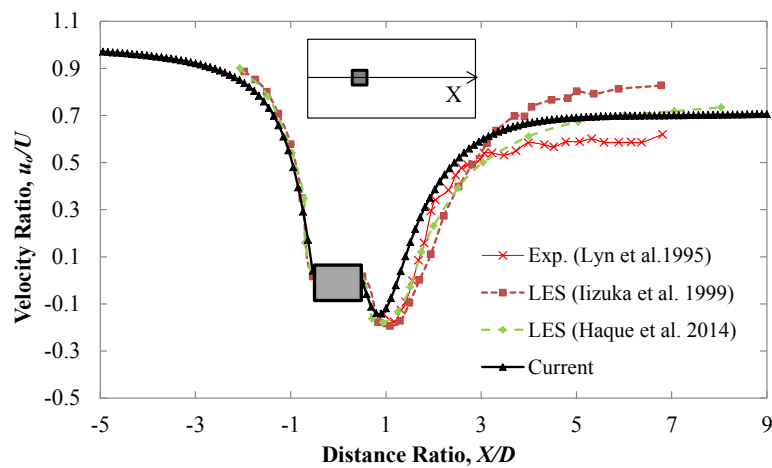


Figure 3.17: Normalized longitudinal velocity distribution along the flow domain at Re_B of 1.22×10^4 . Experimental and numerical result: Lyn *et al.* 1988 at $Re = 2.14 \times 10^4$, Iizuka *et al.* (1999) at $Re = 2.2 \times 10^4$ and Haque *et al.* (2014) at $Re = 2.2 \times 10^4$

3.10.1.3 Elongated Rectangular Cylinder (R of 5)

After checking the performance of the adopted numerical model and setup for the square cylinder, simulation was conducted for an elongated rectangular cylinder where flow reattachment occurs after separation at the leading edge. Analysis was conducted at a Reynolds number (Re_B) of 6.1×10^4 . The steady state force coefficients and mean surface pressure have already been compared with past experimental and numerical results in Section 3.9.2 in Table 3.4 and Fig.3.13. Like square cylinder, here also good coherence could be observed. Both at the flow separation and reattachment zone it has also grasped the mean flow field within desired level. A validation metric (VM) value of 0.90 was obtained.

The rms of surface pressure distribution is plotted in Fig.3.18 along with past experimental work. Unlike mean surface pressure, discrepancy at the trailing edge between the present and past experimental result can be noticed. The present simulation overestimates the magnitude of rms value of surface pressure. This also reflects in the validation metric (VM of 0.68) as it yields lower value than the mean surface pressure. Nevertheless, the trend of the result is grasped efficiently that the location of peak rms value coincides well with the experimental one (Matsumoto *et al.* 2005 and Galli 2005).

No experimental data of velocity distribution was found in the literature for rectangular cylinder having a side ratio (R) of 5 to compare and judge the accuracy of velocity. Therefore, present velocity field was compared with flow field obtained from three-dimensional Large Eddy Simulation (LES) by Bruno *et al.* (2012). Fig.3.19 quantitatively compares various flow features such as, separation thickness, reattachment length and the location of the vortex core at the side surface and after the body. Satisfactory agreement can be noticed between past and present simulation result.

3.10.1.4 Streamlined Bridge Deck

The aim of the present study was to investigate the bridge deck shaping effects on aerodynamic response. Until now we have validated for bluff sections and found good compatibility with past work. As the current numerical setup works well for bluff section where large flow separation occurs, from theoretical point of view the setup should also work well for streamlined section with less flow separation.

There are no so many data available for streamlined bridge deck in the literature. Šarkić *et al.* (2012) measured the mean value of surface pressure distribution for a streamlined bridge deck. We took the opportunity to validate the numerical setup and code again for the streamlined deck by comparing with experimental work of Šarkić *et al.* (2012). The detailed dimension of the deck is shown in Fig.3.20 (a). Simulation was conducted at a Reynolds number (Re_B) of 5.2×10^4 . Fig.3.20 (b) and (c) shows the grid system generated by following the strategy given in Section 3.9.

Fig.3.21 shows the mean surface pressure along with the validation metric (VM). Very good agreement can be observed between experimental and numerical work as predicted earlier. The present simulation slightly overestimated the pressure both at the top and the bottom deck surfaces due to two-dimensional nature of the simulation. Nevertheless, the overall pressure distribution was reproduced quite well and it was also reflected by the validation metric (VM).

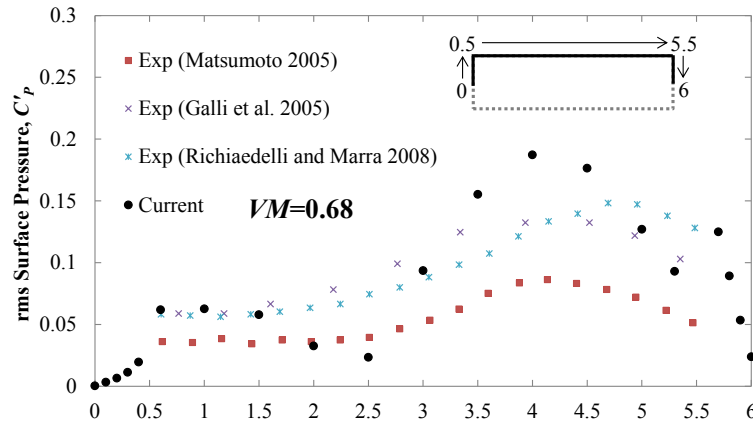
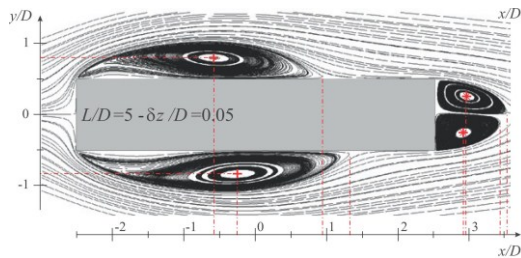
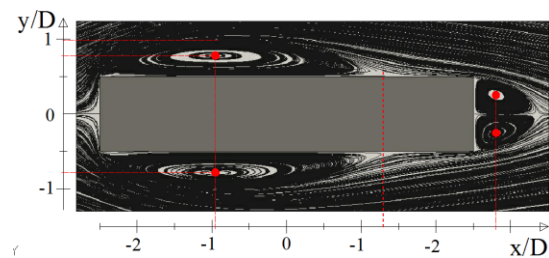


Figure 3.18: rms value of surface pressure distribution around rectangular cylinder of side ratio (R) of 5 at $Re_B = 6.0 \times 10^4$. Experimental results are: Matsumoto (2005) at $Re = 1 \times 10^5$ (as cited in Mannini *et al.* 2010b); Galli (2005) at $Re = 2.1 \times 10^5$; Ricciardelli & Marra (2008) at $Re = 2.7 \times 10^5$ for R of 5



(a) LES by Bruno *et al.* 2012



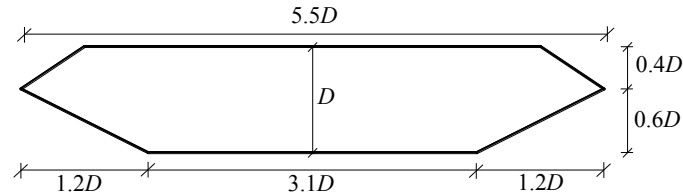
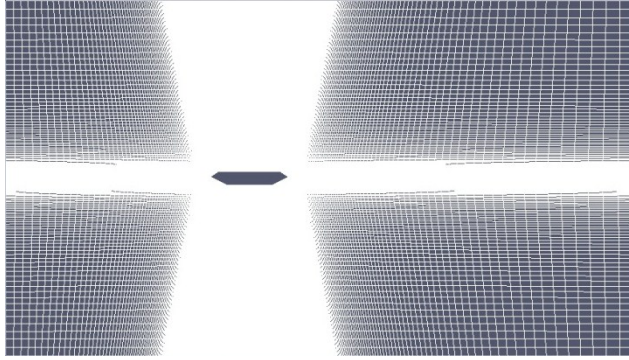
(b) Current Simulation

Figure 3.19: Time-averaged flow pattern around rectangular cylinder having side ratio (R) of 5

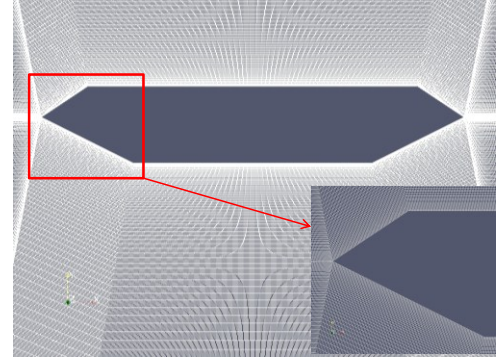
3.10.1.5 Pentagonal Bridge Deck

In the present study along with the streamlined bridge, shaping effects of pentagonal shaped bridge deck was also carried. Hence, it was important to examine and validate the numerical setup for pentagonal shaped bridge as the section was bluffer than streamlined bridge deck. Mean and rms value of surface pressure and velocity distribution for a pentagonal shaped bridge deck were measured by Noda (2010) through wind tunnel investigation. Simulation was run at a Reynolds number of 6.0×10^4 and 20×10^4 to validate the present result by comparing with past work of Noda (2010). The deck had a side ratio (R) of 5 and the bottom plate slope (θ_B) was adjusted to 14° . Fig.3.22 illustrates the grid system adopted for the computation.

Fig.3.23(a) presents the mean surface pressure around the pentagonal shaped bridge deck. The present simulation reproduced the trend of the surface pressure accurately. Specially, at the bottom surface leading edge and top surface trailing edge side it has very good compatibility with the experimental work. Large discrepancy can be observed around the curb on the top deck and at the bottom deck trailing edge side. In fact, large flow separation occurs in those locations as can be seen in Fig.3.24. As a consequence the present simulation failed to grasp the exact value of pressure coefficients on those locations. However, both at the top and bottom deck trailing edge it could reproduce the pressure recovery efficiently.

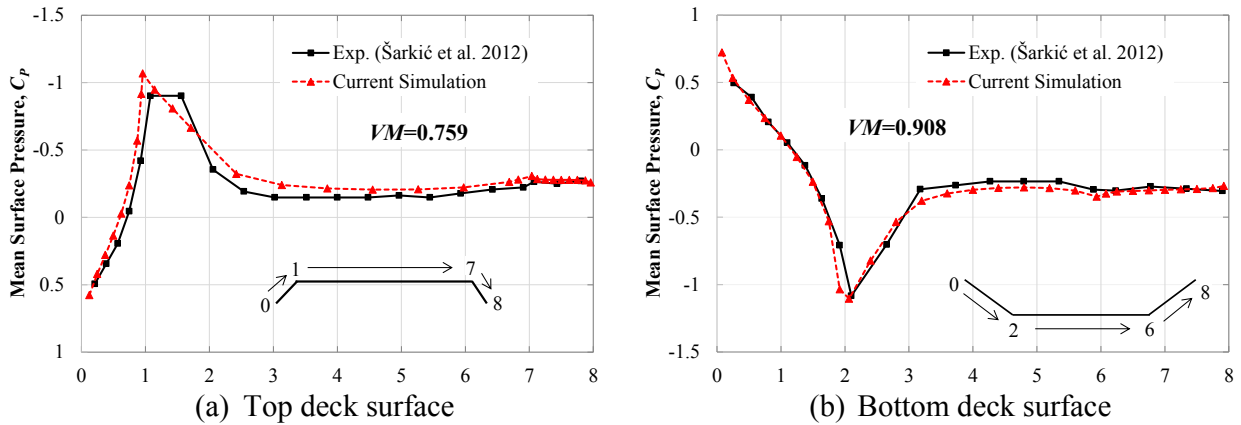
(a) Normalized dimension of the deck (Sarkic *et al.* 2012)

(b) Complete domain grid



(c) Grid near the body

Figure 3.20: Cross-sectional details and the computational grid system adopted for the streamlined bridge deck

Figure 3.21: Mean surface pressure distribution around the streamlined bridge deck compared with past experimental work of Šarkić *et al.* (2012)

Then the rms of surface pressure is plotted in Fig.3.23(b). In contrast to mean surface pressure, the discrepancy between the numerical and experimental work is higher in case of rms pressure. The present simulation failed to reproduce the trend in rms pressure at the leading edge side and underestimated the magnitude. Basically, in unsteady RANS the fluctuating component is modeled based on two transport equation as discussed before and the accuracy deteriorates for complicated geometry where massive flow separation occurs. This was also confirmed in past works (Mannini *et al.* 2010b) where unsteady RANS underestimated the response.

Fig.3.23(a) and (b) also displays the calculated validation metric (VM) based on Eq.3.75. The validation metric also reflects the general observation as we discussed in the previous paragraph.

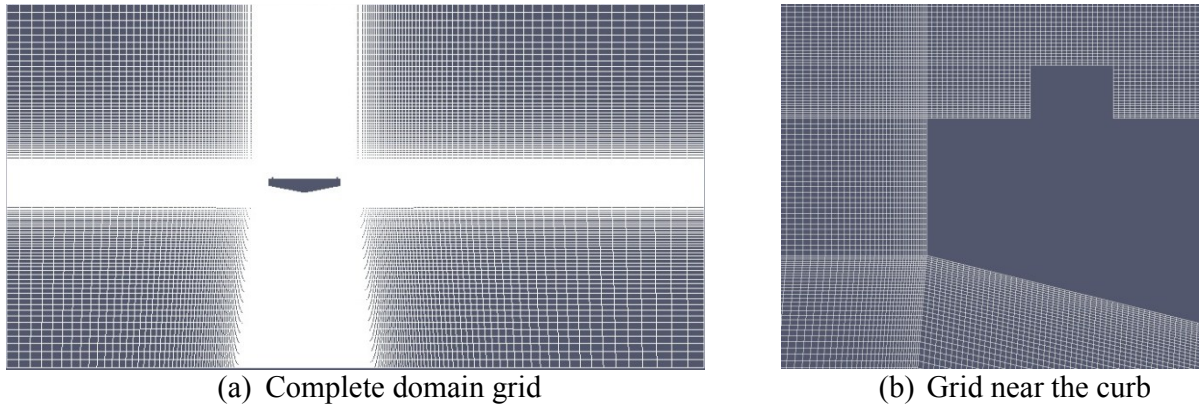
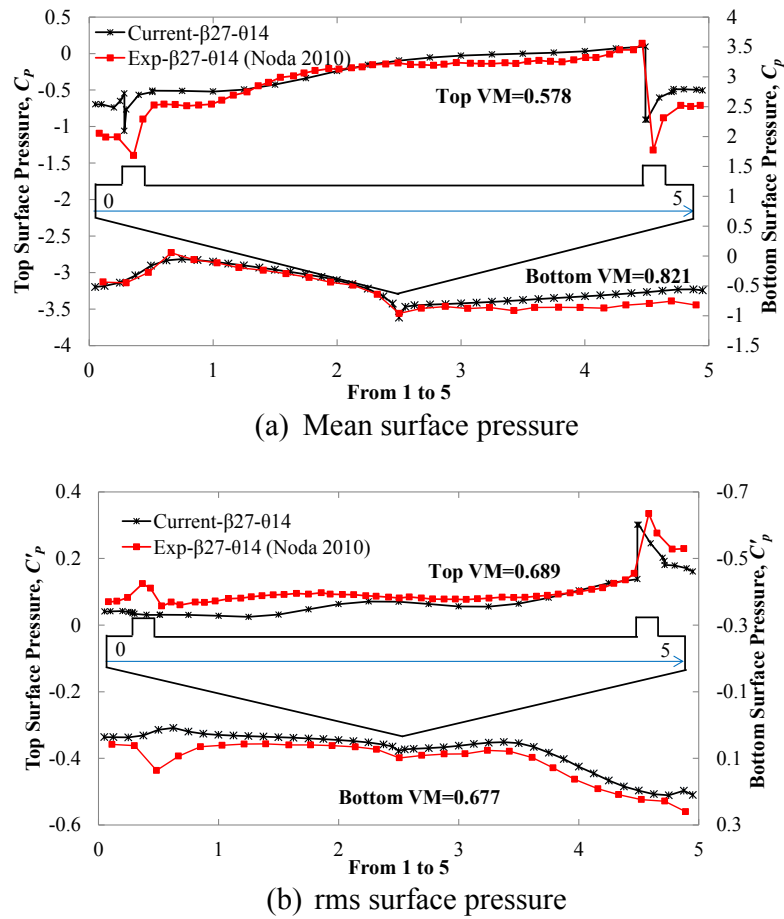


Figure 3.22: Computational grid system adopted for the pentagonal shaped bridge deck

Figure 3.23: Surface pressure distribution around pentagonal shaped bridge deck at a Reynolds number (Re_B) of 6.0×10^4

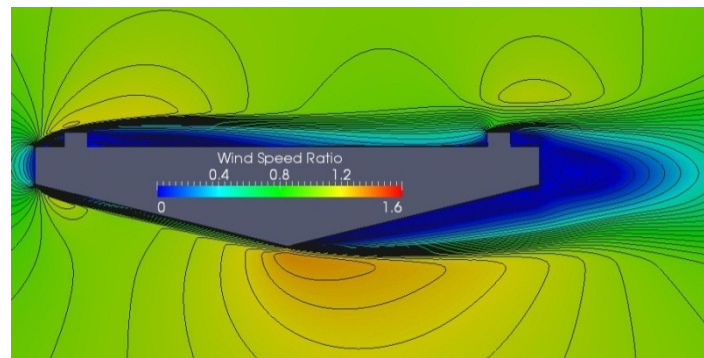
The mean surface pressure has higher metric value over rms surface pressure and mean bottom surface pressure over top surface. The bottom surface mean pressure has the highest metric value of 0.821 and the other metric values are also well above 0.5. Hence we thought by utilizing this level accuracy, one can investigate the trend in result when one specific parameter of interest is changed.

The velocity distribution is compared in Fig.3.24. It is easily apprehensible that the present simulation could reproduce the overall and general tendency of velocity distribution very close to the experimental one. Even the velocity acceleration on the top of the curb and at the bottom surface mid-deck was also grasped very well. However, the numerical wake size is bit larger than the experimental one. This level of discrepancy was accepted as in the presented study basically relative comparison of flow field of different bridge decks was made.

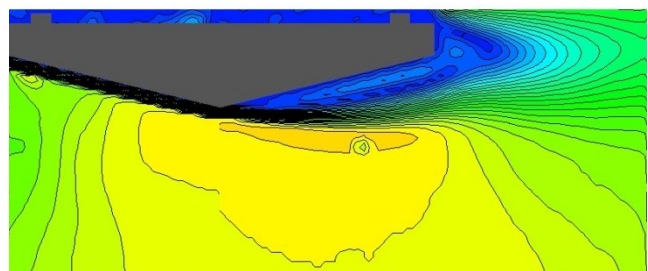
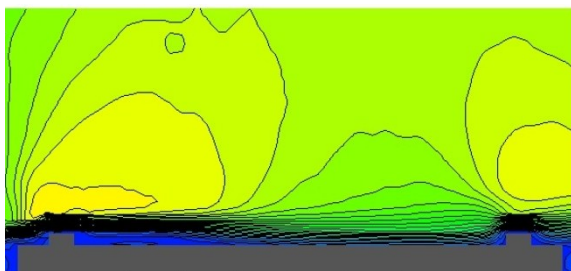
3.10.2 Dynamic Responses

Availability of data for dynamic responses such as flutter derivatives and unsteady pressure are even scarcer than the static aerodynamic response as it requires complicated instrumentation, hard labor and quite expensive. In the current study we mainly focused on flutter derivatives and aerodynamic damping of the bridge decks with and without fairing. The flutter derivatives of the streamlined bridge deck i.e., the deck with fairing were validated by comparing with the flutter derivatives of the Great Belt Bridge deck obtained experimentally by Reinhold *et al.* 1992. In the case of deck without fairing, the flutter derivative results of the sharp edged rectangular cylinder having a side ratio (R) of 5 and a pentagonal shaped bridge deck without fairing based on the wind tunnel experiment by Matsumoto (1996) and Matsumoto *et al.* (1999), respectively were utilized.

Along with the flutter derivate, we also calculated aerodynamic damping based on the magnitude of unsteady pressure ($|C_p|$) and the phase lag (φ). These two properties were validated by



(a) Current simulation at $R_{eB}=20 \times 10^4$



(b) PIV experiemnt (Noda 2010) at $R_{eB}=21 \times 10^4$

Figure 3.24: Comparision of the wind speed ratio around the pentagonal shaped bridge deck. In experimental work same colour bar level was used like the numerical work (0-1.6)

comparing with past work of Matsumoto (1996) for the elongated rectangular cylinder (R of 5). For all the cases the grid system was generated by following the strategy discussed in Section 3.9. The reduced velocity (U/fB_l) was altered by changing the oscillation frequency (f_η and f_α) rather than changing the inlet velocity (U). We experienced that the dynamic responses demand higher efforts to validate as compared to the static responses as those responses are quite sensitive (Sarker *et al.* 2009 and Caracogila *et al.* 2009).

3.10.2.1 Great Belt Bridge Deck

In the present study one of our target bridge deck was the deck with fairing, hence it was important to validate the numerical setup for a similar bridge deck such as the Great Belt Bridge deck. Hence, we conducted simulation for the Great Belt Bridge deck to validate the flutter derivative results. Current results were compared with the experimental results evaluated by Reinhold *et al.* (1992) as cited in Stærdahl *et al.* (2007). Simulation was conducted at a Reynolds number (R_{eB}) of 6.2×10^4 . Flutter derivatives were extracted based on the methodology and formula presented in Chapter 2 (Section 2.3.2.2). The forced vibration simulation was carried out with a heaving (η_o) and torsion (α_o) amplitude of $0.006B$ and 1° , respectively. Only six flutter derivatives were calculated as cited in Stærdahl *et al.* (2007).

Fig.3.25 displays the calculated flutter derivatives. At the first look very good agreement can be noticed between the present computation and past experimental work. However, at higher reduced velocity (U/fB_l) the present numerical result deviates from the experimental works and overestimates the responses. Similar trend was also reported for this kind of streamlined deck in past works (Stærdahl *et al.* 2007, Bai *et al.* 2010, Sarkic *et al.* 2010, Nieto *et al.* 2015 and Patruno 2015).

Noticeable discrepancies can be noted for H_2^* and H_l^* . As reduced velocity (U/fB_l) increases the frequency (f) of the vibration decreases and separation length of the flow increases. As a result the complexity in describing shear layer instabilities increases and the unsteady RANS simulation fails to predict accurately the responses at the flow separation region and the point of flow reattachment (Patruno 2015). That directly affects the flutter derivatives values. However, present simulation had similar level of accuracy to predict H_2^* and H_l^* as like past works (Stærdahl *et al.* 2007, Bai *et al.* 2010, Sarkic *et al.* 2010, and Patruno 2015).

The A_l^* and H_l^* computed directly by exciting the model in heaving mode and from the interdependency relationship among the flutter derivatives as discussed in chapter 2 are compared in Fig.3.25(c) and Fig.3.25(d), respectively. The interdependency relationships predict the flutter derivatives quite accurately and better than the direct computation. Basically, when the model is excited in heaving mode the shear layer separation becomes even more pronounce and accuracy decreases. However, the overall trend in flutter derivative was predicted quite accurately by the current numerical setup. Further, in case of comparative analysis among various shapes of the bridge decks, the remaining amount of the discrepancy can be accepted.

3.10.2.2 Elongated Rectangular Cylinder (R of 5)

Along with the streamlined deck, another interest was the deck without fairing. The deck without fairing usually experiences larger flow separation; therefore it is necessary to check the performance

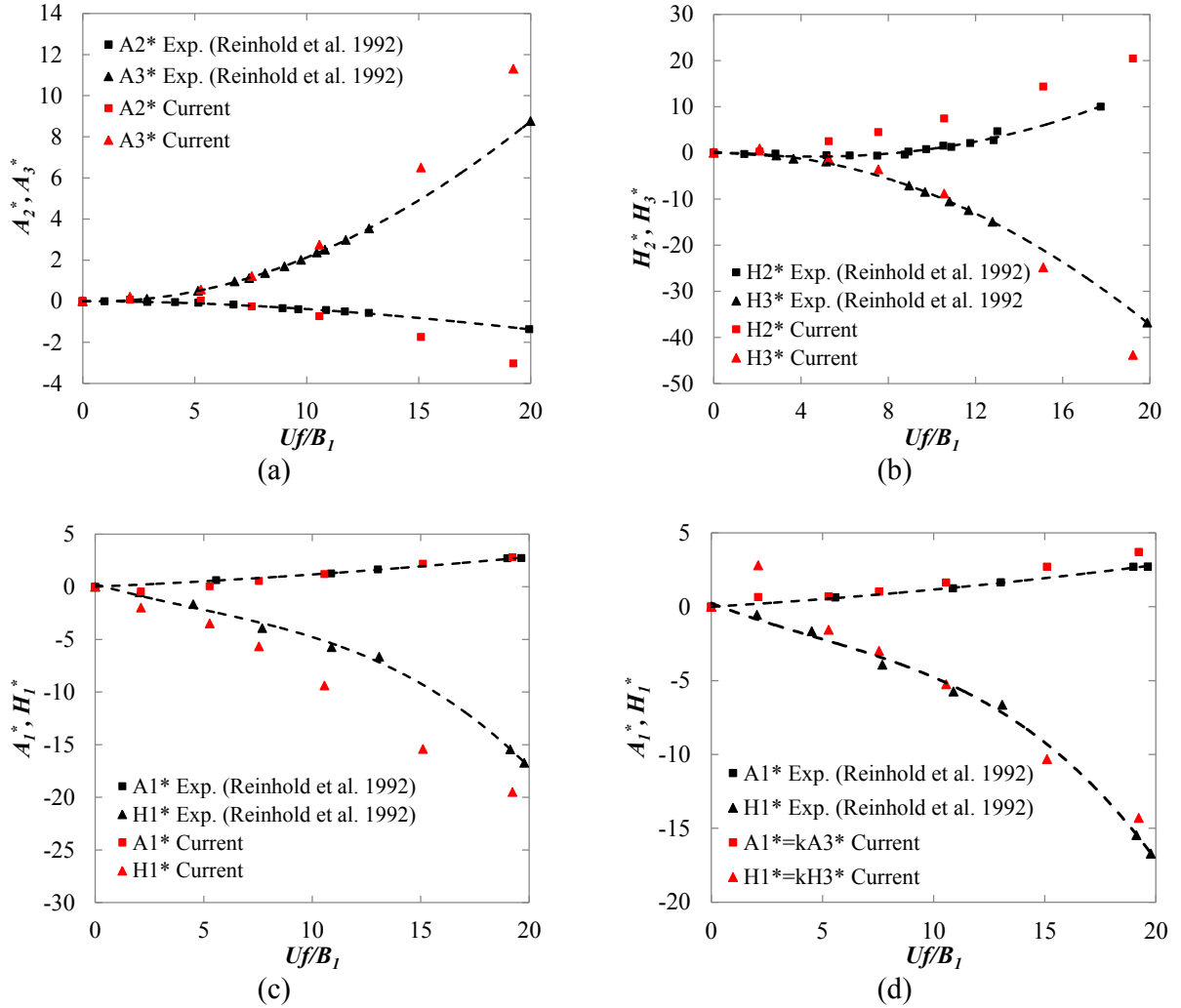


Figure 3.25: Comparison among flutter derivatives of Great Belt bridge deck evaluated numerically (current study) and experimentally (by Reinhold *et al.* (1992) as cited in Stærdahl *et al.* (2007)): (a), (b) and (c) Evaluated directly by torsional and heaving mode vibration and (d) Calculated from the interdependency relationship among the flutter derivatives

of the current simulation for this type of deck having sharp edge. In this section we present the results for the rectangular cylinder with a side ratio (R) of 5. Even though, the rectangular cylinder possesses quite large separation as compared to pentagonal shape bridge deck, we carried out this validation to judge the performance of the present numerical setup in extreme case. Only torsional mode flutter derivatives were considered as for this type of bridge deck only the torsional mode vibration is critical (Kubo *et al.* 2007 and Noda 2010). Simulations were carried out at a Reynolds number (Re_B) of 5.0×10^4 with a torsional amplitude (α_o) of 1° .

The extracted flutter derivatives are reported in Fig.3.26 and compared with past experimental work of Matsumoto (1996). A reasonable accordance can be noticed between past and present numerical result, yet the accuracy deteriorates for the present shape. Discrepancy can be noticed for H_2^* and A_2^* for these two derivatives as compared to other flutter derivatives and similar higher discrepancy was also reported in previous researches (Sarwar *et al.* 2008, Huang *et al.* 2009, Miranda *et al.* 2014, and Nieto *et al.* 2015).

In particular, referring to Fig.3.26, the flutter derivatives of the present work match better to those were extracted by Sarker *et al.* (2009) and some differences can be noticed between the flutter derivatives were extracted by Matsumoto (1996) and Sarker *et al.* (2009). It is really challenging to validate for this type of bluff section, it would be more practical if we can validate our model for more similar section like pentagonal shape deck having less separation. In the next section validation for a pentagonal shaped bridge deck is presented.

Along with the flutter derivatives we also calculated aerodynamic damping of the bridge decks and it is also essential to validate this kind of responses. However, we already have checked the performance of flutter derivatives and that is also a kind of validation for aerodynamic damping as they are also function of the amplitude of unsteady pressure ($|C_p|$) and phase lag (ϕ). However, in the literature there are not much data available regarding the unsteady pressure ($|C_p|$) and the phase lag (ϕ) of the bridge deck or bluff body. Matsumoto (1996) reported the amplitude of unsteady surface pressure ($|C_p|$) and the phase lag (ϕ) distribution for the elongated cylinder (R of 5) in torsional mode of vibration, we took this chance to compare our computed unsteady pressure amplitude ($|C_p|$) and phase lag (ϕ) with past experimental output.

Fig.3.27 reports the amplitude of unsteady pressure ($|C_p|$) and the phase lag (ϕ) distribution for the rectangular cylinder (R of 5). As can be seen simulation with torsional amplitude (α_o) of 1° underestimates the magnitude of unsteady pressure ($|C_p|$) noticeably, yet the phase lag (ϕ) agrees well with the experimental computation. As the unsteady pressure is an amplitude dependent property, thus one more simulation was conducted with a torsional amplitude (α_o) of 2° to maintain similarity with the experimental work believing that will lessen the discrepancy observed in Fig.2.27(a). Fig.3.27 (a) depicts that the compatibility of the unsteady pressure ($|C_p|$) with past experimental work improves dramatically after the increase in the amplitude (α_o) of the torsional vibration, while the magnitude of the phase lag (ϕ) remains unaltered.

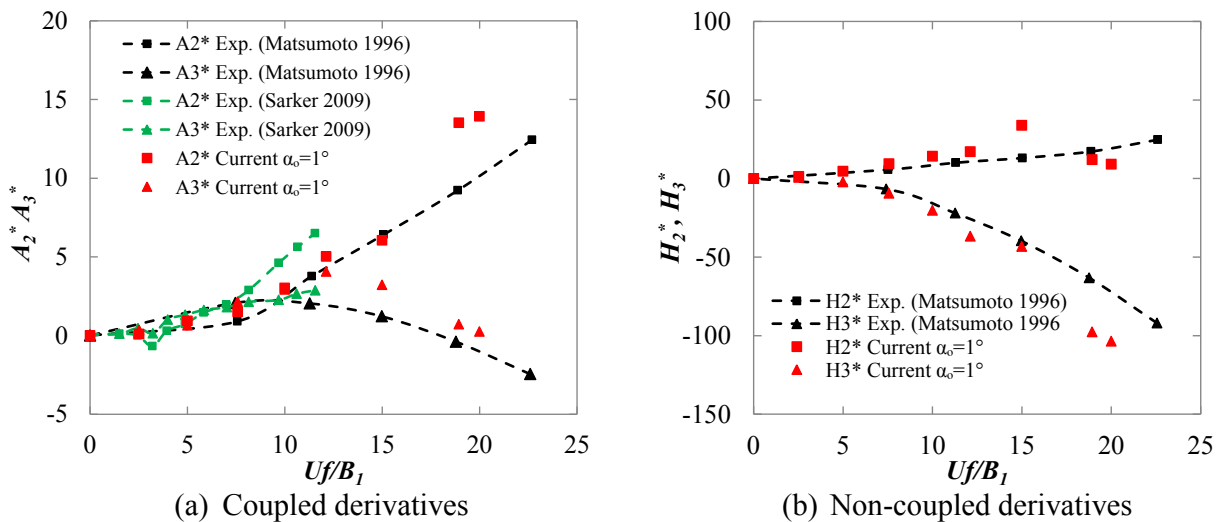


Figure 3.26 : Flutter derivatives of the rectangular cylinder having side ratio (R) of 5 extracted from forced torsional oscillation

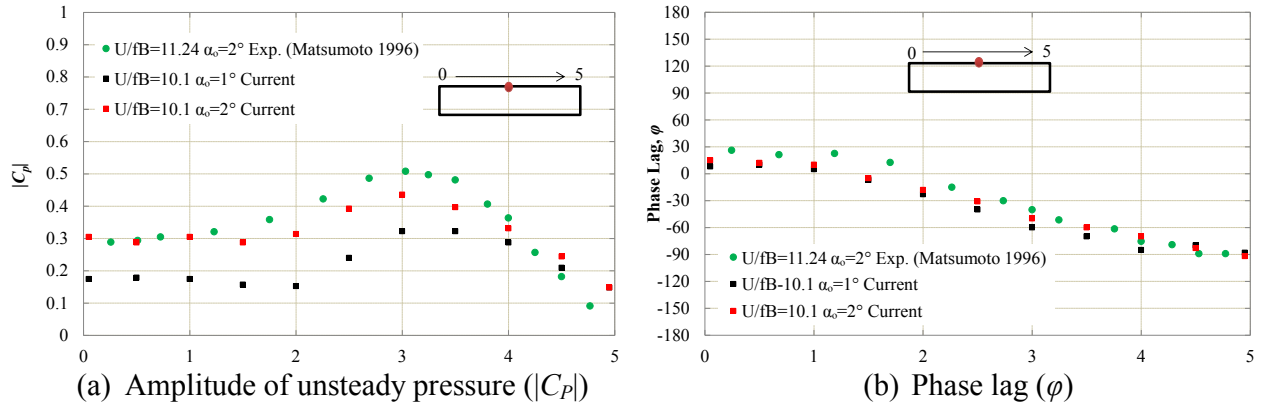


Figure 3.27: Unsteady pressure characteristics of the rectangular cylinder having side ratio (R) 5

3.10.2.3 Pentagonal Bridge Deck without Curb

In previous section the validation for the rectangular cylinder having a side ratio (R) of 5 was discussed. However, our considered bridge deck without fairing was pentagonal in shape and this sort of bridge deck experiences less flow separation than the sharp edged rectangular cylinder (R of 5). The present model should perform better for the pentagonal shaped bridge deck. Fortunately, in the literature we found experimental data of two torsional flutter derivatives (A_2^* and H_3^*) for the pentagonal shaped bridge deck without curb conducted by Matsumoto *et al.* (1999) and tried to validate those two torsional flutter derivatives.

The deck had a side ratio (R) of 6 and a bottom plate slope (θ_B) of 13.13° . Fig.3.28 shows the computational grid system for the pentagonal bridge deck. The Reynolds number (Re_B) was set to 6.0×10^4 and forced torsional vibration simulation was carried out with a torsional amplitude (α_o) of 2° . Fig.3.29 illustrates the computed flutter derivatives along with the experimental results (Matsumoto *et al.* 1999). The present model and numerical setup performs much better for the pentagonal bridge deck and predicted the trend of the flutter derivatives for increasing reduced velocity (U/fB_1) quite well as expected earlier. Specially, the H_3^* matches both qualitative and quantitatively. For A_3^* certain amount of discrepancy can be noticed, yet the decreasing tendency of

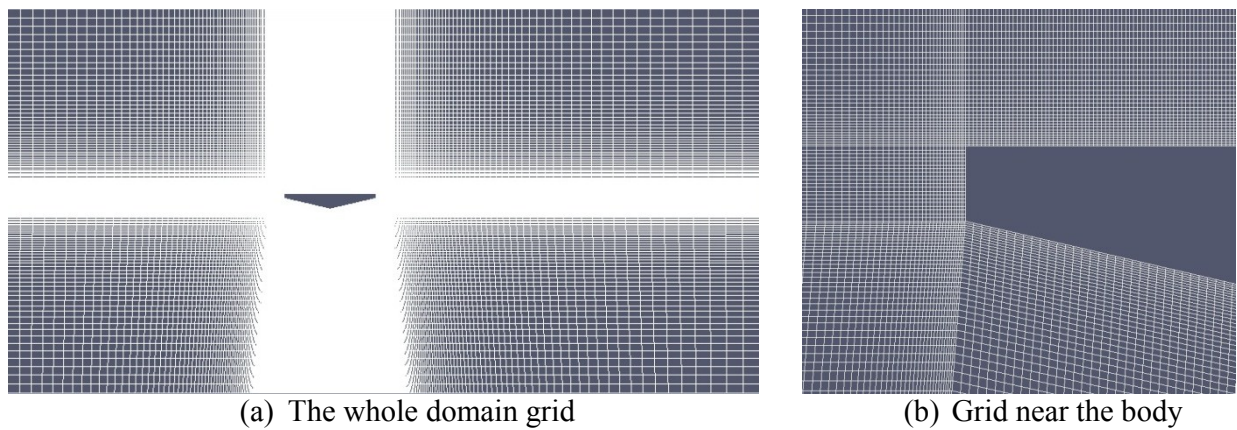


Figure 3.28: Computational grid system for the pentagonal shaped bridge deck without curb

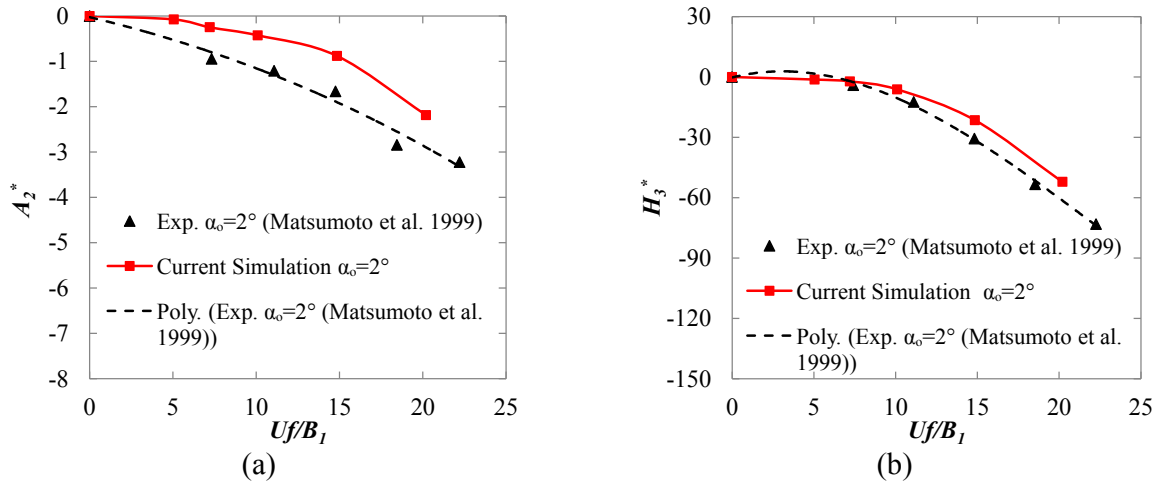


Figure 3.29: Torsional (A_2^* and H_3^*) flutter derivatives of the pentagonal bridge deck at Re_B of 6.0×10^4

A_3^* with the increase in reduced velocity was grasped well. We accepted this level of accuracy as relative comparison of flutter derivatives among similar bridge decks was made lessening the demand of quantitative accuracy.

3.11 Concluding Remarks

This chapter dealt with the description of the computational method adopted in the current study and detailed validations. The governing equations of fluid flow were derived and presented briefly. The turbulence modeling was demonstrated and equations were discretized. A strategy was proposed to generate grid system to obtain converged solution promptly to facilitate the grid generation technique. Both the static and dynamic responses were validated for various bluff bodies and bridge decks with proper validation metric by comparing with past experimental works.

The proposed strategy for generating grid system was found to be very efficient and produces converged solution with less effort. By exploiting the proposed strategy grids for various bridge decks were produced and provided accurate results at the very first trial. The present numerical method and setup could reproduce both the static and the dynamic responses with fairish accuracy. The performance of the utilized methodology devolved for the bluff sections having large flow separation both for the static and the dynamic simulation results. Exclusively for dynamic simulation the accuracy degrades at high reduced velocity.

Nevertheless, the trends of the results were captured quite accurately in almost all the cases both for the static and dynamic responses. Especially for the case of bridge decks with or without fairing the present numerical method and setup worked noticeably better than the sharpened edged bluff sections. We accepted this level of accuracy thinking this would be sufficient to investigate the influence of various shaping parameters on aerodynamic responses as primarily relative comparisons was made among the responses of various shapes.

Chapter 4

Bridge Deck Shaping Effects on Aerodynamics: With Fairing

Long span bridge decks are frequently shaped as a streamlined to improve the aerodynamic response by reducing the along wind loading and suppressing the after-body vortices. Normally, triangular fairings are attached at the leading and trailing edge or decks are shaped hexagonally (by adjusting the bottom plate slope of the deck along with the fairing) to achieve the streamlined shape. There are a number of shaping parameters for this kind of deck: i) Top plate slope (θ_T), ii) Bottom plate slope (θ_B) iii) Width ratio ($W = b/B$) and iv) Side ratio ($R = B/D$).

The aim of the present chapter is to investigate the influence of these shaping parameters on steady state response and the flow field of the bridge decks. The chapter is broadly divided in to two parts. The first part deals with the influence of top (θ_T) and bottom (θ_B) plate slope on aerodynamic response and flow field of the bridge deck with a fixed side (R) and width (W) ratios. The second part deals with the effects of width ratio (W) on steady state responses for a fixed set of top (θ_T) and bottom (θ_B) plate slopes. Along with these, we also discuss the influence of various other shaping and aerodynamic aspects such as, the types of the handrail, the nose location of the edge fairing (y), the side ratio (R) and the Reynolds number effects (ReB). For all the simulation, the grids were generated by following the strategy presented in Chapter 3 and had an average y^+ value near about 2.8 with a maximum value of about 7.5 at the bridge deck periphery. For setting the analysis case, similar numerical setup was adopted as discussed in Chapter 3.

4.1 Behavior of Deck with Edge Fairing

Edge fairings are often attached at the side of the deck to obtain improved aerodynamic responses. Normally, they are applied to the shallow depth bridge deck for medium to long span bridges, such as Deer Isle (USA), Bronx-whitestone (USA), Hakucho (Japan) and Tempozan (Japan) bridges. Edge fairings are also used for pedestrian bridges. Fig. 1 shows edge fairing applied to the Bronx-Whitestone Bridge in USA.

In previous works, mainly wind tunnel investigations were conducted on some specific shapes of the triangular edge fairings to show its effectiveness (Yamaguchi *et al.*, 1986; Nagao *et al.* 1993; De Miranda and Bartoli 2001). Miranda and Bartoli (2001) considered four sections of fairing and conducted wind tunnel experiment. They mentioned that the fairing improves the aerodynamic stability as compared to the basic section. Effects of edge fairing on flutter stability of a two edge box girder bridge were investigated by Sukamta *et al.* (2008). From their wind tunnel experiment it was demonstrated that some suitable fairing shapes can improve the flutter stability.

However, in those works only dynamic response were focused, yet the static responses is also important to reduce the wind load at high wind speed. Moreover, no detailed flow field analysis was conducted to understand the aerodynamic response. Therefore, detailed and systematic investigation are required on edge fairing to know how the variation of fairing shape influences the flow field around the bridge deck and thereafter affects the aerodynamic responses. Therefore, we devoted detailed numerical investigation on triangular edge fairing of different shapes. First the influence of edge fairing on aerodynamic response is tried to clarify for a bridge deck with a side ratio (R) of 5. Then, the practical issues such as the influence of handrail type and the nose location of the fairing are also investigated. All the simulations were conducted at a Reynolds number (Re_B) of 6.0×10^4 .

4.1.1 Influence of Top (θ_T) and Bottom (θ_B) Plate Slopes

Fairing shapes were altered sequentially by changing the top (θ_T) and the bottom plate slope (θ_B) without shifting the leading edge bottom toe point, i.e., the width ($W=b/B$) ratio is 1. Fig.4.2 shows the schematic view of the considered deck section. Based on the survey results as discussed in Chapter 2, the top plate slope (θ_T) of the fairing was varied from 30° to 50° , while the bottom plate slope (θ_B) was varied from 10° to 40° . Simulations were conducted by attaching perforated handrail with curb to the deck. The handrail had a solidity ratio near about 40%. The fairing shape effect was observed on the steady state force coefficients and the Strouhal number (S_f). Surface pressure and flow pattern were visualized elaborately to explain the behavior of global parameters and to comprehend the flow field.

4.1.1.1 Steady State Force Coefficients

Fig.4.3 shows the mean value of global parameters. As can be seen the top (θ_T) and bottom (θ_B) slopes affect the steady state force coefficients significantly. In Figs. 4.3(a) and (b), as the top plate



<http://www.citiesgallery.com/>

Figure 4.1: Edge fairing applied to the Bronx-Whitestone Bridge deck

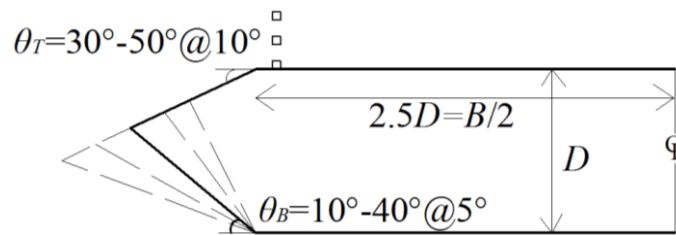


Figure 4.2: Schematic view of the considered bridge deck and various important notations

slope (θ_T) decreases the drag and lift value decreases, yet it doesn't affect the moment value significantly. On the other hand, as the bottom plate slope (θ_B) decreases the drag and lift value decreases too, still the moment increases.

For a range of bottom plate slope (θ_B) from 25° to 15° the deck experiences the lowest drag and experiences negative lift value for any value of the top plate slope (θ_T). From aerodynamic point of view it is always desirable to have negative lift, as it increases the tension in the cable and thereafter improves the stiffness of the bridge system. Therefore, smaller top and bottom plate slope would be a better choice to have less static aerodynamic loading. However, too much small bottom plate slope would increase the drag and moment value significantly.

The rms value of global parameters is another important parameter that provides information about the dynamic or vortex shedding behavior about the deck section. The rms value of steady state force coefficients are plotted in Figs.4.4(a), (b) and (c). The rms value of steady state force coefficients decrease as the top plate slope of the fairing (θ_T) decreases. Similarly behavior also can be found for bottom plate slope (θ_B) for a certain range of slope (θ_B). The rms value decreases up to a bottom plate slope (θ_B) of 15° and then increases again beyond that value.

In Fig.4.4(c), the shedding frequency (f) is expressed in the normalized form of the strouhal number, $S_r = fD/U$. Where the shedding frequency, f , was computed from the peaks in the power spectra of the lift fluctuations. No clear shedding frequencies were found for a range of bottom plate slope (θ_B) from 25° to 15° , when the top plate slope (θ_T) was placed at 40° and 30° . For the same

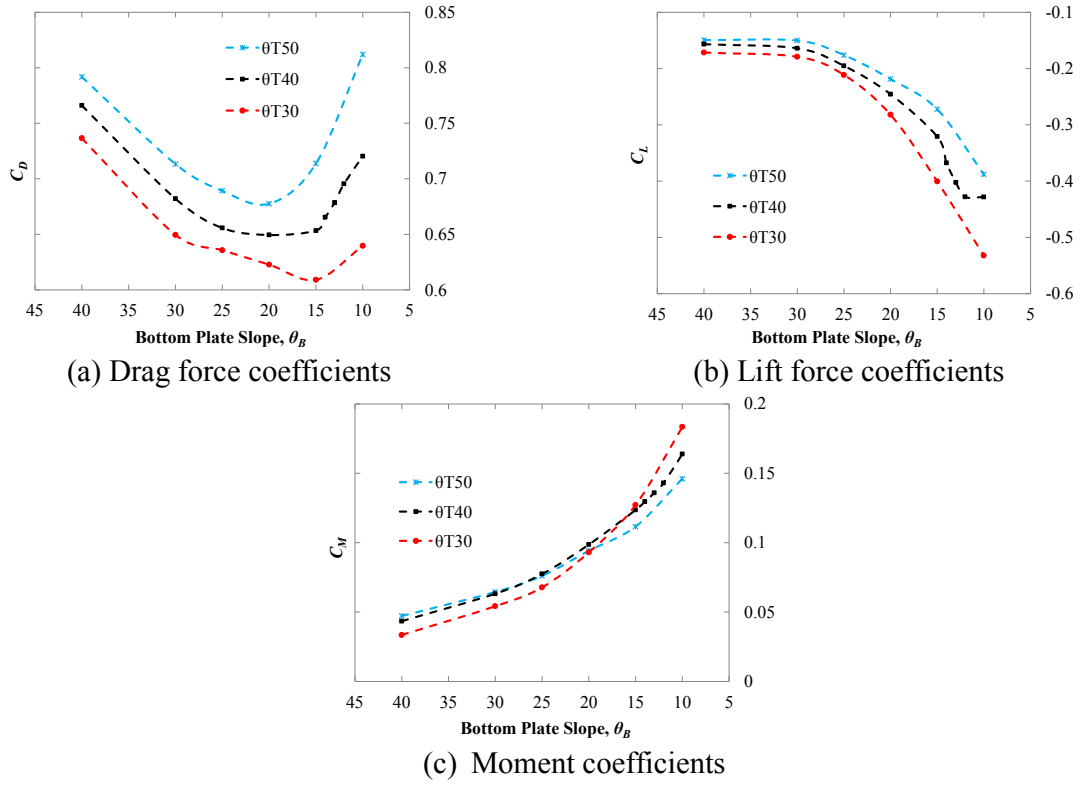


Figure 4.3: Mean value of steady state force coefficients

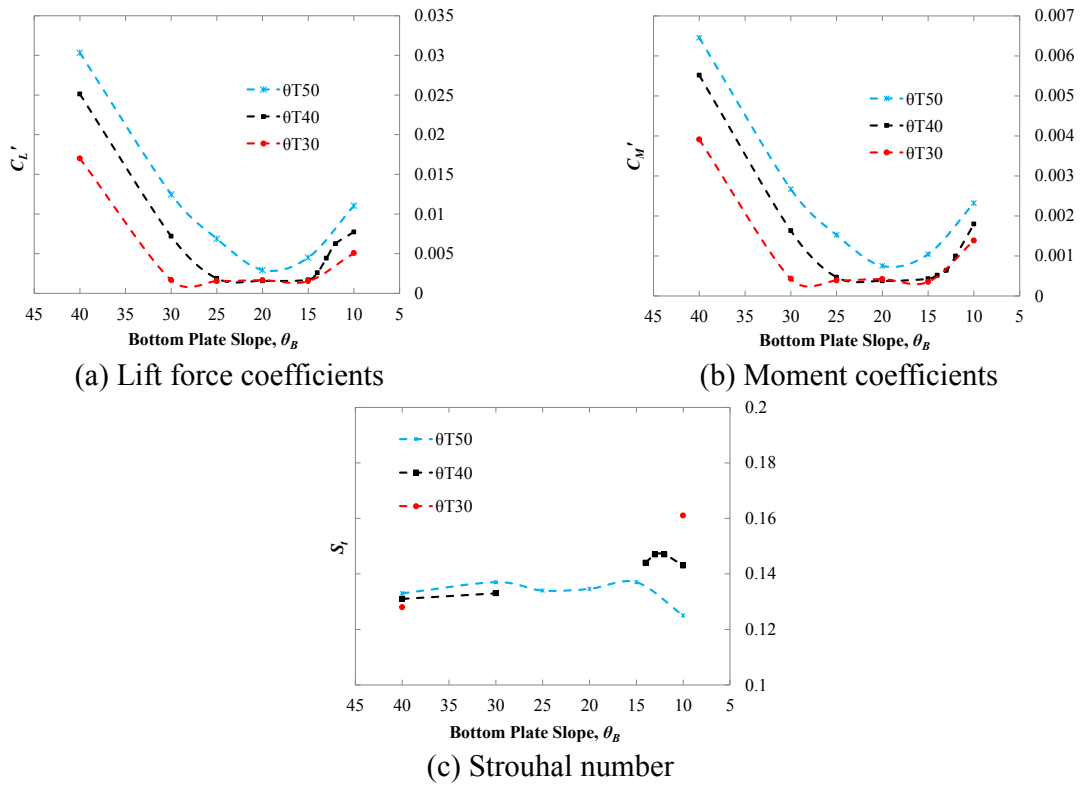


Figure 4.4: rms value of steady state force coefficients and Strouhal number

range of slopes, the drag is less and rms values of steady state force coefficients are the least. In this section we found some trends in results and it is important to explore more in details to understand the responses.

We selected four shapes of fairing for elaborate analysis: i) $\theta_T40-\theta_B40$ ii) $\theta_T40-\theta_B20$ iii) $\theta_T40\theta_B10$ and iv) $\theta_T30-\theta_B10$. For the first three shapes, the top plate slope is same, yet the bottom plate slope decreases gradually. These three sections would explain why the aerodynamic response in Figs.4.3 and 4.4 decrease first then increase again for decreasing bottom plate slope (θ_B). In last two sections, the bottom plate slope (θ_B) is same, yet the top plate slope (θ_T) decreases. By comparing among them it would be clear that why smaller top plate slope has lesser aerodynamic response.

The after-body velocity fluctuations are plotted to in Fig.4.5. The after-body velocity fluctuation provides information regarding the strength of the after-body vortex shedding (Nakamura and Ohya 1984). As can be seen that the velocity fluctuations also shows the similar trend we found in rms value (Fig.4.4). Large fluctuation can be found for $\theta_T40-\theta_B40$, then the fluctuation decreases for $\theta_T40-\theta_B20$ and the fluctuation increases again for $\theta_T40-\theta_B10$. For $\theta_T40-\theta_B20$ the fluctuations is significantly lesser than the other cases and no clear shedding frequency was found for this section.

4.1.1.2 Pressure Distribution

The mean and rms value of surface pressure coefficients for the bridge deck are plotted in Fig.4.6. The pressure variations are plotted only for the selected shapes considered in previous section. As can be seen the top surface pressures are lesser affected as compared to the bottom surface pressure. If we observe the Fig.4.6(a) carefully, it provides us meaningful information. As the top and bottom plate slope (θ_B) decreases the top deck suction also decreases and take part in increasing the negative lift value (Fig.4.3(b)).

On the other hand, the variation of fairing shape affects the bottom surface pressure (Fig.4.6(b)) both at the leading and trailing edge side. At the bottom surface, the leading edge toe is mainly affected by the variation of fairing shape. Large cavity zone appears for $\theta_T40-\theta_B40$ and the location of maximum suction shifts gradually towards the leading edge nose as the bottom plate slope (θ_B) decreases. This kind of leading edge cavity zone is responsible for generating small bubbles, after generation, this bubbles are advected to the downstream and coalescences with the downstream vortexes (Pullin and Perry 1980; Bruno and Mancini 2010; Bruno *et al.* 2010). From

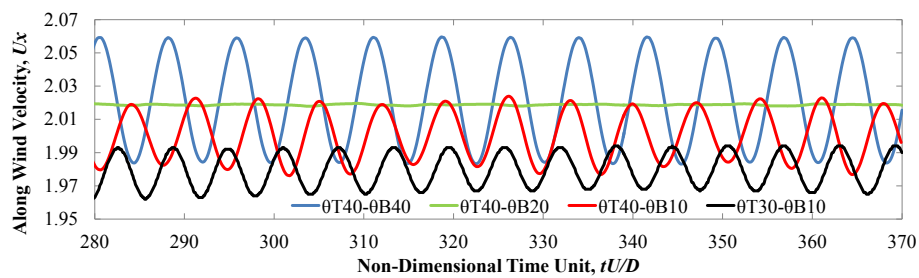


Figure 4.5: After-body velocity fluctuations for selected shapes of fairing. Velocity fluctuations were measured at the point, 1D downstream and 1D down from the trailing edge bottom corner of the bridge deck

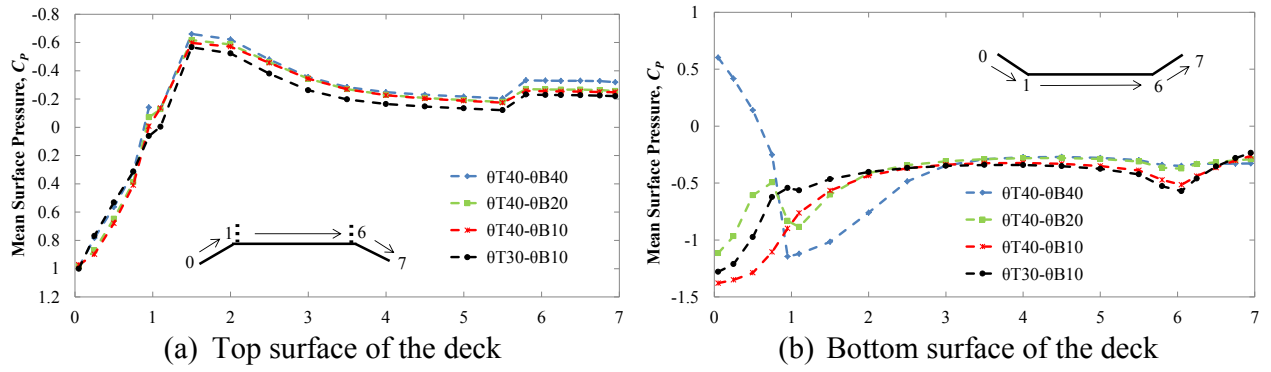


Figure 4.6: Mean surface pressure distribution around the bridge deck

aerodynamic stability point of view, this cavity zone should be as small as possible. However, the another reason behind the negative lift value in Fig.4.6(b) is mainly due to this type of leading and trailing edge suction. For example, for $\theta_T40-\theta_B40$ has the lowest suction and therefore experiences the lowest negative lift value.

The boundary layer velocity profile at the trailing edge for $\theta_T40-\theta_B10$ and $\theta_T30-\theta_B10$ in the vertical plane is plotted in Fig.4.7 for further understanding the trend in results we found in Fig.4.3. Fig.4.7 clearly shows the formation of boundary layer. If we compare Fig.4.6(b) and Fig.4.7, we can easily realize that higher suction has higher velocity. This kind of physics of the flow is not surprising if we see the Bernoulli equation. Due to the variation of velocity, the advection of flow is also affected and thereafter affects the Strouhal number (S_t). If we see in Fig.4.7, $\theta_T30-\theta_B10$ has higher shear layer velocity than $\theta_T40-\theta_B10$, therefore the flow moves faster and Strouhal number (S_t) for $\theta_T30-\theta_B10$ becomes higher than $\theta_T40-\theta_B10$.

Similarly, the drag behavior can also be explained partially based on this kind of physics. If we consider the boundary layer height in Fig.4.7 and compare with the corresponding drag value in Fig.4.3(a), we can easily find a trend that drag increases as the boundary layer become thicker. For example, $\theta_T40-\theta_B10$ has the thicker boundary layer; therefore it experiences the higher drag. While for $\theta_T30-\theta_B10$ has the lower drag as its boundary layer is thinner. The moment value in Fig.4.3(c) is primarily controlled by the pressure distribution on the bottom surface. When the bottom plate slope

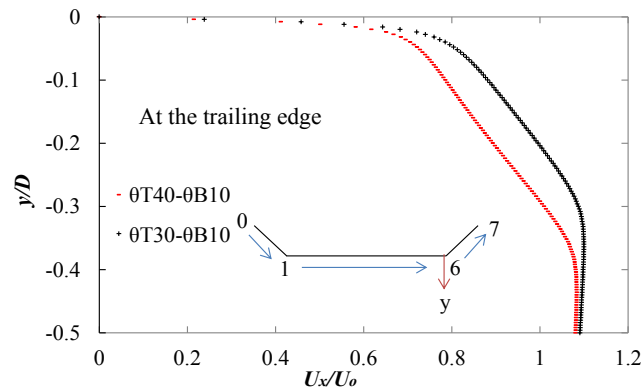


Figure 4.7: Boundary layer velocity profile at the trailing edge

(θ_B) decreases, the nose of the fairing goes down and the bottom surface leading edge suction increases (Fig.4.6(b)). As a result, the positive moment (anti-clockwise) tendency of the bridge deck increases gradually as the bottom plate slope (θ_B) decreases.

The rms value of surface pressure is an important parameter and provides information regarding the general dynamic behavior of the bridge deck. The rms value of the surface pressure is plotted in Fig.4.8. Both the top and the bottom surface rms value of pressures are highly influenced by the change in fairing angles. For mean pressure distribution the bottom surface leading edge was important while for rms pressure both the top and the bottom surface trailing edge are important. This implies that the rms value is mainly affected by the after-body vortex shedding behavior. In the next section, the velocity distributions are plotted and tried to understand the mechanism of aerodynamic response in a better way.

4.1.1.3 Velocity Distribution

From the previous section, we comprehended that the rms value is mainly affected by the after body vortex activity. Here, we plot the instantaneous flow field for the selected fairing sections. Fig.4.9 shows the instantaneous flow fields for θ_T40 - θ_B40 section along one lift cycle. For this type of section there are a number of important flow features. The leading edge top and bottom surface separation and the trailing edge bottom deck surface separation. When large bottom plate slope ($\theta_B=40^\circ$) is utilized then large leading edge top surface cavity zone appears and vortices shed at the trailing edge due to trailing edge flow separation.

In Fig.4.9(a), the V1 vortex is forming and the V2 vortex is moving away from the deck at the mid-deck height location. Therefore, the deck experiences mean lift force. Then, the V2 vortex disappears completely and V1 becomes larger; as a result the deck experiences the maximum lift force. After that, the upper V1 vortex disappears, yet the V2 becomes mature by this time. Therefore, the deck experiences the minimum lift force, then the cycle moves to Fig.4.9(a) again and goes on. For this section, V1 vortex creates an alternating vortex shedding cycle with V2 vortex. Due to this trailing edge after-body vortex shedding, the rms pressure was affected and shows higher value at the trailing edge.

For θ_T40 - θ_B20 the lift fluctuations was completely random and the amplitude of fluctuation was almost zero as we showed earlier, hence we plot the velocity distribution for two extreme

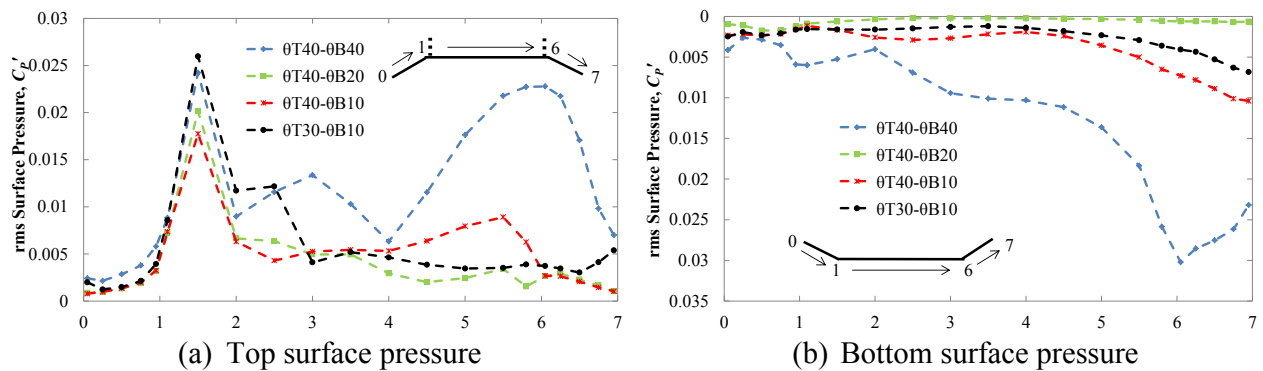


Figure 4.8: rms value of surface pressure around the bridge deck

instances of lift value in Fig.4.10. As can be seen from the figure both the leading edge cavity size and trailing edge separation decrease and the V2 vortex forms far away from the body. However, the V2 vortex can't create vortex cycle with the V1 vortex as the size of the V2 vortex is quite small as compared to the V1 vortex. As a result there is almost no fluctuation of surface of pressure at the trailing edge of the bridge deck. On the other hand, for $\theta_T 40-\theta_B 10$ (Fig.4.11) as the bottom plate slope decreases the nose of the fairing goes further down and the top plate length increases. As a result the V2 vortex forms on the top fairing plate and creates vortex cycle with the V1 vortex. These closely formed vortices increase the rms value of the pressure and velocity again.

Now, finally if we compare between $\theta_T 40-\theta_B 10$ (Fig.4.11) and $\theta_T 30-\theta_B 10$ (Fig.4.12), in case of $\theta_T 30-\theta_B 10$ as the top plate slope decreases the nose goes up. Therefore, the V2 vortex doesn't have enough room to form on the top plate and the interaction of V2 vortex decreases with the deck. Moreover, the size of the V2 vortex also decreases. As a result $\theta_T 30-\theta_B 10$ experiences smaller rms value of pressure and global parameter as compared to the $\theta_T 40-\theta_B 10$. Further, As the top plate slope (θ_T) decreases, the leading edge top surface separation also decreases and increases the negative lift value (Figs.4.3(b) and 4.6(a)).

From the above discussion we understand the mechanism behind the steady state responses we obtained earlier. We found some specific fairing shapes ($\theta_T 40-\theta_B 25$, $\theta_T 40-\theta_B 20$, $\theta_T 30-\theta_B 25$ and $\theta_T 30-\theta_B 15$) have better aerodynamic responses when perforated handrail is attached. However, in practical bridges not only perforated but also solid handrails are attached and curbs are not placed at the side

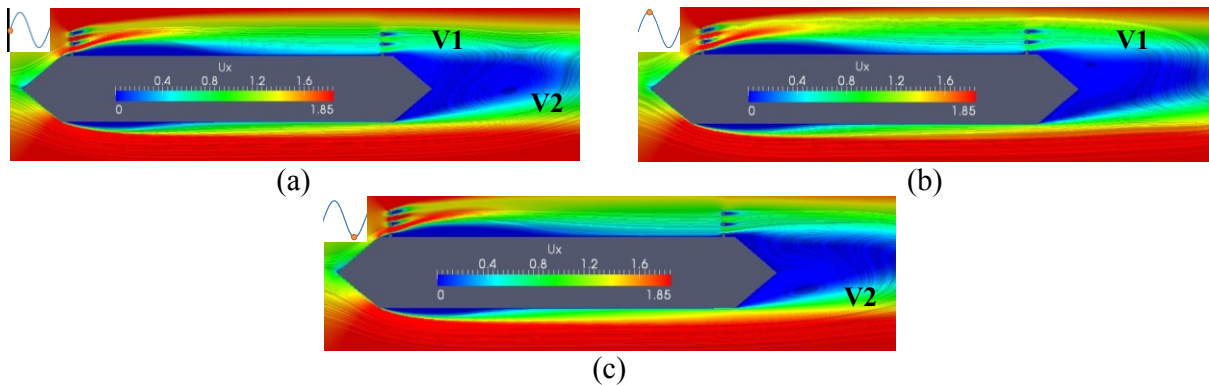


Figure 4.9: Instantaneous velocity field for $\theta_T 40-\theta_B 40$ along one lift cycle at 0° (a), 90° (b) and 270° (c)

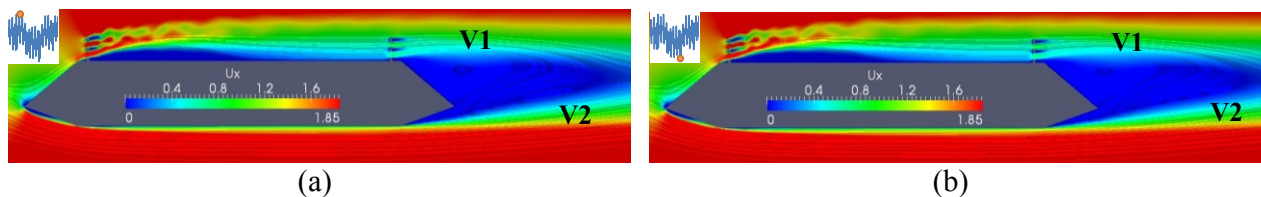


Figure 4.10: Instantaneous velocity field for $\theta_T 40-\theta_B 20$ for maximum (a) and minimum (b) value of lift

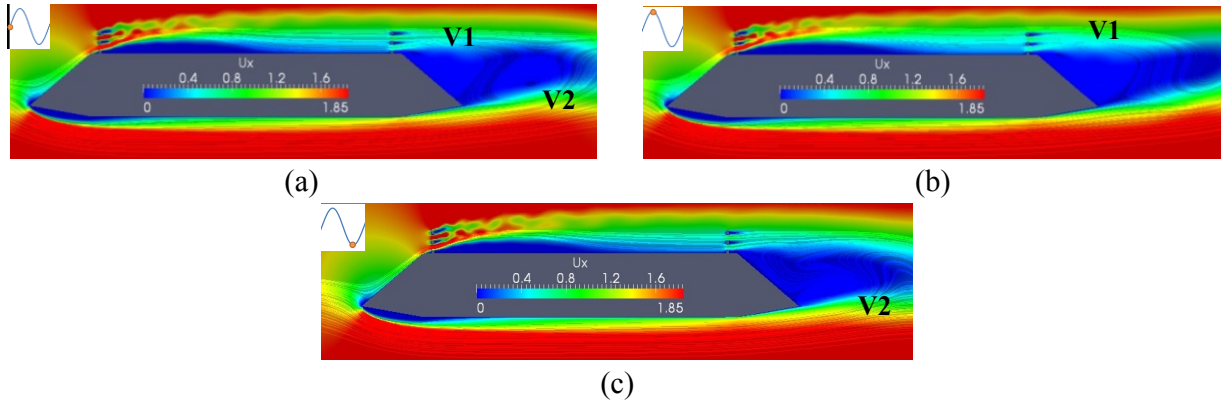


Figure 4.11: Instantaneous velocity field for $\theta_T 40^\circ$ - $\theta_B 10^\circ$ along one lift cycle at 0° (a), 90° (b) and 270° (c)

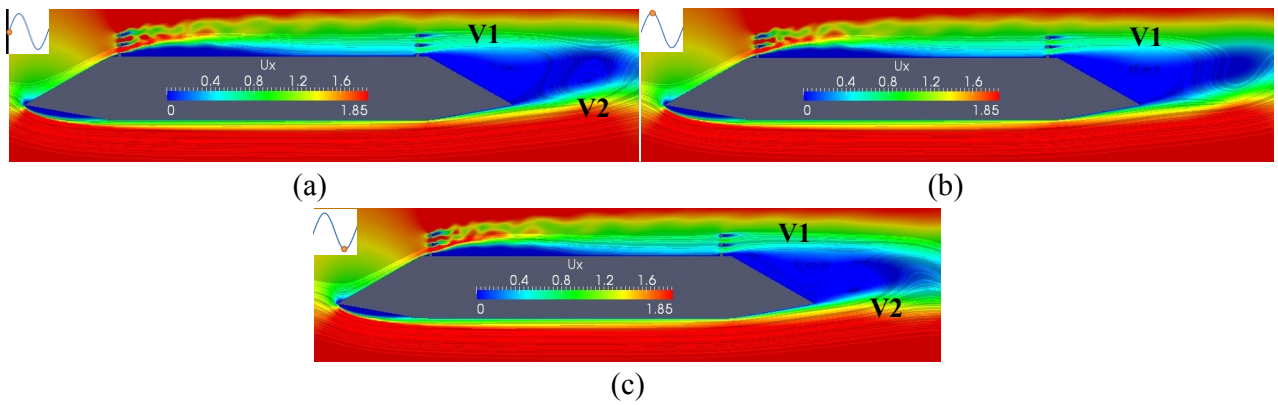


Figure 4.12: Instantaneous velocity field for $\theta_T 30^\circ$ - $\theta_B 10^\circ$ along one lift cycle at 0° (a), 90° (b) and 270° (c)

of the bridge deck. We found some trends in results for various top (θ_T) and bottom (θ_B) plate slopes. Therefore, it is important to know how the variation of solidity ratio of handrails influences the trend in the results. In the following section, a comparison is made between the aerodynamic response of solid, perforated handrail with and without curb cases.

4.1.2 Influence of Handrail Types

In practical bridges along with the perforated handrails, solid handrails are also attached and often perforated handrails are used with the curb at the side of the deck. We already have demonstrated the responses under perforated handrail in the previous section. In this section, we show how the response of bridge deck is influenced when various types of handrail are utilized. Fig.4.13 illustrates various handrails adopted for investigation. The handrails had a solidity ratio of 100% (Fig.4.13(a)), 40% (Fig.4.13(b)) and 30% (Fig.4.13(c)). The Simulations were carried out only for top plate slope

(θ_T) of 40° and bottom plate slope (θ_B) was varied from 10° to 40° . Fig.4.14 shows the mean value of steady state force coefficients and rms value of lift force coefficients as the drag and the moment have almost similar trend in results.

Fig.4.14 depicts that the solid handrail has significantly higher response than the others. As the solidity ratio of the handrail decreases the aerodynamic behavior improves and the perforated handrails without curb shows the lowest aerodynamic responses. However, the most important information is, the trend in the result we found in the last section due to variation of bottom plate slope (θ_B) remains almost same for any type of handrail. Fig. 4.15 displays the flow field in terms of

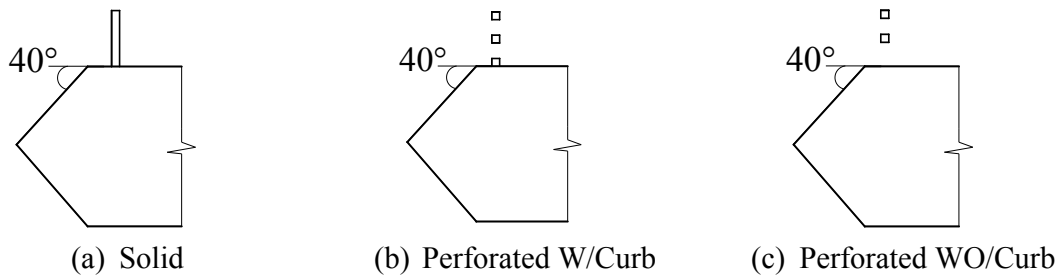


Figure 4.13: Various of types handrails utilized for investigation

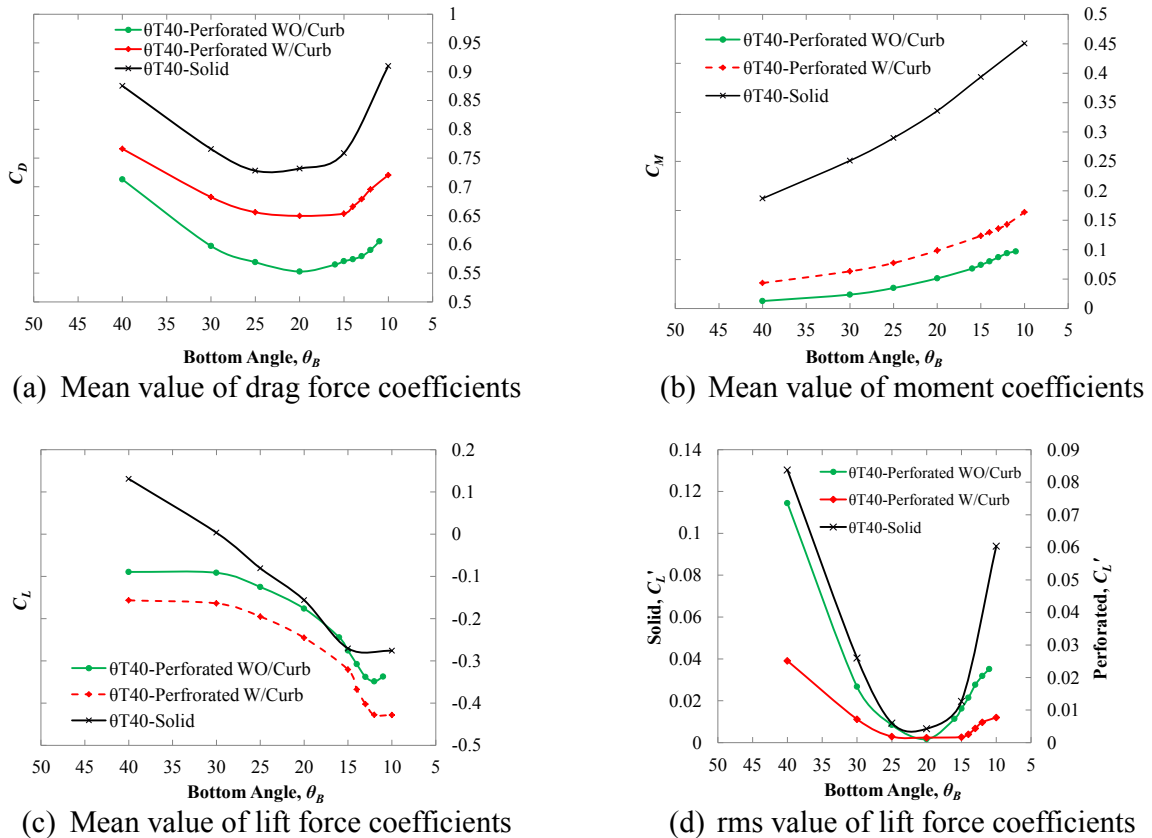


Figure 4.14: Influence of handrail types on steady state force coefficients

streamlines and wind speed ratio around the bridge deck with a bottom plate slope (θ_B) of 20° as it possess better aerodynamic responses. The solid handrail case possess very large vortex on the top deck surface. Both of the perforated cases with and without curb, experience the vortices at the trailing edge of the deck only. Therefore, the perforated cases experience lower fluctuation of aerodynamic coefficients as compared to the solid one. Further, as the solidity ratio of the handrail decreases, the wake size decreases significantly and thereafter decrease the drag. If a relative comparison is made among the flow fields in Fig.4.15, it can be deduced that the deck with the perforated WO/Curb experiences the least flow separation with the smallest wake. As the trend in the results remains almost same for any type of handrails, for the remaining part of the investigation we used perforated handrail WO/Curb as modeling is easier and accuracy of the numerical results enhances due to less flow separation.

4.1.3 Influence of Nose Location

Exclusively for edge fairing, the same sets of top and bottom plate slope can be set with in nose up or nose down situation. Fig.4.16 illustrates schematically the variation of nose location. Therefore, depending on the nose location, the aerodynamic response may also be affected. To know the influence of nose location, we conducted one more set of simulation for a fixed bottom plate slope (θ_B) of 40° by changing the top plate slope (θ_T) from 25° to 11° and compared with the result shown in the last section for reverse combination of slopes i.e., the top plate slope (θ_T) was 40° and the bottom plate slope (θ_B) was varied from 25° to 11° .

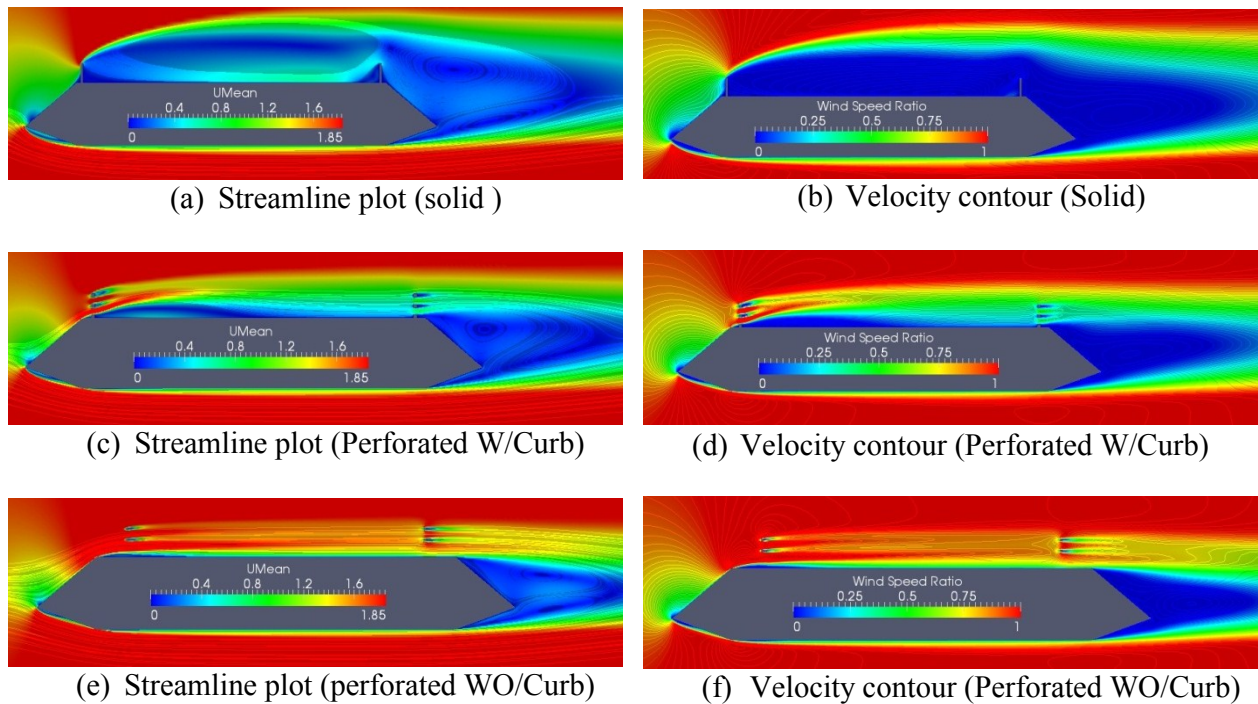


Figure 4.15: Comparison of time averaged flow field distribution around the bridge deck ($\theta_T 40^\circ - \theta_B 20^\circ$) for different handrail type

The mean value of steady state force coefficients and the rms value of lift force coefficients are plotted in in Fig.4.17 for the nose down (θ_T of 40°) and nose up (θ_B of 40°) shape of fairings. By observing Fig.4.17, it can be assured that the responses vary quite noticeably when the nose location changes. Both the mean value of drag force (C_D) and rms value of lift force (C_L') increase as the nose goes up. On the other hand, both the lift (C_L) and moment (C_M) force change the sing. Except magnitude, the direction of moment force doesn't bear any significance from aerodynamic point of view. However, the direction of lift force is important for long-span cable-supported bridges. A positive value of lift force is always alarming for the bridge deck as it pushes the deck upward, the cable tension decreases, decreasing the stiffness of the bridge system and makes the bridge

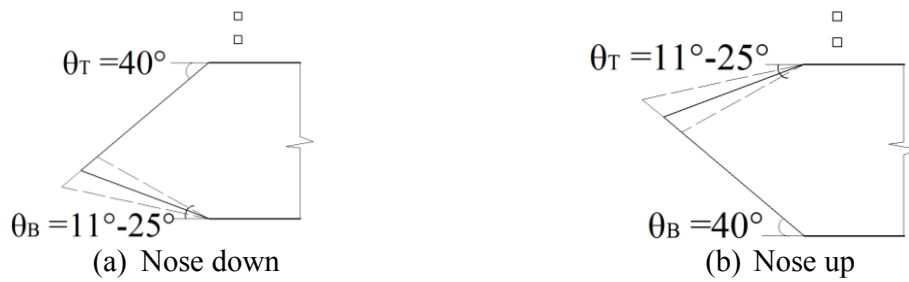


Figure 4.16: The concept of nose location in edge fairing and the range of top and bottom plate slope used for investigation

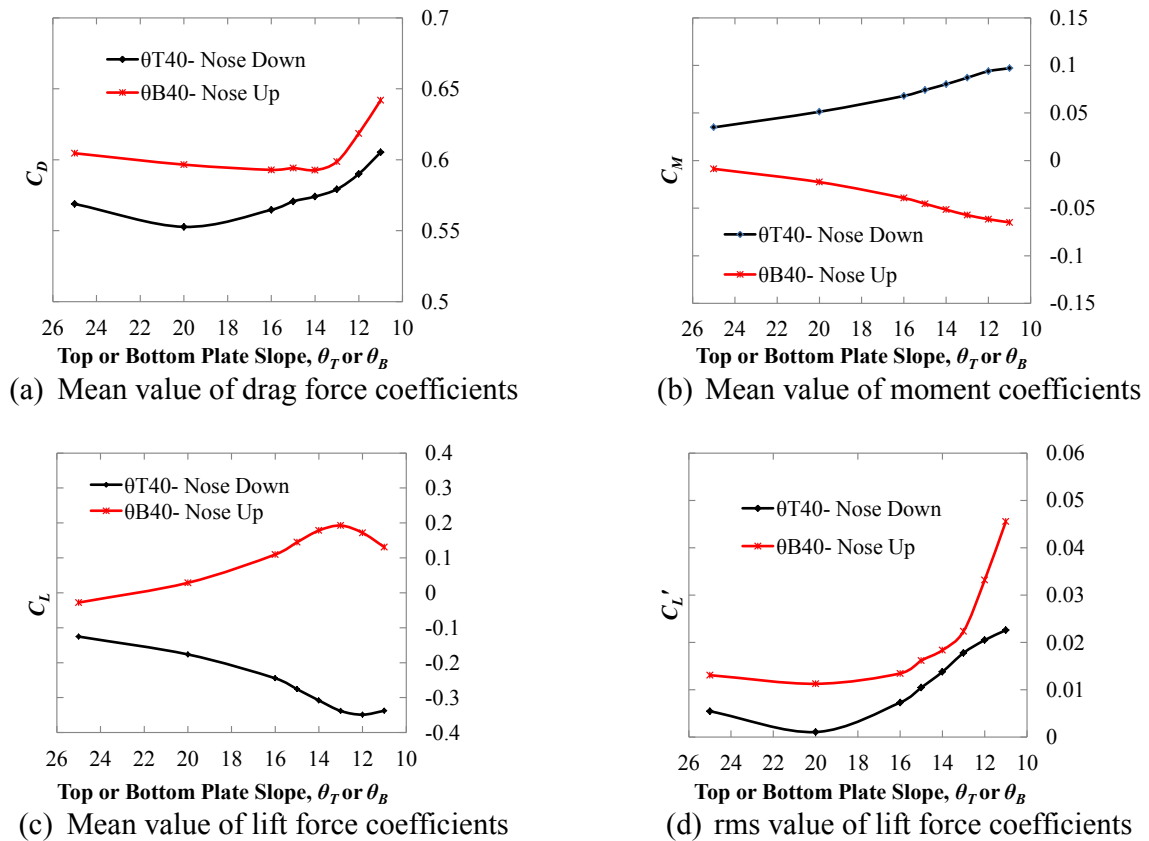


Figure 4.17: Influence of nose location on steady state force coefficients

vulnerable against wind.

Based on the observed aerodynamic response it can be said that the nose down position of fairing possess better aerodynamic behavior than the nose up position. The most critical response would be the mean value of the lift force coefficient (C_L). Fig.4.18 compares the wind speed ratio between two decks: i) $\theta_T40-\theta_B20$ (Nose down) and ii) $\theta_T20-\theta_B40$ (Nose up). The flow field looks almost identical except the leading edge separation alters the location of formation. Interestingly, in case of nose up situation the leading separation forms at the bottom deck surface and increases the downward force, yet the lift shows positive values. Basically, the reason of positive lift value lies behind the velocity of the boundary layer flow. When the nose goes up, the deck top surface becomes flatter than the bottom surface and the flow moves much faster. Fig.4.19 shows the mid-section velocity distribution at the vertical plane. As can be seen when the nose goes up, the top deck boundary layer velocity increases than the nose down situation, decreasing the pressure and increasing the upward force. In case of nose down situation reverse mechanism happens.

4.2 Behavior of Streamlined Bridge Deck

Streamlined bridge deck is one of the popular deck shapes adopted for long-span cable-supported bridges. Fig.4.20 shows two practical applications of streamlined bridge decks in long-span cable-

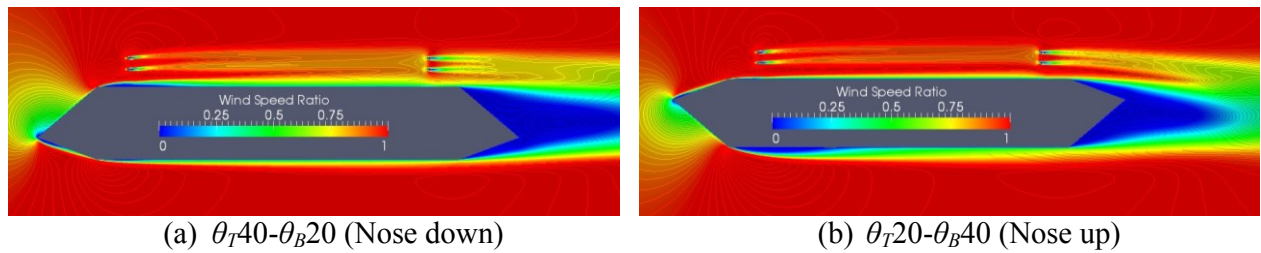


Figure 4.18: Influence of nose location on mean wind speed ratio around the bridge deck

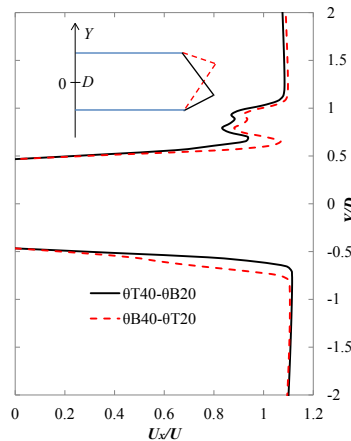
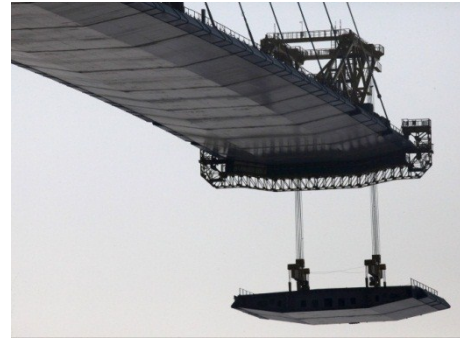


Figure 4.19: Influence of nose location on boundary layer at the mid deck width



<http://www.cpic.de/en/project.php>

(a) Nanjing No.2 Yangtze Bridge



http://russiaprofile.org/photos/52678_7.html

(b) Russky Bridge

Figure 4.20: Application of streamlined bridge deck for practically constructed bridges

supported bridges. In case of streamlined deck, a portion of the bottom deck plate is inclined and a much smaller fairing is attached at the side of the bridge deck that saves substantial amount of material cost. An edge fairing can be transformed into a streamlined deck by shifting the lower edge corner towards inward as shown in Fig.4.21. Therefore, we can combine edge fairing and streamlined deck by a new parameter as introduced earlier in Chapter-2 is the width ratio (W).

We already have discussed in the introduction chapter about the past investigations regarding this kind of deck. Previously only wind tunnel investigation was carried out for investigation the bottom plate slope (θ_B) effects on aerodynamic responses. Wang *et al.* (2009) found that the flutter wind speed increases significantly for a bottom plate slope (θ_B) smaller than 16° and later Larsen and Wall (2012) found that vortex induced vibration disappears for a bottom plate slope around 14.8° . However, the steady state response and the flow field were not analyzed in detail for better understanding the aerodynamic responses for this type of bridge deck. Furthermore, depending on the width ratio (W) the aerodynamic response will also vary. Still a lot more to know about the aerodynamics of the streamlined deck, the influence of bottom plate slope (θ_B), the influence of width ratio (W), the influence of side ratio (R) and the influence of Reynolds number (Re_B) etc. These aspects are discussed sequentially in the following sections.

4.2.1 Influence of Width Ratio (W)

In this section, we present detailed investigation results for the streamlined bridge deck with different width ratios (W). The simulations were conducted at a Reynolds number of 6.0×10^4 same as

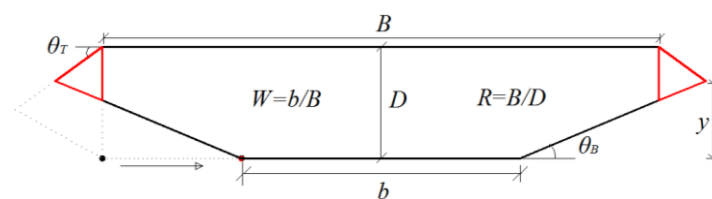


Figure 4.21: Difference of streamlined deck from edge faring and various important notations

the previous analyses to make the comparison rational. Four width ratios (W) 1, 0.7, 0.5 and 0.3 were considered for simulations as shown in Fig.4.22. For each of these width ratios (W), the bottom plate slope (θ_B) was varied from 25° to 11° , and the top late slope (θ_T) was kept fixed at 40° . First the influence of width ratio (W) and bottom plate slope (θ_B) on steady state force coefficients were investigated. Then, the flow fields were analyzed for detecting important flow features and explaining the aerodynamic responses.

4.2.1.1 Steady State Force Coefficients

Fig.4.23 summarizes the mean steady state force coefficients for various width ratios (W). The mean value changes a lot both for the bottom plate slope (θ_B) and width ratio (W). The trend in the results for the lift and moment remain same as like edge fairing ($W=1$) due to variation of bottom plate slope (θ_B), yet the drag shows different trend depending on the width ratio (W). For any value of width ratios (W), the lift decreases and moment increases as the bottom plate slope (θ_B) decreases. On the hand, for drag force, the minimum drag value can be obtained at a large bottom plate slope ($\theta_B=20^\circ$) for large width ratio ($W=1$), yet for smaller width ratio ($W<1$) the minimum drag position sifts gradually towards smaller bottom plate slope (θ_B). However, one trend is obvious that the magnitude of all the force and moment coefficients decreases at small bottom plate slopes ($\theta_B \leq 15^\circ$) for any value of width ratio (W) smaller than 1.

The sensitivity of the aerodynamic response increases as the width ratio (W) decreases. For example, in case of edge fairing ($W=1$) the response varies nominally as the bottom plate slope (θ_B) changes, yet for small width ratio ($W=0.5$ or 0.3) the response alters quite well. Basically, as the width ratio (W) decreases the length of the bottom plate slope increases and their influence on aerodynamic response increases too.

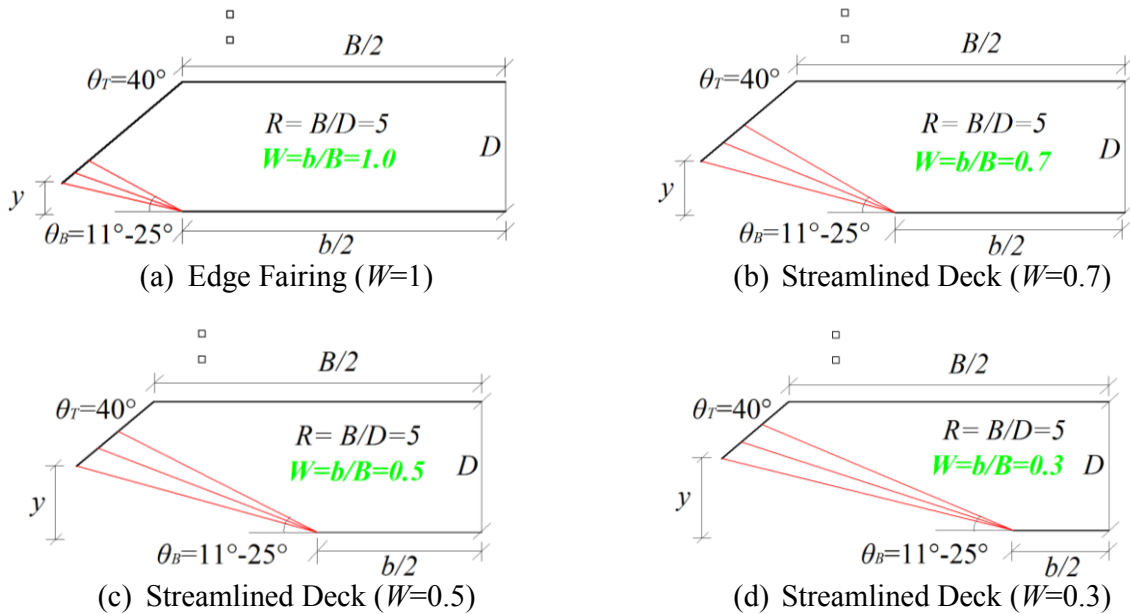


Figure 4.22: Cross-sectional details of the streamlined decks employed for investigation

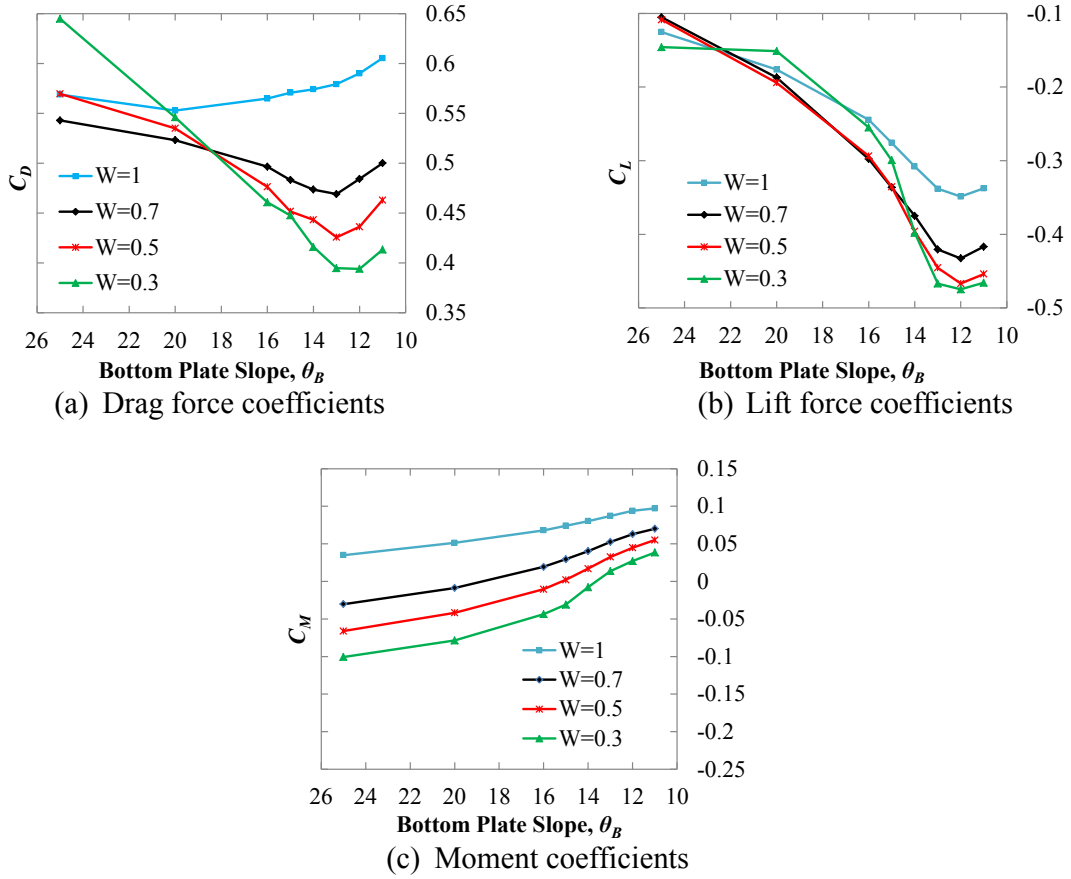


Figure 4.23: Influence of bottom plate slope (θ_B) and width ratio (W) on mean value of steady state force coefficients

A careful observation in Fig. 4.23 explains that there are two distinct zones of bottom plate slope (θ_B) and exhibits similar but opposite trends in results. First one is the, large bottom plate slope zone ($\theta_B=25^\circ-20^\circ$) where aerodynamic responses increases as the width ratio (W) decreases. Another one is the small bottom plate slope ($\theta_B=15^\circ-11^\circ$) zone and the aerodynamic responses decreases as the width ratio (W) decreases. After analyzing static responses, next we examined the rms value of the steady state force coefficients and the Strouhal number (S_t).

The rms value of lift force (C_L) and moment (C_M) coefficients along with the Strouhal number (S_t) are plotted in Fig.4.24. The rms value of the steady state force coefficients also show similar trend in results like the mean value of drag (Fig.4.23(a)) as discussed earlier. For large bottom plate slope ($\theta_B=25^\circ-20^\circ$) the rms value increases and for small bottom plate slope ($\theta_B \leq 15^\circ$) the rms value decreases with the decrease in width ratio (W). Moreover, as the width ratio (W) decreases much wider range of bottom plate slope (θ_B) experiences the least rms value.

However, the strouhal number (S_t) doesn't show any definite trend for large bottom plate slope ($\theta_B=25^\circ-20^\circ$), yet for small bottom plate slope ($\theta_B \leq 15^\circ$) the Strouhal number (S_{tB}) increases with the decreases in width ratio (W). The possible explanation could be, as the width ratio (W) decreases, the shape becomes more streamlined and the shedding the frequency (f_v) increases, increasing the strouhal number (S_t). In the following section the surface pressure distribution of selected shapes are explored for better understanding the response we found in this section.

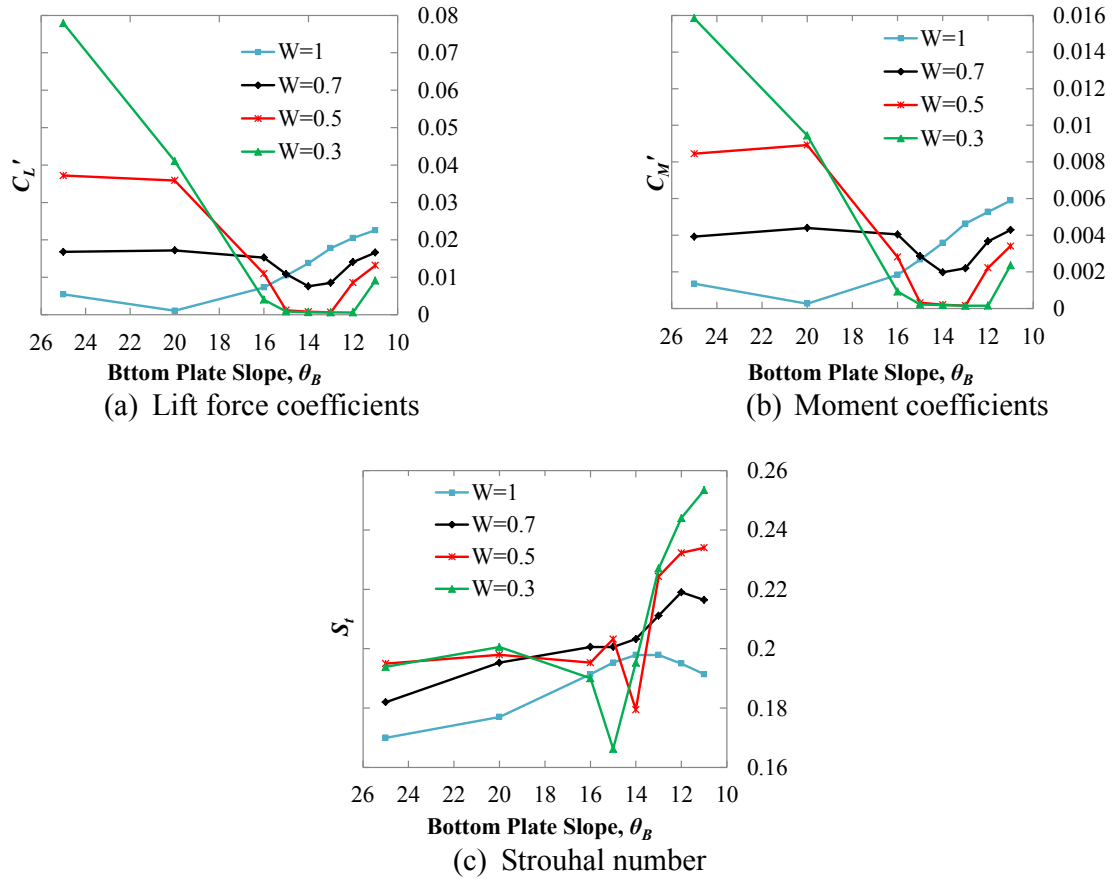
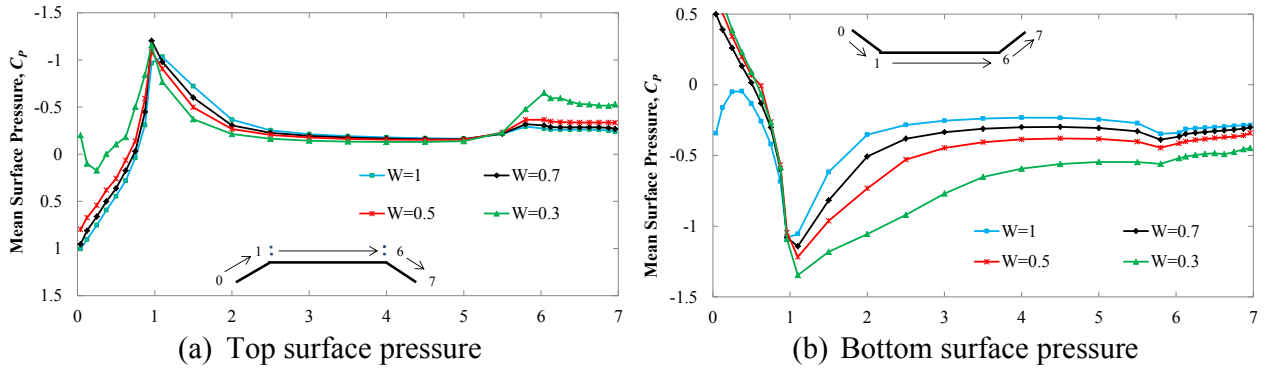
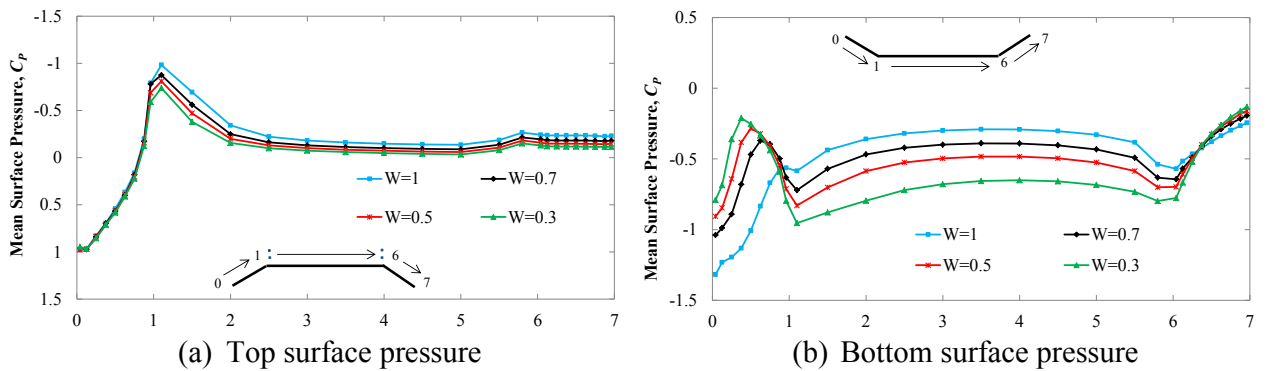


Figure 4.24: Influence of bottom plate slope (θ_B) and width ratio (W) on rms value of steady state force coefficients and the Strouhal number

4.2.1.2 Pressure Distribution

Base on previous investigation we selected two bottom plate slopes from two distinct zones : i) θ_B of 25° and ii) θ_B of 12° for detailed pressure field analysis. The surface pressure distributions of bottom plate slope (θ_B) of 25° and 12° are summarized in Figs. 4.25 and 4.26, respectively for all four width ratios (W). Both of these bottom plate slopes (θ_B of 25° and 12°) have similar pressure distribution except variation in magnitude and rather than the bottom surface the top surface pressure distribution is more influential. The large bottom plate slope (θ_B of 25°) experiences larger suction at the leading edge top and bottom deck surface than the small bottom plate slope (θ_B of 12°).

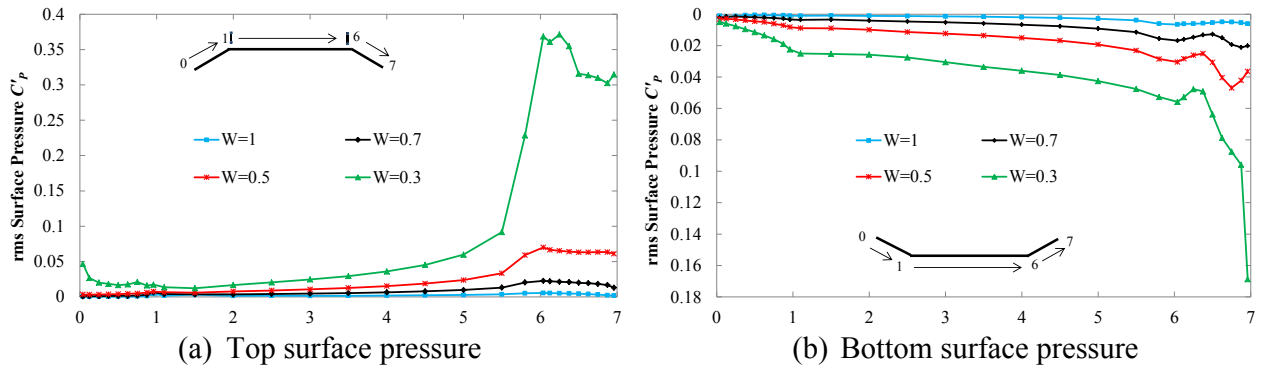
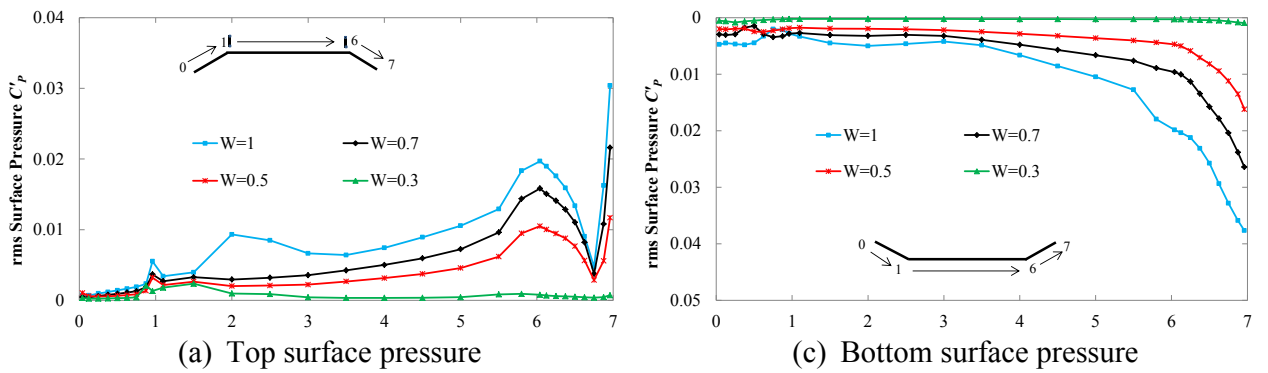
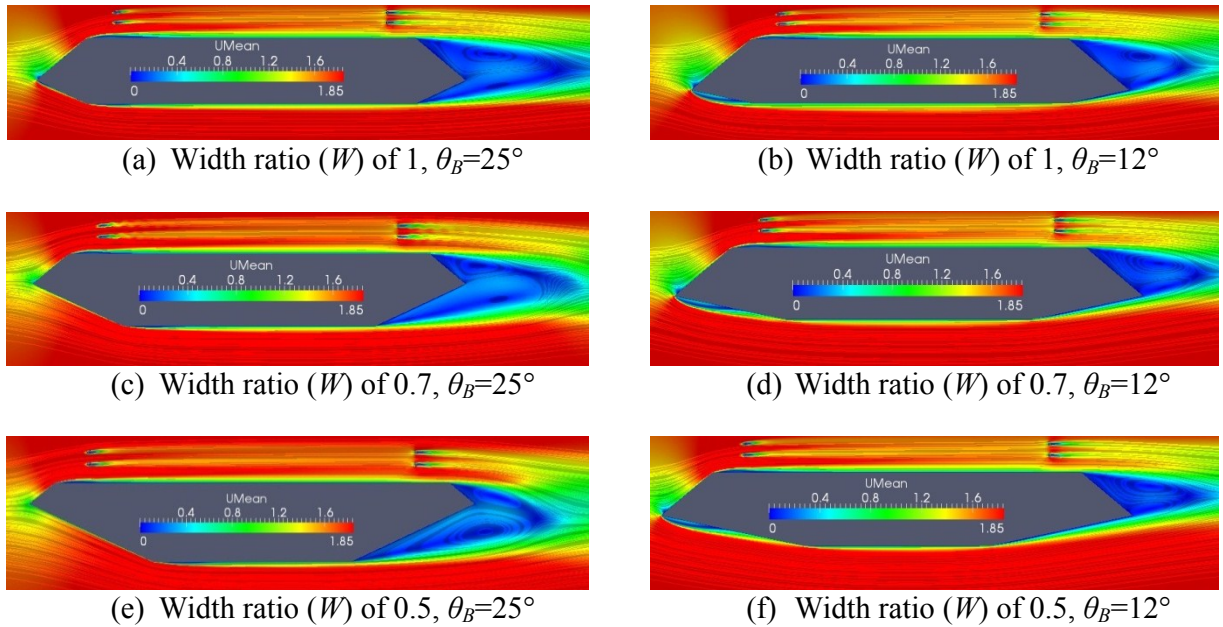
Based on Figs.4.25 and 4.26, the lift characteristics we found in Fig.4.23(b) can be explained well. For any value of bottom pate slope (θ_B of 25° and 12°), as the width ratio (W) decreases the bottom deck suction increases dramatically and increases the negative lift value. Further, in case of small bottom plate slope (θ_B of 12°), smaller pressure recoveries occur at the bottom deck trailing edge side as compared to the large bottom plate slope and resulting higher negative lift for small bottom plate slope (θ_B of 12°) than the large bottom plate slope (θ_B of 25°).

Figure 4.25: Mean surface pressure distribution for bottom plate slope (θ_B) of 25° Figure 4.26: Mean surface pressure distribution for bottom plate slope (θ_B) of 12°

The rms value of surface pressure distributions are plotted in Figs.4.27 and 4.28 for bottom plate slope (θ_B) of 25° and 12° , respectively. The rms value of pressure also shows the similar characteristics we found in Figs.4.24(a) and (b) for large (θ_B of 25°) and small (θ_B of 12°) bottom plate slopes in relation to the width ratio (W). Like edge fairing, here also large rms value can be observed at the trailing edge side. We discussed earlier that the after-body vortex shedding activity is the main cause of large rms fluctuation of pressure at the trailing edge side. In the following section detailed flow field is analyzed.

4.2.1.3 Velocity Distribution

The time averaged velocity distribution for bottom plate slope (θ_B) of 25° and 12° are plotted in Fig.4.29 for selected width ratio (W). For all of these sections, flow separation can be noticed at the leading and the trailing edge side. However, trailing edge side flow separation governs over the leading edge side. In case of large bottom plate slope (θ_B of 25°) the bottom surface trailing edge separation is pronounced and increases as the width ratio (W) decreases. On the other hand, for small bottom slope (θ_B of 12°) there is no trailing edge separation. For small bottom plate slope (θ_B of 12°) the top surface trailing edge separation is curtail. However, as the width ratio (W) decreases the top surface trailing edge separation gradually decreases.

Figure 4.27: rms surface pressure distribution for bottom plate slope (θ_B) of 25° Figure 4.28: rms surface pressure distribution for bottom plate slope (θ_B) of 12° Figure 4.29: Comparison of time averaged velocity distributions around the bridge decks for bottom plate slopes (θ_B) of 25° and 12°

Based on this discussion we can explain the trend in results we obtained previously for drag (Fig.3.23(a)) and rms value (Figs.4.24(a) and (b)). For large bottom plate slope (θ_B of 25°) as the width ratio (W) decreases the nose of the fairing goes up and the bottom surface trailing edge separation increases, increasing the vortex activity and wake size. Therefore, for large bottom plate slope (θ_B of 25°) the drag and rms value of steady state force coefficients increases with the decrease in width ratio (W).

Similarly, for small bottom plate slope (θ_B of 12°) as the width ratio (W) decreases the nose of the fairing goes up decreasing the top surface trailing separation without any bottom surface trailing edge separation. As a result the wake becomes smaller at smaller width ratio (W) resulting decrease in drag and rms value of steady state force coefficients. However, for bottom plate slope (θ_B) of 12° , a width ratio (W) of 0.3 is required so that the nose location (y/D see Fig/4.21) becomes high enough and the top surface wake becomes less influential. There must be some margins of nose height (y/D), if the nose goes above that height the top surface wake becomes small and vortex becomes less influential when there is no trailing edge separation.

By take the curl of the velocity vector ($\nabla \vec{U}$), the vorticity distribution around the bridge deck can be obtained. Fig.4.30 shows the vorticity around the bridge deck for bottom plate slope (θ_B) of 14° and 12° . The nose locations (y/D) are indicated at the title of the corresponding figures. As can be seen for bottom plate slope (θ_B) of 14° no clear after-body vortex activity can be noticed when the nose height (y/D) reaches to 0.47 for the width ratio (W) of 0.5. However, for the same width ratio (W) the bottom plate slope (θ_B) of 12° has the nose height (y/D) of 0.42 and still shows clear after-

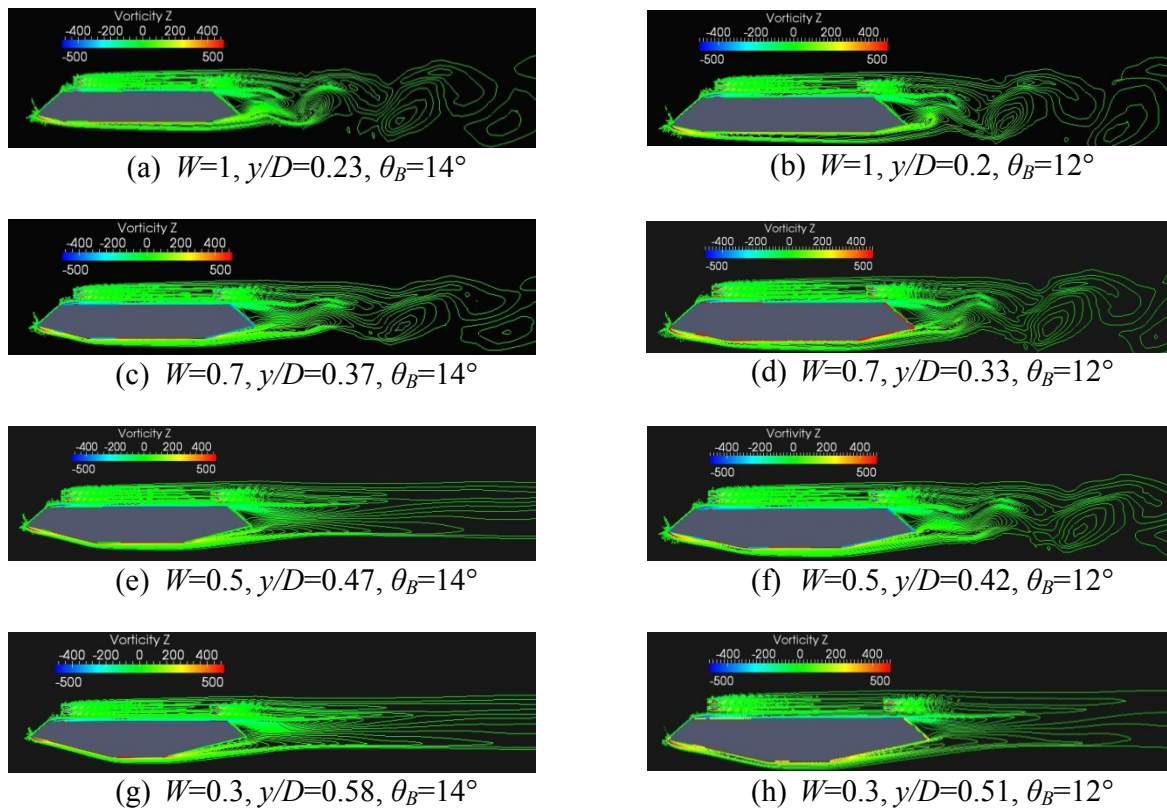


Figure 4.30: Comparison of Vorticity plot around bridge deck for bottom plate slopes (θ_B) of 14° and 12°

body vortices. As the width ratio decreases further ($W=0.3$), the nose height (y/D) increases to a value of 0.51 and the after-body vortex activity weakens. Therefore, we can presume that for smaller bottom plate slope ($\theta_B \leq 15^\circ$) i.e., the shapes without having the bottom surface trailing edge separation, nose should be tried to place on the upper half of the deck to obtain less aerodynamic forces and to reduce the after-body vortex activity.

Based on our analysis we found that for large width ratio ($W=1$) i.e., edge fairing, larger bottom plate slope ($\theta_B=20^\circ-25^\circ$) possess better aerodynamic response. However, for small width ratio ($W \leq 0.7$) i.e., streamlined deck, smaller bottom plate slope ($\theta_B \leq 15^\circ$) owns lesser aerodynamic responses. More precisely we would like to say that when the width ratio (W) decreases the bottom plate slope (θ_B) also required to be decreased to obtain better aerodynamic response.

Before constructing long-span cable-supported bridges, their decks are often investigated in wind tunnel for selecting the most appropriate configurations. Therefore, to justify our outcomes, we plotted the relationships between the width ratio (W) and the bottom plate slope (θ_B) in Fig.4.31(a) of practically constructed bridge we surveyed in chapter 2. Fig.4.31(a) clearly shows the positive slope of the plot i.e., as the width ratio (W) of the bridge deck decreases, the bottom plate slope (θ_B) decreases too.

Based on above mentioned discussion and understanding, the trend of top plate slope (θ_T) in practical bridges can also be predicted. The effectiveness of the top plate slope (θ_T) appears mainly by keeping the nose up and decreasing the vortex size on the top fairing. Therefore, in case of edge fairing, by decreasing the top plate slope (θ_T) aerodynamic performances can be improved as the nose goes (Shown already) upward. However, when the width ratio decreases, the nose of the fairing moves upward, as a result, the influence and applicability of top plate slope (θ_T) decreases. Hence, the trend of the top plate slope (θ_T) would be, for large with ratio ($W=1$) smaller top plate slope (θ_T) should be used and for small width ratio ($W \leq 0.7$) large top plate slope (θ_T) to reduce the size of the fairing from economic point of view. Fig.4.31(b) depicts the similar trend we predicted.

4.2.2 Influence of Side Ratio (R)

Previous all the simulations were conducted for a specific side ratio (R) of 5 and we got some trend in the results. Now it is important to explore does the trends in the result alters depending on the side ratio (R) or not. One new set of simulation was conducted for the bridge deck with a side ratio (R) of 8 and width ratio of (W) of 0.55. The top plate slope (θ_T) was set to 40° and the bottom plate slope (θ_B) was varied from 25° to 11° . The Reynolds number was kept same as the previous sections.

Fig.4.32 presents the important force coefficients for side ratio (R) 5 and 8. The results of side ratio (R) of 8 are compared with side ratio (R) of 5 with a width ratio (W) of 0.5. As can be seen from the figure the trend in the results remains almost unchanged when the side ratio (R) alters from 5 to 8 for the same width ratio (W). It should be also noted that even though the width ratio is same the nose locations are different from the same bottom plate slopes (θ_B). However, as we can notice from the figure the variation of the nose location doesn't affect the trend in results.

Therefore, the results we presented in the last section for side ratio (R) of 5 with various width ratios (W), can be utilized for explaining the response of the bridge deck with higher side ratio (R) by

maintaining similarities in width ratio (W). Fig.4.33 compares the time averaged velocity field around the bridge decks for a bottom plate slope (θ_B) of 14° . The bridge deck with side ratio (R) of 8 possess a bit smaller wake as compared to the side ratio (R) of 5 as the nose goes up for higher side ratio (R), yet the overall flow behavior is quite similar.

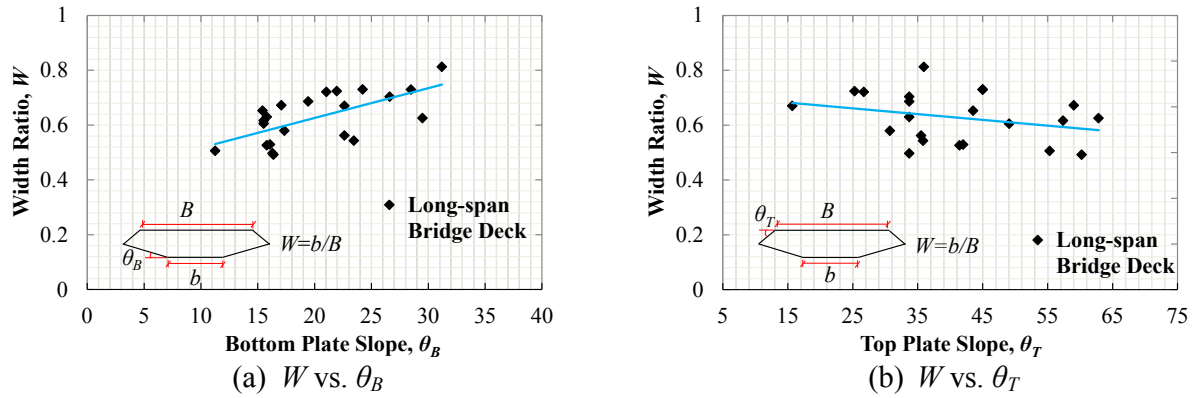


Figure 4.31: Relationship between the width ratio (W) and the inclined plate slopes (θ_B and θ_T) of practically constructed streamlined bridge decks

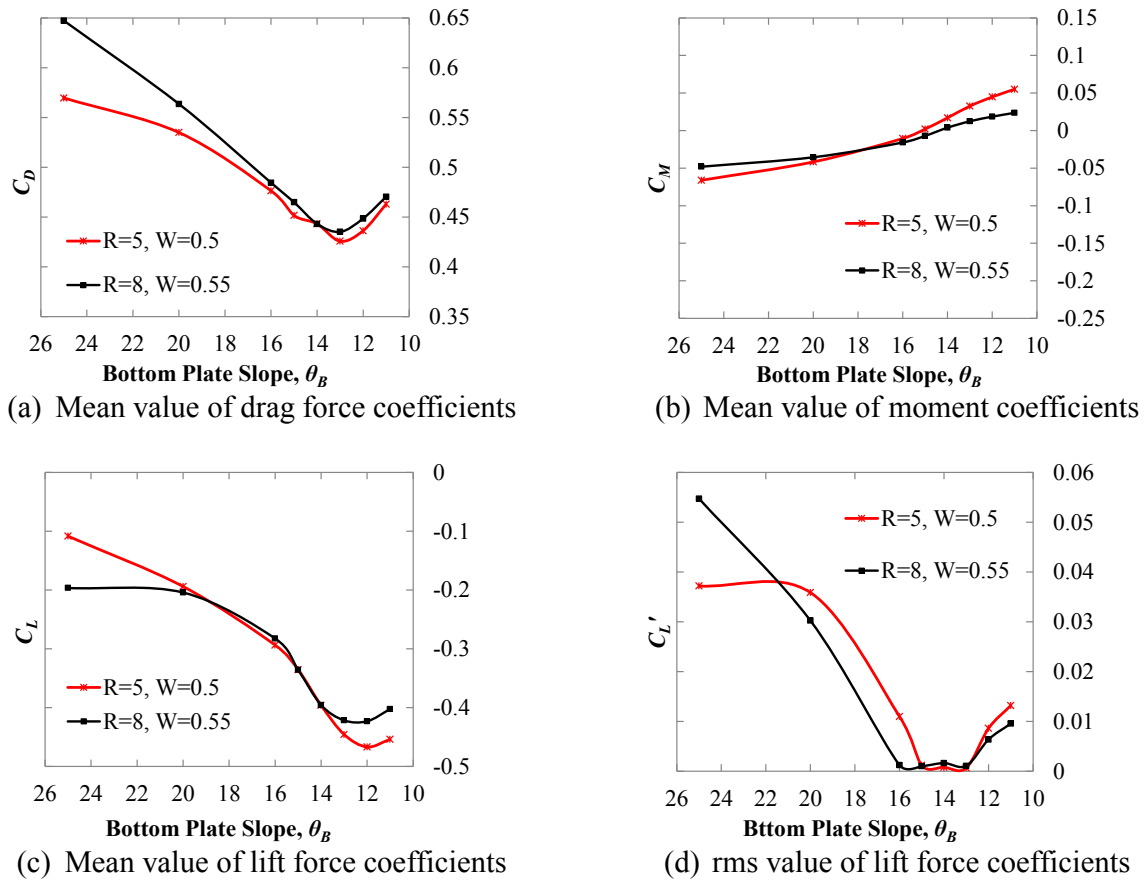


Figure 4.32: Influence of side ratio (R) on steady state force coefficients

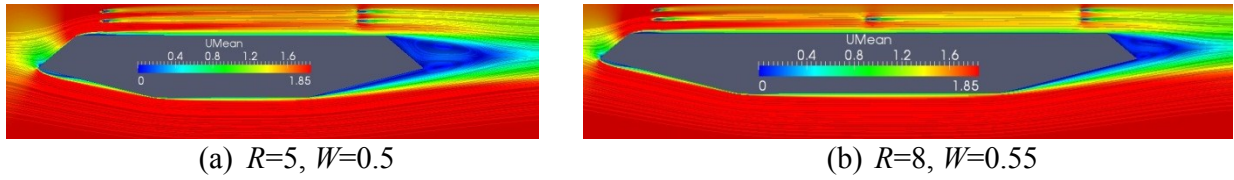


Figure 4.33: Comparison of time averaged velocity distributions around the bridge deck for side ratio (R) of 5 and 8 with a bottom plate slope (θ_B) of 14°

4.2.3 Influence of Reynolds Number (R_{eB})

In previous sections, all the simulations were conducted at a particular wind velocity that means Reynolds number (R_e) was same. However, practical bridges experiences very large Reynolds number during their design life time and important aerodynamic instability such as flutter also occurs at high Reynolds number (R_{eB}). Therefore, it is worthy to explore the Reynolds number (R_{eB}) effects on bridges decks.

Conducting simulation at high Reynolds number (R_{eB}) is quite expensive as large numbers of grids are required to model the thin boundary layer and to make the simulation stable, small time step is demanded. It is quite ambitious to conduct simulation at high Reynolds number (R_{eB}) for large number of sections to observe the trend in results. In the last sections we already explored the flow field and found some important flow features such as the deck top surface leading edge separation, deck bottom surface leading and trailing edge separations. Further, we also interpreted their roles on steady state responses. Therefore, it is more rational to investigate the Reynolds number (R_{eB}) effects for a particular section and observe how those important flow features behaves. With this intention, we investigated the Reynolds number (R_{eB}) effects on a streamlined deck with a bottom plate slope (θ_B) of 14° . The Reynolds number (R_{eB}) was altered from 1.65×10^4 to 16.5×10^4 by varying the inlet wind velocity (U).

Fig.4.34 plots the mean and rms value of steady state force coefficients versus the Reynolds number (R_{eB}). The mean value of the coefficients becomes almost Reynolds number (R_{eB}) independent beyond a value of 13.0×10^4 . Except the drag, the rms value of lift and moment also have similar tendency. To understand the trend in mean value of steady state force coefficients, the time averaged velocity distributions are plotted for three Reynolds number values in Fig. 4.35.

Fig.4.35 shows that the bottom surface leading and the trailing edge is mostly affected due to increase in Reynolds number (R_{eB}). To visualize the effects more clearly, the boundary layer velocity distributions are plotted in Fig.4.36. Fig.4.36(a) depicts that as the Reynolds number (R_{eB}) increases the top surface leading edge separation increases, yet the flow reattachment tendency increases (Fig.4.36(b)). The bottom surface leading edge separation also increases with the increases in Reynolds number (R_{eB}). However, the bottom deck trailing edge side separation decreases and stops completely when the Reynolds number (R_{eB}) increases and reaches up to value of 13.0×10^4 , respectively.

Schewe and Larsen (1998) and Schewe (2001) carried out wind tunnel investigation to visualize the Reynolds number effects on bluff bodies and trapezoidal bridge decks by oil flow experiment. For the trapezoidal bridge section the experiment was carried out up to transcritical

range of Reynolds number (R_{eB}). Their observation is summarized in Fig.4.37. Their Reynolds number (R_{eB}) was quite high, even though our findings agree well with their experimental results. Specially, at the bottom surface leading and the trailing edge side it has very good agreement. However, at the top surface leading edge side, we found that both the separation and reattachment increases with the increases in Reynolds number (R_{eB}). Similarly, they also found that reattachment tendency increases, yet the separation tendency decreases with the increases in Reynolds number (R_{eB}). The possible reason of variation could be the variation in deck shape, as our bridge deck has a much longer fairing as compared to their one. Still, the present simulation could reproduce the overall effects of Reynolds number (R_{eB}) on flow field quite accurately.

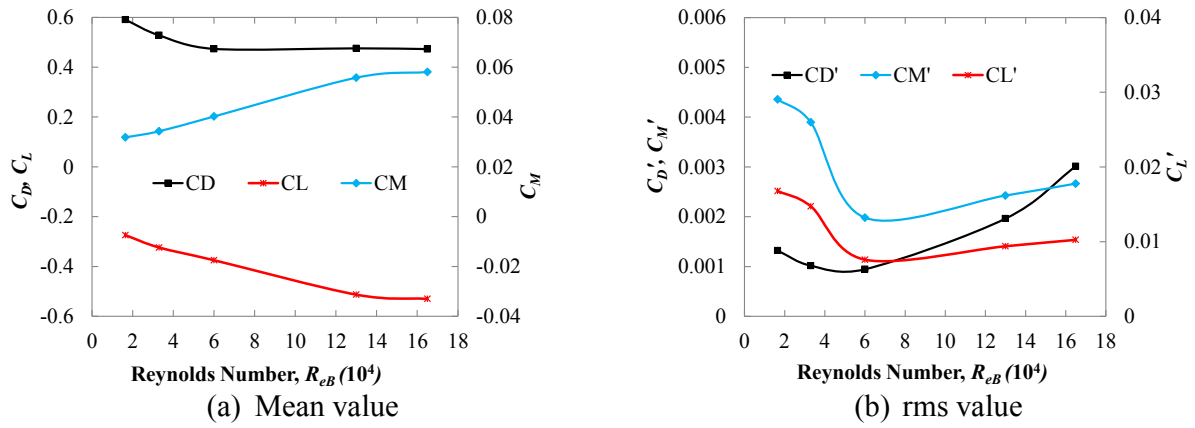


Figure 4.34: Reynolds number effects (R_{eB}) on mean and rms value of steady state force coefficients

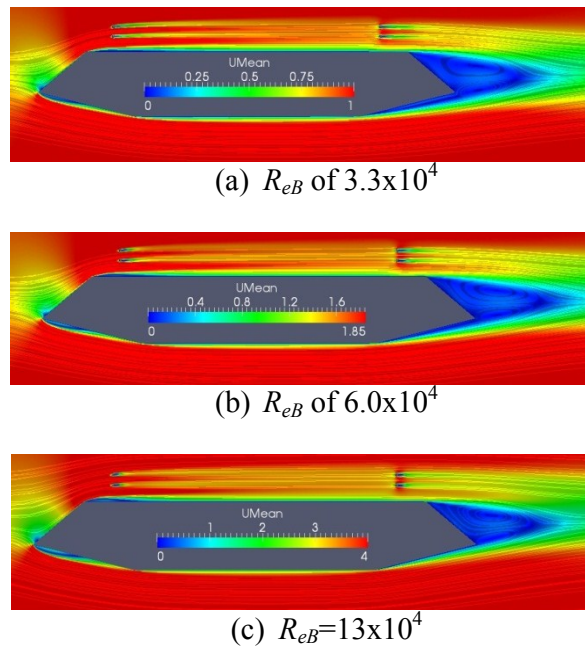


Figure 4.35: Reynolds number effects on time averaged velocity field for a bottom plate slope (θ_B) of 14°

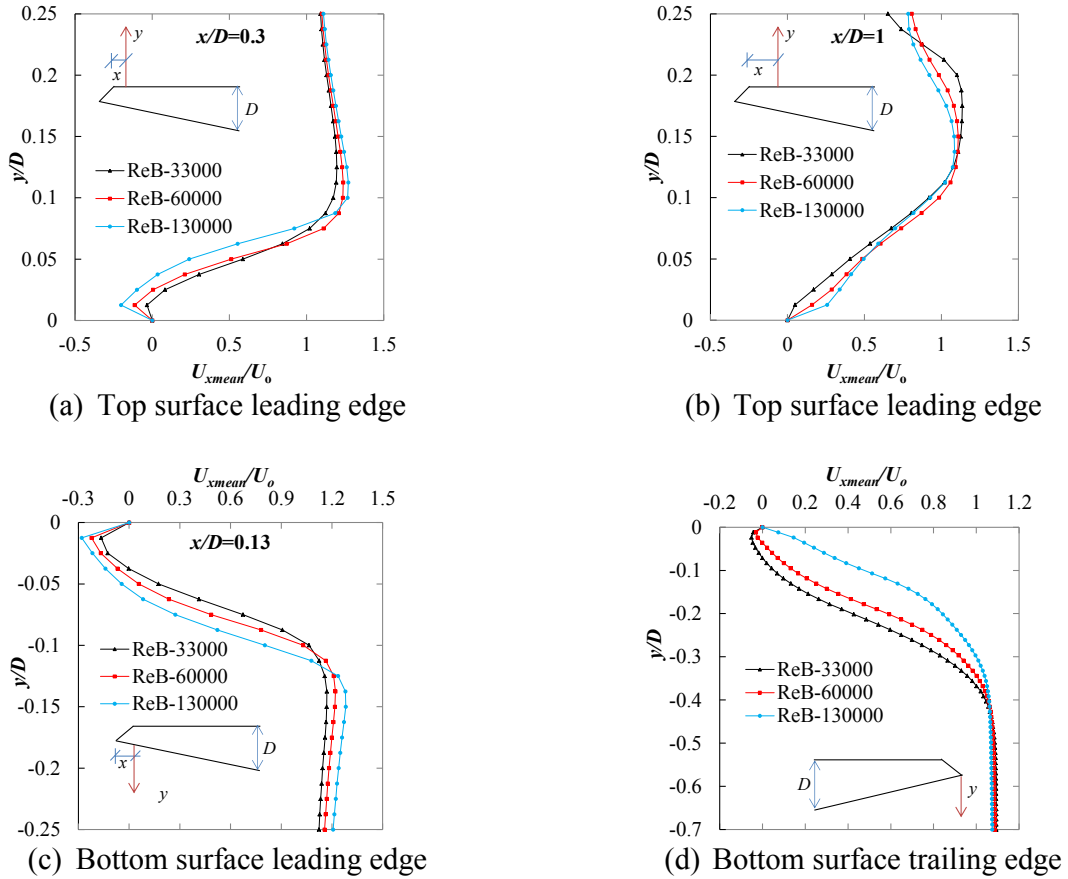


Figure 4.36: Reynolds number (R_{eB}) effects on various important flow features for streamlined deck

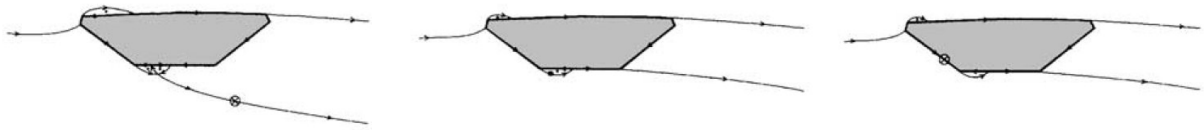


Figure 4.37: Reynolds number effects on flow field of a bridge section obtained by Schewe (2001). The Reynolds number (R_{eB}) in the figure increases from left to right up to a value of 15×10^5

Based on this observation, the trend in mean value of steady state force coefficients can easily be explained. As the Reynolds number (R_{eB}) increases the bottom surface trailing edge separation decreases, decreasing the wake size and thereafter decreases the drag. While the leading edge bottom surface separation increases with the increase in Reynolds number (R_{eB}) that increases the negative lift value. Therefore, there would be some differences in flow field for low wind speed and high wind speed aeroelastic phenomena. For example, at vortex shedding wind speed range for small bottom plate slope ($\theta_B \leq 15^\circ$), small separation may exist at the trailing edge side. On the other hand, at flutter wind speed range that separation will stop completely. For a deck with too small bottom plate slope ($\theta_B \ll 15^\circ$) that variation of separation at the trailing edge due to Reynolds number (R_{eB})

may not exist or will be negligible. However, the decrease in trailing edge separation may increase the flutter wind speed or not and its role of flutter instability is not clear yet. In chapter 6, their probable roles on dynamic response are investigated.

4.3 Concluding Remarks

In this chapter, the influence of various shaping parameters on steady state responses and flow field were presented. Primarily, the effects of top plate slope (θ_T), bottom plate slope (θ_B), width ratio (W) and Reynolds number (Re_B) on steady state responses were examined. Flow fields were analyzed in detailed in terms of pressure and velocity distribution for understanding the obtained aerodynamic responses.

We found for deck with fairing there are three important flow features: i) Top surface leading edge flow separation, ii) Bottom surface leading edge flow separation and iii) bottom surface trailing edge flow separation. The leading edge separations affect the mean value of the steady state force coefficients and the trailing edge bottom surface separation affects the drag and the rms value of the fluctuations. In addition the lift value is also affected by boundary layer flow velocity depending on the orientation of the top (θ_T) and bottom (θ_B) plate slope. For any combination of top (θ_T) and bottom (θ_B) plate slope, the flow moves faster on the smaller slope side surface and increases the lift value normal to that side.

For large width ratio ($W=1$), larger bottom plate slopes ($\theta_B=20^\circ-25^\circ$) experiences less drag, nominal negative lift and less after-body vortex activity. For this range of bottom plate slopes (θ_B), the bottom surface trailing edge separation remains small and the nose stays relatively higher position, decreasing the space to form vortices on the top surface trailing edge and improves the aerodynamic performance comparatively. By using smaller top plate slope ($\theta_T \leq 40^\circ$), the nose location can be shifted further upward and aerodynamic responses can be bettered for edge fairing.

On the other hand, for streamlined deck, as the width ratio (W) decreases the nose goes too high for large bottom plate slopes ($\theta_B=20^\circ-25^\circ$). As a result, the flow separates completely at the bottom surface trailing edge and aerodynamic performance deteriorates. For small width ratio ($W \leq 0.7$) bridge deck, small bottom plate slopes ($\theta_B \leq 15^\circ$) works better. For small bottom plate slope ($\theta_B \leq 15^\circ$) as the width ratio (W) decreases the nose goes up and the vortex formation area on the top surface trailing edge decreases, yet the bottom surface trailing edge flow doesn't separate massively. Therefore, wake becomes small and improves the aerodynamic behavior. Further, for small bottom plate slopes ($\theta_B \leq 15^\circ$) when the nose goes on the upper half of the deck ($y/D > 0.5$), the top surface trailing edge vortex becomes less influential and improves the response significantly, decreasing the importance of top plate slope (θ_T).

The trend we found in the results didn't alter significantly depending on the types of handrail and side ratio (R). However, Reynolds numbers affected the responses noticeably. At high Reynolds ($Re_B \geq 20 \times 10^5$) number the leading edge top and bottom surface separation increases and the bottom surface trailing edge separation decreases. At low Reynolds number ($Re_B \leq 6 \times 10^4$) the bottom surface trailing edge flow separation stops partially for small bottom plate slope ($\theta_B \leq 15^\circ$) as boundary layer separation still exists. However, at high Reynolds number ($Re_B \geq 20 \times 10^4$) that trailing edge separation stops completely for the bridge deck with small bottom plate slope ($\theta_B \leq 15^\circ$).

From the flow field analysis we found a number of important flow features such as the leading edge top and bottom surface separations and the trailing edge bottom surface separation. We clarified their roles on steady state responses and behavior due to increase in Reynolds number (R_{eB}). However, their roles on dynamic responses such as vortex induced vibration and flutter instabilities are not clear yet. In chapter 6 their possible roles on dynamic responses are tried to clarify.

Chapter 5

Bridge Deck Shaping Effects on Aerodynamics: Without Fairing

Cable-supported bridges are one of the most popular and widely used bridge configurations adopted by engineers for medium to long span bridges. However, they are aerodynamically vulnerable due to their inherent flexibility. The bridge deck should be shaped to reduce aerodynamic loading and susceptibility to aero-elastic phenomenon such as vortex shedding and flutter instability. Usually, the bridge decks are shaped as streamlined by adjusting the bottom plate slope of the bridge deck and fairings are attached at the side of the bridge deck to control the flow and to improve the aerodynamic stability as we discussed in the last chapter. However, addition of these extra devices increases the construction and maintenance cost.

Therefore, along with the streamlined deck with fairing, bridge decks are also shaped without fairing for example Adige Bridge in Italy (Patruno 2015). Specially, in Japan a number of bridge decks have been shaped without fairing in hexagonal shape such as Takeshima Ohashi Bridge, Shintenmom Bridge, Oshima Bridge, Kesennuma Bridge and Ikara Ohashi Bridge etc. Basically, the concept came from the pentagonal shaped bridge deck (without fairing) proposed by Kubo *et al.* 2007. For these type of deck, the bottom deck flow is controlled by the bottom plate slope (θ_B), whilst the top deck flow is controlled by positioning the curb on the top deck, this technique is known as separation interference method (SIM) (Yoshida *et al.* 2006 and Kubo *et al.* 2008).

Like the streamlined bridge deck (with fairing), the pentagonal and hexagonal bridge decks (without fairing) also have similar shaping parameters i.e., the bottom plate slope (θ_B) and the width ratio (W). However, the fluid flow behavior around the bridge deck without fairing would be different from the bridge deck with fairing. Therefore, the trend in the results we found in the last chapter due to variation of shaping parameters may alter. Further, this kind of bridge decks has new shaping parameters such as the curb angle (β) and the curb height (h/D). Therefore, we carried out detailed investigation on shaping effects of bridge deck without fairing on its aerodynamics.

In this chapter the detailed investigation results for bridge decks without fairing are presented. The chapter is broadly divided into two parts. In the first half of the chapter we deal with the pentagonal shape bridge deck and its aerodynamics. In the second half of the chapter, we focus on the aerodynamic response and flow field of the hexagonal shaped bridge deck. Along with shaping aspects, we also examined some other important issues such as Reynolds number effects and the influence of inspection rails on the aerodynamics of bridge deck without fairing. Most of the simulations were conducted at a Reynolds number (Re_B) of 6.0×10^4 . The grids were generated by following the strategy presented in chapter 3 and had an average y^+ value of near about 2 and a maximum y^+ value of around 8.2 around the bridge deck boundary. Numerical setup similar to chapter 3 was used for simulating the fluid flow around the bridge deck.

5.1 Behavior of Pentagonal Bridge Deck

An aerodynamically stable deck shape for cab-stayed bridge was proposed by Kubo and his associates (Yoshida *et al.* 2006; Kubo *et al.* 2007 and Noda *et al.* 2009) as shown in Fig.5.1. For this section no additional devices are required to increase the aerodynamic stability of the deck. One of the advantageous points in this type of shape is that it exhibits negative lift values at high wind speed. Therefore, at high wind speeds the cable tension and total stiffness of the bridge system increases. Kubo *et al.* (2007) also showed the influence of bottom plate slope (θ_B) on flutter and vortex shedding behavior using wind tunnel experiments. They found that a bottom plate slope (θ_B) of 12° has the lowest aerodynamic loading (specially, the drag was the lowest) and high flutter wind speed.

Then, Noda *et al.* (2009) and Noda (2010) clarified the cause of negative lift value from surface pressure distribution and PIV measurement for a pentagonal shaped bridge deck with a bottom plate slope of 14° . Their findings showed that it was the separated shear layer at the leading edge bottom toe that generates suction and increases the negative lift value. From the PIV experiments of Noda *et al.* (2009) some of the flow mechanisms were identified.

However, there is more to reveal about the aerodynamics of this type of section. Noda *et al.* (2009) showed the role of the leading edge bottom deck separation on static lift force at a particular Reynolds Number (Re_B). Even so, there were a number of other flow features such as top deck leading edge separation and bottom deck trailing edge separation. Their behavior and role on aerodynamic response is not yet clear. Further, Kubo *et al.* (2007) showed that all the steady state force coefficients exhibited very high sensitivity, when the bottom plate slope (θ_B) was altered at flutter wind speed. All of those flow features will have a role in controlling the static and dynamic aerodynamic response of the bridge deck. Further the Reynolds number (Re_B) effect is also required

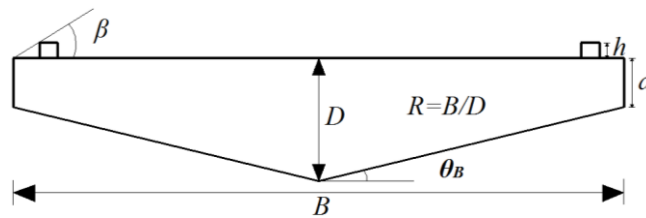


Figure 5.1: Cross-section of the pentagonal bridge deck and important notations

to be clarified as the bridges are required to operate over a wide range of Reynolds number (R_{eB}).

Furthermore, the effectiveness and flow mechanism of curb angle (β) was demonstrated based on a square cylinder of side ratio ($R=B/D$ of 1) (Kubo *et al.* 2008). For a small side ratio ($R \approx 1$) cylinder the separated shear layer at the leading edge goes directly at the downstream of the body, yet for bridge deck section with large side ratio ($R \geq 5$) the flow reattaches at the side of the cylinder. The effectiveness of curb angle (β) and flow field for the bridge deck section would be different from that of a small side ratio bluff body. Moreover, depending on the curb height the response will also differ. In the following sections these issues are discussed one by one.

5.1.1 Influence of Bottom plate Slope (θ_B)

In this section, the effect of bottom plate slope (θ_B) on steady state force coefficients and flow field is demonstrated at a Reynolds number (R_{eB}) of 3.9×10^4 . Three curb angles (β) of 27° , 30° and 33° were checked and the curb height (h/B) was set to 0.025. The bottom plate slope (θ_B) was varied from 10° to 16° by varying the side ratio (R) from 6.45 to 4.75, respectively. The depth (D) of the deck was varied to alter the bottom plate slope (θ_B) without changing the width (B) and the side depth (a/B) of the deck. The side depth (a/B) height was set to 0.067. In past experimental work (Yoshida *et al.* 2006 and 2007) the bottom plate slope was varied by following the same procedure. These results may have a side ratio (R) effect, however, to maintain coherence with past experimental work the same procedure was chosen.

5.1.1.1 Steady State Force Coefficients

The mean and rms value of steady state force coefficients for varying bottom plate slopes (θ_B) are plotted in Fig.5.2. As can be seen the bottom plate slope (θ_B) has much larger influences on force coefficients rather than the curb angle (β). However, the smaller curb angle (β) of 27° has less aerodynamic responses. Kubo *et al.* (2007) also found that a curb angle (β) of 27° had slightly higher critical flutter wind speed than the other curb angles (β). The discussion about the curb angle is not deepened here, in the next section the influence of curb angle and height are discussed in detailed.

Fig.5.2 depicts that the smaller bottom plate slope (θ_B) has less magnitude of force coefficients, regardless of the curb angle (β). For any value of bottom plate slope (θ_B) from 16° to 10° , the deck experiences a negative lift. In Fig. 5.2(d) and (f) the rms value of lift and moment decreases significantly as the bottom plate slope (θ_B) decreases. Like streamlined section, here also

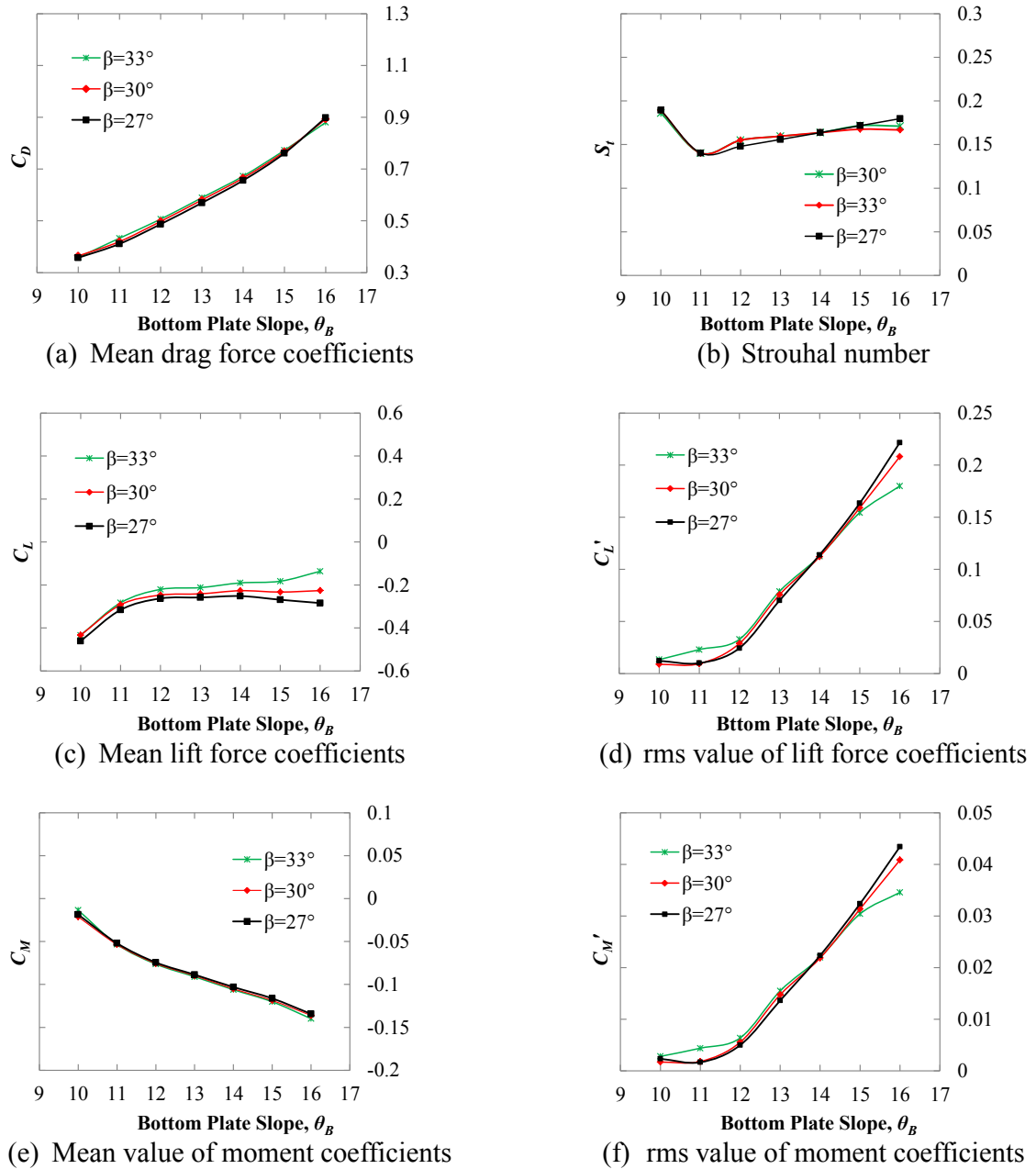


Figure 5.2: Influence of bottom plate slope (θ_B) on mean and rms value of steady state force coefficients

we found that small bottom plate slope (θ_B) possess better aerodynamic responses, yet as compared to streamlined deck in case of pentagonal deck much smaller value of bottom plate slope (θ_B) is required to obtain the best response.

In the literature experimental data of flutter wind speed for varying bottom plate slope (θ_B) is available; hence we took this opportunity to compare the trend in the result with the literature. Past experimental work has shown that flutter wind speed increases as the bottom plate slope (θ_B)

decreases and vortex shedding instability stops for a bottom plate slope (θ_B) of smaller than 19° (Yoshida *et al.* 2006, Kubo *et al.* 2007 and Noda *et al.* 2010). Fig.5.3 shows that a deck with a curb angle (β) of 30° the reduced flutter wind speed increases as the bottom plate slope (θ_B) decreases. The present rms value of lift and moment has similar trends in the result of the flutter wind speed obtained previously (Kubo *et al.* 2006 and 2007). But it should be noted that this similarities in the results can't be considered as a general case.

5.1.1.2 Pressure Distribution

The mean and rms values of surface pressure distribution for the selected deck sections with a bottom plate slope (θ_B) of $11^\circ, 12^\circ, 14^\circ$ and 16° are plotted in Figs.5.4 and 5.5, respectively. In the case of mean surface pressure the bottom deck pressure is more influential than the top deck surface when the bottom plate slope (θ_B) is altered. The mean surface pressure distribution is mainly affected at the leading and trailing edge of the deck due to variation of the bottom plate slope (θ_B). As the bottom plate slope decreases (as a/D ratio increases) the bottom deck leading edge side negative pressure area increases and the trailing edge side negative pressure decreases. Basically, this kind of negative pressure indicates the separation of the shear layer from the deck surface.

Based on the mean surface pressure the trend in steady state force coefficients can also be explained. For example, for a small bottom plate slope ($\theta_B=11^\circ$) the deck experiences an increased downward force (negative pressure increases) at the leading edge side bottom surface and a decreased downward force (negative pressure decreases) at the trailing edge side bottom surface. As a result the overall positive moment (anti-clockwise) tendency of the deck increases, that decreases the negative moment value (Fig.5.2(e)). Similarly, as the leading edge side negative pressure increases the negative lift (downward) value tendency increases for a small bottom plate slope (θ_B) of 11° .

Unlike the mean surface pressure the rms pressure is actually affected at the trailing edge side as shown in Fig.5.5. As the bottom plate slope (θ_B) decreases, the trailing edge side rms value also decreases. This should be due to the after-body vortices activity as we already discussed in chapter 4. The instantaneous velocity distributions along one lift cycle are plotted in Fig.5.6 for the bridge deck with a bottom plate slope (θ_B) of 14° to reconfirm the idea.

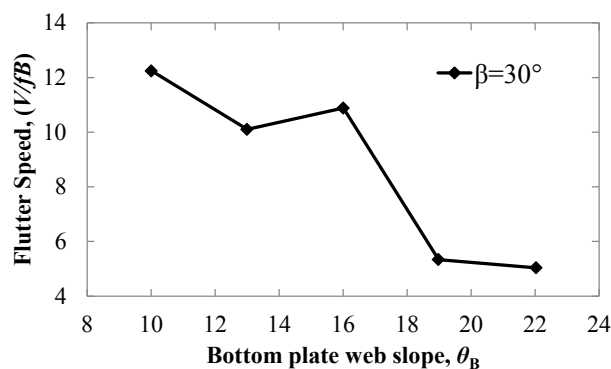


Figure 5.3 Influence of bottom plate slope (θ_B) on flutter wind speed (U/fB) for curb angle (β) of 30° based on the experimental work by Kubo *et al.* (2007)

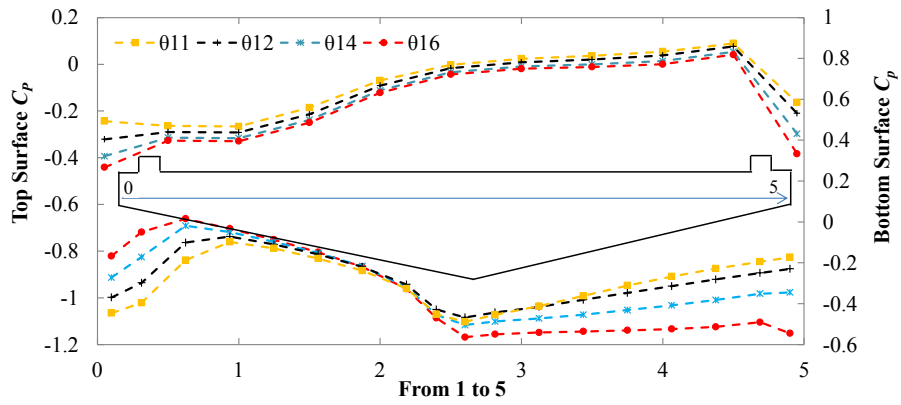


Figure 5.4: Mean surface pressure distribution around the bridge deck section with a curb angle (β) of 27° for various bottom plate slopes (θ_B)

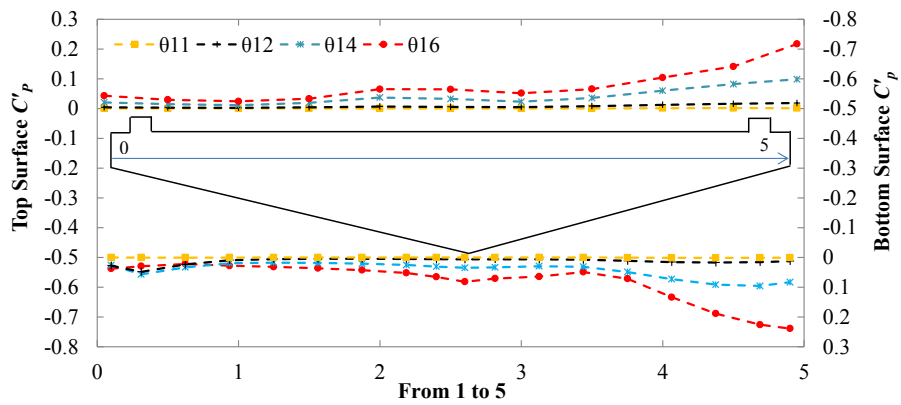


Figure 5.5: rms surface pressure distribution around the bridge deck section with a curb angle (β) of 27° for various bottom plate slopes (θ_B)

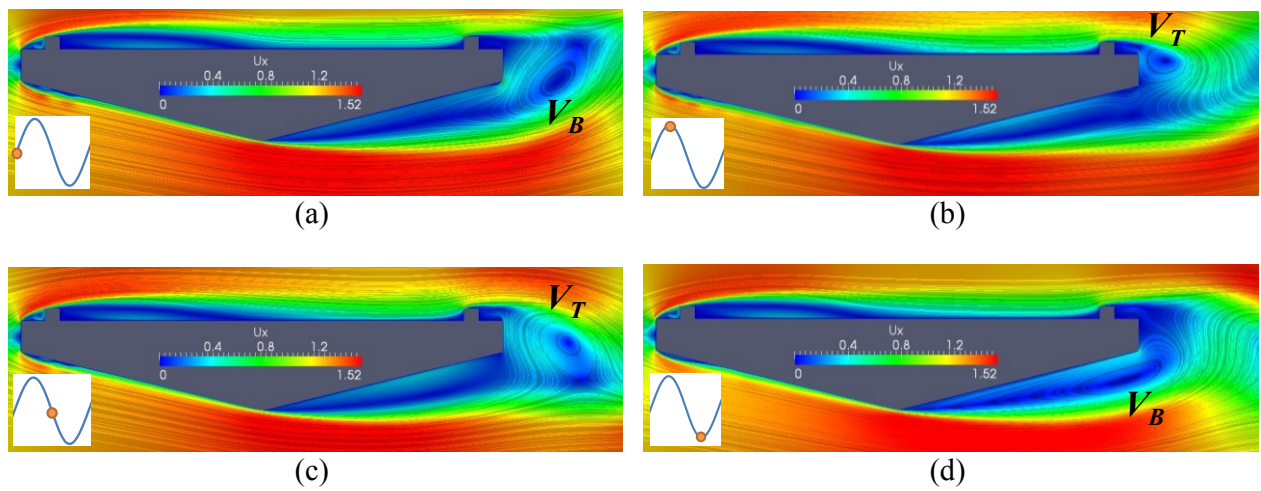


Figure 5.6: Instantaneous velocity field for deck shape having bottom plate slope (θ_B) of 14° along one lift cycle at 0° (a), 90° (b), 180° (c) and 270° (d)

5.1.1.3 Velocity Distribution

The time averaged velocity fields for the selected bridge deck sections are plotted in Fig.5.7. The velocity distribution agrees well with mean pressure distribution as shown in Fig.5.4 and makes it easier to understand the mean and rms pressure distributions. As can be seen the wake size decreases as the bottom plate slope decreases and the deck experiences smaller rms fluctuations. The reason of a smaller wake size at the smaller bottom plate slope is due to the decrease in the trailing edge side flow separation. As a result the vortex may form just after the deck with smaller size rather than very close to the trailing edge bottom deck surface as shown in Fig.5.7(c). For streamlined bridge deck, we also found similar tendency as shown in chapter 4. Therefore, at bottom plate slope (θ_B) of 19° the after-body vortex size would increase further and may excite the structure to vibrate. That's how Kubo *et al.* (2007) observed vortex induced vibration for bridge deck with a bottom plate slope (θ_B) of 19° . To observe the flow field for large bottom plate slope ($\theta_B=19^\circ$), one more simulation was conducted at a bottom plate slope (θ_B) of 19° and the flow field is compared along with the other decks in Fig.5.7(d). The figure reflects the thought we approximated.

Figs.5.8 and 5.9 displays the velocity distribution at the trailing edge and 0.5D downstream of the deck. The flow separation can be seen clearly at the trailing edge and decreases gradually as the bottom plate slope (θ_B) decreases. Thus the wake size decreases as shown in Fig.5.9. As a result both the drag and the rms value of steady state force coefficients decreases. This implies that the deck having smaller wake may require a larger wind speed for flutter to occur. This guess is also applicable for streamline bridge deck as we discussed earlier. However, this is just a conjecture based on present observations and demands a further elaborate investigation.

In this section we obtained some trends in the steady state force coefficients and we could clarify them through an analysis of the pressure and velocity distributions. However, we found the minimum drag value for a bottom plate slope (θ_B) of 11° , while Kubo *et al.* (2007) found the minimum drag at a bottom plate slope of 12° . We shouldn't miss the point that experimental results

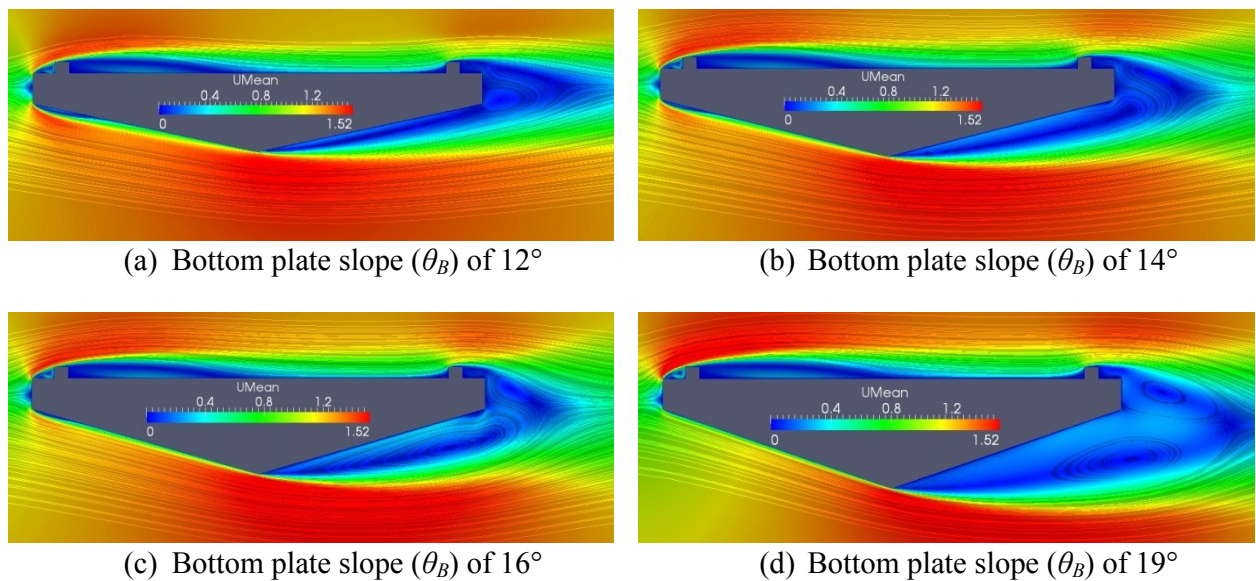


Figure 5.7: Influence of bottom plate slope (θ_B) on time averaged flow field around the bridge decks

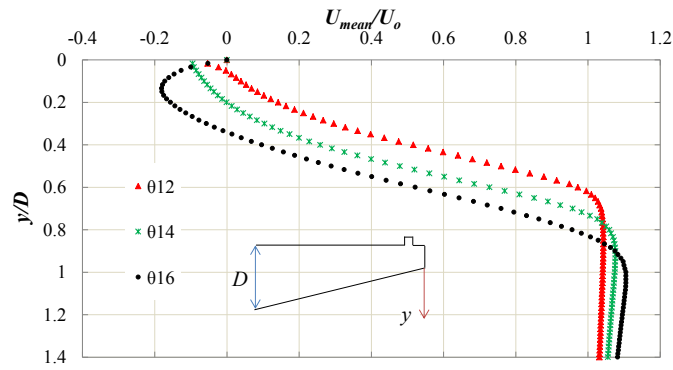


Figure 5.8: Influence of bottom plate slope (θ_B) on trailing edge separation

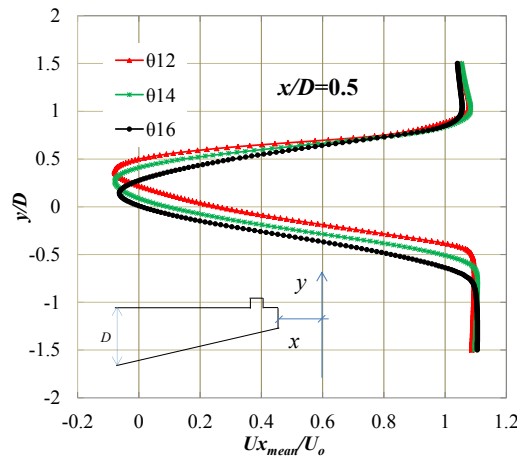


Figure 5.9: Influence of bottom plate slope (θ_B) on the wake size of the bridge deck

were carried out at the flutter wind speed range. There must be some Reynolds number effects. This issue is discussed elaborately later in a section dedicated particularly for discussing Reynolds number (Re_B) effects. In the following sections, the influence of curb angle (β) and curb height (h/D) on aerodynamics are introduced.

5.1.2 Influence of Curb Height (h/D)

From the practical point of view, there is not much room to change the location and height (h/D) of the curb. In fact, they are always tried to put at the end of the deck to maximize the usable area and the curb can't be too high. The height of the curb (h/D) was increased gradually from 0 to 0.2 without changing the curb angle (β) as shown in Fig.5.10. The curb angle (β) and bottom plate slope (θ_B) was set at 30° and 11° , respectively. All the simulations were conducted for a bridge deck with a constant side ratio (R) of 5. The simulations were performed at a Reynolds number (Re_B) of 6.0×10^4 .

Fig.5.11 shows the relations between the steady state force coefficients and the curb heights (h/D). The curb height (h/D) affects the force coefficients significantly. Specially, the lift force coefficient is affected the most. In Fig.5.11(b) the moment increases gradually as the curb height (h/D) increases. However, the drag and lift force coefficients exhibited the most important trend in the result. Both the drag and lift force value decreases with the increase in curb height and reaches to a minimum value at a curb height (h/D) of 0.1. Then, the drag and lift value increases again with the further increase in curb height (h/D). However, the rms value doesn't vary noticeably beyond a curb height (h/D) of 0.1.

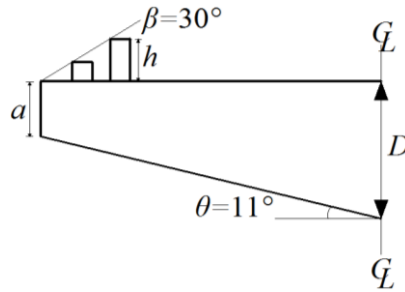
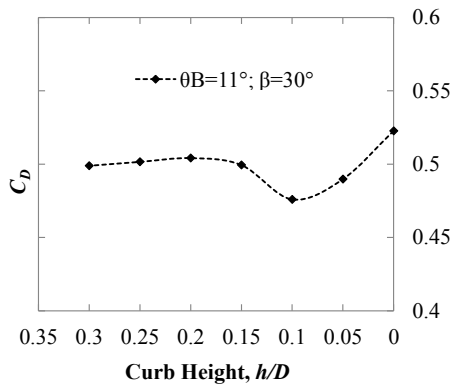
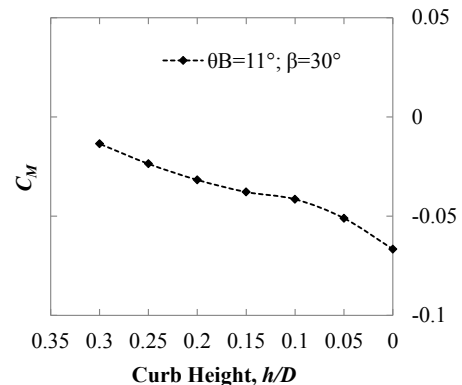


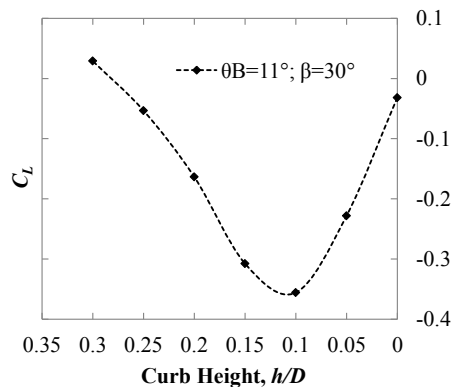
Figure 5.10: Procedure of changing curb height (h/D) for a fixed curb angle ($\beta=30^\circ$)



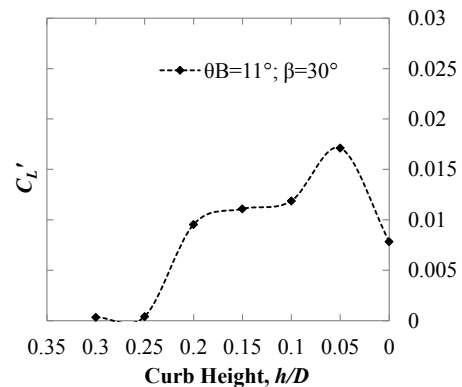
(a) Mean value of drag force coefficients



(b) Mean value of moment coefficients



(c) Mean value of lift force coefficients



(d) rms value of lift force coefficients

Figure 5.11: Influence of curb height (h/D) on mean and rms value of steady state force coefficients

The wind speed ratios for the selected curb heights (h/D) are shown in Fig.12. As can be seen when there is no curb is attached to bridge deck it experiences very large leading edge top surface separation. However, the separation decreases significantly when an optimum curb height (h/B) of 0.1 is attached to the bridge deck. As a result the negative lift value increases. Unlike short bluff bodies, for elongated bluff bodies the SIM enhances the flow reattachment tendency and improves the aerodynamic response. For curb height (h/D) larger than 0.1, the leading edge separation increases again and the negative lift value decreases as a consequence. When the curb is attached to the bridge deck, it not only affects the leading edge flow field but also the trailing edge flow field. Fig.5.13 plots the boundary layer velocity distribution at the trailing edge of the bridge deck. As can be seen for a curb height (h/D) of 0.1 the bridge deck possesses the lowest separation and wake size. As a result the deck experiences the minimum drag force for a curb height of 0.1.

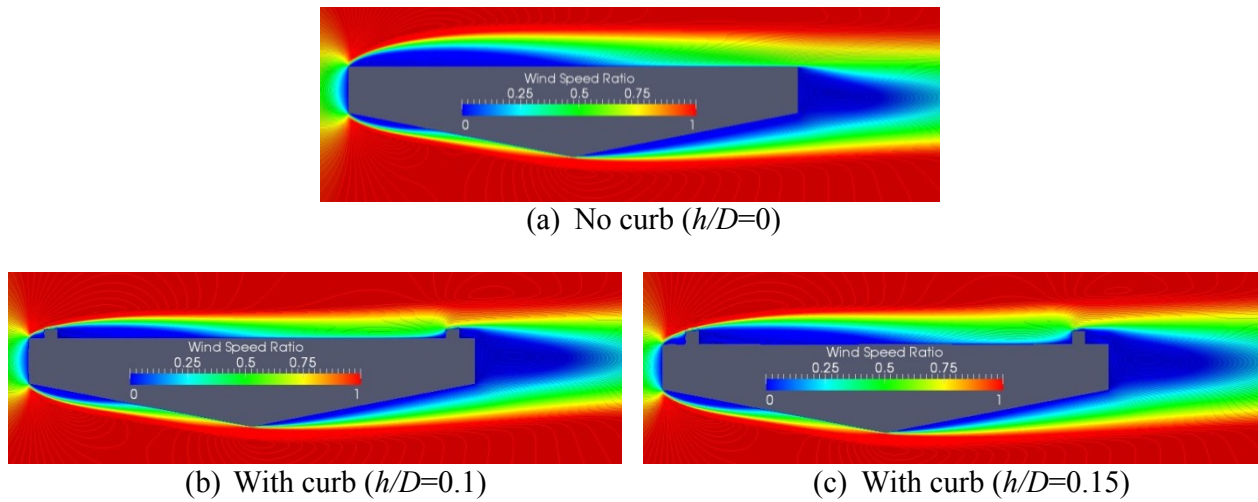


Figure 5.12: Influence of curb height (h/D) on wind speed ratio around the bridge decks

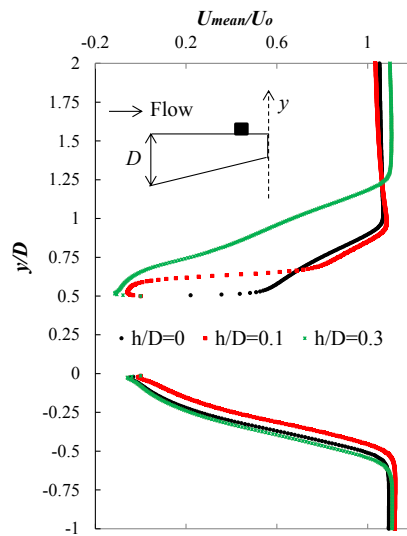


Figure 5.13: Influence of curb height (h/D) on trailing edge slow separation

5.1.3 Influence of Curb Angle (β)

Curb angle (β) was varied from 20° to 40° at an interval of 5° to investigate the influence of curb angle (β) on steady state force coefficient for a bridge deck with a side ratio (R) of 5. The curb height (h/D) was kept fixed at 0.125 and the curb angle was varied by shifting the curb location. Two bottom plate slopes (θ_B) of 11° and 14° were utilized as smaller bottom plate slope had better aerodynamic behavior. Simulations were performed at a Reynolds number (Re_B) of 6.0×10^4 .

Fig.5.14 shows the selected steady state force coefficients for various curb angles (β). As can be seen the bottom plate slope (θ_B) has higher influences on steady state force coefficients than the curb angle (β) as we found earlier. Curb angle (β) doesn't noticeably affect the mean value of drag and the moment coefficients, yet affects the mean value of lift at the present Reynolds number (Re_B). The deck experiences minimum lift forces for a curb angle (β) of 30° to 25° . At larger curb angle (β) the mean value of lift increases and the rms value decreases slightly. To understand this kind of trend in results, the wind speed ratios are plotted in Fig.5.15. Similar to curb height (h/D), here also the variation of curb angle (β) mainly affects the top deck leading edge flow separation. The flow mechanism for curb angle (β) is quite similar to the curb height (h/D). For a specific range of curb angle ($\beta=30^\circ$ - 25°) the top deck leading edge separation remains small, as a result the negative lift

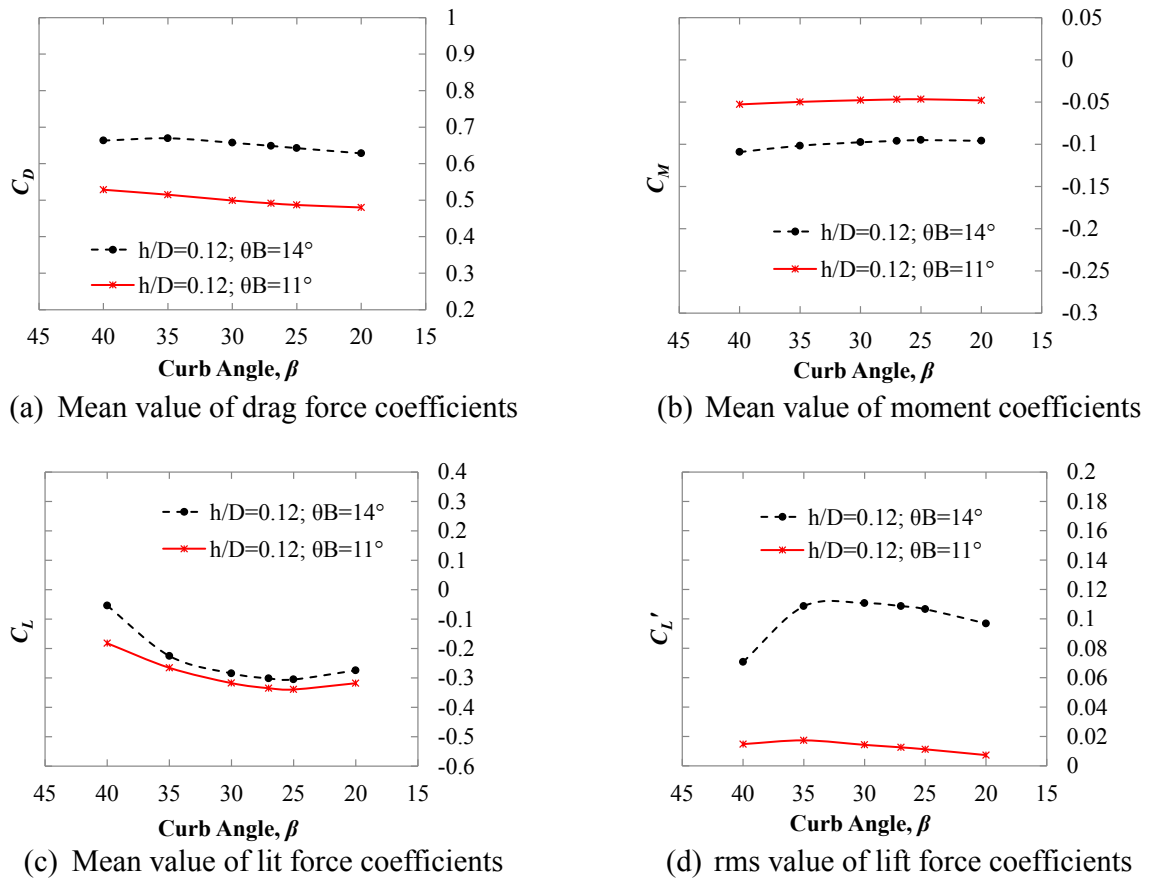
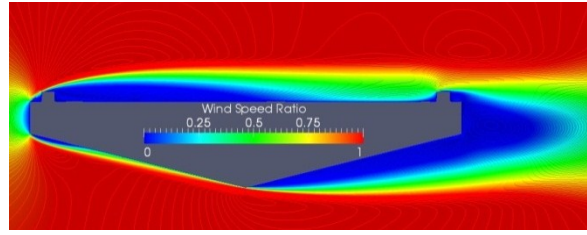
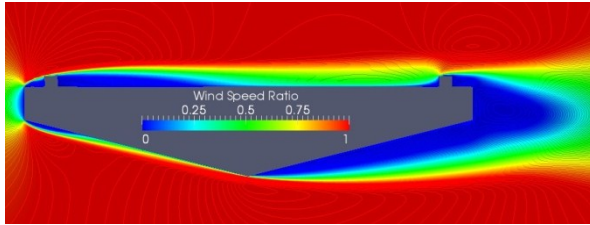
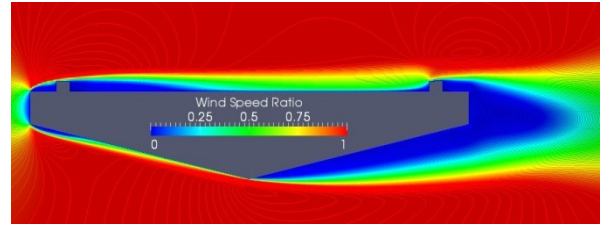


Figure 5.14: Influence of curb angle (β) on steady state force coefficients

(a) Curb angle (β) of 40° (b) Curb angle (β) of 27° (c) Curb angle (β) of 20° Figure 5.15: Influence of curb angle (β) on wind speed ratio around the bridge decks

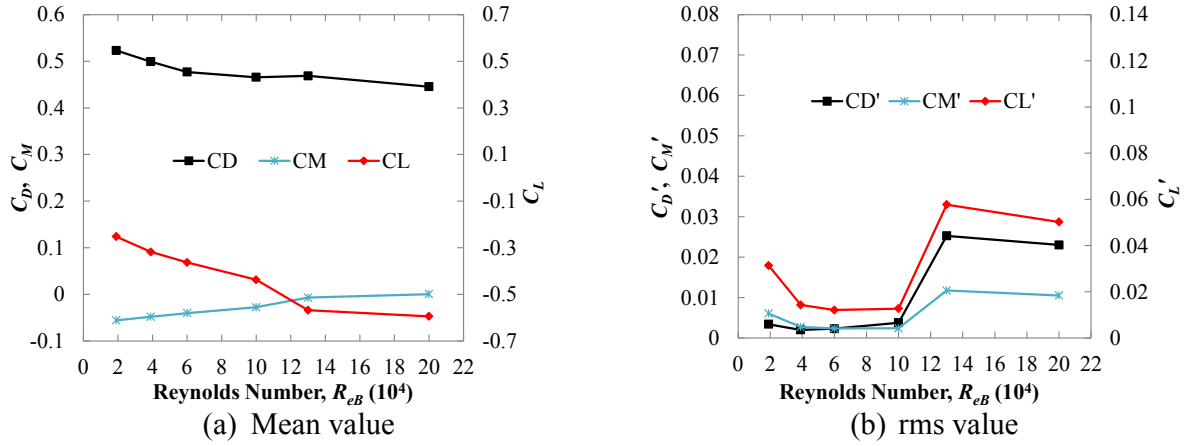
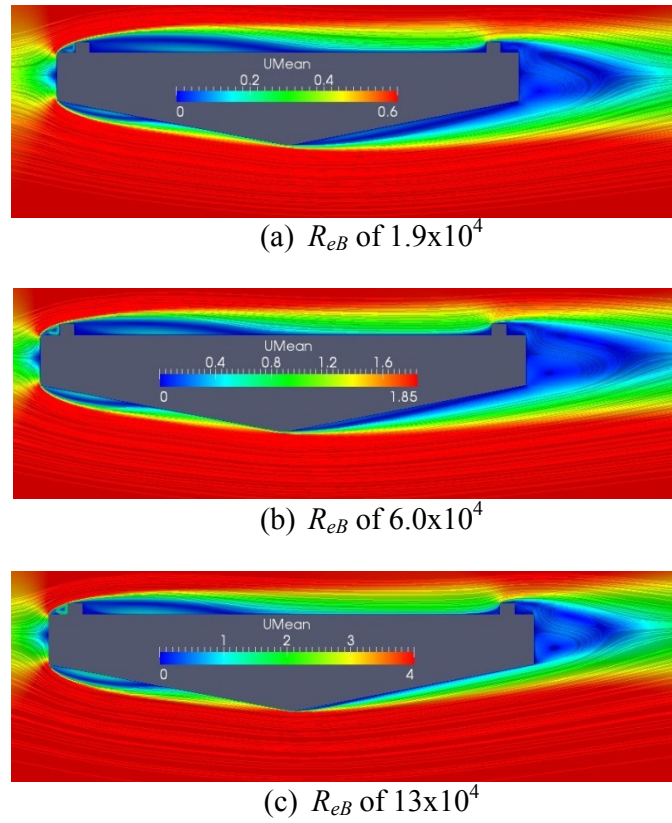
value increases. Beyond that range of curb angle, the separation increases, decreasing the negative lift value of the bridge deck.

5.1.4 Influence of Reynolds Number (R_{eB})

Simulations were carried out for five different Reynolds numbers ($R_{eB} = 1.9 \times 10^4 - 20 \times 10^4$) to show the trend in the results due to increase in Reynolds number (R_{eB}). Particularly, for exploring Reynolds number (R_{eB}) effects on the mean steady state force coefficients and the flow field. Investigation was conducted for one specific deck shape with a side ratio (R) of 5 and bottom plate slope (θ) of 11° . The Reynolds number (R_{eB}) was increased by increasing the inlet velocity and keeping the dimension of the bridge decks same. For the Reynolds number (R_{eB}) up to 6.0×10^4 , the average y^+ value was around 2. For higher Reynolds numbers (R_{eB}) of 13×10^4 and 20×10^4 the first grid height (y) was decreased, yet the average y^+ value reached up to about 2.8 and 4.1, respectively.

Fig.5.16 depicts the influence of the Reynolds number (R_{eB}) on steady state force coefficients. The dependency of the response on Reynolds number (R_{eB}) can be seen clearly in Fig.5.16. However, the general tendency looks almost similar to streamlined bridge deck. Both the mean and rms response become almost independent of the Reynolds number (R_{eB}) for a value higher than 13×10^4 . The mean value gradually decreases as the Reynolds number (R_{eB}) increases until a value of 13×10^4 , then becomes stable. The lift force coefficient (C_L) remains negative as the Reynolds number (R_{eB}) increases. This is good sign that even at a higher velocity the bridge will experience even larger downward forces increasing the total stiffness of the bridge system.

Based on our investigation we found some important aerodynamic flow features for pentagonal bridge deck such as the leading edge top surface separation, the bottom surface leading and trailing edge separation. Fig.5.17 represents the mean velocity distribution for three Reynolds numbers (R_{eB}). As can be seen the increase in Reynolds number affects the flow field noticeably at

Figure 5.16: Influence of Reynolds number (R_{eB}) on steady state force coefficientsFigure 5.17: Influence of Reynolds number (R_{eB}) on flow field for the pentagonal bridge deck

high Reynolds number (R_{eB}) range ($\geq 13 \times 10^4$). The top deck shear layer separation length decreases as the Reynolds number increases. The decrease in the top deck separation length strengthens the concepts of Separation Interference Method (SIM), even at high wind speed.

To clarify the Reynolds number (R_{eB}) effects on the flow features more precisely, the velocity distributions are plotted at three different locations in Fig. 5.18. As can be seen the flow behavior is quite similar to the streamlined bridge deck. Clear flow separation can be seen for small Reynolds

number ($Re_B \leq 6.0 \times 10^4$) both at the top deck leading edge side and bottom deck trailing edge the, yet the flow separation decreases and stops at the high Reynolds number (Re_B of 13×10^4). However, the bottom deck leading edge side separation increases with the increase in Reynolds number (Re_B). This increase in bottom surface leading edge separation and decrease in top deck leading edge separation increases the downward lift force, while the decrease in bottom deck trailing edge flow separation reduces the after-body wake size and directly affects the mean drag value resulting in a smaller value. Similar phenomena were observed by Schewe (2001) as we discussed in the last chapter.

In section 5.1.1 we found that a bottom plate slope (θ_B) of 11° has the least rms response due to small trailing edge flow separation at a Reynolds number (Re_B) of 3.9×10^4 . At high Reynolds number ($Re_B = 13 \times 10^5$) the trailing edge flow separation stops completely and forms boundary layer (Fig.5.18(c)). Based on this explanation it can be presumed that at a higher Reynolds number ($Re_B = 20 \times 10^4$), the separation may stops at bottom plate slope (θ_B) larger than 11° . As a result, the

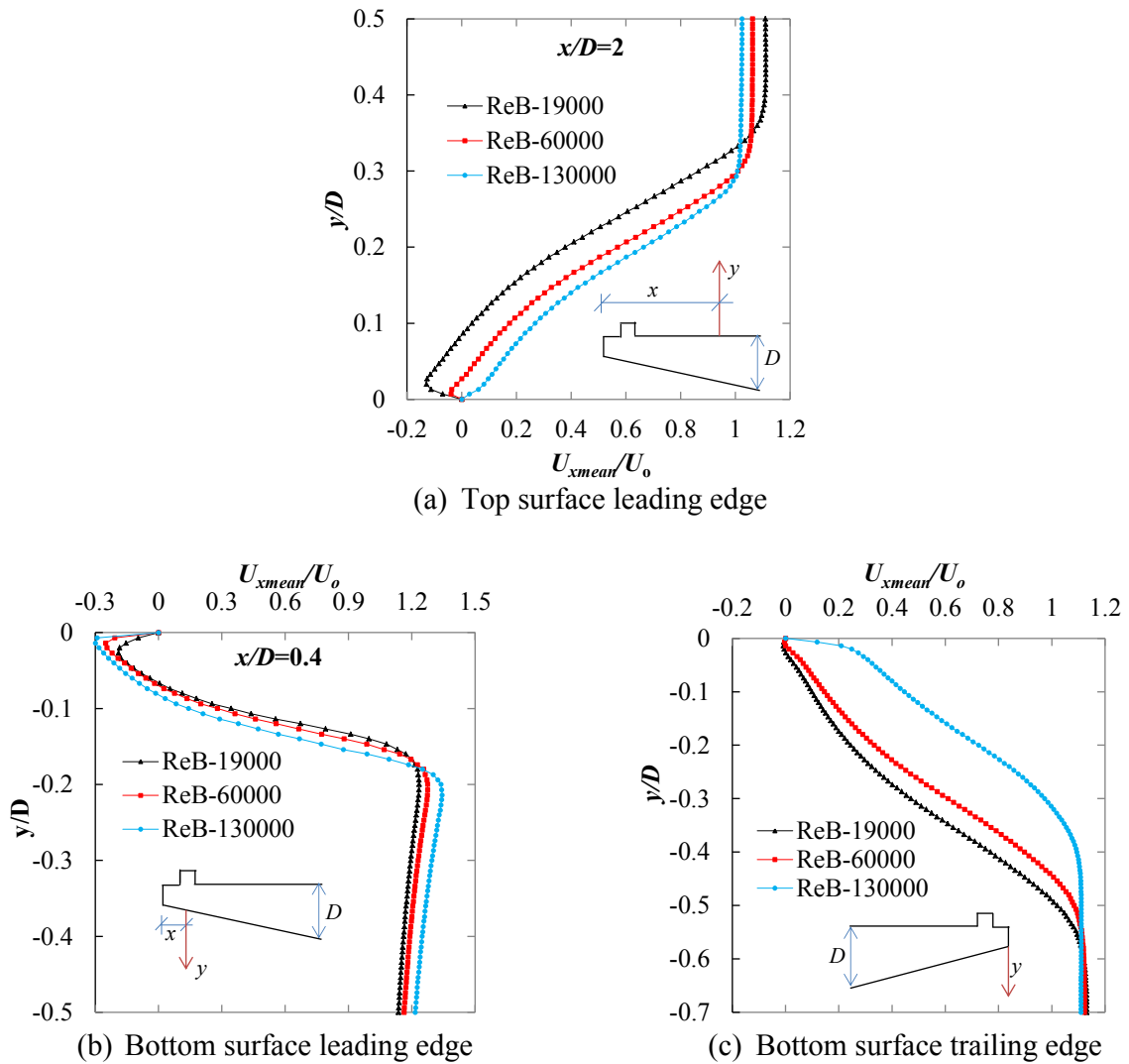


Figure 5.18: Influence of Reynolds number (Re_B) on various flow features

drag decreases due to decrease in relative wake size (as a larger bottom plate slope has a smaller a/D ratio). Therefore, at a high Reynolds number ($Re_B \geq 20 \times 10^5$) the optimum aerodynamic response can be found at a bottom plate slope (θ_B) higher than 11° . This could be a possible explanation why Kubo *et al.* (2007) obtained the least drag force at a bottom plate slope (θ_B) of 12° .

5.2 Behavior of hexagonal Bridge Deck

In the last section we demonstrated the responses and flow behavior for the pentagonal bridge deck for various shaping parameters and flow conditions. Like past experimental work (Yoshida *et al.* 2006 and Kubo *et al.* 2007), we also found that for the pentagonal bridge deck a small bottom plate slope (θ_B) of around 12° possess better aerodynamic behavior at high Reynolds number (Re_B). Based on past experimental observation, the bottom plate slope (θ_B) has been placed at around 12° for a number of practically constructed bridge decks.

However, practically constructed bridges are hexagonal in shape as shown in Fig.5.19. In variation to the pentagonal shape, the hexagonal shape owns one more new shaping parameter i.e., the width ratio ($W=b/B$) as defined previously. In the last chapter we showed that depending on the width ratio (W) the trend in the result alters a lot for the streamlined bridge deck. Moreover, we also provided the survey results for this type of bridge decks in chapter 2 showing that the width ratio (W) varies noticeably. Therefore, question arises how the response and the trend in the results alters when the deck shape is altered from pentagon to hexagon.

In this section we present the detailed investigation results on the hexagonal shaped bridge deck for various shaping parameters. The pentagonal and hexagonal bridge decks were connected through the width ratio (W). For a pentagonal shape bridge deck the width ratio (W) is 0, as it doesn't have any bottom horizontal plate width (b). A width ratio (W) value higher than 0 indicates the bridge deck is hexagonal in shape. Both the influence of width ratio (W) and bottom plate slope (θ_B) were considered. Practical issue such as the influence of side ratio (R), handrail and inspection rail were also taken into account. All the simulations were conducted at a Reynolds number (Re_B) of 6×10^4 and the side ratio (R) was kept fixed at 5.

5.2.1 Influence of Width Ratio (W)

The width ratio (W) ratio was varied from 0 to 0.3. The maximum value of width ratio was selected based on the survey results as presented in chapter 2. For each width ratio (W), the bottom plate slope (θ_B) was varied from 20° to 10° as shown in Fig.3.20. The curb angle (β) and height (h/D) was set to 30° and 0.1, respectively. It is worthy to mention that in case of streamlined deck the width ratio was decreased gradually, yet for this type of bridge deck the width ratio (W) was increased from 0 to 0.3. Further, the nose location goes down (y/D) for this type of bridge deck with the increase in width ratio (W).

Fig.5.21 demonstrates the influences of width ratio (W) and bottom plate slope (θ_B) on steady state characteristics of the force coefficients. Like streamlined bridge, hexagonal bridge deck also

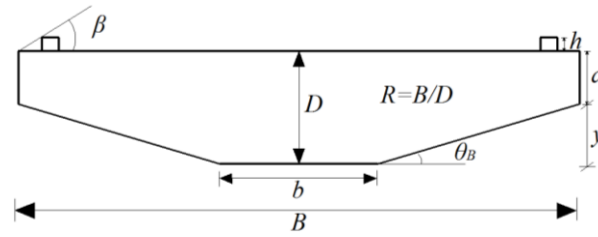
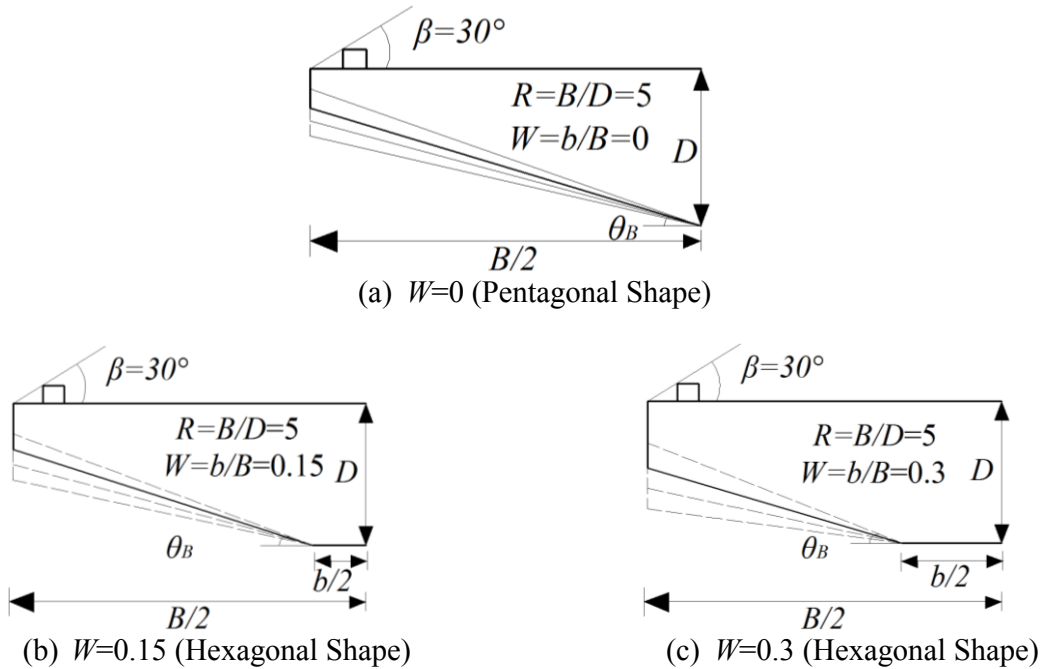
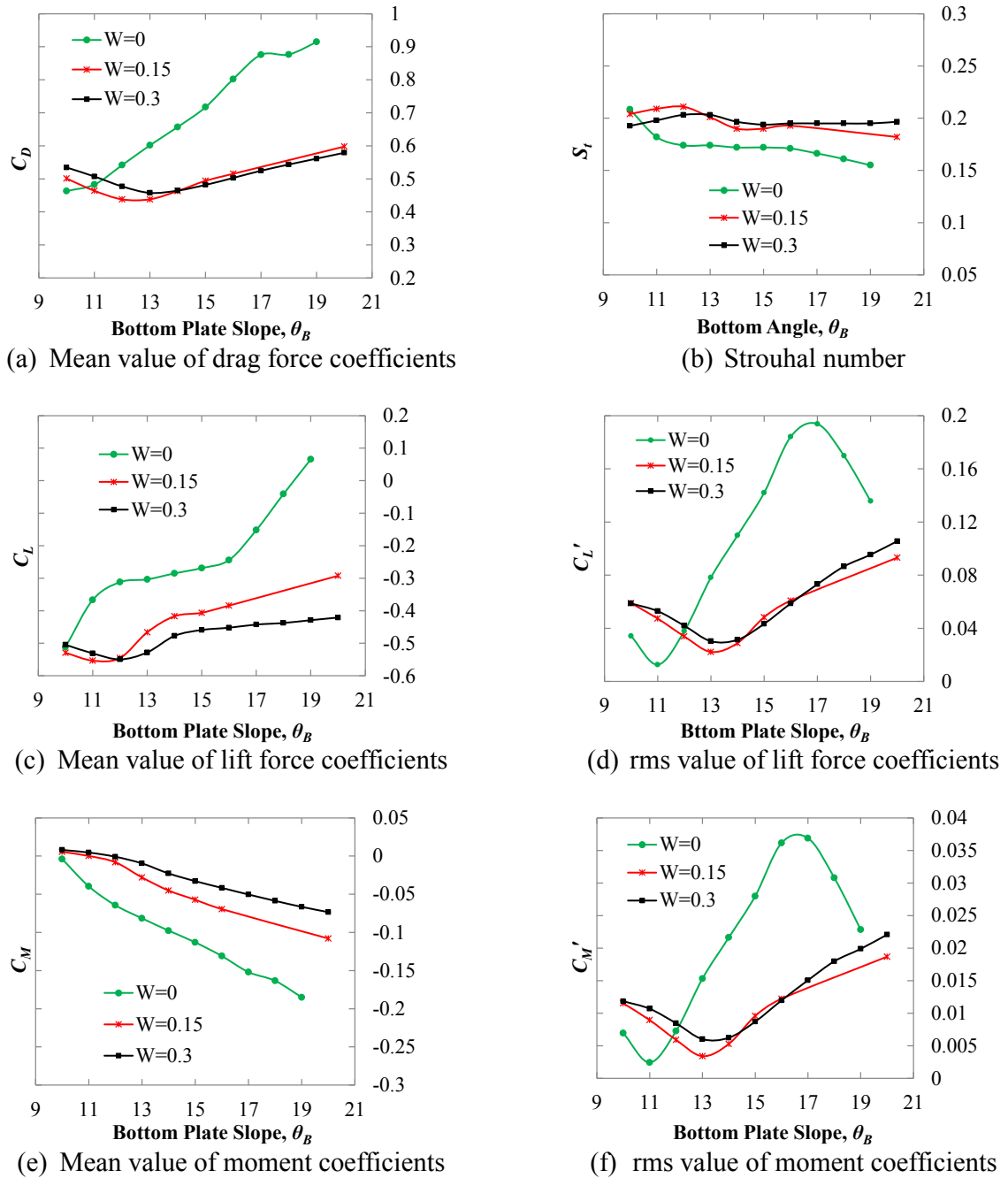


Figure 5.19: Cross-sectional view of the hexagonal bridge deck and importation notations

Figure 5.20: Procedure changing the width ratio (W) and bottom plate slope (θ_B) for deck without fairing

shows sensitivity to the width ratio (W). However, the sensitivity of bottom plate slope (θ_B) decreases significantly as the width ratio (W) increases i.e. shifts from pentagon to hexagon. This is because, as the width ratio increases the length of the bottom plate slope (θ_B) decreases (Fig.5.20), as a result the sensitivity of the bottom plate slopes (θ_B) on steady state force coefficients decreases too.

Another important trend is as the deck changes from pentagonal ($W=0$) to hexagonal shape ($W=0.15$ and 0.3), the location of minimum drag and rms value of the force coefficients shifts from small to larger bottom plate slope (θ_B) of around 13° . Further, depending on the width ratio (W) value the trend and magnitude doesn't vary noticeably for hexagonal bridge decks ($W=0.15$ and 0.3). However, for hexagonal bridge decks ($W=0.15$ and 0.3) the lift value (C_L) increases significantly as compared to the pentagonal bridge decks ($W=0$). This is also should be mentioned that in the last section for pentagonal shaped bridge deck, the bottom plate slope was altered by changing the side ratio (R) and here in this section for pentagonal bridge deck the bottom plate slope was varied by

Figure 5.21: Influence of width ratio (W) on steady state force coefficients

changing the nose location. However, no significant variation was found in the results for these two strategies to change the bottom plate slope (θ_B) for the pentagonal bridge deck.

In the last chapter we showed that either pressure distribution or velocity distribution alone can explain the trend in the result very well. Fig.5.22 compares the time averaged velocity distribution for the selected pentagonal and hexagonal bridge decks. As can be seen hexagonal bridge deck has larger bottom surface leading edge separation and smaller trailing edge separation.

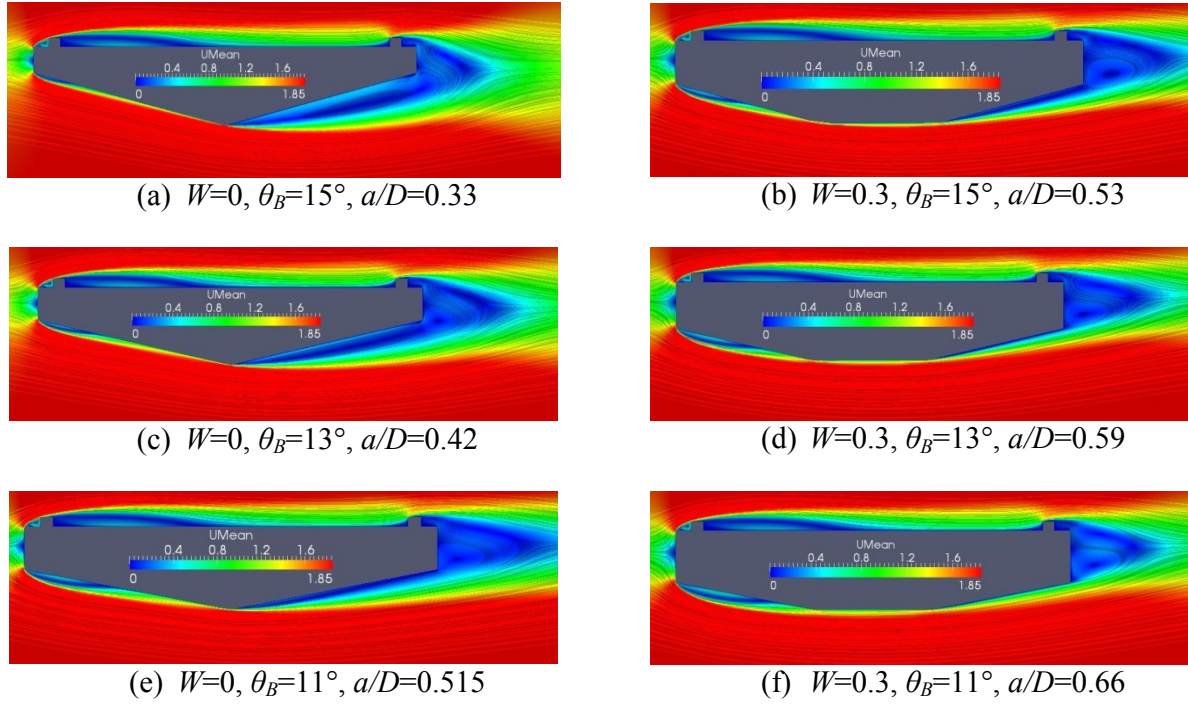


Figure 5.22: Influence of bottom plate slope (θ_B) on flow field for the pentagonal and hexagonal bridge deck

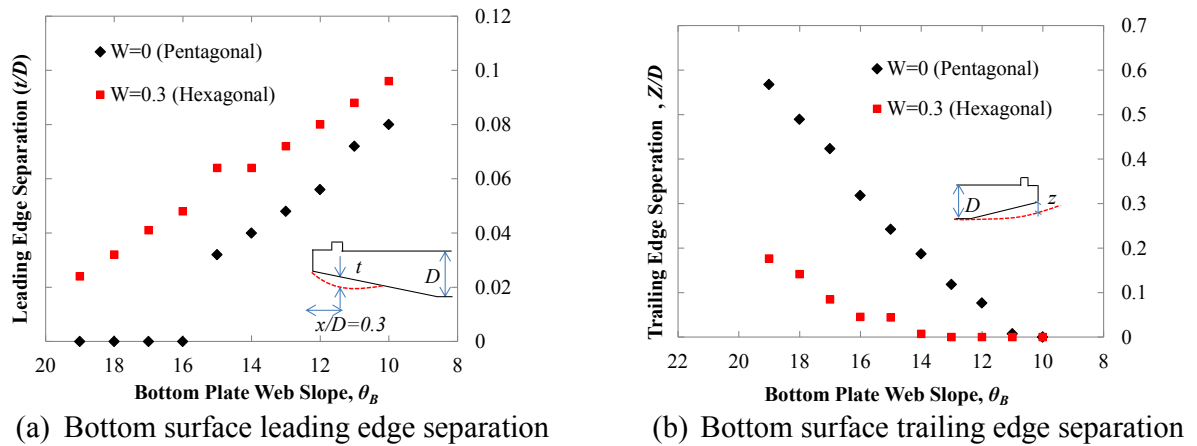


Figure 5.23: Influence of bottom plate slope (θ_B) on leading and trailing edge flow separation

From the velocity distribution in the vertical plane we calculated the boundary layer separation height at the leading and trailing edge of bridge decks. Fig.5.23 plots the bottom surface leading edge and trailing edge separation height for various bottom plate slopes (θ_B). Fig.5.23 reflects the general observation we made earlier in quantitative manner. The hexagonal bridge deck has larger leading edge separation and smaller trailing edge separation. Further, in case of hexagonal deck, the trailing edge flow separation stops at larger bottom plate slope (θ_B) at around 13°

Based on this observation, the trend in the steady state force coefficients can be explained. In case of hexagonal bridge deck, it has larger bottom surface leading edge separation, in another word,

larger downward force. This leading edge separation provides extra downward force than pentagonal bridge and increases the negative lift value. While the drag and rms value depends on the wake size and trailing edge separation. For pentagonal bridge trailing edge separation stops at a bottom plate slope (θ_B) of 11° , yet for hexagonal bridge deck the separation stops at much larger bottom plate slope ($\theta_B=13^\circ$). As the trailing edge separation stops, then the wake size is nothing but the side depth (a/D). For example, in Fig.5.22(b), for bottom plate slope (θ_B) of 15° , still there is trailing edge separation. Hence, the total wake size is larger ($z+a$) and the section possesses larger drag and rms value. If the bottom plate slope is decreased to 13° (Fig.5.22(d)), the trailing edge separation stops and the total wake size decreases ($a/D=0.59$), as a result the drag and rms value decreases. However, further decrease in bottom plate slope to 11° (Fig.5.22(f)), increases the wake size ($a/D=0.66$) again as the side depth (a) increases.

5.2.2 Influence of Inspection Rail

In practical bridges inspection rails are often attached at the bottom deck surface to install the overhead and gantry cranes. The deck shapes we discussed earlier in this and the last chapter, the bottom surface of the deck plays an important role for controlling the flow and keeping it attached to the deck surface. Presence of handrail will surely disturb the flow and thereafter the responses. Further, location of the handrail will also influence the responses. In this section we discuss the influence of inspection rail and its location on aerodynamic responses. Simulation was conducted for hexagonal bridge deck with a bottom plate (θ_B) slope of 11° . The influences of four different locations of inspection rails were explored. Fig.5.24 illustrates the locations of inspection rails utilized for the investigation.

Table 1 compares the important aerodynamic responses among various cases of inspection rails. As can be seen attachment of the inspection rail increases the drag and reduces the negative lift value and the shedding frequency. If we compare among the locations of inspection rail, Case-III and IV have lower responses than the other two cases. The most important criteria would be the sign of the lift force and the magnitude of the drag force. As the table depicts, Case-III and IV have negative lift value while other two cases possess positive lift value. Further, for those two cases the drag was also lower than the other cases.

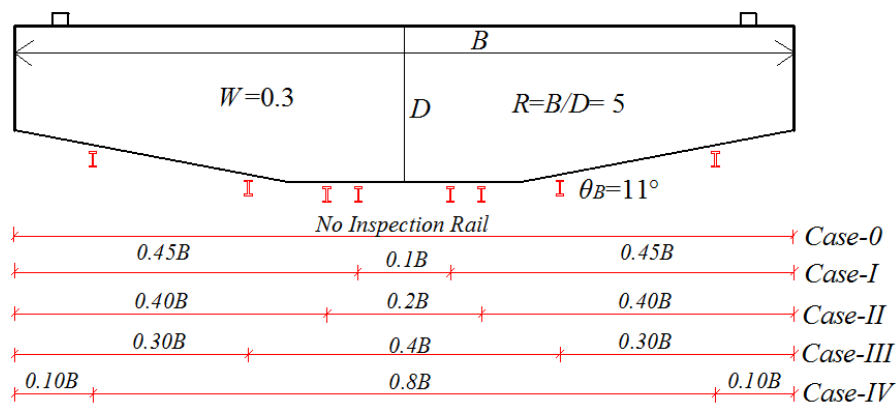
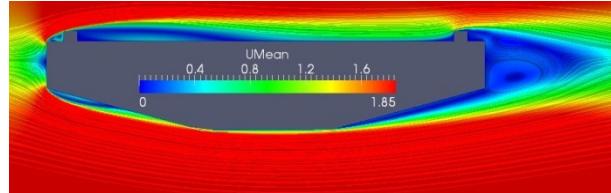


Figure 5.24: Inspection rail and its location

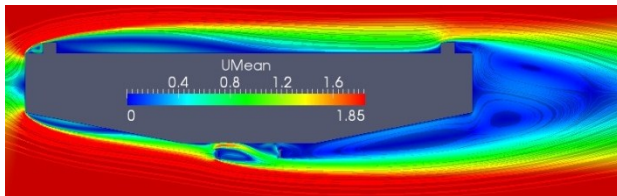
Fig5.25 shows the time averaged flow pattern for all five cases we considered in this section. The trend in Fig.5.25 is similar to the trend we found in Table 1. The inspection rail influences the bottom deck flow significantly. Due to the presence of the inspection rail, the early flow separation occurs at the bottom deck surface. Cases-I and II have the largest separation, as a consequence the shear layer velocity decreases, decreasing the negative lift value and Strouhal number (S_t). This separated flow would also affect the wake of the deck and thereafter the responses. To observe the wake behavior, velocity distribution at $0.25D$ downstream of the deck is plotted at Fig.5.26. Here also, the case-I and case-II have much larger wake size as compared to the other cases and the Case-IV has the smallest wake size as compared to the other three cases and very close to the basic section (Case-0). Therefore, the inspection rail should be placed at the inclined web plate rather than at the bottom horizontal plate (b) from aerodynamic point of view.

Table 5.1: Influence of inspection rail and its location on aerodynamic response

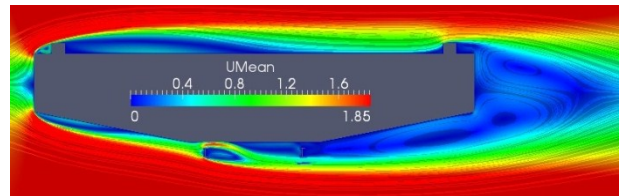
Case No.	Mean Drag (C_D)	Mean Lift (C_L)	Mean Moment (C_M)	rms Lift (C_L')	rms Moment (C_M')	Strouhal No. (S_t)
0	0.507	-0.531	0.0046	0.0529	0.0106	0.198
I	0.724	0.011	-1.5721	0.0348	0.0940	0.131
II	0.649	0.024	-1.6181	0.0502	0.1332	0.129
III	0.623	-0.205	-0.8020	0.0334	0.1124	0.157
IV	0.569	-0.272	-0.3455	0.0459	0.1737	0.177



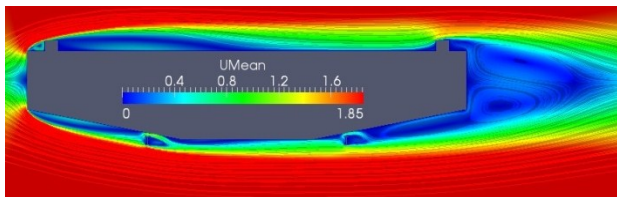
(a) Case-0



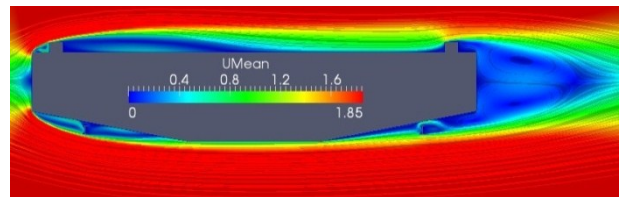
(b) Case-I



(c) Case-II



(d) Case-III



(e) Case-IV

Figure 5.25: Influence of inspection rails on the flow field around the bridge deck

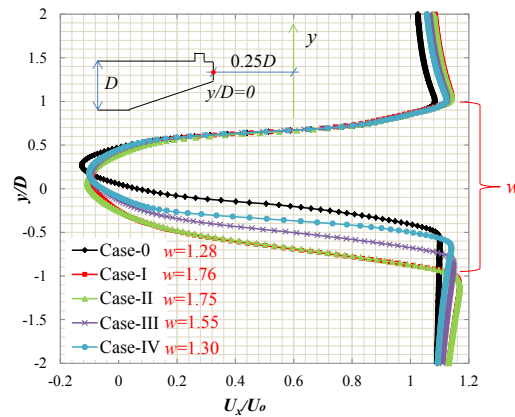


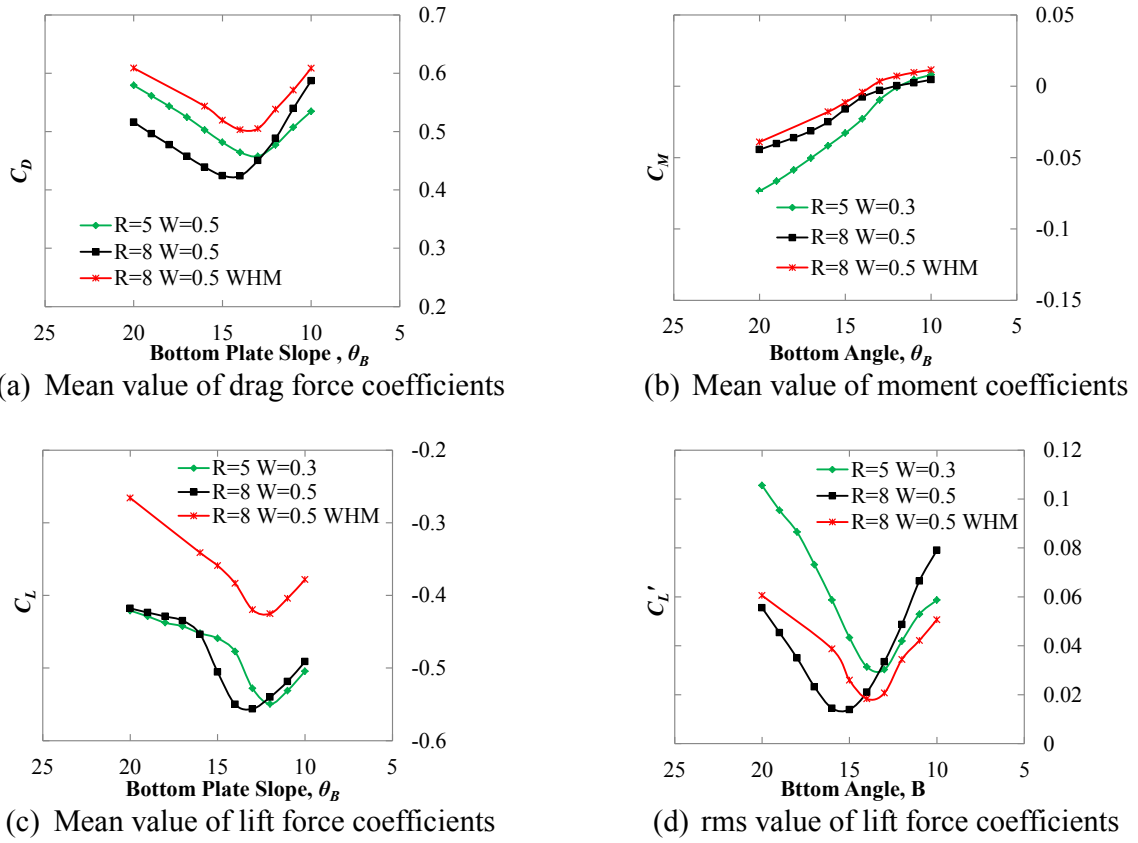
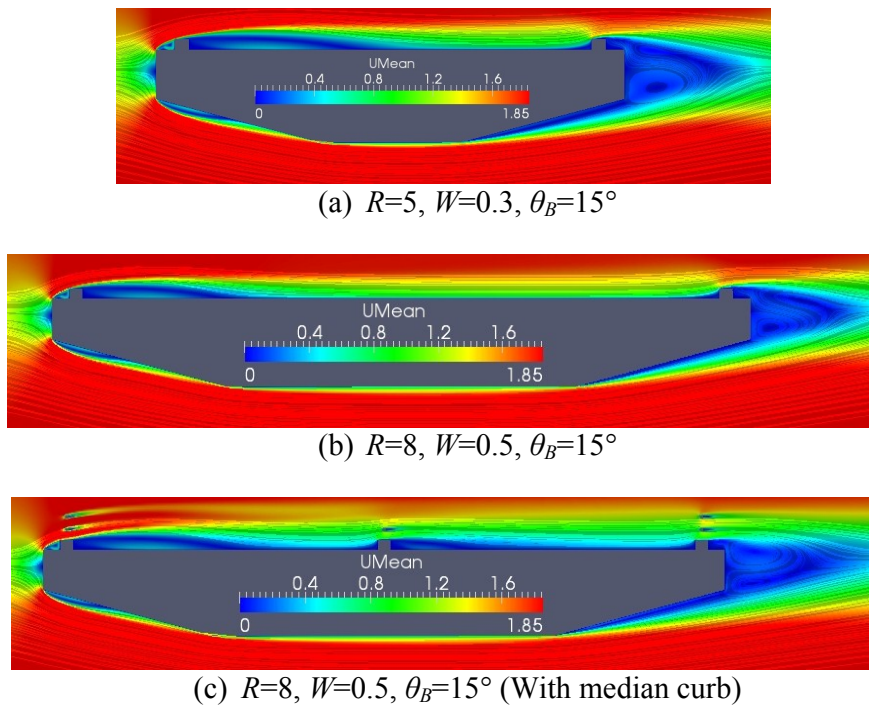
Figure 5.26: Influence of inspection rail on the bridge deck wake size (w)

5.2.3 Influence of Side Ratio (R) and Median Curb

This section demonstrates the influence of side ratio (R) on aerodynamics of the hexagonal bridge decks. Using this opportunity we also checked the effects of handrails and median curb. Two sets of simulation were conducted. The first one is for side ratio (R) of 8 without handrail and median curb. For the second set of simulation, both the handrail and the median curb (WHM) were installed. For both of these cases, a width ratio (W) of 0.5 was chosen. The bottom plate slope (θ_B) was varied from 20° to 10° . The Reynolds number (Re_B) was set to 9.7×10^4 for the deck with a side ratio (R) of 8, yet the inlet velocity (U) was kept same among all the simulations.

The steady state force coefficients for the bridge deck with a side ratio (R) of 5 and 8 are compared in Fig.5.27. Except the mean value of moment (C_M), the other responses show quite noticeable sensitivity to the variation side ratio (R) and the presence of the median curb. The mean lift (C_L) value doesn't alter significantly when the side ratio (R) changes, yet the negative lift value decreases significantly due to addition of handrail and median curb. However, the mean drag value and rms of lift force show sensitivity to the side ratio (R), handrail and median curb. When the side ratio (R) increases from 5 to 8, the optimum response shifts to the larger bottom plate slope ($\theta_B = 15^\circ$). With the addition of handrail and median curb, the bottom plate slope (θ_B) for optimum response decreases again and shifts to a value near about 14° - 13° .

The time averaged flow fields are summarized for a particular bottom plate slope in Fig.5.28. By observing the flow it can be confirmed that the presences of the median curb governs the responses rather than the handrail. Definitely, the presence of handrail increases the drag. However, it doesn't disturb the boundary layer flow behavior. On the other hand the median curb directly takes part to disturb the boundary layer flow field. When the side ratio (R) is increased from 5 to 8, the bottom horizontal plate (b) becomes longer. Hence, the separation tendency of the flow decreases and the trailing edge separation stops at a larger bottom plate slope (θ_B). That's how the optimum location of bottom plate slope (θ_B) increase for large side ratio (R). When the median curb is attached to the top deck, it makes the flow slower and the trailing edge flow separation appears again for the same bottom plate slope (Fig.5.29). Therefore, smaller bottom plate (θ_B) is required for stopping the trailing edge flow separation and the optimum location shifts.

Figure 5.27: Influence of side ratio (R) and median curb on steady state force coefficientsFigure 5.28: Influence of side ratio (R) and median curb on flow field around the bridge deck

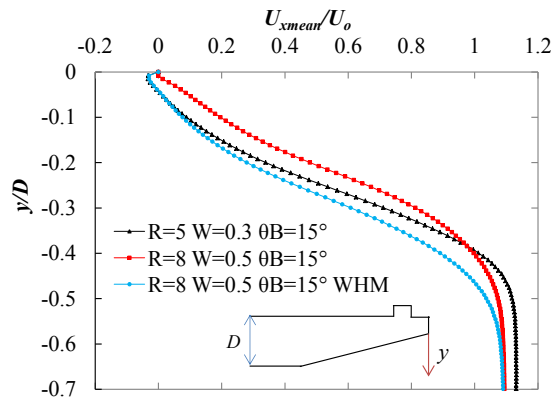


Figure 5.29: Influence of side ratio (R) and median curb on the trailing edge boundary layer flow separation

5.3 Concluding Remarks

This chapter provided an overview of the influences of various shaping parameters such as bottom plate slope (θ_B), curb angle (β), curb height (h/D), width ratio (W) and side ratio (R) etc. on the aerodynamics of the bridge deck without fairing. In addition, effects of Reynolds number (Re_B) were also explored. As a basic conclusion, pentagonal bridge deck exhibits better aerodynamic performance than the hexagonal bridge. Hexagonal bridge deck requires much larger bottom plate slope (θ_B) to reach the optimum steady state responses. Depending on the location of inspection rail and presence of the median curb the aerodynamic behavior alters quite noticeably. Further, Reynolds number (Re_B) effects on bridge deck without fairing are also found to be similar to the bridge deck with fairing.

Similar to the bridge deck with fairing, bridge deck without fairing also owns some important flow feature such as the top surface leading edge flow separation, bottom surface leading and trailing edge flow separation etc. Their roles on controlling steady state responses are also similar to the bridge deck with fairing. However, unlike bridge deck with fairing, in case bridge deck without fairing the negative lift force was controlled by the leading edge flow separation.

We found that Separation Interference Method (SIM) improves the aerodynamic performance of bridge decks by shortening the top surface leading edge flow separation and better performance can be obtained by placing the curb angle (β) and height (h/D) at 27° and .01, respectively. Similar to past experimental work of Kubo *et al.* (2007), we also found that small bottom plate slope ($\theta_B=11^\circ$) possess minimum aerodynamic responses. A smaller bottom plate slope (θ_B) the trailing edge separation stops and improves the aerodynamic behavior. With the increases of Reynolds number (Re_B) the trailing edge separation stops at a larger bottom plate slope (θ_B) and value of optimum bottom plate slope (θ_B) increases. That's how the minimum drag value was obtained at a bottom plate slope (θ_B) of 12° in past experimental work (Kubo *et al.* 2007).

Aerodynamic responses increases and becomes less sensitive to the bottom plate slope (θ_B) when the deck shape is altered from pentagon to hexagonal shape. Further, depending on the width (W) and side ratio (R), larger bottom plate slope (θ_B) is required to obtain the optimum aerodynamic

responses. At larger width (W) and side ratio (R), the width of the bottom horizontal plate (b) increases. Therefore, the flow remains attached to the trailing edge even at large bottom plate slope (θ_B) at around 15° . However, when the median curb is attached to the section, the flow becomes slower; requiring smaller bottom plate slope ($\theta_B=14^\circ$ - 13°) to stop the trailing edge separation.

Installation of inspection rail and median curb affects the flow field significantly. Based on our investigation it came out that inspection rail should be placed at the inclined bottom plate rather than the bottom horizontal plate (b) to reduce the trailing edge separation. On the other hand, median curb should be placed at the mid-width of the bridge deck. In case the median curb is placed near the edge curb, it may jeopardize the effectiveness of SIM.

Chapter 6

Bridge Deck Shaping Effects on Dynamic Response

The aerodynamic response of long-span cable-supported bridge decks can be broadly divided into steady state and dynamic responses. Steady state response mainly indicates the deformation of the deck due to static wind actions such as drag, lift and moment. On the other hand, dynamic responses are associated with the vibration of the bridge deck due to dynamic wind actions such as vortex induced vibration and flutter instability. From wind resistant design point of view both of these responses are important and treated carefully during the design procedure.

In the last two chapters we explored the influence of various shaping parameters on steady state responses of the bridge deck with and without fairing. Based on our investigation we found a number of important trends in the results due to variation of shaping parameters and some important flow features those controls the static responses. However, those findings were based on steady state responses only. It is equally important to examine the influence of shaping parameters on dynamic responses too.

We choose some particular sections having distinct steady state response and checked their dynamic response characteristics. In addition, the trend and aerodynamic response we found can be explained by means of some common flow features such as the leading edge top and bottom surface

flow separation and the trailing edge flow separation. It is also demanding to explore the implication of those flow features on dynamic responses.

This chapter focuses on the shaping effects on dynamic response of the bridge decks. Flutter derivatives of some particular shapes were calculated to evaluate their flutter characteristics both for the deck with and without fairing. Unsteady pressure characteristics were explored to predict the role of various important flow features on aerodynamic damping characteristics. Forced-vibration simulations were conducted with low amplitude not to hamper the characteristics of the flow features. A heaving amplitude (η_o/B) of 0.006 and torsional amplitude (α_o) of 1° were utilized to conduct the forced vibration simulation.

The chapter is broadly divided into two parts. The first part deals with the bridge deck with fairing and second part addresses the bridge deck without fairing. All the simulations were conducted at a Reynolds number (Re_B) of 5.0×10^4 for basic section only without any handrail. Aerodynamic analyses were carried out by employing the procedure presented in chapter 2. Methodology discussed in chapter 3 (Secs. 3.7 and 3.10.2) was used to setup model for the dynamic simulation.

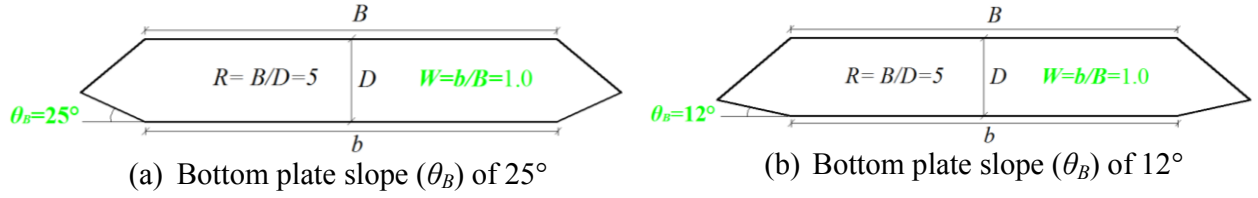
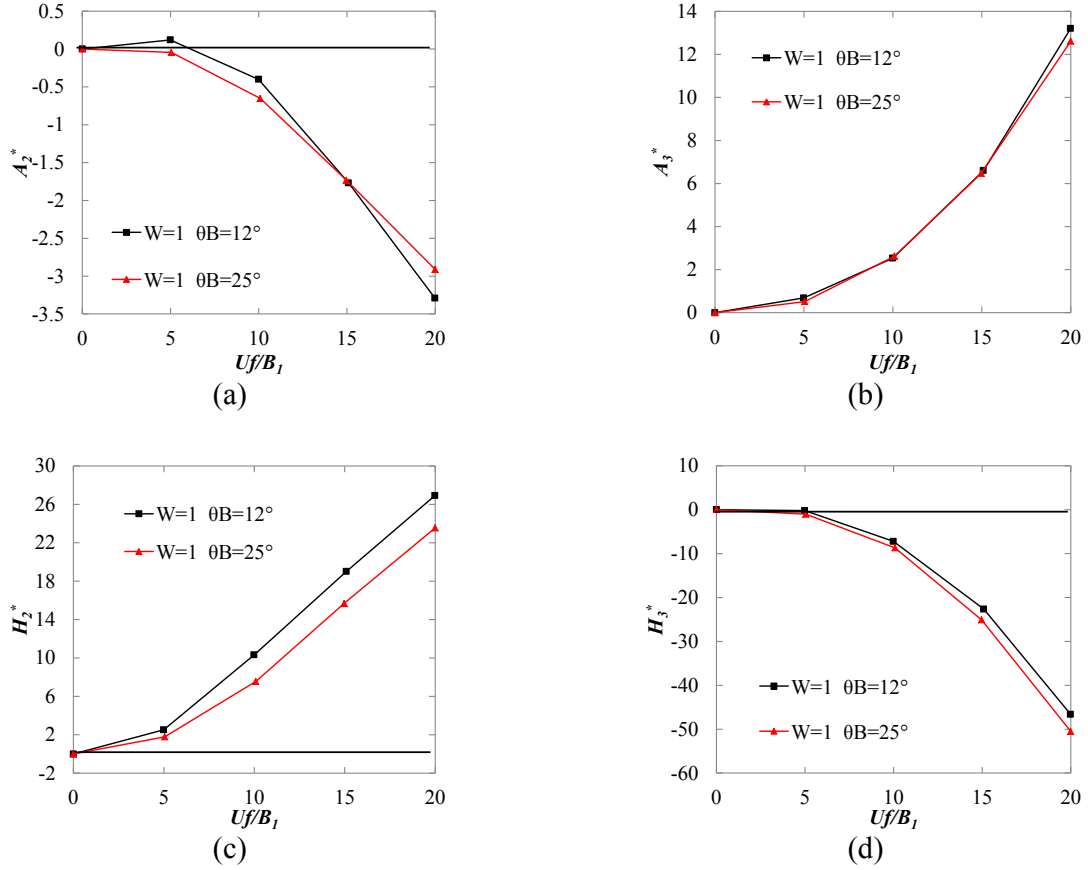
6.1 Behavior of Bridge Deck with Fairing

The behavior and influence of bottom plate slope (θ_B) on aerodynamic response showed different trend depending on the width ratio (W) for bridge deck with fairing. Therefore, we selected the width ratio (W) of 1 and 0.5 to observe the influence of bottom plate slope (θ_B) on dynamic response. Both the torsional and heaving mode flutter derivatives were calculated. Torsional flutter derivatives were extracted by conducting forced vibration simulation in torsional mode, yet the heaving mode flutter derivatives were obtained by employing the interdependency relationships among flutter derivatives. The relationships were discussed in Chapter 2 (Sec.2.3.2.2) and validated later in chapter 3 (Sec.3.10.2.1). Simulations were conducted at a Reynolds number (Re_B) of 5.0×10^4 . The reduced velocity (U/fB_I) was altered from 5 to 20 at an interval of 5 by changing the frequency (f) of vibration. The deck section had a side ratio (R) of 5 and simulation was conducted for basic section only without any handrail. The grid had an average y^+ value of around 2 with a maximum y^+ value of near about 6.50.

6.1.1 Bridge Deck with Edge Fairing ($W=1$)

In case of the bridge deck with edge fairing we found a trend in the result that, for a range of bottom plate slope (θ_B) of 25° - 20° , the aerodynamic responses were optimum and experienced the least flow separation. The aerodynamic response increased significantly for the bottom plate slope (θ_B) smaller than 15° . We selected two deck sections from these two distinct zones: i) $\theta_B=25^\circ$ and ii) $\theta_B=12^\circ$ to observe their dynamic response. Fig.6.1 compares the considered bridge deck sections.

Fig.6.2 summarizes the torsional flutter derivatives for these two deck shapes. The variation of the bottom plate slope (θ_B) affects all the torsional flutter derivatives except the A_3^* . From torsional

Figure 6.1: Comparison of the considered bridge deck for the edge fairing ($W=1$)Figure 6.2: Influence of bottom plate slope (θ_B) on torsional mode flutter derivatives for the width ratio (W) of 1

flutter point of view the A_2^* would be the most important derivative and from coupled flutter point of view H_3^* . From torsional flutter point of view, the deck with a bottom plate slope (θ_B) of 25° has better behavior as it possess larger negative value of A_2^* as compared to the 12° case. On the other hand, from coupled flutter point view 12° case has a bit better stiffness than the 25° case as it has smaller value of H_3^* . However, at low reduced velocity (Uf/B_1 of 5), the deck with a bottom plate slope (θ_B) of 12° has higher possibility of torsional vibration than for 25° case. By exploiting the interdependency relationship among flutter derivatives, the heaving mode flutter derivatives were derived and plotted in Fig.6.3. In case of heaving mode, the A_1^* and H_1^* are the two most important flutter derivatives. The bridge deck with a bottom plate slope (θ_B) of 25° has larger aerodynamic damping over 12° case in heaving mode too. Even so, the variation of bottom plate slope (θ_B) doesn't affect the A_1^* .

We found that both in torsional and heaving mode, the bridge deck with a bottom plate slope (θ_B) of 25° have a bit larger aerodynamic damping than 12° case. To obtain a better idea about the distribution of damping forces around the bridge deck, the unsteady pressure characteristics were explored as discussed in chapter 2. In addition this would also give us some information about the role of various important flow features that took place for this kind of bridge decks.

To recall the position and extent of various important flow features for these deck shapes, the time averaged velocity fields are compared in Fig.6.4. Differences in the flow field can be noticed conspicuously at the bottom surface leading and trailing edge side. By comparing the unsteady pressure characteristics for these two shapes, the role of those flow features can be understood in some extent.

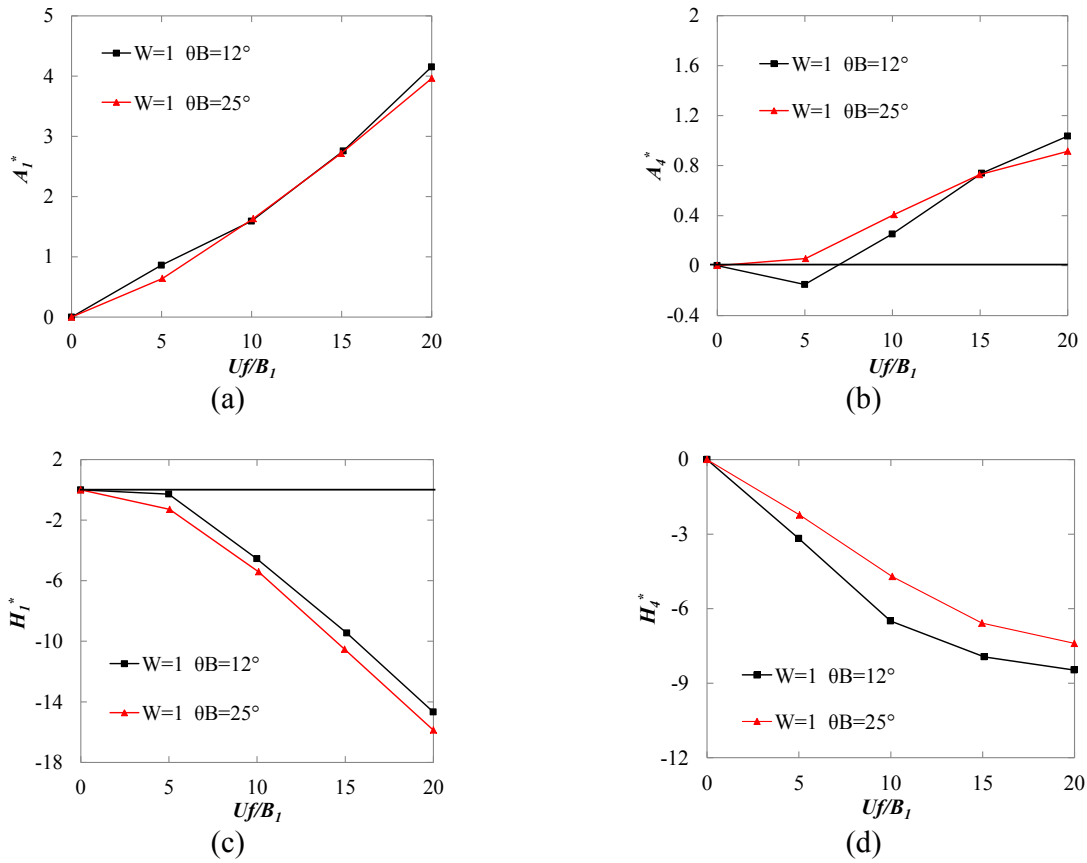


Figure 6.3: Influence of bottom plate slope (θ_B) on heaving mode flutter derivatives for the width ratio (W) of 1 determined from the interrelationship among the flutter derivatives

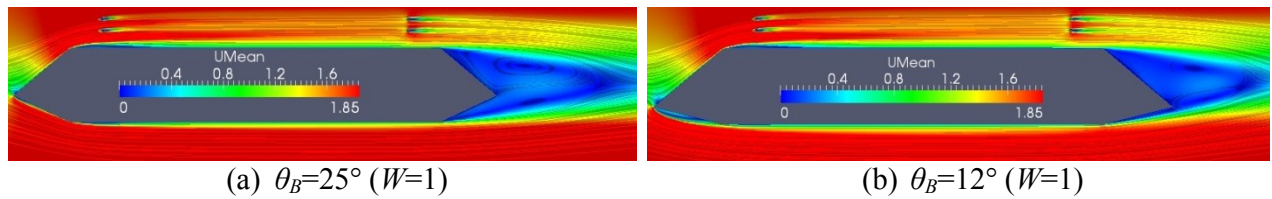


Figure 6.4: Comparison of time averaged velocity field for large and small bottom plate slopes (θ_B) of the bridge deck with the width ratio (W) of 1

Fig.6.5 compares the work done by the unsteady pressure in torsional mode for these two decks at reduced velocity (U/fB_l) of 5 and 15. In general, the damping lies on the top and bottom surface of the leading edge corner of bridge deck, while the excitation lies on the leading and trailing edge side fairing surface. The variation of bottom plate slope (θ_B) mainly affects the bottom surface leading and trailing edge side rather than top surface. At low reduced velocity ($U/fB_l=5$), the bottom surface leading edge corner separation acts as an excitation force. For bottom plate slope (θ_B) of 12° , it has wider separation area at the leading edge corner as compared to 25° case and similar trend can be found in Fig.6.5(c). However, the top surface leading edge separation provides damping to the system. Both the at the top and bottom surface, the trailing edge separation is mostly excitation force. The deck with a bottom plate slope of 25° has smaller excitation than 12° case. At high reduced ($U/fB_l=15$), the pressure characteristics remains same, yet the magnitude of damping and excitation force decreases.

To obtain the idea about the unsteady pressure characteristics in heaving mode, forced vibration simulations were conducted at reduced velocity (U/fB_l) of 5. The work done by the unsteady pressure is plotted in Fig.6.6. As can be seen, the characteristics of work done in heaving mode are almost similar to that of the torsional mode. Here also the deck with a bottom plate slope (θ_B) of 25° has smaller excitation at the trailing edge fairing than the 12° case, improving the aerodynamic damping characteristics of the bridge deck.

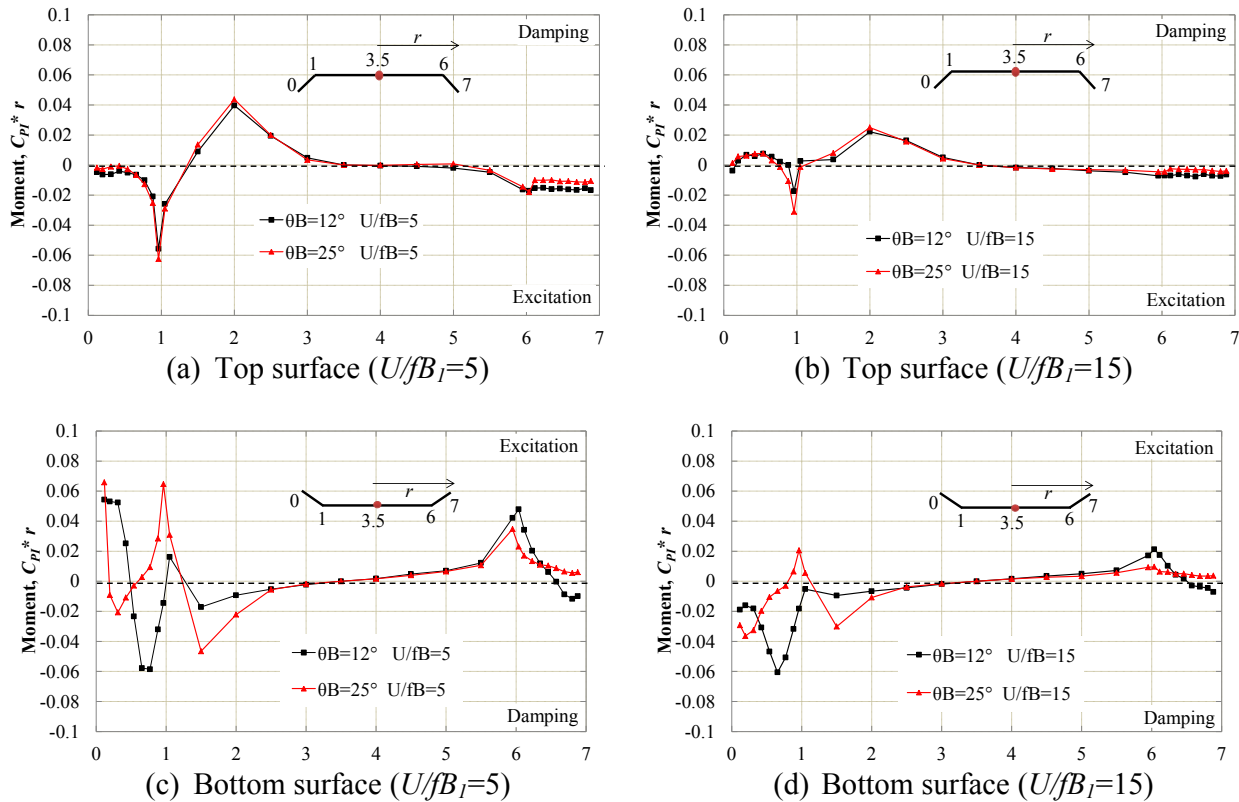


Figure 6.5: Influence of bottom plate slope (θ_B) on work done by the unsteady pressure in torsional mode for the width ratio (W) of 1

6.1.2 Streamlined Bridge Deck (W=0.5)

The streamlined bridge deck showed opposite trend in the result due to variation of bottom plate slope (θ_B) in relation to the deck with edge fairing. In case of streamlined bridge deck, the bridge deck with small bottom plate slope ($\theta_B \leq 15^\circ$) had a better aerodynamic responses as compared to the large bottom plate slope ($\theta_B = 20^\circ \sim 25^\circ$). Therefore, similar to the edge fairing case, for streamlined deck also we selected the bridge deck with same bottom plate slopes (θ_B) of 25° and 12° as shown in Fig.6.7.

Fig.6.8 depicts the torsional mode flutter derivatives for bottom plate slopes (θ_B) of 25° and 12° . As can be seen in case of streamlined case, flutter derivatives are more sensitive to the variation of bottom plate slope (θ_B) as compared to the edge fairing case (in Fig.6.2). The bottom plate slope (θ_B) of 12° has larger negative value of A_2^* than the 25° case indicating better torsional flutter stability. At low reduced velocity ($U/fB_I=5$) the variation is quite small and increases gradually as the reduced velocity (U/fB_I) increases.

For long-span bridge deck coupled flutter is another important aspect. The bottom plate slope (θ_B) of 12° has also better responses from coupled flutter standpoint as it possess smaller value of H_3^* . In terms of A_3^* , it shows reverse behavior, however, the variation in magnitude of A_3^* due to change in bottom plate slope (θ_B) is quite small as compared to the H_3^* . The heaving mode flutter derivatives were calculated from the interdependency relationships are plotted in Fig.6.9. In case of

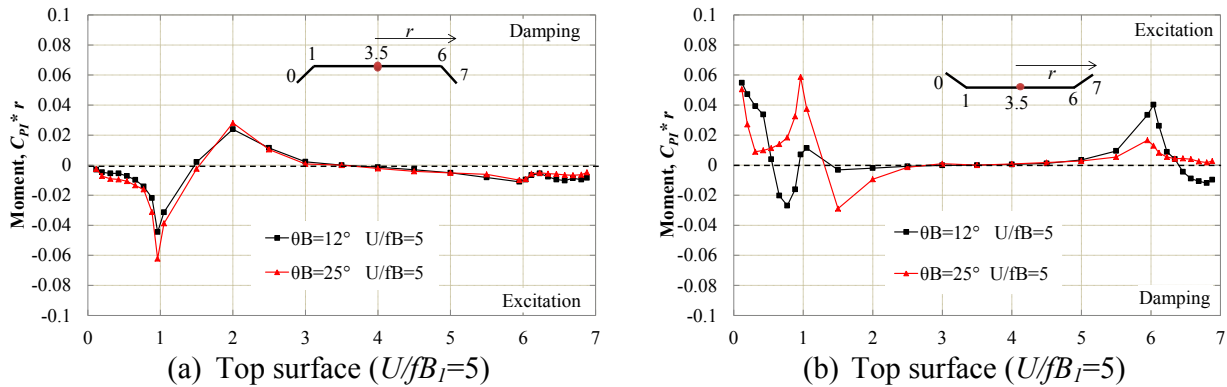


Figure 6.6: Influence of bottom plate slope (θ_B) on work done by the unsteady pressure in heaving mode for the width ratio (W) of 1

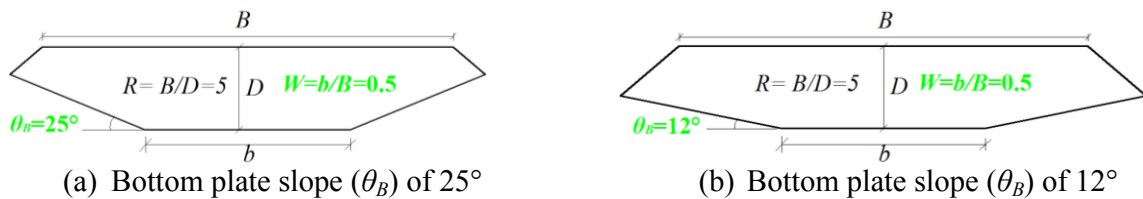


Figure 6.7: Considered bridge deck with distinct aerodynamic responses for the streamlined bridge deck

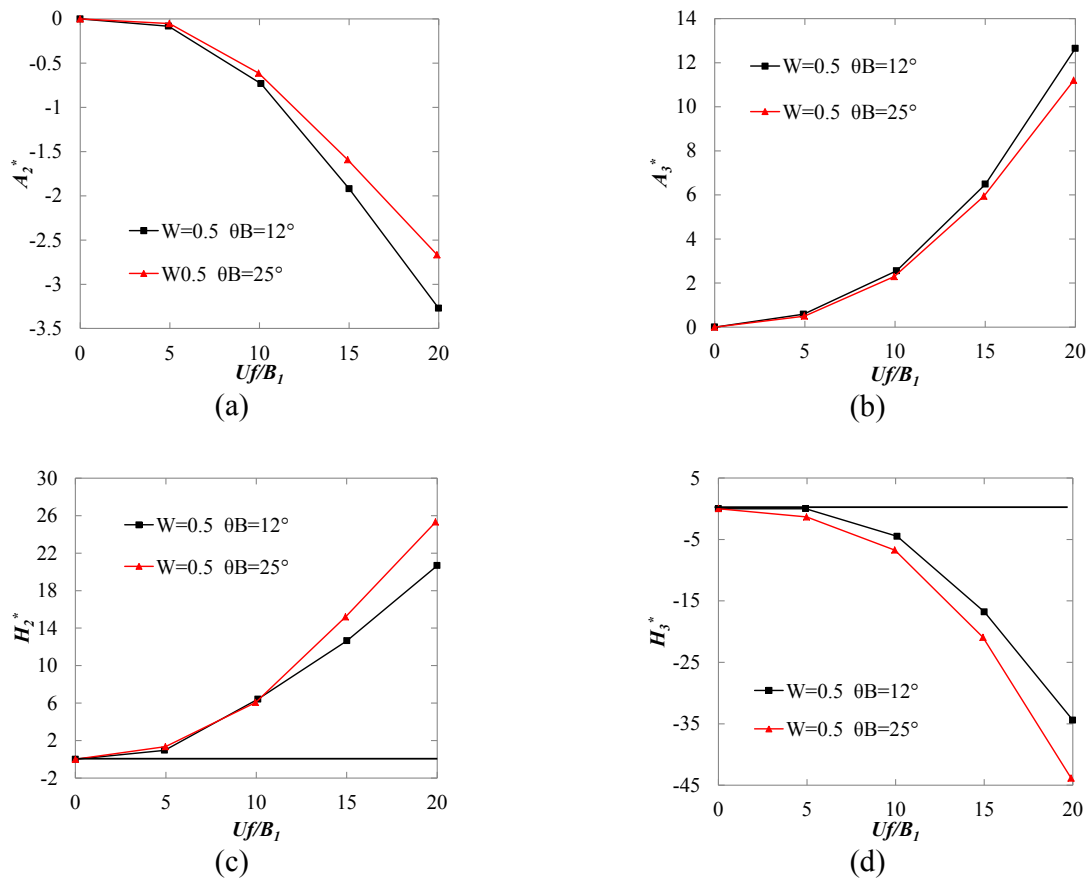


Figure 6.8: Influence of bottom plate slope (θ_B) on torsional mode flutter derivatives for the width ratio (W) of 0.5

heaving mode, the bottom plate slope (θ_B) of 12° has a bit smaller value of H_1^* than 25° and other flutter derivatives doesn't show any definite trend. However, the value of H_1^* remains negative in both of these cases. Therefore, result obtained based on A_2^* and H_3^* should be given priority.

Fig.6.10 compares the time averaged velocity distribution around the considered bridge decks to retrieve the flow fields. The bridge deck with bottom plate slope (θ_B) of 12° has smaller trailing edge separation and nose down situation as compared to the 25° case. Fig.6.11 shows the work done by the unsteady pressure characteristics in torsional mode. The characteristics of work by the unsteady pressure for streamlined ($W=0.5$) case are similar to the bridge deck with edge fairing as shown in Fig.6.5. However, the magnitude of the excitation force increases in the present case. Similar to edge fairing, here also the trailing edge separation is excitation force and the top surface corner provides damping force to the system. If a relative comparison is made between Fig.6.10 and 6.11, then it can be deduced that a deck with a larger separation ($\theta_B=25^\circ$) has completely excitation at the trailing edge side. However, the deck with a smaller bottom plate slope (θ_B) has mostly damping at the trailing edge side. In addition, in chapter 4 we also showed that a deck with a bottom plate slope (θ_B) of 25° had larger rms fluctuation, this also coincides with Fig.6.11. At higher reduced velocity the magnitude of damping and excitation force decreases. Moreover, in case of bottom plate slope (θ_B) of 12° , the leading edge bottom surface separation becomes damping completely at high reduced velocity ($Uf/B_l=15$).

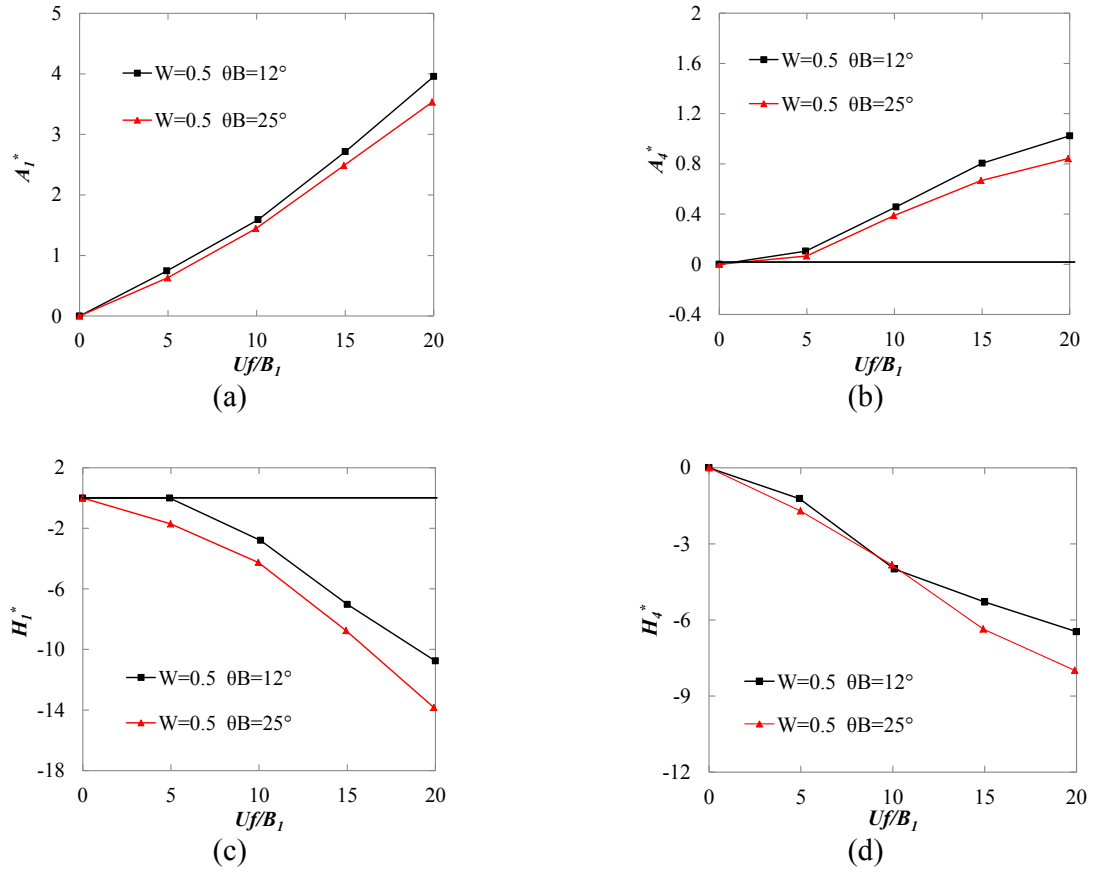


Figure 6.9: Influence of bottom plate slope (θ_B) on heaving mode flutter derivatives for the width ratio (W) of 0.5 determined based on the interrelationship among the flutter derivatives

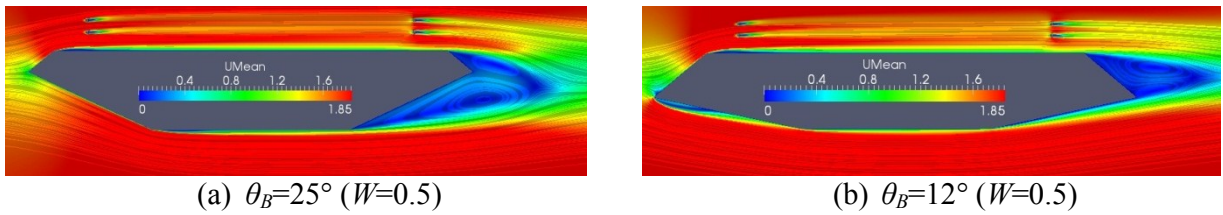


Figure 6.10: Comparison of time averaged velocity field for large and small bottom plate slopes (θ_B) of the bridge deck with a width ratio (W) of 0.5

Additional simulation was conducted at a reduced velocity (Uf/B_1) of 5 to obtain an idea about the distribution of work done by the unsteady pressure in heaving mode. Fig.6.12 shows the work done by the unsteady pressure in heaving mode. A like edge fairing case ($W=1$), the general trend in the distribution is similar to the torsional mode. The excitation force exists at the leading and trailing edge side fairing surface and a bottom plate slope (θ_B) of 25° has larger excitation force as compared to the 12° case.

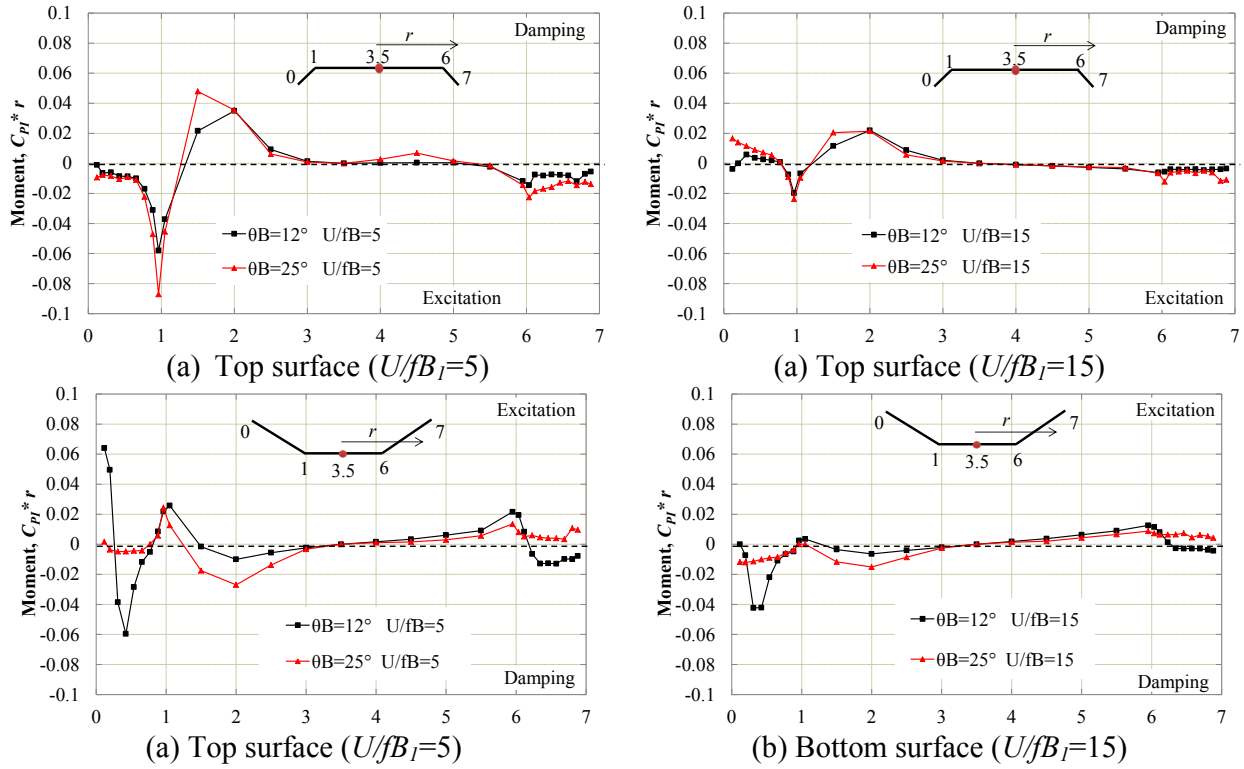


Figure 6.11: Influence of bottom plate slope (θ_B) on work done by the unsteady pressure in torsional mode for width ratio (W) of 0.5

In the last and this sections, we have shown the influence of bottom plate slope (θ_B) on dynamic response for a fixed width ratio (W). However, comparison can also be made among the decks having different width ratio (W) for a fixed bottom plate slope (θ_B). By comparing Figs.6.2 and 6.8 for torsional mode and Figs.6.3 and 6.9 for heaving mode, the influence of width ratio (W) on dynamic response can be understood. As can be seen the variation of width ratio (W) primarily affects the A_3^* and H_3^* . As the width ratio (W) decreases, the nose goes upward and improves the coupled flutter behavior of the bridge deck.

6.2 Behavior of Bridge Deck without Fairing

For bridge deck without fairing, we choose two important aspects: i) The influence of Separation Interference Method (SIM) and ii) The influence of the bottom plate slope (θ_B). Simulations were conducted in torsional mode only, as torsional mode instability was the main concern for this type of pentagonal shaped bridge (Kubo *et al.* 2007). Simulations were conducted at a Reynolds number (Re_B) of 5.0×10^4 . The reduced velocity (U/fB_l) was altered from 5 to 20 at an interval of 5 by changing the frequency (f) of vibration. The curb angle (β) and height (h/D) was set to 30° and 0.115 respectively. The grid had an average y^+ value of around 2.15 with a maximum y^+ value near about 8.25.

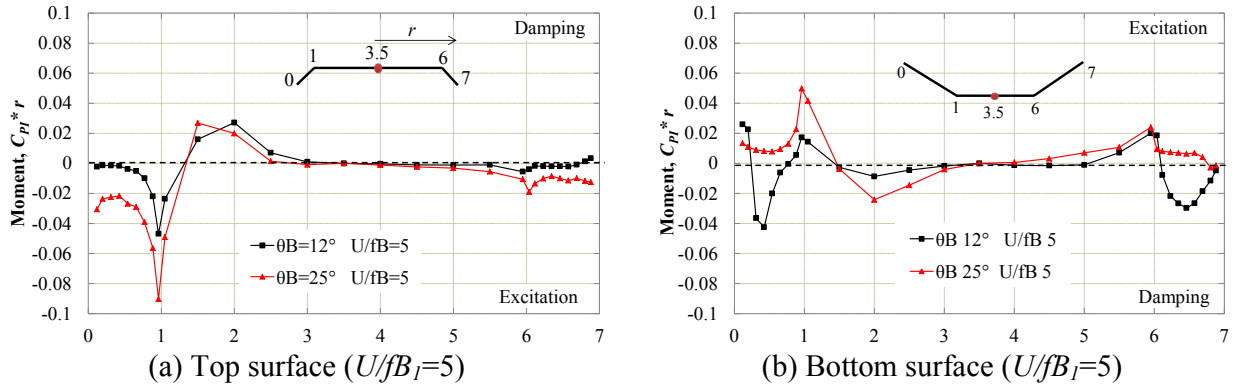


Figure 6.12: Influence of bottom plate slope (θ_B) on work done by the unsteady pressure in heaving mode for width ratio (W) of 0.5

6.2.1 Influence of Separation Interference Method (SIM)

In chapter 5, we showed that addition of curb at an optimum angle (β) and height (h/D) reduces the steady state responses significantly. Specially, the top surface leading edge separation decreased when the curb was placed at the leading edge side. To evaluate the effectiveness and influence of SIM on dynamic response, flutter derivatives were calculated. A bridge deck with a side ratio (R) of 5 and a bottom plate slope (θ_B) of 12° was considered. Fig.6.13 depicts schematic view of the deck sections. Forced-vibration simulation was conducted for the bridge deck with and without curb.

Fig.6.14 illustrates the influence of SIM on torsional flutter derivatives. Except the A_2^* and H_3^* , the other two flutter derivatives rarely alters due to addition of curb to the bridge deck. In case of with curb situation, the coupled derivatives H_3^* has smaller value indicating better stability than the without curb case. However, the most important criteria would be the sign and magnitude of A_2^* and is the most sensitive flutter derivatives found to be in Fig.6.14. As can be seen when there is no curb attached to the bridge deck, it shows almost positive value for the complete range of reduced velocity. However, the magnitude of A_2^* becomes negative and increases significantly when the curb is attached to the section. This implies that the SIM improves both the vortex shedding and torsional flutter stability of the bridge decks without fairing under wind actions.

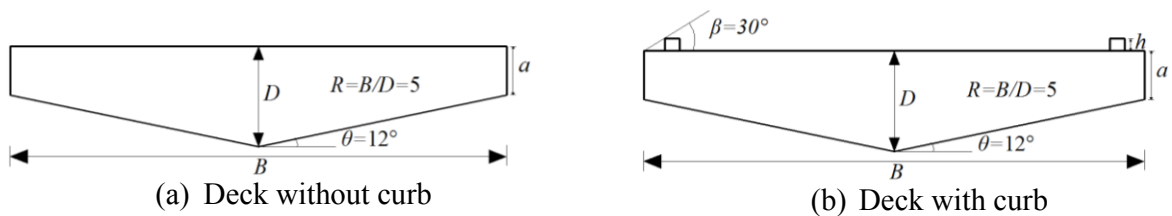


Figure 6.13: Considered bridge deck to show the influence of SIM on flutter derivatives

The time averaged flow fields are plotted in Fig.6.15. The difference in the flow separation at the leading edge top surface is clear. For these two bridge decks the top surface unsteady pressure characteristics are summarized in Fig.6.16. At the leading edge side mainly excitation can be observed. When the curb is attached to the section, the excitation force increases a bit at the leading edge corner, yet drops significantly just after curb location. The effectiveness of SIM can be better noticed at higher reduced velocity ($U/fB_1=15$) in Fig.6.16(b). At the leading edge side, the separated flow works as an excitation force for the without curb case and that become damping force when the curb is attached to the section.

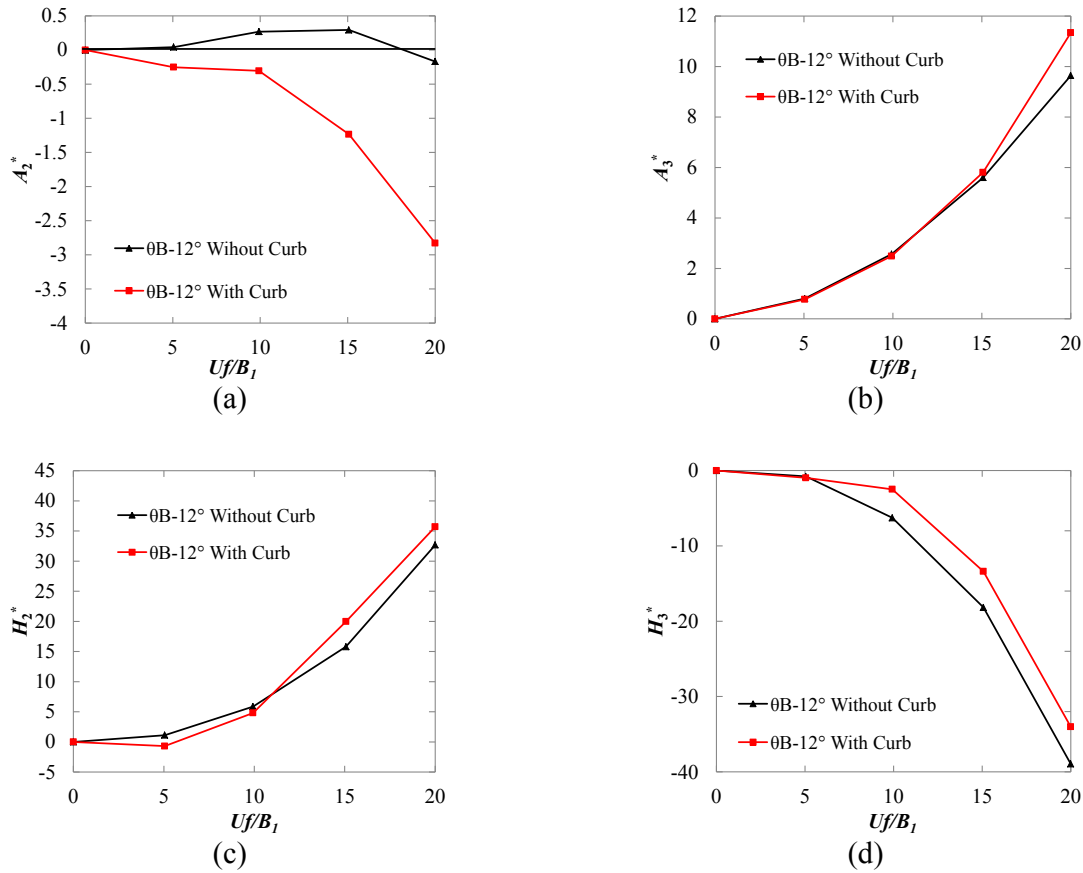


Figure 6.14: Influence of SIM on torsional flutter derivatives

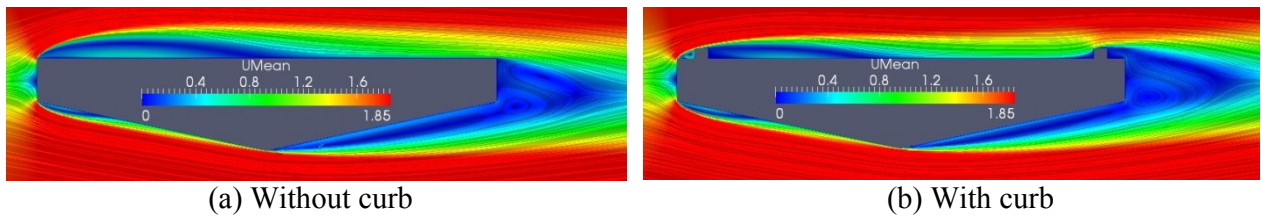


Figure 6.15: Influence of SIM on the flow field ($\theta_B=12^\circ$ and $R=5$)

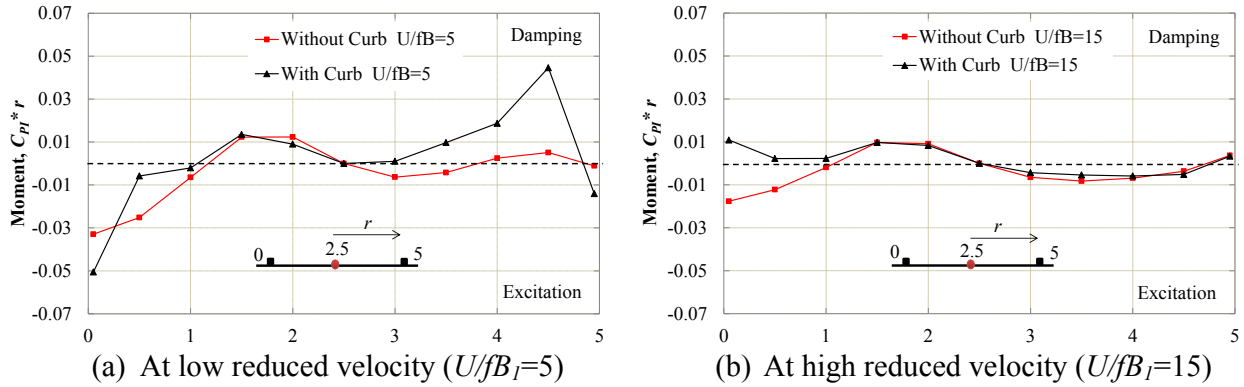


Figure 6.16: Influence of SIM on unsteady pressure characteristics of the deck top surface

6.2.2 Influence of Bottom Plate Slope (θ_B)

For pentagonal bridge deck, smaller bottom plate slope ($\theta_B=12^\circ$) possessed better steady state responses as compared to the large bottom plate slope ($\theta_B=15^\circ$). Fig.6.17 compares the considered bridge sections. Flutter derivatives for the bridge deck with a bottom plate slope (θ_B) of 15° were calculated and compared with the bottom plate slope (θ_B) of 12° evaluated previously in Fig.6.18. No significant influence of bottom plate slope (θ_B) on the flutter derivatives was found. Based on H_3^* , a bottom plate slope (θ_B) of 15° has slightly better stability than the 12° case. In the meantime, a bottom plate slope (θ_B) of 12° has slightly higher damping (A_2^*) than the 15° case. However, A_2^* is considered as a more reliable and efficient coefficient to predict the torsional instability of structures (Matsumoto 1996, Matsumoto *et al.* 1999 and Matsumoto *et al.* 2008a) than the other coefficients. Therefore, we should prioritize the trend shown by A_2^* i.e., the deck with a bottom plate slope (θ_B) of 12° has better torsional flutter stability than the 15° case.

Fig.6.19 compares the time averaged velocity distribution for these two bridge decks. The differences can be primarily observed at the bottom surface leading and trailing edge sides. A relative comparison between the unsteady pressure distributions would explain the role of those flow features on dynamic response. Fig.6.20 depicts the work done by the unsteady pressure for these two bridge decks. The variation of the bottom plate slope (θ_B) mainly affects the bottom surface pressure characteristic. A slight variation of the top surface pressure characteristic can be found at the trailing edge side where the flow reattachment occurs. Similar to last section, here also we find that this kind of top surface reattachment flow acts as a damping force at low reduced velocity ($U/fB_l=5$) and becomes excitation force at higher reduced velocity ($U/fB_l=15$).

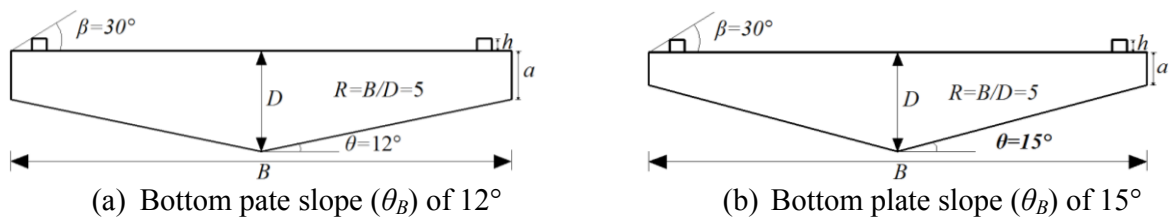


Figure 6.17: Considered bridge deck to show the influence of bottom plate slope on torsion flutter

On the other hand, the bottom surface leading edge separation is damping at low reduced velocity ($U/fB_f=5$) and remains as a damping at high reduced velocity ($U/fB_f=15$). The trailing edge flow separation shows different trend. At low reduced velocity ($U/fB_f=5$), this works as a damping force and at high reduced velocity ($U/fB_f=15$) this becomes excitation. Further, section with a larger separation ($\theta_B=15^\circ$) possesses a bit larger damping and excitation at low and high reduced velocity, respectively, as compared to the section with smaller flow separation ($\theta_B=12^\circ$). Therefore, this type of trailing edge flow separation decreases the torsional flutter stability at high reduced velocity. They will play an important role for initiating the flutter instability. This provides an explanation why in experimental work (Kubo *et al.* 2007) higher flutter wind speed was obtained at a smaller bottom plate slope ($\theta_B \leq 13^\circ$). Further, this also justifies the conjecture we made in chapter 5 that, a deck with small trailing edge separation may have higher flutter wind speed.

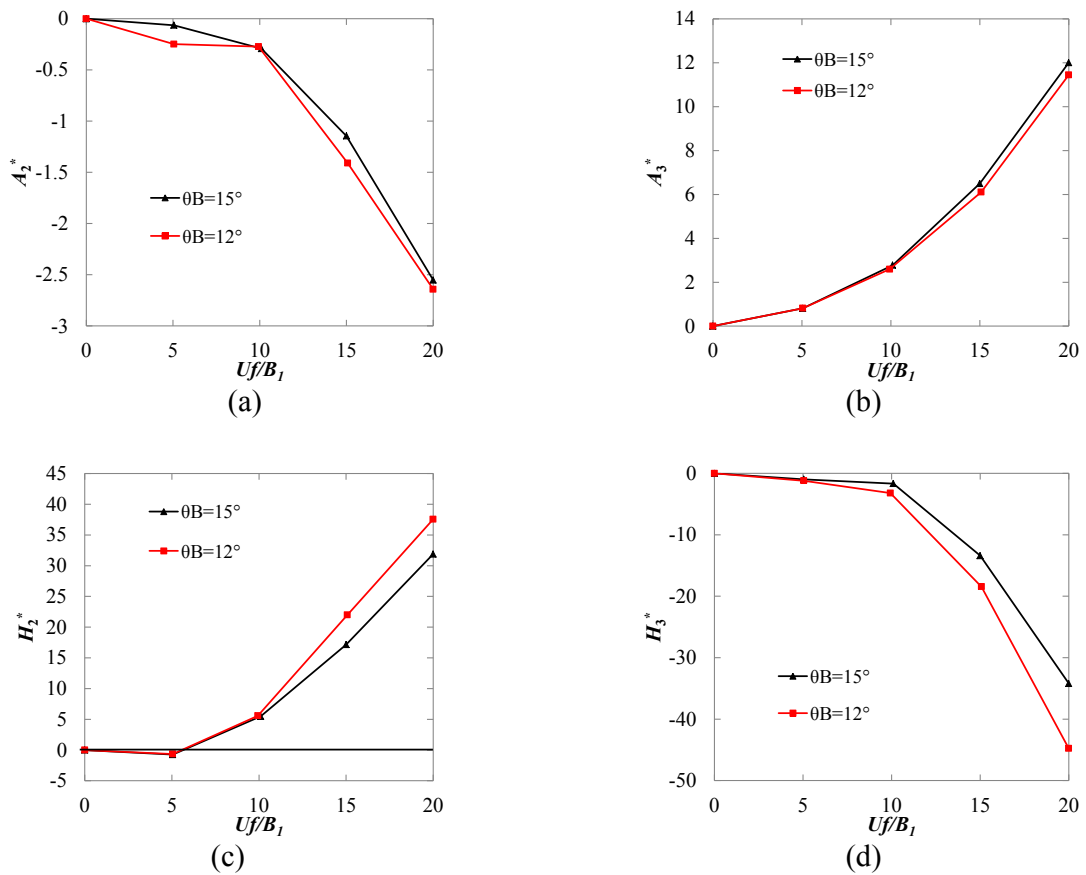


Figure 6.18: Influence of bottom plate slope (θ_B) on torsional flutter derivatives

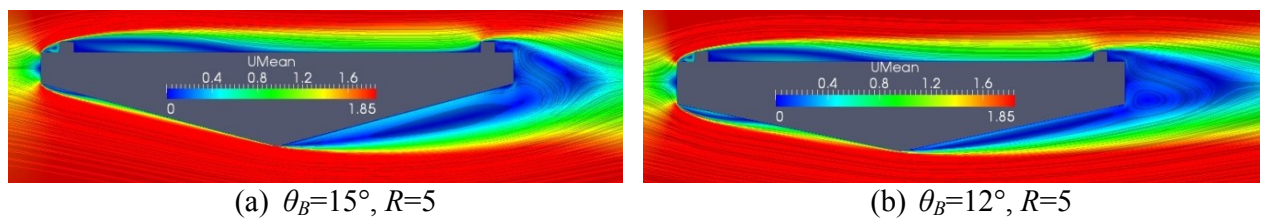


Figure 6.19: Influence of bottom plate slope (θ_B) on time averaged velocity field

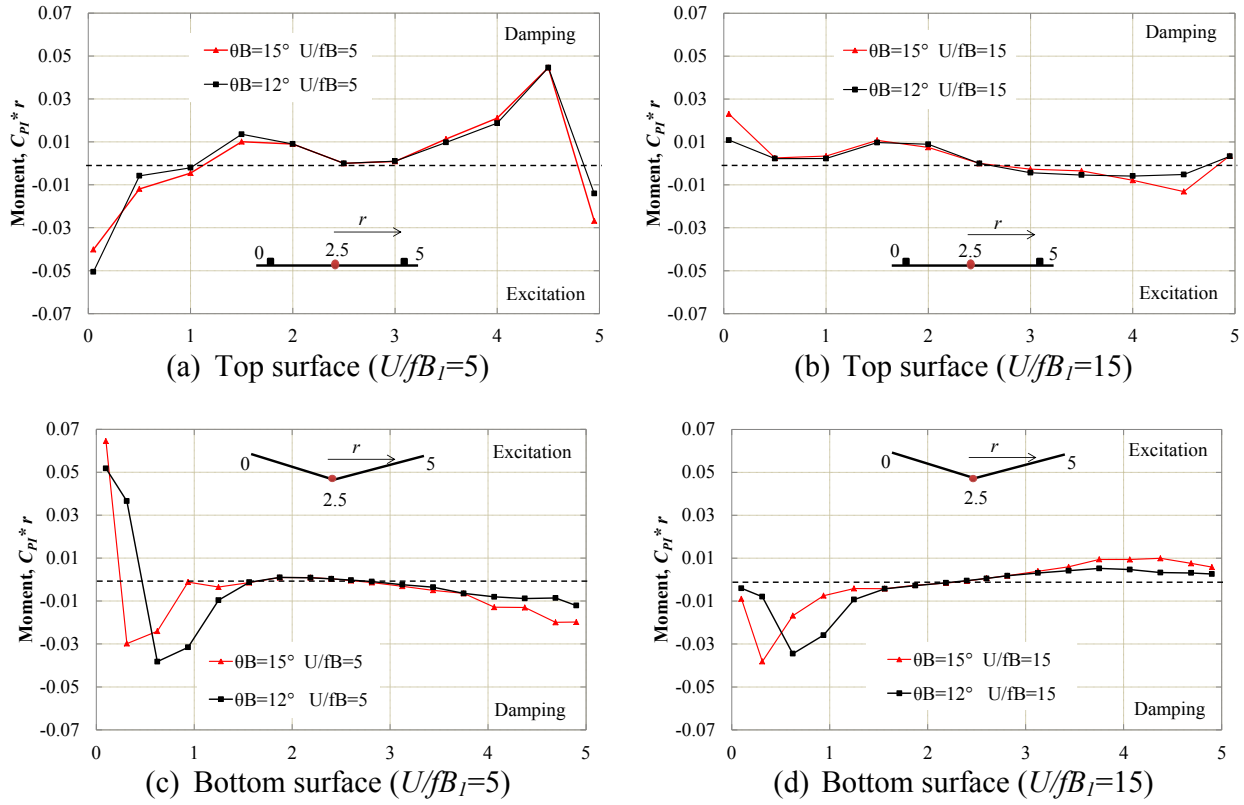


Figure 6.20: Influence of bottom plate slope (θ_B) on unsteady pressure characteristics

6.3 Concluding Remarks

The main objective of this chapter was to explore the influence of important shaping parameters on dynamic response of the bridge decks. Based on our previous observation in chapter 4 and 5, some specific deck shapes were chosen to check their aeroelastic characteristics by means of flutter derivatives. Along with this, the implication of various flow features on aeroelastic instability were also tried to reveal through unsteady pressure characteristics.

Both in the case of bridge deck with and without fairing, the variation of shaping parameters mainly affected the A_2^* , H_3^* and H_I^* derivatives. It was found that the trend we found in the dynamic response also has similar trends in result that we obtained in steady state response for bridge deck with fairing. For the bridge deck with edge fairing ($W=1$), comparatively large bottom plate slope ($\theta_B=25^\circ$) had better dynamic responses as compared to the small bottom plate slope ($\theta_B=12^\circ$). For deck with large bottom plate slope ($\theta_B=25^\circ$) had larger damping both in the torsional and heaving mode. In case of streamlined bridge deck, reverse behavior was found. The deck with a small bottom plate slope ($\theta_B=12^\circ$) exhibited better stability from torsional and coupled flutter point of view with respect to the deck with a large bottom plate slope (θ_B).

For bridge deck with fairing, the damping force mainly exists at the leading edge top and bottom surface corner just after the fairing, while the excitation force exists at the leading and trailing edge fairing surface. However, if the fairing has sufficient length with less separation at the

trailing edge side, damping exists at the end of the fairing. In contrary to this, small fairing length with large flow separation at the trailing edge, experiences large excitation force.

The Separation Interference Method (SIM) method is found to be effective for dynamic response as well. The placement of curb at optimum angle (β) and height (h/D), improves the torsional damping characteristics of the system significantly. The trend we found in steady state response also holds for dynamic response. A pentagonal bridge with small bottom plate slope ($\theta_B=12^\circ$) possess a little bit larger damping due to smaller trailing edge flow separation as compared to the large bottom plate slope ($\theta_B=15^\circ$).

In case of deck without fairing, the leading edge top and bottom surface separation works as a excitation force at low reduced velocity ($U/fB_l=5$) and becomes damping at high reduced velocity ($U/fB_l=15$). In contrary to leading edge, the bottom surface trailing edge separation is mainly damping force at low reduced velocity ($U/fB_l=5$) and acts as a excitation force at high reduced wind velocity ($U/fB_l=15$).

Chapter 7

Conclusions

The aim of the present study was to explore and reveal the influence of various shaping parameters on aerodynamics of long-span cable-supported bridge decks. To pursue that, detailed numerical investigation was carried out for the bridge deck with and without fairing. Various important shaping parameters such as Top plate slope (θ_T), bottom plate slope (θ_B), width ratio (W), and side ratio (R) were taken into consideration and their influences on static and dynamic responses were investigated. Flow fields were analyzed for explaining the trends in the results and knowing the significance of various common flow features on aerodynamic responses.

In the last few chapters, several individual observations were made and separate conclusions were drawn at the end of each chapter. In this chapter we have synthesized all those individual conclusions for easier understanding the findings of the present study. The chapter consists of two sections. The first section presents the main findings of the presents study. We divided the findings broadly into two categories. In the first part, we listed the findings corresponding to the objective related to the flow mechanisms of the aerodynamic responses. The second part of the section sum up the findings related to the shaping parameters for the practical application. The last section highlights the limitations of the present study and provides direction for future research.

7.1 Main Findings of the Study

Related to the flow mechanism

In case of bride deck with fairing, the negative lift value is generated by the fast moving

boundary layer flow at the bottom deck surface. Exclusively for edge fairing ($W=1$), the leading edge bottom surface separation governs over the boundary layer velocity to increase the negative lift value. On the other hand, in case of bridge deck without fairing, the leading edge top and bottom surface separations are the main cause of negative lift value. When, there is no variation in the top surface flow separation, the bottom surface leading edge flow separation along controls the lift force.

Both for the case of bridge deck with and without fairing, the drag reduction is mainly caused by the stop in bottom surface trailing edge flow separation and the nose location. When the trailing edge flow separation stops, the deck with higher nose location (y/D) will experiences the lesser drag force. However, to obtain optimum drag response, the trailing edge separation should be stopped completely at the boundary layer.

Similar to the drag force, the after-body vortex shedding tendency also depends on the trailing edge flow separation and the nose location (y/D) for both of these decks. When the trailing edge flow separation stops, the vortex forms on the trailing edge top fairing (with fairing) or at the side of the bridge decks (without fairing). Therefore, when there is no flow separation, the deck with higher nose location will possess smaller wake. As a result, size of the vortex decreases and reduces the susceptibility to vortex induced vibration. Further, when the nose (y/D) is placed on the upper half ($y/D \geq 0.5$) of the bridge deck, the strength and tendency of after-body vortex diminishes significantly.

In general, for bridge deck with fairing ($0.3 \leq W$, $R \geq 5$), the trailing edge flow separation almost stops at a bottom plate slope (θ_B) of 15° or any value smaller than that, while for the bridge deck without fairing ($0 \leq W \leq 0.3$, $R = 5$) comparatively smaller bottom plate slope (θ_B) of around 12° is required. Basically, in case of bridge deck with fairing, there is sufficient width of horizontal bottom plate (b) to travel the flow horizontally before traveling at the trailing edge plate; as a result, the flow remains attach to the trailing edge inclined bottom plate at a larger bottom plate slope (θ_B) of around 15° . On the other hand, for bridge deck without fairing ($0 \leq W \leq 0.3$, $R = 5$), the flow travel on the leading edge inclined bottom plate, gains large inertial force towards downward before traveling at the trailing edge inclined plate. Therefore, much smaller bottom plate slope ($\theta_B \approx 12^\circ$ for $W=0$) is required to maintain the flow attached to the trailing edge inclined bottom plate. As long as the width and side ratio increases ($W \geq 0.5$, $R \geq 8$) of the bridge deck without fairing, the flow separation stops at larger bottom plate slope ($\theta_B \approx 15^\circ$) similar to the bridge deck with fairing.

The Reynolds number effects are found to be similar both for bridge deck with and without fairing. The increase in Reynolds number (R_{eB}) increases the bottom surface leading edge flow separation, yet decreases the top surface leading edge and bottom surface trailing edge flow separation. Therefore, at high Reynolds number ($R_{eB} \geq 20 \times 10^4$), the trailing edge flow separation stops at a larger bottom plate slope (θ_B) as compared to the low Reynolds number ($R_{eB} \leq 6 \times 10^4$).

Similar to the Reynolds number (R_{eB}) effect, in case of bridge deck without fairing, when a curb of optimum angle (β) and height (h/D) is attached, the boundary layer flow moves faster and the top surface leading edge and bottom surface trailing edge flow separation decreases. However, if the top surface flow is obstructed by placing a curb with an angle or height other than optimum value or median curb is installed, the boundary layer flow becomes slower at the bottom surface of the deck. As a result, the trailing edge separation increases requiring smaller bottom plate slope (θ_B) to stop the trailing edge flow separation.

In case of bridge deck with fairing, the variation of bottom plate slope (θ_B) affects the damping characteristics. The damping force mainly exists at the leading edge top and bottom surface corner of

the deck. The deck with less separation experiences less excitation and the excitation exists at the leading and trailing edge side inclined surface of the fairing. The variation of width ratio (W) mainly affects the coupled flutter behavior. In general, as the width ratio (W) decreases, the nose goes upward and improves the coupled flutter behavior. We also found that the deck having a mid-height nose location has a better stability against coupled flutter as compared to the too much nose up situation.

For bridge deck without fairing, the leading edge top and bottom surface separations work as a excitation at low reduced velocity ($U/fB_l=5$) and becomes damping at high reduced velocity ($U/fB_l=15$). In contrast to the leading edge separation, the trailing edge separation is damping at low reduced velocity ($U/fB_l=5$) and acts as an excitation force inputting energy to the system at high reduced velocity ($U/fB_l=15$). Therefore, from torsional flutter point of view, trailing edge flow separation should be given priority as compared to the leading edge flow separation.

Related to the Shaping Parameters

The value of optimum bottom plate slope (θ_B) depends on the type of bridge deck (with or without fairing) and width ratio (W). In case of bridge deck with fairing, a bottom plate slope of 20° - 25° shows better aerodynamic responses for a width ratio (W) of 1. For small width ratio ($0.3 \leq W \leq 0.7$), the value of optimum bottom plate slope (θ_B) varies from 12° - 15° depending on the width ratio (W) and Reynolds number (R_{eB}). However, in general, a bottom plate slope (θ_B) of 14° possesses better aerodynamic performances for any value of width ratio (W) smaller than 0.7 and should perform well at high Reynolds number (R_{eB}).

In case of bridge deck without fairing, a bottom plate slope (θ_B) of 12° owns better aerodynamic responses for pentagonal bridge deck. When the deck is shaped hexagonally, the optimum location varies between 15° - 13° depending on the width ratio (W), side ratio (R), and placement of median curb. Therefore, in general, a bottom plate slope (θ_B) of 12° can be used for hexagonal bridge deck without fairing too. For this general recommendation, the hexagonal bridge deck will possess a bit larger wake and leading edge separation as compared to the optimum bottom plate slope (θ_B).

For large width ratio ($W=1$), a top plate slope (θ_T) of 40° can be used to obtain better aerodynamic performance for smaller ($\theta_T=30^\circ$) top plate slope, the size of the fairing increases significantly. For small width ratio ($W \leq 0.7$), larger top plate slope ($\theta_T > 40^\circ$) can be used to reduce the size of the fairing as no significant advantage can be obtained from aerodynamics point of view by using small top plate slope (θ_T).

In general, a small value of width ratio (W) provides better aerodynamic responses for smaller bottom plate slope (to ensure stop in trailing edge flow separation). As the width ratio (W) decreases, the length of the inclined bottom plate increases and the nose location (y/D) goes up, decreasing the after-body wake size. Therefore, for small width ratio (W) bridge deck when smaller bottom plate slopes are adopted, we recommend to place the nose on the upper half ($y/D \geq 0.5$) of the bridge deck. However, too much nose up ($y/D \approx 0.75$) or nose down ($y/D \approx 0.25$) situation deteriorates the aerodynamic performance of the section.

The range of Reynolds number ($R_{eB} \leq 20 \times 10^4$) we explored, based on that we can say, aerodynamic analysis should be carried out at least at a Reynolds number (R_e) of around 2.5×10^4 to

obtain stable results in the subcritical range of Reynolds number (R_{eB}). At high Reynolds number (R_{eB}) the drag decreases and the negative lift value increases.

The effectiveness of Separation Interference Method (SIM) can be improved by attaching the curb at an optimum angle (β) and height (h/D) of 27° and 0.1, respectively. The median curb should be tried to place at the center of the bridge deck; otherwise it may deteriorate the performance of the SIM. A better location for installing the inspection rail would be at the inclined bottom plate of the bridge deck to reduce the trailing edge separation and after-body wake size.

7.2 Areas of Future Research

In the present study, unsteady RANS simulation was employed for investigating shaping effects on aerodynamic responses and flow fields of the bridge decks. However, due to inherent limitation of unsteady RANS simulation, it could not reproduce the Impinging Leading-Edge Vortices (ILEV) (Naudascher & Rockwell 1994). For sharpened edged-bluff bodies ILEV significantly influences the base suction (Tan *et al.* 2004), shedding frequency (Mills *et al.* 2003) and torsional flutter stability (Matsumoto *et al.* 1996 and Kubo *et al.* 1992).

The ILEV are primarily generated from the leading edge separation area. However, our considered deck shapes possess significantly small leading edge separation. Specially, the bridge deck with fairing owns very thin leading edge flow separation. The significance of IELV for these type deck is lesser than the sharpened edge bluff bodies (Shiraishi and Matsumoto 1983) as the separation thickness is too small (Tylor *et al.* 2012 and present investigation). Even though, Tylor *et al.* (2012) found trace of small bubbles generate from those separated areas. Therefore, it would be interesting to explore the influences of those small ILEVs on aerodynamic responses. Based on our investigation some particular sections with distinct flow behavior can be chosen and detailed numerical investigation can be carried out by employing improved numerical method such as Large Eddy Simulation (LES) or Direct Numerical Simulation (DNS) to explore the effects of IELV on static and dynamic responses.

Further, in the present study we conducted two-dimensional simulation to research on aerodynamics of the bridge decks due to variation of cross-sectional geometry under smooth flow only. However, the natural wind is turbulent and the flow around bridge deck is three dimensional in nature. The unsteady nature of the bridge deck in the span-wise direction will alter depending on the three dimensionality of the flow and the nature of incoming turbulence. Therefore, from practical point of view the present simulations provided conservative results in relation to the actual one. Moreover, in this work we clarified Reynolds number effects up to a nominal range to show the trend in the results. For practical bridges this value may reach up to $Re \approx 10^7$ (Schewe and Larsen 1998). Therefore, numerical investigation for exploring the three-dimensional response and flow field of the bridge deck due to variation of cross-sectional geometry at a high Reynolds number (R_e) under turbulent flow would be an important future work.

In addition, we focused on closed box bridge deck only with a maximum side ratio (R) of 8. However, open box (Bottom surface is open) bridge deck with fairing are often adopted for cable-supported bridges. The mechanism and effectiveness of fairing for this kind of open girder bridge

deck would be different from that of a closed girder bridge deck as the bottom surface leading edge separated shear layer will roll up in between the girders instead of going at the trailing edge side. Moreover, the optimum fairing angle may also vary from that of a closed box bridge girder as the bottom surface is no longer the control surface. Furthermore, the side ratio (R) of the bridge deck may reach up to a value of 12. Therefore, the investigation of the present study can be further extended for open box bridge deck with a higher side ratio ($R > 8$) to compare the trend in the results and flow field with the current one for additional valuable information.

Bibliography

AIAA, 1998. Guide for the Verification and Validation of Computational Fluid Dynamics Simulations. *American Institute of Aeronautics and Astronautics*, AIAA-G-077-1998, Reston, VA, 1998.

Ammann, O.H., Von Karman, T. and Woodruff, G.B., 1941. The failure of the Tacoma Narrows Bridge. *Report to the Federal Works Agency*, 28 March 1941.

Anderson, J.D., 1995. Computational Fluid Dynamics: The Basics with Application. *McGraw-Hill*.

Anderson, J.D., 2010. Fundamentals of Aerodynamics. *McGraw-Hill*, Fifth Edition.

Bai, Y., Sun, D. and Lin, j., 2010. Three dimensional numerical simulations of long-span bridge aerodynamics using block-iterative coupling and DES. *Computers and Fluids*, 39, 1549-1561.

Bartoli, G. and Righi, M., 2006. Flutter mechanism for rectangular prisms in smooth and turbulent flow. *Journal of Wind Engineering and Industrial Aerodynamics*, 94(5), 275–91.

Bartzis, J.G., Vlachogiannis, D. and Sfetsos, A., 2004., Thematic area 5: Best practice advice for environmental flows. *The QNET-CFD Network Newsletter*, 2(4), 34-39.

Battista, R.A., 2000. Reduction vortex-induced oscillation of Rio-Niterio by dynamic control devices. *Journal of Wind Engineering and Industrial Aerodynamics*, 84, 273-288.

Bearman, P.W. and Obasaju, E.D., 1982. An experimental study of pressure fluctuations on fixed and oscilattig square-section cylinders. *Journal of Fluid Mechanics*. 119, 297-321.

Behr, M., Hastretier, D., Mittal, S. and Tezduyar, T.E., 1995. Incompressible flow past a circular cylinder: dependence of the computed flow field on the location of the lateral boundaries. *Computer Methods in Applied Mechanics and Engineering*, 123, 309-316.

Billah, K.Y., and R.H. Scanlan., 1991. Resonance, Tacoma Narrows bridge failure, and undergraduate physics textbooks. *American Journal of Physics*, 59 118-124.

Blazek, J. 2003. Computational Fluid Dynamics: Principles and Applications. *Elsevier*, Second Edition.

- Blocken, B., 2014. 50 years of computation wind engineering: past, present and future. *Journal of Wind Engineering and Industrial Aerodynamics*, 129, 69-102.
- Bogunovic-Jakobsen, J. and Hjorth-Hansen, E., 1995. Determination of the aerodynamic derivatives by a system identification method. *Journal of Wind Engineering and Industrial Aerodynamics*, 57(2-3), 295-305.
- Bos, F., 2009. Numerical simulation of flapping foil and wind aerodynamics: Mesh de-formation using radial basis functions, PhD Thesis, *Technical University Delft* (2009).
- Brancaleoni, F. and Diana, G., 1993. The aerodynamic design of messina strait bridge. *Journal of Wind Engineering and Industrial Aerodynamics*, 48(2-3), 395-409.
- Briggs, W.L., Henson, V.E. and McCormick, S.F., 2000. A multigrid tutorial: Second edition. *SIAM publication*.
- Bruno, L. and Mancini, G., 2002. Importance of deck details in bridge aerodynamics. *Structural Engineering International*, 12(4), 289-294.
- Bruno, L., Fransos, D., Coste, N. and Bosco, A., 2010. 3D flow around a rectangular cylinder: A computational study. *Journal of Wind Engineering and Industrial Aerodynamics*, 98, 263-276.
- Bruno, L., Coste, N. and Fransos, D., 2012. Simulated flow around a rectangular 5:1 cylinder: Spanwise discretization effects and emerging flow features. *Journal of Wind Engineering and Industrial Aerodynamics*, 104-106, 203-215.
- Brusiani, F., De Miranda, S., Patruno, L., Ubertini, F. and Vaona, P., 2013. On the evaluation of bridge deck flutter derivatives using RANS turbulence model. *Journal of Wind Engineering and Industrial Aerodynamics*, 119, 39-47.
- Caracogila, L., Sarkar, P.P., Haan, F.L., Sato, H. and Murakoshi, J., 2009. Comparative and sensitivity study of flutter derivatives of selected bridge deck sections, Part 2: Implications on the aerodynamic stability of long-span bridges. *Engineering Structures*, 31, 2194-2202.
- Casey, M. and Wintergerste, T., 2000. Best Practice Guidelines, ERCOFTAC Special Interest Group on Quality and Trust in Industrial CFD. *ERCOFTAC*, Brussels.
- CFD-Online, 2015. Dimensionless wall distance (y plus), <http://www.cfd-online.com/Wiki/>, accessed 28 July, 2015.
- Chen, X., 2007. Improved understanding of bimodal coupled bridge flutter based on closed-form solutions. *Journal of Structural Engineering, ASCE*, 60, 22-31.
- Chen, X., Matsumoto, M., and Kareem, A., 2000. Aerodynamic coupling effects on flutter and buffeting of bridges. *Journal of Engineering Mechanics, ASCE*, 126(1), 17-26.
- Chen, A., He, X. and Xiang, H., 2002. Identification of 18 flutter derivatives of a bridge decks. *Journal of Wind Engineering and Industrial Aerodynamics*, 90, 2007-2022.

- Chowdhury, A.G. and Sarkar, P.P., 2003. A new technique for identification of eighteen flutter derivatives using a three-degree-of-freedom section model. *Engineering Structure*, 25(12), 1763–72.
- Cooper, J., 1998. World's longest suspension bridge opens in Japan. United States *Department of Transportation- Federal Highway Administration*, 62(1).
- Cowan, I.R., Castro, I.P. and Robins, A.G., 1997., Numerical considerations for simulations of flow and dispersion around buildings. *Journal of Wind Engineering and Industrial Aerodynamics*, 67 and 68, 535-545.
- Dennie, J. and Hall, J.E., 1809. The Port Folio, Vol. III. *Bradford and Inskip*, Philadelphia, New-York.
- De Miranda, M. and Bartoli, G., 2001. Aerodynamic optimization of decks of cable-stayed bridges. Cable-Supported Bridges – Challenging Technical Limits. *Proceeding of IABSE Conference*, Seoul Korea, 12-14 June, 34-41.
- Dermirdžic, I. and Perić, M., 1988. Space conservation law in finite volume calculations of fluid flow. *International Journal of Numerical Methods in Fluid*, 8, 1037-1050.
- Dewan, A., 2011. Tackling Turbulent Flows in Engineering. *Springer*.
- Diana, G., Falco, M., Cheli, F. and Cigada, A., 1999. Experience gained in the messina bridge aeroelastic project. *Long-span bridge and aerodynamic*, Edited by Miyata, Fujisawa and Yamada, *Springer*, 155-180.
- Donea, J., Huerta, A., Ponthot, J.-Ph., Rodríguez-Ferran, A., 2004. Encyclopedia of Computational Mechanics, Volume 2 Solids and Structures. Chapter Arbitrary Lagrangian– Eulerian Methods. *Wiley*, Chichester, 413–438.
- Drikakis, D. and Rider, W., 2005. High-Resolution Methods for Incompressible and Low-Speed Flows. *Springer*.
- Dwight, R.P., 2004. Robust mesh deformation using the linear elasticity equations, in H. Deconinck & E. Dick, eds, 'Computational Fluid Dynamics 2006', *Springer*.
- Farquharson, F.B., 1949. Aerodynamic Stability of Suspension Bridges, *University of Washington, Part I–IV*, 1949.
- Ferziger, J.H. and Perić, M., 2002. Computational Methods for Fluid Dynamics. *Springer*, Second Edition.
- Fletcher, R., 1976. Conjugate gradient methods for indefinite systems. Watson, G. and Alistair ed. Numerical Analysis, Lecture Notes in Mathematics, *Springer*, Berlin.
- Fletcher, C.A.J., 1996. Computational Techniques for Fluid Dynamics: Volume 2: Specific Techniques for Different Flow Categories. *Springer*, Second Edition.
- Frandsen, J., 2001. Simultaneous pressure and acceleration measured full-scale on the Great Belt East suspension bridge. *Journal of Wind Engineering and Industrial Aerodynamics*, 89, 95-129.

Franke, J., Hirsch, C., Jensen, A.G., Krüs, H.W., Schatzmann, M., Westbury, P.S., Miles, S.D., Wisse, J.A., Wright, N.G., 2004. Recommendations on the use of CFD in wind engineering. In: van Beeck, J.P.A.J. (Ed.), *Proceedings of the International Conference on Urban Wind Engineering and Building Aerodynamics*. COST Action C14, Impact of Wind and Storm on City Life Built Environment. Von Karman Institute, Sint-Genesius-Rode, Belgium, 5–7 May 2004.

Franke, J., Hellsten, A., Schlünzen, H. and Carissimo, B. (Eds.), 2007. Best practice guideline for the CFD simulation of flows in the urban environment. *COST Office Brussels*, ISBN 3-00-018312-4.

Fujino, Y. and Yoshida, Y., 2002. Wind-Induced vibration and control of the Trans-Tokyo bay bridge crossing. *Journal of Structural Engineering, ASCE*, 128(8), 1012-1025.

Fujino, Y., Kimura, K. and Tanaka, H., 2012. Wind Resistant Design of Bridges in Japan: Developments and Practices. *Springer*, Tokyo, Japan.

Fujino, Y. and Siringoringo, D., 2013. Vibration mechanisms and controls of long-span bridges: A review. *Structural Engineering International, ISBSE*, 23(3), 248-268.

Galli, F., 2005. Comportamento aerodinamico di strutture snelle non profilate: approccio sperimentale e computazionale. Master's thesis, *Politecnico di Torino*, Turin, Italy.

Gu, M., Xiang, H.F. and Chen, A.R., 1994. A practical method of passive TMD for suppressing wind-induced vertical buffeting of long-span cable-stayed bridges and its application. *Journal of Wind Engineering and Industrial Aerodynamics*, 51, 203-213.

Hackbusch, W. and Trottenberg, U., 1982. Multigrid Methods, Lecture notes in mathematics 960, *Springer*, Berlin.

Haque, M.N., Katsuchi, H., Yamada, H., and Nishio, M., 2013. Numerical simulation for effects of wind turbulence on flow field around rectangular cylinder. *Journal of Structural Engineering (JSCE)*, 59A, 605-615.

Haque, M.N., Katsuchi, H., Yamada, H. and Nishio, M., 2014. Investigation of flow fields around rectangular cylinder under turbulent flow by LES. *Engineering Application of Computational Fluid Mechanics*, 8(3), 396-406.

Haque, M.N., Katsuchi, H., Yamada, H. and Nishio, M., 2015. A numerical study on aerodynamics of pentagonal shaped cable-supported bridge deck. *Journal of Structural Engineering, JSCE*, 61A, 375-387.

Hirsch, C., 1991. Numerical computation of internal and external flows: *John Wiley & Sons*.

Hoffmann, K.A. and Chiang, S.T., 2000. Computational Fluid Dynamics, Volume 3. *EES*, Fourth Edition.

Holmes, J.D., 2004. Wind Loading of Structures. *Taylor & Francis*, United Kingdom.

- Honda, A., Shiraishi, N., Matsumoto, M., Fuse, Y., Sumi, K. and Sasaki, N., 1993. Aerodynamic stability of kansai international airport access bridge. *Journal of Wind Engineering and Industrial Aerodynamics*, 49, 533-542.
- Huang, L., Liao, H., Wang, B., Li, Y., 2009. Numerical simulation for aerodynamic derivatives of bridge deck. *Simulation, Modeling, Practice and Theory*, 17, 719–729.
- Houriga, K., Thompson, M.C. and Tan, B.T., 2001. Self-sustained oscillations in flows around long blunt plates. *Journal of Fluid and Structures*, 15, 387-398.
- Issa, R.I., 1986. Solution of the implicitly discretized fluid flow equations by operator-splitting. *Journal of Computational Physics*, 62, 40-65.
- Izuka, S., Murakami, S., Tsuciya, N. and Mochida, A., 1999. LES of flow past 2D cylinder with imposed inflow turbulence. *Wind Engineering into the 21st Century*, Larsen, Larose & Livesey (eds), 1999, Balkema, Rotterdam.
- Jasak, H., 1996. Error Analysis and Estimation for the Finite Volume Method with Application for Fluid Flows. PhD Thesis, *Imperial College*, London.
- Jasak, H., Weller, H. G. and Nordin, N., 2004. In-cylinder CFD simulation using a c++ object-oriented toolkit. *SAE Technical paper*, 2004-01-0110.
- Jasak, H. and Tokuvic, Z., 2010. Dynamic mesh handling in OpenFOAM applied to Fluid-Structure interaction simulation. *V European Conference on Computational Fluid Dynamics*, Lisbon, Portugal, 14-17 June, 2010.
- Jensen, L., 2013. Halogland Suspension Bridge, Narvik, Norway. *IABSE Denmark Mini-seminar*. Denmark.
- Jiang, X. and Lai, C-H., 2009. Numerical Techniques for Direct and Large-Eddy Simulations. *CRC Numerical Analysis and Scientific Computing Series*.
- Jinyuan, T., Guan, H.Y. and Chaoqun, L., 2006. Computational Fluid Dynamics: A practical approach. *Butterworth -Heinemann Newton*, MA, USA.
- Jurado, J.A., Hernandez, H., Nieto, F. and Mosquera, A., 2011. Bridge Aeroelasticity: Sensitivity Analysis and Optimal Design. *WIT Press*, UK.
- Juretic, F., 2004. Error analysis in Finite Volume CFD. PhD thesis, *Imperial College*, London.
- Kawatani, M., Kim, J., Uejima, H., and Kobayashi, H., 1993. Effects of turbulent on vortex-induced oscillation of bridge girders with basic sections. *Journal of Wind Engineering and Industrial Aerodynamics*, 49, 477-486.
- Kelkar, K. M. and Patankar, S. V., 1992. Numerical prediction of vortex shedding behind a square cylinder. *International Journal of Numerical Methods in Fluids*, 14(03), 327.

- Kubo, Y., Hirata, K. and Mikawa, K., 1992. Mechanism of aerodynamic vibrations of shallow bridge girder sections. *Journal of Wind Engineering and Industrial Aerodynamics*, 41-44, 1297-1308.
- Kubo, Y., Honda, K., Tasaki, K., and Kato, K., 1993. Improvement of aerodynamic instability of cable-stayed bridge deck by separated flows mutual interference method. *Journal of Wind Engineering and Industrial Aerodynamics*, 49, 553-564.
- Kubo, Y., Yoshida, K., Tuji, E., Kimura, K. and Kato, K., 2007. Development of aerodynamically stable bridge girder cross section for long span bridges. *Proceedings of 12th International Conference on Wind Engineering*, 1-6 July, Cairns, Australia, 239-246.
- Kubo, Y., Hayashida, K. Noda, T. and Kimura, K., 2008. Mechanism on reduction of aerodynamic forces and suppression of aerodynamic response of a square prism due to separation interface method. *Proceedings of 6th International Colloquium on Bluff Body Aerodynamics and Applications*, 20-24 July, Milano, Italy, 1-4.
- Kumarasena, T.S., 1989. Deer Isle bridge: Field and computed vibrations. *Journal of Structural Engineering*, ASCE. 115(9), 2313-2328.
- Larsen, A., 1993. Aerodynamic aspects of the final design of the 1624m suspension bridge across the great belt. *Journal of Wind Engineering and Industrial Aerodynamics*, 48, 261-285.
- Larsen A. and Walther, J.H., 1998. Discrete vortex simulation of flow around five generic bridge deck sections. *Journal of Wind Engineering and Industrial Aerodynamics*, 77 & 78, 591-602.
- Larsen, A., Esdahl, S., Anderson, J.E. and Vejrum, T., 2000. Storebælt suspension bridge- vortex shedding excitation and mitigation by guide vanes. *Journal of Wind Engineering and Industrial Aerodynamics*, 88, 283-296.
- Larsen, A. and Wall, A., 2012. Shaping of bridge girders to avoid vortex shedding response. *Journal of Wind Engineering and Industrial Aerodynamics*, 104-106, 159-165.
- Lee, B.E., 1975. The effect of turbulence on the surface pressure field of a square prism. *Journal of Fluid Mechanics*. 69(02), 363-282.
- Lesoinne, M. and Farhat, C., 1996. Geometric conservation laws for flow problems with moving boundaries and deformable meshes, and their impact on aeroelastic computations. *Computer Methods in Applied Mechanics and Engineering*, 134, 71-90.
- LeVeque, R.J., 2002. Finite Volume Methods for Hyperbolic Problems. Cambridge Texts in Applied Mathematics.
- Lin, T.Y. and Chow, P., 1991. Gibraltar Strait crossing, a challenge to bridge and structural engineering. *Structural Engineering International*, ISBSE, 1(2), 53-58.
- Lohner, R. and Yang, C., 1996. Improved ALE mesh velocities for moving bodies. *Communications in numerical methods in engineering*, 12, 599-608.

- Loitsyanskiy, L.G., 1995. Mechanics of Liquids and Gases. 6th edition, Begell House, *New York and Wallingford*, 1995.
- Lyn, D.A, Eunav, S., Rodi, W. and Park, J.H., 1995. A laser-Doppler Velocimetry study of ensemble averaged characteristics of the turbulent near wake of a square cylinder. *Journal of Fluid Mechanics*, 304, 285-319.
- Mannini, C., Šoda, A., Ralph, V. and Schewe, G., 2010a. Unsteady RANS simulation of flow around a bridge section. *Journal of Wind Engineering and Industrial Aerodynamics*, 98, 742-753.
- Mannini, C., Šoda, A. and Schewe, G., 2010b. Unsteady RANS modeling of flow past a rectangular cylinder: Investigation of Reynolds number effects. *Computers and Fluids*, 39(09), 1609-1624.
- Matsumoto, M., Shiraishi, N., Shirato, H., Stoyanoff, S. and Yagi, T., 1993. Mechanism of, and turbulence effect on vortex-induced oscillations for bridge box girders. *Journal of Wind Engineering and Industrial Aerodynamics*, 49, 467-476.
- Matsumoto, M., 1996. Aerodynamic damping of prisms. *Journal of Wind Engineering and Industrial Aerodynamics*, 59, 159-175.
- Matsumoto, M., Kobayashi, Y. and Shirato, H., 1996. The influence of aerodynamic derivatives on flutter. *Journal of Wind Engineering and Industrial Aerodynamics*, 60, 227-239.
- Matsumoto, M., Daito, Y., Yoshizumi, F., Ichikawa, Y. and Yabutani, T., 1997. Torsional flutter of bluff bodies. *Journal of Wind Engineering and Industrial Aerodynamics*, 69-71, 871-882.
- Matsumoto, M., Yoshizumi, F., Yabutani, T. and Nakajima, N., 1999. Flutter stabilization and Heaving-branch flutter. *Journal of Wind Engineering and Industrial Aerodynamics*, 83 (1-3), 289-299.
- Matsumoto, M., Shirato, H., Yagi, T., Shijo, R., Eguchi, A. and Tamaki, H., 2003. Effects of aerodynamic interferences between heaving and torsional vibration of bridge decks: the case of tacoma narrows bridge. *Journal of Wind Engineering and Industrial Aerodynamics*, 91, 1547-1557.
- Matsumoto, M., Mizuno, K., Okubo, K., Ito, Y. and Matsumiya, H., 2007. Flutter instability and recent development in stabilization of structures. *Journal of Wind Engineering and Industrial Aerodynamics*, 95, 888-907.
- Matsumoto, M., Shirato, H., Mizuno, K., Shijo, R. and Hikida, T., 2008a. Flutter characteristics of H-shaped cylinders with various side-ratios and comparison with characteristics of rectangular cylinders. *Journal of Wind Engineering and Industrial Aerodynamics*, 96 (6-7), 963-970.
- Matsumoto, M., Okubo, K., Ito, Y., Matsumiya, H. and Kim, G., 2008b. The complex branch characteristics of coupled flutter. *Journal of Wind Engineering and Industrial Aerodynamics*, 96 (10-11), 1843-1855.
- Matsuyama, A., 2013. Study on Aerodynamic Stabilization Mechanism of Separation Interference Method for Bridge Girder Cross Section. *Masters dissertation*, Department of Civil Engineering, Yokohama National University. 1-92.

- Macdonald, J., Irwin, P. and Fletcher, M., 2002. Vortex-induced vibrations of the second severn crossing cable-stayed bridge full-scale and wind tunnel measurements. *Proceedings of the ICE-Structures and Buildings*, 152(2), 123-134.
- Menter, F.R., 1992a. Performance of Popular Turbulence Models for Attached and Separated Adverse Pressure Gradient Flow, *AIAA Journal*, 30, 2066–2072.
- Menter, F.R., 1992b. Improved Two-equation $k-\omega$ Turbulence Models for Aerodynamic Flows. *NASA Technical Memorandum, TM-103975*, NASA Ames, CA.
- Menter, F., 1994. Two-equation Eddy-viscosity Turbulence Model for Engineering Applications. *AIAA Journal*, 32, 1598–1605.
- Menter, F., 1997. Eddy-viscosity Transport Equations and their Relation to the $k-\epsilon$ Model, Trans. ASME, *Journal of Fluids Engineering*, 119, 876–884.
- Menter, F., Hemstrom, B., Henriksson, M., Karlsson, R., Latrobe, A., Martin, A., Muhlbauer, P., Scheuerer, M., Smith, B., Takacs T. and Willemsen, S., 2002. CFD Best Practice Guidelines for CFD Code Validation for Reactor-Safety Applications. Report EVOL-ECORA-D01, Contract No. FIKS-CT-2001-00154.
- Menter, F.R., Kuntz, M. and Langtry, R., 2003. Ten years of industrial experience with the SST turbulence model. *Proceedings of Turbulence, Heat and Mass Transfer 4*, 12-17, October, Antalya, Turkey, 625–632.
- Mills, R., Sheridan, J. and Hourigan, K., 2002. Response of base suction and vortex shedding from rectangular prisms to transverse forcing. *Journal of Fluid Mechanics*, 461, 25-49.
- Mills, R., Sheridan, J. and Hourigan, K., 2003. Particle image velocimetry and visualization of natural and forced flow around rectangular cylinders. *Journal of Fluid Mechanics*, 478, 299-323.
- Miranda, S.D., Patruno, L., Ubertini, F. and Vairo, G., 2014. On the identifications of the flutter derivatives of bridge deck via RANS turbulence models: Benchmarking on rectangular prisms. *Engineering Structures*, 76, 359-370.
- Miyata, T., Miyazaki, M. and Yamada, H., 1983. Pressure distribution for wind induced vibrations of box girder bridges. *Journal of Wind Engineering and Industrial Aerodynamics*, 14, 223-234.
- Miyata, T., Hikori, M. and Yasuda, M., 1992. Circumstances of wind-resistance design examinations for very long suspension bridge. . *Journal of Wind Engineering and Industrial Aerodynamics*, 42, 1371-1382.
- Mizota, T., Yamada, H., Kubo, Y., Okajima, A., Knisely, C.W., Shirato, H., 1988. Aerodynamic characteristics of fundamental structures, part 1, section 2. *Journal of Wind Engineering*, 36, 50–52 (in Japanese).
- Myerscough, M., 2013. Suspension bridges: Past and present. *The Structural Engineering*, 91(7), 12-21.

- Nagao, F., Utsunomiya, H., Oryu, T. and Manabe, S., 1993. Aerodynamic efficiency of triangular fairing on box girder bridge. *Journal of Wind Engineering and Industrial Aerodynamics*, 49, 565–574.
- Nagao, F., Utsunomiya, H., Yoshioka, E., Ikeuchi, A. and Kobayashi, H., 1997. Effects of handrails on separated shear flow and vortex-induced oscillation. *Journal of Wind Engineering and Industrial Aerodynamics*, 69-71, 819-827.
- Nakaguchi, H., Hashimoto, K. & Muto, S., 1968. An experimental study on aerodynamic drag of rectangular cylinders. *Journal of the Japan Society of Aeronautical and Space Sciences*, 16, 1-5.
- Nakamura, Y. and Ohya, Y., 1984. The effects of turbulence on the mean flow past two-dimensional rectangular cylinders. *Journal Fluid Mechanics*, 149, 255-273.
- Nakamura, Y. and Nakashima, M., 1986. Vortex excitations of prisms with elongated rectangular, H and Γ section. *Journal of Fluid Mechanics*, 163, 149-169.
- Naudascher, E. and Rockwell, D., 1994. Flow-induced vibration-An engineering guide. *Rotterdam : A. A. Balkema*.
- Nieto, F., Kusano, I., Hernandez, S. and Jurado, J.A., 2010. CFD analysis of the vortex-shedding response of twin-box deck cable-stayed bridge. In *Proceedings of 5th International Symposium on Computational Wind Engineering*, North Carolina, USA, 23-27 May, 1-8.
- Nieto, F., Owen, J.S., Hargreaves, D.M. and Hernandez, S., 2015. Bridge deck flutter derivatives: efficient numerical evaluation exploiting their independencies. *Journal of Wind Engineering and Industrial Aerodynamics*, 136, 138–150.
- Noda, T., Kubo, Y., Kimura, K., Kato, K., Okubo, K. and Yoshida, K., 2009. The effect of lower flange slope on the aerodynamic stability on a pentagonal cross-section girder. *Journal of Civil Engineering (JSCE)* 65(3), 797-807, (Japanese).
- Noda, T., 2010. Study on development of narrow width deck section for suspension bridge. PhD dissertation, Graduate school engineering, *Kyushu Institute of Technology*, Japan, 2010 (Japanese).
- Oberkampf, W.L. and Trucano, T.G., 2002. Verification and validation in computational fluid dynamics. *Progresses in Aerospace Sciences*. 38(03), 209-272.
- O-connor, C., 1993. Roman bridges. *Cambridge University bridge*, UK.
- Ohtsuki, Y., 1978. Wind tunnel experiments on aerodynamic forces and pressure distributions of rectangular cylinders in a uniform flow. *Proceedings of 5th Symposium on Wind Effects on Structures*, Tokyo, Japan, 169- 175.
- Okajima, A., 1982. Strouhal numbers of rectangular cylinders. *Journal Fluid Mechanics*, 123, 37-398.
- Okajima, A., 1983. Flow around a rectangular cylinder with a section of various width/height ratios. *Journal of Wind Engineering*, 17, 1-19.

- OpenFOAM, 2015a. Programmer's guide. Version 2.4.0, OpenFOAM Foundation Ltd., United Kingdom.
- OpenFOAM, 2015b. User guide. Version 2.4.0, OpenFOAM Foundation Ltd., United Kingdom.
- Otsuki, Y., Washizu, K., Tomizawa, H. and Ohya, A., 1974. A note on the aeroelastic instability of a prismatic bar with square section. *Journal of Sound and Vibration*, 34(2), 233-248.
- Owen, J.E., 1996. The prototype testing of Kessock bridge: response to vortex shedding. *Journal of Wind Engineering and Industrial Aerodynamics*, 60, 91-108.
- Patankar, S., 1980. Numerical Heat Transfer and Fluid Flow. *McGraw-Hill*.
- Patruno, L., 2015. Accuracy of numerically evaluated flutter derivatives of bridge deck sections using RANS: Effects on the flutter onset velocity. *Engineering Structures*, 89, 49-65.
- Pocha, J.J., 1971. On unsteady flow past cylinders of square cross-section, Ph.D. Thesis, Department of Aeronautics, *Queen Mary College*, London.
- Pope, S.B., 2000. Turbulent Flows. *Cambridge University Press*.
- Prandtl, L., 1927. Ueber den Reibungswiderstand strömender Luft. *Ergebn. Aerodyn. Versuchsanst. Göttingen*, 3, 1-5.
- Press, W.H., Teukolsky, S.A., Vetterling, W.T. and Flannery, B.P., 2007. Numerical recipes: the art of scientific computing. Third edition, *Cambridge University Press*, New-York.
- Pullin, D. and Perry, A., 1980. Some flow visualization experiments on the starting of vortex. *Journal of Fluid Mechanics*, 97(2), 239-255.
- Reinhold, T.A., Brinch, M. and Damsgaard, A., 1992. Wind tunnel test for the great belt link. *Proceedings of 1st International Symposium on Aerodynamics of Large Bridges*, Rotterdam, 255-267.
- Ricciardelli, F. and Marra, A.M., 2008. Sectional aerodynamic forces and longitudinal correlation on a vibrating 5:1 rectangular cylinder. In *Proceedings of 6th International Colloquium on Bluff Body Aerodynamics and Applications*, Milano, Italy, 20-24 July.
- Roache, P.J., 1998. Verification and validation in computational science and engineering. *Hermosa Publishers, Albuquerque*, New Mexico.
- Sagaut, P., 2005. Large Eddy Simulation for Incompressible Flows: An Introduction. *Springer*.
- Sakai, Y., Ogawa, K., Shimodoi, H., and Saitoh, T., 1993. An experimental study on aerodynamic improvements for edge girder bridges. *Journal of Wind Engineering and Industrial Aerodynamics*, 49, 459-466.
- Sakamoto, H., Haniu, H. and Kobayashi, Y., 1989. Fluctuating force acting on rectangular cylinders in uniform flow on rectangular cylinders with fully separated flow. *Transactions of the Japan Society of Mechanical Engineers, Series B*, 55(516) 2310- 2317.

- Sarkar, P.P., Jones, N.P., Scanlan, R.H., 1992. System identification for estimation of flutter derivatives. *Journal of Wind Engineering and Industrial Aerodynamics*, 42(1–3), 1243–54.
- Sarkar, P.P., Caracogila, L., Haan, F.L., Sato, H. and Murakoshi, J., 2009. Comparative and sensitivity study of flutter derivatives of selected bridge deck sections, Part 1: Analysis of inter-laboratory experimental data. *Engineering Structures*, 31, 158-169.
- Šarkić, A., Fisch, R., Höffer, R. and Bletzinger, K., 2012. Bridge flutter derivatives based on computed, validated pressure fields. *Journal of Wind Engineering and Industrial Aerodynamics*, 104-106, 141-151.
- Sarwar, M.W., Ishihara, T., Shimada, K., Yamasaki, Y., and Ikeda, T., 2008. Prediction of aerodynamic characteristics of a box girder bridge section using the LES turbulence model. *Journal of Wind Engineering and Industrial Aerodynamics*, 96, 1895-1911.
- Sarwar, M.W. and Ishihara, T., 2010. Numerical study on suppression of vortex-induced vibrations of a box girder bridge section by aerodynamic countermeasures. *Journal of Wind Engineering and Industrial Aerodynamics*, 98, 701-711.
- Scanlan, R.H. and Rosenbaum, R., 1951. Aircraft vibration and flutter. *Macmillan*, New York (reprint, Dover, 1968).
- Scanlan, R.H. and Tomko, J.J., 1971. Airfoil and bridge deck flutter derivatives. *Journal of the Engineering Mechanics, ASCE*, 97, 1717-1737.
- Scanlan, R.H., Beliveau, J.G. and Budlong, K.S., 1974. Indicial Aerodynamic functions for bridge decks. *Journal of Engineering Mechanics, ASCE*, 100, 657-672.
- Scanlan, R.H., Jones, N.P. and Singh, L., 1997. Inter-relations among flutter derivatives. *Journal of Wind Engineering and Industrial Aerodynamics*, 69-71, 829-837.
- Scaperdas, A. and Gilham, S., 2004. Thematic Area 4: Best practice advice for civil construction and HVAC. *The QNET-CFD Network Newsletter*, 2(4), 28-33.
- Schewe, G. and Larsen, A., 1998. Reynolds number effects in the flow around a bluff bridge deck cross section. *Journal of Wind Engineering and Industrial Aerodynamics*, 74-76, 829-838.
- Schewe, G., 2001. Reynolds-number effects in flow around more-or-less bluff bodies. *Journal of Wind Engineering and Industrial Aerodynamics*, 89, 1267-1289.
- Schlichting, H., 1979. Boundary Layer Theory, 7th Edition, New York(USA): *McGraw-Hill*.
- Shewchuk, J.R., 1994. An introduction to the conjugate gradient method without the agonizing pain. *School of Computer Science, Carnegie Mellon University*.
- Shimada, K. and Ishihara, T., 2002. Application of a modified k– ϵ model to the prediction of aerodynamic characteristics of rectangular cross-section cylinders. *Journal of Fluids and Structure*, 16(04), 465–485.

- Shirai, S. and Ueda, T., 2001. Aerodynamic simulation by CFD of flat box girder of super-long span suspension bridge. In *proceedings of fifth Asia-pacific conference on wind engineering*, Kyoto, Japan, 21-24, October.
- Shiraishi, N. and Matsumoto, M., 1983. On classification of Vortex-Induced oscillation and its application for bridge structures. *Journal of Wind Engineering and Industrial Aerodynamics*, 14, 419–430.
- Simiu, E. and Scanlan, R.H., 1996. Wind Effects on Structures: Fundamentals and Applications to Design. *Wiley publisher*.
- Simiu, E. and Miyata, T., 2006. Design of Buildings and Bridges for Wind. *John Wiley and Sons, Hoboken, USA*.
- Singh, L., Jones, N.P., Scanlan, R.H. and Lorendeaux, O., 1996. Identification of lateral flutter derivatives of bridge decks. *Journal of Wind Engineering and Industrial Aerodynamics*, 60(1–3), 81–9.
- Sohankar, A., 2008. Large Eddy Simulation of flow past rectangular-section cylinder : Side ratio effects. *Journal of Wind Engineering and Industrial Aerodynamics*, 96(05), 640-655.
- Sohankar, A., Davidson, L. and Norberg, C., 1995. Numerical simulation of unsteady flow around a square two-dimensional cylinder. *Proceeding of Twelfth Australasian Fluid Mechanics Conference*, 10-15 December, 1995, Sydney, Australia, 517-520.
- Sohankar, A., Davidson, L. and Norberg, C., 1998. Low- Reynolds- number flow around a square cylinder at incidence: study of blockage, onset of vortex shedding and outlet boundary condition. *International Journal for Numerical Methods in Fluids*, 26(01), 39-56.
- Stærdahl, J.W., Sørensen, N., and Nielsen, S.R.K., 2007. Aeroelastic Stability of Suspension Bridges using CFD. In M. Majowiecki (Ed.), *Proceedings of International Symposium of the International Association for Shell and Spatial Structures (IASS) : Structural Architecture - towards the future looking to the past*: Venice, Italy, 3-6 December 2007.
- Stern, F., Wilson, R.V., Coleman, H.W. and Paterson, E.F., 2001a. Comprehensive approach to verification and validation of CFD simulations-part 1: Methodology and procedures. *Journal of Fluids Engineering*, 123, 793–802.
- Stern, F., Wilson, R.V., Coleman, H.W. and Paterson, E.F., 2001b. Comprehensive approach to verification and validation of CFD simulations-part 2: Application for RANS simulation of cargo/container ship. *Journal of Fluids Engineering*, 123, 803–810.2001.
- Strommen, E. and Hjorth-Hansen, E., 2001. On the use of tuned mass dampers to suppress vortex shedding induced vibration. *Wind and Structures*, 4, 19-30.
- Sukamta, Nagao, F., Noda, M. and Muneta, K., 2008. Aerodynamic stabilizing mechanism of a cable stayed bridge with two edge box girder. In *Proceedings of 6th International Colloquium on Bluff Body Aerodynamics and Applications*, Milano, Italy, 20-24 July.

- Svensson, H., 2012. Cable-Stayed bridges: 40 Years of experience worldwide. *Ernst & Sohn, A Willey Company*. Germany.
- Swank, J.M., 1892. History of the Manufacture of Iron in All Ages. *The American Iron and Steel Association*, Philadelphia.
- Sweby, P.K., 1984. High resolution schemes using flux limiters for hyperbolic conservation laws. *SIAM Journal of Numerical Analysis*, 21(05), 995–1011.
- Takada, T., 2011. 鋼コンクリート複合構造とした長大中路式アーチ橋の計画・設計. *Civil Engineering Consultant*, 252. 48-51 (in Japanese).
- Tamura, T. and Ito, Y., 1996. Aerodynamic characteristics and flow structures around a rectangular cylinder with a section of various depth/breadth ratios. *Journal of Structural and Construction Engineering* (Transactions of Architectural Institute of Japan), 486, 153-162.
- Tan, B.T., Thompson, M.C. and Hourigan, K., 2004. Flow past rectangular cylinders: receptivity to transverse forcing. *Journal of Fluid Mechanics*, 515, 33-62.
- Tanaka, H., 1999. Aerodynamic design of the great belt east bridge. *Long-span bridge and aerodynamic*, Edited by Miyata, Fujisawa and Yamada, Springer, 203-230.
- Tatsumi, M., 2010. Steel Cable-Stayed bridges-Technologies and its progress. *Japan Society of Civil Engineers (JSCE), Steel Structures Series 20* (in Japanese).
- Terres-Nicoli, J., King, J. and Kim, J., 2007. Wind effects for the 3rd Millennium Bridge. *Proceedings of 12th International Conference on Wind Engineering*, 1-6 July, Cairns, Australia, 2215-2222.
- Terres-Nicoli, J.M. and Kopp, G.A., 2009. Mechanism of the vertical vortex induced vibration of Storebaelt bridge. *Proceedings of 11th America Conference on Wind Engineering*, Puerto Rico, June 22-26, 1-16.
- Taylor, Z.J., Gurka, R. and Kopp, G.A., 2009. Geometric effects on shedding frequency for bridge sections. *11th America's conference on Wind Engineering*, San Juan, Puerto Rico, June 22-26, 2009.
- Taylor, Z.J., Gurka, R. and Kopp, G.A., 2012. Features of the turbulent flow around symmetric elongated bluff bodies. *Journal of Fluid and Structures*, 27, 250-265.
- Tezduyar, T.E., Sathe, S., Pausewang, J., Schwaab, M., Christopher, J. and Crab-tree, J., 2008. Interface projection techniques for fluid-structure interaction modeling with moving-mesh methods. *Computational Mechanics*, 43, 39-49.
- Theodorsen, T., 1935. General theory of aerodynamic instability and the mechanics of flutter. *NACA report*, 496.
- Thomas, P.D. and Lombard, C.K., 1979. Geometric conservation law and its application to flow computations on moving grids. *AIAA Journal*, 17 (10), 1030-1037.

- Tominaga, Y., Mochida, A., Yoshie, R., Kataoka, H., Nozu, T., Yoshikawa, M., Shirasawa, T., 2008., AIJ guidelines for practical applications of CFD to pedestrian wind environment around buildings. *Journal of Wind Engineering and Industrial Aerodynamics*, 96(10-11), 1749-1761.
- Toro, E.F., 2009. Riemann Solvers and Numerical Methods for Fluid Dynamics. *Springer*, Third Edition.
- Tran, A.D., Katsuchi, H., Yamada, Y. and Nishio, M., 2014. Numerical analysis for effect of flap on wind across box girder section. *Journal of Structural Engineering, JSCE*, 60A, 387-396.
- Trein, C.A., 2009. Study on the unsteady pressure characteristics of bluff bodies focusing on flutter stabilization of long-span bridges. Ph.D. dissertation, *Kyoto University*, Japan:
- Trein, C.A., Shirato, H., 2010. Coupled flutter instability from the unsteady pressure characteristics point of view. *Journal of Wind Engineering and Industrial Aerodynamics*, 99 (2-3), 114-122.
- Tubin, F., 2005. Relationships among aerodynamic admittance functions, flutter derivatives and static coefficients for long-span bridges. *Journal of Wind Engineering and Industrial Aerodynamics*, 93, 929-950.
- Tuković, Z., 2005. Finite volume method on domains of varying shape (in Croatian), Ph.D. thesis, *Faculty of mechanical engineering and naval architecture, University of Zagreb*.
- Tuković, Z. and Jasak, H., 2007. Updated lagrangian finite volume solver for large deformation dynamic response of elastic body. *Transactions of FAMENA*, 31, 55-70.
- Tuković, Z. and Jasak, H., 2012. A moving mesh finite volume interface tracking method for surface tension dominated interfacial fluid flow, *Computers and Fluids*, 55, 70-84.
- Tylor, R., 2002. Tiber river bridges and the development of ancient city of Rome. *The Water of Rome, Journal*, 2, 1-20.
- Versteeg, H. and Malalasekera, W., 2007. An Introduction to Computational Fluid Dynamics: The Finite Volume Method. *Pearson*, Second Edition.
- Virola, J., 2013. The Taizhou Bridge: great 3-tower suspension bridge in China. *RIA 3/2013*. (<http://koti.kontu.la/jvirola/ria-taizhou.pdf>).
- Wang, Q., Liao, H., Li, M. and Xian, R., 2009. Wind tunnel study on aerodynamic optimization of suspension bridge deck based on flutter stability. *The Seventh Asia-Pacific Conference on Wind Engineering*, November, 8-12, Taiwan, 1-8.
- Wangsadinata, W., 1997. The Sunda strait bridge and its feasibility study as a link between Jawa and sumatera. *Report to BPP Teknologi*, Jakarta, May 1, 1997.
- Wardlawm, R.L., 1992. The improvement of aerodynamic performance, *Aerodynamic of large bridges*. Edited by A. Larsen, Balkema, Rotterdam, 59.
- Watanabe, S. and Fumoto, K., 2008. Aerodynamic study of a slotted box girder using computational fluid dynamics. *Journal of Wind Engineering and Industrial Aerodynamics*, 96, 1885-1894.

- Wesseling, P., 1992. An introduction to multigrid methods. *John Wiley & Sons*, Australia.
- Wilcox, D.C., 2006. Turbulence Modeling for CFD. *DCW Industries*, Third Edition.
- Xian, H. and Ge, Y., 2007. State-of-the-art of long-span bridge engineering in China. *Frontier in Architecture and Civil Engineering*, 1(4), 379-388.
- Yamada, H., Miyata, T. and Ichikawa, H., 1992. Measurement of aerodynamic coefficients by system identification methods. *Journal of Wind Engineering and Industrial Aerodynamics*, 42(1-3), 1255-63.
- Yamaguchi, K., Suzuki, S., Kitahara, T., Takeuci, T., Miyazaki, M. and Kazama, K., 1986. Effects of venting and fairing on vortex-induced oscillations and flutter of box bridge deck. *Proceedings of National Symposium on Wind Engineering*, 9, 217-222 (Japanese).
- Yoshida, K., Kubo, Y., Tsuji, E., Kimura, K. and Kato, K., 2006. Effects of lower plate slope on the aerodynamic characteristics of a pentagonal cross section bridge deck. *Proceedings of 19th National Symposium on Wind Engineering*, Japan, 295-300 (Japanese).
- Yu Ng, P.P., 2007. The Bridge Engineering 2 Conference. *Proceedings of Bridge Engineering 2 Conference*, University of Bath, UK.
- You, Q., He, P., Dong, X., Zhang, X. and Wu, S., 2007. Sutong Bridge- A cable-stayed bridge with main span of 1088 m. *IABSE congress*, 12/2007.